Geomechanical Analysis of Caprock Integrity

A Thesis

Submitted to the College of Graduate Studies and Research

In Partial Fulfillment of the Requirements

for the

Degree of Doctorate of Philosophy

in the

Department of Civil and Geological Engineering

University of Saskatchewan

Saskatoon

by

Hamidreza Soltanzadeh

PERMISSION TO USE

The author has agreed that the library, University of Saskatchewan, may make this thesis freely available for inspection. Moreover, the author has agreed that permission for extensive copying of this thesis for scholarly purposes may be granted by the professors who supervised the thesis work recorded herein or, in their absence, by the head of the Department or the Dean of the College in which the thesis work was done. It is understood that due recognition will be given to the author of this thesis and to the University of Saskatchewan in any use of the material in this thesis. Copying or publication or any other use of the thesis for financial gain without approval by the University of Saskatchewan and the author's written permission is prohibited.

Requests for permission to copy or to make any other use of material in this thesis in whole or part should be addressed to:

> Head of Department of Civil Engineering
> University of Saskatchewan
> Engineering Building
> 57 Campus Drive
> Saskatoon, Saskatchewan
> Canada, S7N 5A9

Hamidrzea Soltanzadeh
August 1st , 2009

Abstract

To safely store carbon dioxide in enhanced oil recovery/ CO_2 sequestration projects it is important to ensure the integrity of the caprock during and after production and injection. A change in fluid pressure and temperature within a porous reservoir will generally induce stress changes within the reservoir and the rocks that surround it. Amongst the potential hazards resulting from these induced stress changes is the reactivation of existing faults or fractures and inducing new fractures, which may breach the hydraulic integrity of the caprock that bounds the reservoir.

The theories of inclusions and inhomogeneities have been used in this research to derive semi-analytical and closed-form solutions for induced stress change during pore pressure change within a reservoir and in the surrounding rock, under plane strain and axisymmetric conditions. Methods have been developed to assess fault reactivation and induced fracturing during injection or production within a reservoir. The failure stress change concept for a Coulomb failure criterion has been used to study the likelihood of fault reactivation and induced fracturing within the reservoir. Formulations have been adopted to calculate the critical pressure change for fault reactivation and induced fracturing within the reservoir and in the surrounding rock during injection and production. Sensitivity analysis has been performed to study the effects of different parameters such as initial in-situ stress, reservoir geometry, reservoir depth, reservoir "tilt" or dip , material property contrast between the reservoir and surrounding rock, fault geometry, fault strength, and intact rock strength. General patterns of induced stress change, in-situ stress evolution, fault reactivation, and induced fracturing have been identified.

The developed methodologies have been applied to six different case studies: fault reactivation analysis in the entire field for a synthetic case study; induced fracturing analysis in the entire field in a synthetic case study; fault reactivation and induced stress change analysis within the Ekofisk oil reservoir in North Sea; fault reactivation analysis in the Lacq gas reservoir in France; the Weyburn-Midale EOR/CO$_2$ Storage project in southeast Saskatchewan; and acid gas injection in Zama oil field, Alberta. The results of these case studies show good consistency with field observation, and physical and numerical models.

The generality, simplicity, and straightforwardness of the developed methodologies, along with their flexibility to model different plausible scenarios and their ease of implementation for systematic sensitivity analyses makes them suitable for decision-making and uncertainty management, specifically in early stages of reservoir development or site assessment for geological sequestration of carbon dioxide.

ACKNOWLEDGEMENT

DEDICATION

This work is dedicated to:

Reyhaneh Haghighi

TABLE OF CONTENTS

Chapter 2- Literature review on production- and injection-induced stress change within and surrounding porous reservoirs

Chapter 3 - Induced stress change modeling

Chapter 6 - Case Studies

LIST OF TABLES

LIST OF FIGURES

Chapter 1

Introduction

1.1. Background

Geological storage of harmful wastes under ground is not a new issue. By 1968 in excess of 110 deep industrial-waste injection wells in the United States were being used to inject a large variety of waste in many different conditions (Warner, 1968). In the 1990's, the idea of geological storage of carbon dioxide (CO_2) began to be investigated (e.g., Koide et al., 1992). Nowadays, storage of greenhouse gases such as carbon dioxide under ground is one of the hottest topics in environmental debates on global climate change, attracting attention because of its high storage capacity and the reasonable execution cost. The Weyburn-Midale CO_2 Monitoring and Storage Project in Southeast Saskatchewan, the Sleipner CO_2 storage project in the North Sea, and the In Salah CO_2 Storage project in Algeria are some current examples of full-scale CO_2 storage projects. However, current concerns exist due to potential risks such as seismic reactivation of the field area as well as environmental and health concerns on leaking CO_2 from the storage unit to atmosphere or groundwater. These concerns, along with economic and technical risks, make a decisive need to develop efficient risk management methods to carry out an evaluation of the prospective risks and to employ practical methods to minimize those risks.

1.2. Risks of geological storage of carbon dioxide

During and after injection, the potential risks of underground CO_2 storage include escape of CO_2 from the reservoir (leakage), seismicity, ground movement and

displacement of brine. Many cases have been documented in which earthquakes, sometimes as large as 5.5 on the Richter scale, have been induced by production or injection of gas or water (e.g., Wesson and Nicholson, 1987; Grasso, 1992; Guha, 2000; Adushkin et al., 2000; Sminchak and Gupta., 2003; Ottemöller et al., 2005). Although there have been some efforts to explain the process leading to the seismicity in hydrocarbon production fields (e.g., Roest and Kuilman, 1994; Segall et al., 1994), still there is no clear and straightforward assessment tool to describe induced seismicity during both production and injection. The mechanisms of ground surface movement during production have been under study for many years (e.g., Geertsma, 1973; Feignier and Grasso, 1990; Chin and Nagel 2004), but still prediction is difficult (Hettema et al., 2002). In addition, there are many evidences of well failure caused by horizontal ground movement and faults sliding during production (Bruno, 1992; Hilbert et al., 1996). Brine displacement, when injecting CO_2 in an aquifer, depends too much on local/regional conditions to draw general conclusions on the risk caused by it (Damen et al., 2003).

The main goal of geological storage is trapping CO_2 underground for an unlimited period of time. Therefore, evaluation of leakage potential of CO_2 from the reservoir is one of the major requirements for site selection and evaluation. Depending on the time period, the CO_2 trapping mechanism could be different. Long-term trapping is based on the solubility and ionic reaction, geochemical and/or irreducible saturation (Jimenez, 2006). However, in the short-term or injection phase, the integrity of the caprock must be considered as the main trapping mechanism. Therefore, for geological storage of CO_2, the integrity assessment of the caprock is very critical. Leakage of CO_2 from the reservoir can also take place through or along wells and by failure in the caprock (Figure 1.1). A caprock failure includes a variety of mechanisms resulting into CO_2 migration through high permeability zones in the caprock or through faults and fractures, which extend into the caprock.
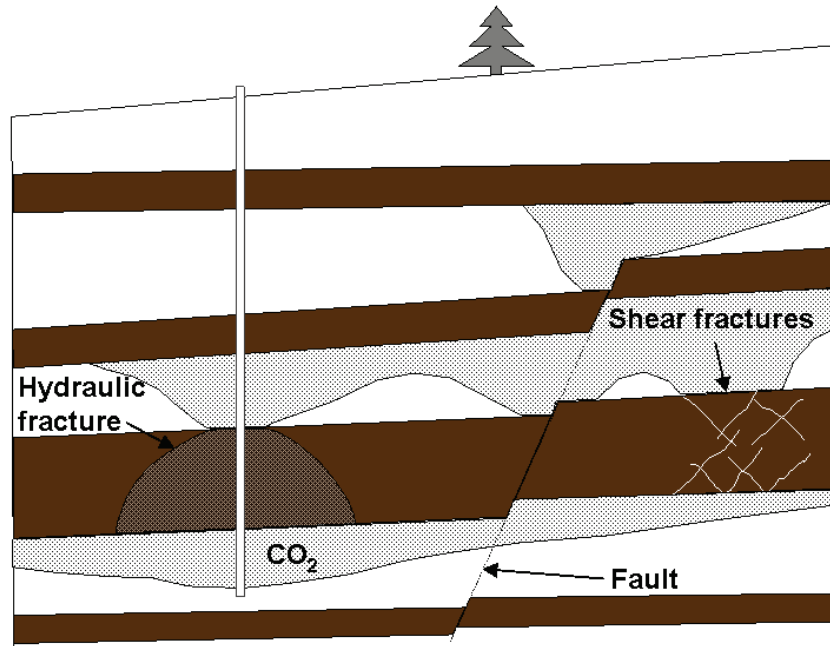
Figure 1.1. Different possible hazards induced by CO_2 injection within a reservoir

Leakage through faults and fractures is generally considered to be the most important natural leakage pathway (Khilyuk et al., 2000). These risks are called geomechanical risks due to the fact that they are related to the geomechnaical response of the reservoir and caprock to pressure and temperature change within the reservoir.

1.3. Geomechanical risks of CO_2 geological storage

As mentioned above, geomechanical mechanisms are among the main concerns about short-term integrity of the caprock. Changing the pore fluid pressure and temperature in a reservoir will result in the generation of mechanical stresses in the vicinity of the reservoir. The potential exists for these stresses to induce failure in the reservoir's bounding seal. These failure events may result in relatively permeable flow paths that enable leakage of the reservoir fluids into the surrounding geological formations, and potentially to ground surface or into shallow aquifers. As such, when evaluating the suitability of a reservoir for CO_2 storage, it is important to recognize the types of failure mechanisms that may occur, and their likelihood.

Jimenez and Chalaturnyk (2002) have categorized typical geomechanical risks that may lead to leakage by influencing the hydraulic integrity of caprock during and after injection of CO_2 gases in three different groups: storage-induced, storage-activated and tectonic activity (Figure 1.2). In their work, storage-induced mechanisms include capillary leakage, hydraulic fracturing and shear fracturing. Storage-activated mechanisms include fault reactivation and reactivation of pre-existing fractures. Tectonically active regions are considered separately, and may be avoided by locating the project site in non-seismic regions. Wellbores are other features which may leak after geomechanical instabilities as well as other mechanisms. The current research includes analyzing induced shear and tensile fracturing, fault reactivation and pre-existing features reactivation. All of these hazards may lead to leakage and/or seismic events. Particular emphasis in previous and ongoing work has been placed on quantifying the factors that control leakage risks through wellbores (e.g., Celia et al., 2004; Carey et al., 2007; Barlet-Gouédard et al., 2008) and it has been out of scope of this research.

1.4. Geomechancial modeling

Any model consists of three main parts: data, system and results. Regardless of the confidence in the analyzing system, preparing data for analysis is an important part
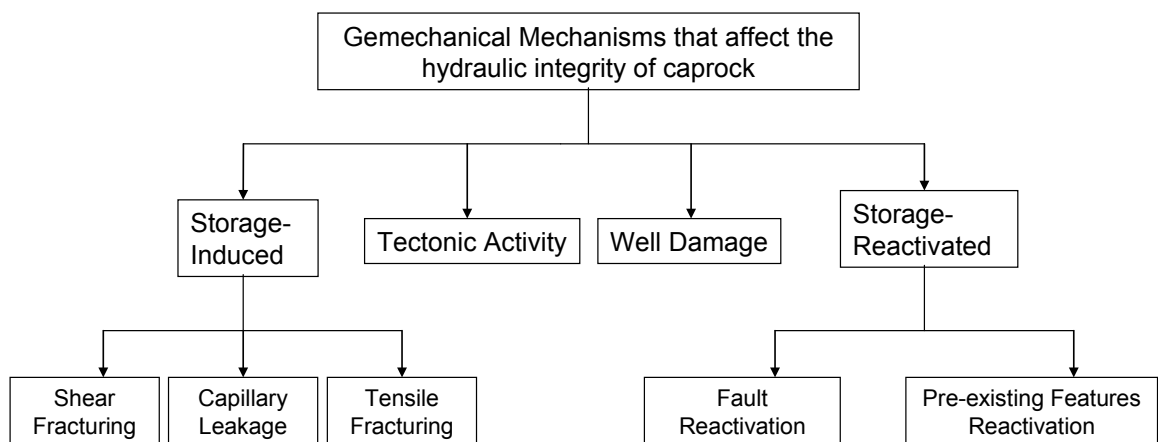
Figure 1.2. Different categories of geomechanical risks, revised after Jimenez and Chalaturnyk (2002)

of a model system. Generally, for a geomechanical model of a CO_2 storage project there are different groups of required data including: geometry of reservoir and geological features, geomechanical and geothermal properties, fluid properties and fluid flow-related properties, field production/injection history and future plans, wellbore characteristics, seismological and leakage history of the project[1]. In an ideal case, all of these data may be used in a perfect analyzing system to find the probability of geomechanical risks. Although completeness of the analysis system may require more data, sometimes shortage of proper data may lead to using a less complicated model. In general, the process of data collection for a model depends on the description of intention, availability of data and requirements of the analytical system.

The existing models for geomechanical analysis of reservoirs might be categorized in three different groups: simple analytical models, semi-analytical models and numerical models. Simple analytical models have been developed by using basic concepts of uniaxial poro-elasticity (e.g., Hawkes et al., 2005), reservoir normal compaction (e.g., Goulty, 2003), or frictional equilibrium mechanisms (e.g., Holt et al., 2004). Semi-analytical models implement analytical solutions accompanied by numerical integration procedures to find the stress change distribution throughout a field. These models are usually developed using the assumption of a poroelastic material behaviour for the reservoir and the surrounding rocks (e.g., Segall, 1985). In addition, usually they are constrained by simplified geometrical and fluid flow assumptions. To consider more complicated characteristics of problems, such as more realistic geometry and material properties, the use of numerical models is essential. One of the most important advantages of some numerical models is their ability to model discontinuities, such as faults and weak shear zones that exist in the field.

Regardless of the underlying physical principles and solution methods of selected models, they may be applied to reservoir geomechanics in two different ways: to provide general solutions, or site-specific solutions. General solutions are developed to give a better understanding of reservoir behaviour with very general characteristics.

---

[1] It is worthy to note that in the case of CO_2 storage in depleted oil and gas reservoirs, the history of production may have an important influence on geomechanical behaviour of the field during injection.

They are usually used to conduct sensitivity analysis to find the importance of different properties and parameters on the response of the reservoir and its bounding seal. Alternatively, site-specific solutions are developed to investigate a particular phenomenon (e.g., surface subsidence, fault reactivation, or induced fracturing) within a particular field. However, previous efforts to characterize geomechanics-related leakage risks through caprocks have either been too general to provide a well-defined methodology for establishing a framework for caprock integrity analysis (e.g., Streit and Hillis, 2002; Hawkes et al., 2005), or too site-specific to be of value for application in a broader range of storage design processes (e.g., Orlic, 2005).

1.5. Objectives

A key to the success of long-term CO_2 storage in a reservoir is the hydraulic integrity of the geological formations that bound it. The initial integrity of this "bounding seal" is governed by geological factors. The overall objective of this research project was to develop a better understanding of the potential for leakage caused by geomechanical processes during CO_2 storage. The specific objectives were:

- To develop computational tools (spreadsheets and/or computer programs) for investigating fault reactivation and induced shear and tensile[2] fracturing which can be used for a quantitative process for identifying potential leakage pathways for candidate storage reservoirs
- To validate the developed tools against published case histories and numerical models.

The results will be useful both for initial site assessment (i.e., to assess the potential that leakage pathways created during hydrocarbon production) and for the preliminary design of planned storage operations.

---

[2] There are two aspects of induced tensile fracturing. One that pertains to near-well stress concentrations and the conditions required to generate a relatively localized tensile (hydraulic) fracture at the wellbore wall. The second that pertains to the stress state throughout the remainder of the reservoir, and the conditions required to generate a large-scale tensile fracture. This project will focus on the latter.

1.6. Research Project Scope

The focus of this research project has been on depleted hydrocarbon reservoirs used for CO_2 storage, even though many of the models developed are also useful for other CO_2 geological storage methods such as saline aquifers and coal seams. This research project has not addressed the assessment of initial fault seal properties, which have been assumed to be good for reservoirs that have proven to contain significant hydrocarbon volumes, but rather on the geomechanical factors that may have introduced (or enhanced) leakage pathways at some point during the reservoir's producing life, or may do so during planned injection and storage operations. The research project includes analysis of tensile and shear fracture inititation, fault reactivation and other pre-existing features reactivation.

In this research project, the major work has been on developing generalized and easily applicable models that can be applied to a large variety of CO_2 geological storage projects and in cases where data availability is limited. The research project has focused on parameter sensitivity analyses and the development of general-purpose design charts, rather than site-specific analyses.

The models developed have been adopted only for geomechanical analysis and not for the process of fluid/gas migration through faults and fractures. In this research project, the major tool for stress-strain analysis has been two dimensional elastic modeling. The applied criteria for rock failure and fault reactivation have been the Coulomb and Drucker-Prager failure criteria. Model development was implemented in general form; this assisted in applying the model to different cases and projects with no need to acquire data from costly and time-consuming field tests and experiments. The following conservative assumption have been made: any failure in the rock will result in significant permeability increase (Hickman et al., 1997; Wiprut and Zoback, 2000, Zoback, 2007). As such, the hydraulic behavior of the interface of faults and fractures has not been addressed. As mentioned above, in the case of CO_2 storage in depleted oil and gas reservoirs, the history of production may have an important influence on the geomechanical behaviour of the field during injection. In addition, the performance of

the reservoir during production might be a very helpful guideline to predict its behaviour during injection. In light of these facts, particular attention has been paid to hydrocarbon production case studies and exploitation operational histories in this research project. The geomechanical effects of temperature change due to injection of fluids have been studied in this research although for idealized boundary conditions. The interaction of fluid flow/temperature change with rock deformation is out of scope of this research. As a byproduct of this research, some procedures have been developed to assess the risk of injection/production-induced earthquakes. .

1.7. Methodology

1) Conduct a literature review to compile a list of different mechanisms leading to:
    a. Stress change due to the pore pressure/temperature change within reservoirs.
    b. Fault reactivation due to stress change.
    c. Rock fracturing due to stress change, including shear and tensile fracturing.
2) Review similar site-specific analyses for the Weyburn project in Saskatchewan and hydrocarbon production projects such as the Lacq gas field in France, the Ekofisk oil field in the North Sea.
3) Derive analytical solutions, based on the theories of nuclei of strain, inclusions, and inhomogeneities, for geomechanical stress/strain analysis of reservoirs and surrounding rocks.
4) Integrate the aforementioned stress/strain analysis models with failure assessment approaches, such as Coulomb Failure Stress Change (ΔCFS), to develop tools to identify the possibility of fracturing or reactivation during fluid injection/production. Such analysis may help to understand general patterns of anticipated fracturing or reactivation.
5) Evaluate the developed tools and procedures using field data and modeling results acquired from existing case studies in the literature

6) Run a comprehensive series of simulations, to quantify the effects of the following types of parameters on caprock integrity risks: reservoir thickness, reservoir shape, contrast between reservoir and caprock mechanical properties, reservoir depth, and reservoir tilt (dip).

7) Apply the adopted methodology to selected case studies.

1.8. Novel work presented in this thesis

Although the application of Eshelby's inclusion theory and the theory of inhomogeneities to the study of poroelastic reservoirs has been undertaken by previous investigators, and various stress analysis models have previously been applied to the study of fault reactivation and induced fracturing in and around porous reservoirs, a number of gaps were found in both of these areas. The novel work presented in this thesis was undertaken to fill these gaps. Following is a summary of the novel aspects of this thesis:

- Applying the theory of inclusions to derive equations for induced stress changes: (a) within reservoirs of the following shape embedded in a full-space - prolate spheroid, sphere, and elliptic cylinder; and (b) within and around horizontal or tilted reservoirs with rectangular or elliptical cross-sections under plane strain conditions, when embedded in a half-space;

- Applying the theory of inhomogeneities to derive equations for induced stress changes: (a) within reservoirs with oblate spheroid, prolate spheroid, penny-shaped, elliptical cylinder and circular cylinder shapes for a full-space; and (b) within and around a reservoir with elliptical cross-section in a plane strain solution for a half-space;

- Implementing the concept of Coulomb Failure Stress for studying the likelihood of fault reactivation and for identifying critical fault dip angles for fault reactivation;

- Using the above-noted equations and concepts to derive equations for critical reservoir pressure change for fault reactivation for plane strain and three-dimensional scenarios;

- Using the above-noted equations and concepts to derive equations for the likelihood of induced fracturing;
- Using the above-noted equations and concepts to derive equations for the critical pressure change for induced fracturing for plane strain and three dimensional scenarios;
- Using the above-noted analytical approaches to systematically study patterns of induced stress change, stress evolution, fault reactivation and induced fracturing;
- Applying all of the above to the study of six specific case studies.

1.9. Structure of the thesis

This thesis includes seven chapters. The current chapter describes the background, description of intention, objectives, scope, and methodology of this research project. A literature review on the measurement, mechanisms, and modeling of induced stress change plus methodologies for fault reactivation and fracturing induced by reservoir pressure change is given in Chapter 2. Chapter 3 focuses on developing new closed-form and semi-analytical solutions for the problem of induced stress change using the theories of inclusions and inhomogeneities. Chapters 4 and 5 propose methodologies for fault reactivation and analysis of induce fracturing by reservoir pressure change, respectively. In Chapter 6 the methodologies developed in this research project are applied to six different case studies including: two synthetic case studies. Chapter 7 summarizes the thesis and its conclusions.

Chapter 2

Literature review on production- and injection-induced stress change within and surrounding porous reservoirs

2.1. Introduction

Any model used to analyze the potential geomechanical risks for CO_2 storage must include two main modules: One for analysing stress change induced by CO_2 injection and another for analyzing the behavior of geological features (e.g., intact rock, existing fractures, and faults) in response to the induced stress change. However, sometimes it is difficult to distinguish between these two modules because of their highly integrated nature. In this chapter, a literature review on different proposed mechanisms, and models developed for the prediction of induced stress change, is given. In addition, the application of such models to fault reactivation is reviewed.

2.2. Induced stress change measurement

Due to the difficulty of directly measuring vertical and maximum horizontal stresses in sedimentary basins, studies on stress change have mostly concentrated on measuring and predicting minimum horizontal stress change ($\Delta\sigma_{Hmin}$) - the magnitude of which can be more readily measured. The sensitivity of σ_{Hmin} to pore pressure change has long been recognized in the petroleum industry, most notably by those working on

hydraulic fracturing (Santarelli et al., 1996). As such, there are several published case histories showing the relationship between pore pressure change and the change in minimum horizontal stress (see Table 2.1).

To relate the minimum horizontal stress change to pore pressure change (ΔP), a linear trend has been interpreted by many different investigators (e.g., Teufel and Rhett, 1991; Zoback and Zinke, 2002; Goulty, 2003; Hawkes et al., 2005;). Such a relationship can be written as:

$$\Delta \sigma_{H\min} = K \Delta P \qquad\qquad (2.1)$$

A number of published values of K interpreted for different fields are presented in Table 2.1. These results indicate that K ranges from 0.24 to 0.84. Table 2.1 shows a clear distinction between chalk and sandstone reservoirs. Chalk reservoirs typically have larger K-values than sandstone reservoirs. One might intuitively expect that, for a given lithology, K-values would increase with porosity. The data reported in Table 2.1 seem to be generally consistent with this trend, although there are some discrepancies which cannot be resolved with the information available.

All values of K in Table 2.1 were measured during fluid production operations (i.e., decreasing pore pressure). Due to the hysteretic character of reservoir rocks, a substantial difference between production and injection (i.e., unloading and loading of rock) effects is expected (Holt et al., 2004). A measurement of injection-induced stress change was reported by Santarelli et al. (1996) for an unnamed, poorly consolidated sandstone reservoir in the Norwegian sector of the North Sea, operated by Saga Petroleum. The results showed that no significant change in stress occurred in the reservoir (less than 4%) after injection. This result contrasted significantly with the K values of 0.42 and 0.70 interpreted for this reservoir during production (Table 2.1, Reference 10). The magnitude of this hysteresis effect may be considerably less in other reservoirs, depending for example on the degree of over- or under-consolidation and cementation of the reservoir rock, initial reservoir pressure (e.g., over-pressuring), magnitude of the pressure change, and reservoir depth.

Table 2.1. Stress change measurement within reservoirs

Field	Measured value of K	Porosity (%)	Reservoir Rock	Stress regime	Comments
Vicksburg Formation, south Texas	0.53 [1],[2] 0.48 [3]	21% [4]	Stacked deltaic sands [1]	Listric normal (growth) faults [1]	Stress-pressure depletion data taken from three fields, the McAllen Ranch, the Javellina and the McCook fields [1]
Ekofisk, central North Sea	0.8 on all three different regions: crest, flank, and outer flank [5] 0.84 ±0.02 on the crest and 0.82±0.09 on the flank and 0.77±0.06 on the outer flank [6]	30-48% [7]	High porosity chalk [1]	Normal [7]	The measurements were subdivided into three sections: crest, flank and outer flank of the reservoir [7]
Waskom, east Texas	0.46 [1]	7-16% [8]	Sandstone-rich sediments [1]	N/F (i.e., Not found by authors)	Data for the combined lithologies (sandstone, siltstone, limestone and shales) indicate a depletion response of 0.57 [1]
Magnus, U.K. sector of North Sea	0.68 [1]	21% [9]	Submarine fan sandstones in rotated fault blocks [1]	Normally faulted, present-day stress regime is uncertain [1]	
Valhall, Central North Sea	0.76 [5] 0.7 on the crest, 0.88 on the flank [7] 0.7 ±0.04 on the crest and 0.84±0.04 on the flank [6]	20-50% [7]	Soft chalk [7]	Normal [7]	
Unnamed in North Sea operated by Saga Petroleum	0.70 in the central part and 0.42 in the southern part [10]	N/F	Poorly consolidated sandstone [10]	N/F	$K \approx .04$ was interpreted during fluid injection. [10]
Gulf of Mexico – Field X	0.54 [11]	18-33% [11]	Deltaic sandstone [11]	Normal [11]	
McAllen Ranch field, Texas	0.5 [2]	14% [12]	Sandstone [2]	Normal [1]	
Venture Field, Nova Scotia	0.56 [13]	N/F	Sandstone [14]	N/F	
Rullison Field, Colorado	0.24 [3]	8% [15]	Sandstone [3]	N/F	Gas deposit is an aggregate of hundreds of separate small accumulations in discontinuous sandstone bodies. [16]
Rotliegend field, North Sea	0.69 [3]	15-20% [16]	Sandstone [3]	N/F	
Eldfisk, North Sea	0.84 [3]	17-50% [17]	Soft chalk [17]	N/F	
Wytch Farm Field, England	0.65 [1] , 0.55 [13]	10-18% [18]	Sandstone [1]	Normal [1]	

(1) Addis, 1997 (2) Khan and Tuefel, 1996 (3) Khan et al., 2000 (4) Al-Shaieb et al., 2000 (5) Tuefel and Rhett, 1991 (6) Goulty, 2003 (7) Zoback and Zinke, 2002 (8) Desbrandes and Yildiz, 1991 (9) Strachan et al., 2004 (10) Santarelli et al., 1996 (11) Chan and Zoback, 2002 (12) Tucker, 1979 (13) Wu and Addis, 1998 (14) Lubomir and Urrea, 1990 (15) Coffler et al., 1970 (16) LaFleur and Johnson, 1973 (17) Cook and Berkke, 2004 (18) Brown et al., 2000

2.3. Mechanisms of stress change

Due to the complexity and heterogeneity of geological formations, the large spatial and temporal dimensions of geological features, and the lack of field test data, still no integrated explanation for the mechanisms of stress change during injection or production has been presented. However, there have been some attempts to explain the different possible mechanisms for stress change. In general, two categories of mechanisms including poro-mechanical behaviour of rocks and frictional equilibrium have been introduced to interpret the stress change effect during pore pressure change within a reservoir.

2.3.1. Poro-mechanical mechanism

The mechanical interaction between solid rock and its pore fluid can be explained using poro-mechanical models which consider the rock as a two or three phase matrix including solids and fluids. Due to this mechanism, depending on the overconsolidation rate and cemented nature of the reservoir, reservoir deformation follows either a reloading path (i.e., stiff response) or a loading path (i.e., soft response) path during depletion, which corresponds to increases in effective stresses. During injection, a decrease in effective stresses within the reservoir occurs which leads to elastic unloading (i.e., stiff response) (Goulty, 2003). Usually, the stiff response of the reservoir during either production or injection is assumed to be linear and reversible, i.e., poroelastic. In this condition, it is possible to use poroelastic models to analyze the change in stress state. For instance, as it is commonly used, the uniaxial compaction model for a reservoir gives the following result (e.g., Addis, 1997):

$$\frac{\Delta \sigma_H}{\Delta P} = \alpha \frac{1 - 2v}{1 - v} \tag{2.2}$$

Where $\Delta \sigma_H$ indicates the change in horizontal stress within the reservoir and α and v, respectively, are Biot's coefficient and Poisson's ratio of the reservoir rock. Due to its simplicity and the limited amount of required input data, poroelastic modeling has been widely used by researchers to study geomechanical behavior of reservoirs (e.g., Addis,

1997, Zoback and Zinke, 2002; Goulty, 2003; Hawkes et al., 2005;). However, making a decision to choose between an elastic or elastoplastic model has been one of the main challenges for geomechanical modeling. Elastic models have been considered sufficiently reasonable when the pore pressure change is slow enough or sensibly small (Morita et al., 1989) or when the reservoir rock is well-cemented (Dake, 2001) or overconsolidated (Goulty, 2003). However, inelastic deformations have been recorded for unconsolidated sand (Dake, 2001) and chalk (Johnson et al., 1989). Studies of Engelder and Fischer (1994) on the overpressured parts of the North Sea graben in United Kingdom and the Sable sub-basin of the Scotian Shelf in Canada show that choosing poroelastic behaviour can reasonably explain the patterns of horizontal stress change in these fields.

As a practical tool, subsidence records can be used to study poro-mechanical reservoir behavior during production. For instance, Segall et al. (1994) applied an elastic model to analyse the Lacq gas reservoir based on the existing linear correlation between subsidence and reservoir pressure change. Based on the ground-surface subsidence behavior the aforementioned reservoirs, two groups of reservoirs have been categorized by Hettema et al. (2002). A group of reservoirs (e.g., Lacq gas reservoir, France), have a near-linear subsidence pattern. The rocks are usually well cemented and often old. These reservoirs are relatively deep (> 2 km) and their ground-surface subsidence is often small (less than a few decimeters). The second group (e.g., Ekofisk oil and gas reservoir, North Sea) initially show little compaction and subsidence, which indicates elastic behavior of the reservoir; subsequently, elastoplastic deformation of the reservoir starts. These shallow depth reservoirs (<2 km) have high porosity, contain poorly cemented granular aggregates such as sand and silt, and have beds of highly fractured chalk and diatomite.

2.3.2. Frictional Equilibrium

In critical state mechanics, where the stress state reaches the rock failure criterion, rock will redistribute stresses after failure (i.e., fracturing/faulting). Townend and Zoback (2001) believe that in-situ stresses in the crust are mainly controlled by this

mechanism. In this condition, depending upon the in-situ stress regime (e.g., normal, thrust or strike-slip faulting), there is a critical relationship between the stresses, where faults have the optimum dip angle. For example, in a normal fault stress regime, with zero fault surface cohesion and fault coefficient of friction of μ_s (Holt et al., 2004, Addis, 1997):

$$\frac{\Delta \sigma_H}{\Delta P} = 1 - (\sqrt{1 + \mu_s{}^2} - \mu_s)^2 \qquad (2.3)$$

It is believed that in an overconsolidated reservoir the competition between elastic deformation and frictional equilibrium determines the stress behaviour of the reservoir (Goulty, 2003).

2.4. Stress arching effect

The assumption of uniaxial deformation has been one of the most popular approaches to model the poro-mechanical behaviour of reservoirs. For this type of model, the reservoir is considered to be constrained laterally, and to deform solely in the vertical direction (Khan et al., 2000). Hawkes et al. (2005) considered a uniaxial compression scenario for a reservoir and used a Coulomb failure criterion to predict the range of fault dip angles which might be reactivated within reservoirs during injection and production. Streit and Hillis (2002) applied the same methodology to investigate the observed induced seismicity in the Ekofisk oil field, North Sea.

The uniaxial poroelastic model is, strictly-speaking, only appropriate for laterally infinite reservoirs. In a practical sense it is useful for reservoirs that are very thin relative to their lateral dimensions, but it is certainly not a realistic model for all reservoir geometries. For instance, lenticular sandstone reservoirs have a clearly different stress change path than do blanket sandstone reservoirs (Khan et al., 2000). In addition, many reservoirs form in folded formations which are tilted, to some extent, with respect to the principal in-situ stress directions (e.g., Lacq gas reservoir in France). Also, the uniaxial model may not be a realistic assumption if there is a significant contrast between the reservoir and the surrounding rock, which is the case for many

16

reservoirs (Morita et al., 1989), especially if reservoir does not have large lateral dimensions.

If a reservoir was a free body, effective stress changes would simply result in its contraction or expansion. However, the reservoir is "attached" to the surrounding rock, which works against the reservoir tendency to contract/expand. Due to this competition between internal driving forces and external constraints, anisotropic changes in total stress may be induced depending on reservoir geometry, mechanical property contrasts between the reservoir and its surrounding rock, and the distribution of pore pressure within the reservoir (Figure 2.1). This phenomenon has been called arching (e.g., Mulders, 2003).

Due to the fact that there can be changes in vertical stress as well as horizontal stress within and outside of a reservoir, arching ratios have been defined to give a more general explanation of stress change patterns. Arching ratios are most appropriate for poroelastic materials, where there is a linear relationship between the change in stress and the change in pore pressure and they are defined as follows (Mulders, 2003):

$$\gamma_H = \Delta\sigma_H / \Delta P , \; \gamma_V = \Delta\sigma_V / \Delta P \tag{2.4}$$
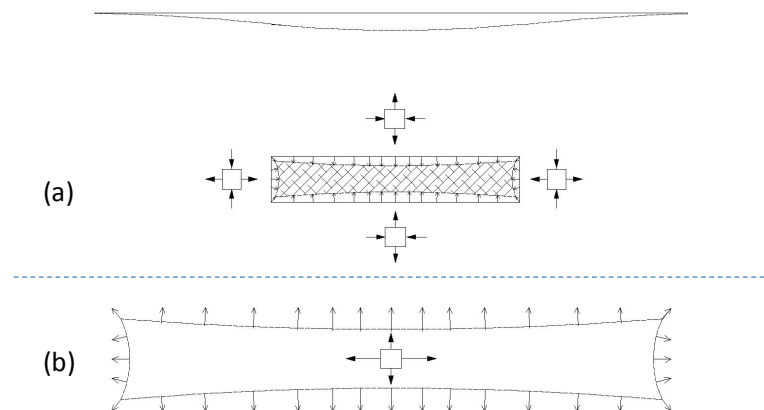
Figure 2.1. Total stress change (a) around and (b) within a reservoir induced by production

where γ_H and γ_V, respectively, are horizontal and vertical stress arching ratios; $\Delta\sigma_H$ and $\Delta\sigma_V$, respectively, are horizontal and vertical stress change and ΔP is the reservoir's pore pressure change.

The value of the vertical stress arching ratio has commonly been considered negligible for reservoirs of large lateral extents (i.e., reservoirs that deform uniaxially) (e.g., Zoback and Zinke, 2002). Unfortunately, in practice, there is no field measurement to assess the importance or magnitude of this effect. Analytical and numerical models do show, however, that arching may have a very significant effect leading to a reduction of contractile strains within a reservoir and a redistribution of in-situ stresses. For instance, Mulders (2003) stated that, for small reservoirs made up of weak rocks, about 50% of the vertical effective stress change may be arched away (i.e., $\gamma_V \cong 0.5$). Using 3D modeling, Kenter et al. (1998) interpreted that there was likely 20% to 30% vertical arching (i.e., $\gamma_V \cong 0.2$ to 0.3) during depletion of the Shearwater gas reservoir in the northern North Sea.

Stress path ratio (R_σ) is another useful parameter that accounts for both induced horizontal and vertical stresses changes within a reservoir. It is defined as the ratio of the effective horizontal stress change to the effective vertical stress change (Khan et al., 2000; Schutjens et al., 2001):

$$R_\sigma = \Delta\sigma_H' / \Delta\sigma_V' \tag{2.5}$$

2.5. Induced stress change modeling

In addition to the simple analytical approaches presented above (e.g., uniaxial elastic deformation mechanism and frictional equilibrium mechanism), some useful closed-form solutions exist for induced stress change within the reservoir (e.g., Segall and Fitzgerald, 1998; Fjær et al., 2008). Moreover, there are two main groups of models for stress analysis within and around reservoirs: semi-analytical models and numerical models. Semi-analytical models implement analytical solutions accompanied with numerical integration procedures to find the stress change distribution throughout a

field. In fact, these models do not discretize differential equations and their only discretization occurs in the numerical integration scheme. They are often capable of assessing stress changes both within a reservoir and in the surrounding rocks. These models are also based on simplified geometrical and fluid flow assumptions, and they are usually developed using the assumption of linear poroelastic material behaviour for the reservoir and the surrounding rocks (e.g., Segall, 1985).

To analyze more complicated reservoirs, accounting for more realistic geometries and rock/fluid behaviour, the use of numerical models is required. Numerical models use discretization methods in both the space and time domains and solve the resultant equations to find displacements, strains, fluid pressure, and stresses. These models commonly use finite element, finite difference, or discrete element methods for discretization. One of the most important advantages of some numerical models is their ability to model discontinuities, such as faults and weak shear zones that exist in the field.

A brief summary of several models developed and/or used to study induced stress changes, as well as some key parameter sensitivities identified using these models, is given in Table 2.2.

2.5.1. Semi-analytical analysis

Although semi-analytical models are not able to consider some of the complexities of real problems, usually the accuracy and the stability of semi-analytical models are more reliable than those of the numerical models. In any case, semi-analytical solutions for poroelastic stress and strain fields induced by subsurface fluid pressure changes are extremely useful because of their relative ease of implementation and their suitability for parameter sensitivity analyses (Wong and Lau, 2008). These methods generally try to solve the poroelastic equilibrium equations which, in their general form, are (Segall, 1992):

$$\mu \nabla^2 u_i + \frac{\mu}{1-2\nu} \frac{\partial^2 u_j}{\partial x_i \partial x_j} - \alpha \frac{\partial P}{\partial x_i} + f_i = 0 \qquad (2.6)$$

Table 2-2. Sensitivity analysis for the induced stress within reservoirs by different semi-analytical and numerical models

Title	Parameter[1]	Segall and Fitzgerald (1998)	Gambolati (1999)	Khan et al. (2000)	Mulders (2003)	Rudnicki (1999)
General features of the model	Analysis approach	Analytical (theory of inclusions)	Numerical	Numerical	Numerical	Analytical (Theory of inhomogeneities)
	Spatial limits of analysis	Within the reservoir/immediate surrounding rock	Within/outside the reservoir	Within the reservoir	Within/outside the reservoir	Within the reservoir
	Model dimensions	Axisymmetric	Axisymmetric	Axisymmetric	Plane strain Axisymmetric	Axisymmetric
Reservoir Geometry	Depth	N/A (solved for a full-space)	Not sensitive[2]	N/A (it had been considered constant during all analyses)	N/A (it had been considered constant during all analyses)	N/A (It is solved for a full-space)
	Aspect ratio (thickness/length)	γ_V increases. γ_H decreases.	N/A	R_σ increases.	γ_V increases. γ_H decreases.	γ_V increases. γ_H decreases.
	Shape	Penny-shaped	Disk-shaped	Disk-shaped	Ellipsoidal and disk-shaped	Ellipsoidal
	Size	Not dependent on size	A very specific size modeled	N/A	N/A	Not dependent on size
	Tilt Angle	N/A	N/A	N/A	γ_V increases. γ_H decreases.	N/A
Elastic Properties	Contrast in shear modulus ($R_\mu=\mu^*/\mu$)	N/A	N/A	R_σ increases.	N/A	γ_V and γ_H decrease.
	Reservoir Poisson's ratio	N/A	N/A	R_σ increases.	γ_V and γ_H decrease.	γ_V and γ_H decrease.
	Surrounding rock Poisson's ratio	N/A	N/A	R_σ decreases.	Negligible	Negligible
Transversely Anisotropy	of reservoir	N/A	N/A	R_σ Increases.[3]	N/A	N/A
	of surrounding rock	N/A	N/A	R_σ decreases.[3]	N/A	N/A
	of both reservoir and surrounding rock	N/A	N/A	R_σ increases.[3]	N/A	N/A
Plasticity	Plasticity of reservoir	N/A	N/A	R_σ decreases.[3]	N/A	N/A
	Plasticity of surrounding rock	N/A	N/A	R_σ increases.[3]	N/A	N/A
	Plasticity of both reservoir and surrounding rock	N/A	N/A	R_σ increases.[3]	N/A	N/A

1. For all parameters, the correspondent influence of increasing in the parameter is studied.
2. Consider the fact that in this model, the problem was solved for a particular case with a specific geometry (i.e., a very thin reservoir).
3. All these results are found by assuming very specific properties (anisotropic/plastic) for the rock.

where u_i are the displacement components, μ denotes the shear modulus, ν is the Poisson's ratio, P is the pore pressure and f_i represent the body forces.

Theory of strain nuclei

One of the first solutions for homogeneous, poroelastic media was derived using the "nuclei of strain" concept (Love, 1944; Mindlin and Cheng, 1950). This model is applied to problems where the material properties of the reservoir are the same as the surrounding rock (i.e., homogenous problem). This model was used by Geertsma (1966) to find the subsidence of reservoirs where the pore pressure change within the reservoir was considered constant over the entire reservoir. Du and Olson (2001) applied the theory of strain nuclei in a discrete way to study subsidence for different arrangements of production wells. Wong and Lau (2008) also used this theory to study the observed ground surface heave resulting from steam injection in Cold Lake oil sand reservoir in Alberta, Canada. Segall (1985) applied the theory of strain nuclei to analyze the stress distribution and fault reactivation potential in rocks surrounding a depleting reservoir in Coalinga, California. He used the model in combination with a fluid extraction formulation to simulate pore pressure change during a constant rate of production from a line of wells placed in the center of the reservoir. Baranova et al. (1999) tried to re-develop essentially the same model to study induced seismicity in the Western Canada Sedimentary Basin. As re-analyses done by this author have shown, their modelling was wrong because they did not correct a typing mistake existing in the original paper. An axisymmetric version of the model had been introduced by Segall (1992) and was successfully applied to Lacq gas reservoir to analyse and predict subsidence (Segall et al., 1994). The theory of strain nuclei is mainly restricted to the assumption of identical properties for the reservoir and surrounding rock. This theory will be addressed in detail in the next chapter.

Theory of inclusions

According to Eshelby (1957), an inclusion is a region in a homogeneous isotropic elastic medium that would undergo an arbitrary strain if it was unbounded, but

1

due to the constraint imposed by matrix that surrounds it, the strain field within it is modified. In his well-known papers on this subject, Eshelby (1957, 1959) showed that the inclusion problem is equivalent to solving the equations of elastic equilibrium for a homogeneous body with a known body force distribution.

Segall and Fitzgerald (1998) suggested using the theory of inclusions for an ellipsoidal inclusion (i.e., reservoir) in a full-space, to evaluate the possibility of fault reactivation within a reservoir during its depletion. When the reservoir is an axisymmetric reservoir with a thickness considerably less than its lateral dimensions, they proposed using an formulation for stress change within a reservoir given by Mura (1982). They applied this formulation to study the induced stress change within the Ekofisk reservoir. They also implemented this solution, in conjunction with a simplified implementation of the Coulomb Failure Stress Change concept, to investigate the general patterns of fault reactivation within the reservoir and in the rock immediately adjacent to it. Their analyses showed that, during production, there is a tendency towards fault reactivation within the reservoir and adjacent to its lateral flanks in a normal fault stress regime. Similarly, they showed a tendency towards reactivation in overlying and underlying rocks in a thrust fault stress regime. The main limitations of this model are: considering the reservoir in a full space (i.e., surrounding rock that extends to infinity in all directions); a very particular form for the reservoir geometry (i.e., elliptical); and identical material properties for both reservoir and surrounding rock (i.e., neglecting heterogeneity throughout the field).

Theory of inhomogeneities

The inability to account for material property contrasts is a key limitation of the previously discussed methods. There are many reservoirs which have remarkably different mechanical properties from the surrounding rock. For instance, for some overpressured high-porosity chalk reservoirs in North Sea the stiffness of some reservoir is 20 times lower than the surrounding rock. The opposite condition has been observed for low-porosity tight sandstones in the Unites States (Morita et al., 1989). The contrasts

between the reservoir and surrounding rock may significantly affect the magnitudes of induced stresses (Khan et al, 2000).

When the inclusion (i.e., reservoir) and matrix (i.e., surrounding rock) have different elastic properties, the inclusion is referred to as an inhomogeneity. Eshelby (1957) showed that the problem of an ellipsoidal inhomogeneity with constant eigenstrains can be transformed into an equivalent inclusion problem. Rudnicki (1999) used Eshelby's theory of inhomogeneities to solve for induced stress changes within a penny-shaped reservoir located in a full-space when the material properties of the reservoir and surrounding rock are different. He concluded that the full-space assumption is a good approximation for inhomogenities in the crust for which the depth is greater than the lateral extent. He applied this theory in conjunction with a Coulomb failure criterion for faults which are optimally oriented for frictional sliding; it was shown that, for a thrust fault stress regime, faults always tend towards stabilization during production and towards reactivation during injection. For a normal fault stress regime, the fault reactivation tendency was shown to depend on the fault surface frictional angle and the stress path. The latter parameter is a function of reservoir aspect ratio (e = thickness/width), the ratio of shear moduli in the reservoir to the surrounding rock, and Poisson's ratios of these two bodies.

Borehole stability model

Chen and Teufel (2001) used a model which originally had been provided by Ochs et al. (1997) for the purpose of studying the evolution of in-situ stresses around boreholes due to production from a well within a horizontal, elastic, isotropic and homogeneous layer with impermeable upper and lower boundaries. A plane strain condition was assumed, meaning that the thickness of the reservoir remains constant. Integration of two-dimensional Green functions was applied for solving the problem. Considering the fact that the method was developed for a transient fluid flow-stress coupling condition around a borehole, it looks too local to be applied to large reservoirs. In addition, there are some important, inconvenient assumptions for the model. The most important fact is that the reservoir is of cylindrical shape with a constant thickness,

which means that the significant vertical compaction of the reservoir is ignored in modeling. Moreover, it is considered that the tangential and radial stress changes are principal minimum and maximum stress changes; however, in most cases, this is not an acceptable assumption for practical purposes.

2.5.2. Numerical analysis

In many cases such as fault reactivation or induced fracturing analyses, to find more exact solutions for stress change, it is nessecary to relax our assumptions of idealized material behavior, pressure distribution, reservoir geometery, etc. Further to handling these factors, and others, more realistically, numerical models have the signifcant advantage of being able to consider pore pressure-stress coupling while solving coupled geomechanical flow and geomechanical equations.

Applied numerical models for the study of induced stress change that occur during both production and injection may be categorized in two main groups: general solutions and site-specific solutions. General solutions are developed to give a better understanding of the reservoir behaviour with very general characteristics. Generally, they are accompanied with sensivity analysis to find the importance of different properties and parameters on the medium response to fluid pressure change. Alternatively, site-specific solutions are developed to investigate a particular phenomenon (e.g., surface subsidence, fault reactivation, induced fracturing) within a specific field. This phenomenon is usually the consequence of stress changes, and the foremost attention in these problems is usually given to the study of the intended phenomenon.

Table 2.3 lists some numerical models which have been used to study the consequences of production or injection within specific reservoirs around the world. These models mainly were constructed to study the observed or expected induced seismicity in producing reservoirs or to study the caprock integrity of reservoirs as containers for the injected fluids.

Table 2.3. A list of reviewed numerical models applied for geomechanical hazard assessment during fluid production/injection within reservoirs

Field	Assumed initial stress regime	Purpose of study	Degree of coupling between geomechanical and fluid flow models	Software for geomechanical analysis - numerical approach	Gemoetry	Rock constitutive model + Failure criterion	Fault constitutive model	Results and comments
Eleved gas reservoir, Netherland [1]	Normal fault	Observed Induced seismicity in the field during production	Coupled, but the extent of coupling is not been described.	FLAC^{2D} - Finite difference	Plain strain	Elasto-plastic; Mohr-Coulomb	N/F – strength modeled by Mohr-Coulomb failure criterion	▪ the induced displacements on the fault's surface used as the indicator for reactivation of the fault and also for calculating the magnitude of expected seismic events ▪ The results supported the occurrence of observed induced seismicity in the past history of the reservoir
Field B, North Sea [2]	Thrust fault	Evolution of stresses and the displacement of faults as the result of production	Explicit one way coupling	N/F – Finite element	Plain strain	Elasto-plastic; Drucker-Prager –Van-Eekelen yield criterion	elsto-plastic joint elements with Mohr-Coulomb frictional criterion	▪ The induced normal and shear displacements on the fault used as the indicators for fault reactivation. ▪ Some faults become reactivated after depletion.
Sleipner CO$_2$ sequestration project, North Sea [3]	Strike-slip fault	To study the caprock integrity (fractures)	N/F	VISAGE - Finite element	Axisymmetric	Elasto-plastic; Mohr-Coulomb	N/A	▪ Fault reactivation was not studied ▪ The results show no evidence of induced fracturing in the caprock as a result of CO$_2$ injection in the saline aquifer beneath it.
Sleipner CO$_2$ sequestration project, North Sea [3]	N/F	To study the caprock integrity	Coupled, but the extent of coupling is not been described..	DIANA - Finite element	Plain strain	Elasto-plastic; Mohr-Coulomb	N/F – strength modeled by Mohr-Coulomb failure criterion	▪ Modeled with this fictitious assumption that CO$_2$ would be injected into the same formation which the gas in this field has been produced. ▪ The results of this project predict no sign of the integrity deterioration for the caprock as a result of CO2 injection.
Florina natural CO$_2$ accumulation, Greece and Montmiral natural CO$_2$ accumulation in France [4]	N/F	To study the caprock integrity	Coupled, but the extent of coupling is not been described...	DIANA - Finite element	Plain strain	Elasto-plastic; Mohr-Coulomb	N/F – strength modeled by Mohr-Coulomb failure criterion	▪ Both fields have been commercially exploited. ▪ Modeling was conducted for three stages: past CO$_2$ extraction; Future CO$_2$ extraction, and possible future CO$_2$ extraction ▪ A possible slip along faults during injection was predicted

Table 2.3 (continued). A list of reviewed numerical models applied for geomechanical hazard assessment during fluid production/injection within reservoirs

Field	Assumed initial stress regime	Purpose of study	Degree of coupling between geomechanical and fluid flow models	Software for geomechanical analysis - numerical approach	Gemoetery	Rock constitutive model + Failure criterion	Fault constitutive model	Results and comments
Weyburn-Midale CO_2 Storage and Monitoring Project[5]	Different scenarios (i.e., normal, thrust, strike-slip and isotropic)	To study the caprock integrity	Explicit one way modeling	$FLAC^{3D}$ - Finite difference	Three dimensional	Elasto-plastic; Hoek-Brown and Mohr-Coulomb	N/A - strength modeled by Mohr-Coulomb failure criterion	▪ The reservoir and caprock are safe if the pressures are kept below hydraulic fracturing pressure. ▪ During injection the potential for the reactivation of strike-slip faults is significant. It is medium for reverse (thrust fault) regime and small for normal fault regime
A synthetic case study – deep underground injection of supercritical CO_2[6]	isotropic	Spread of CO2 Plume, ground surface uplift, Induced stress change and its effect on permeability, hydraulic fracturing and fault reactivation	Coupled, but the extent of coupling is not been described.	Tough2 (for fluid flow simulation) and FLAC3D (for geomechancial analysis)	Plain-starin	Poroelastic	Poroelastic vertical fault zone - strength modeled by Mohr-Coulomb failure criterion	▪ Breakthrough of CO_2 from caprock was studied by defing a high porosity fractured vertical fault zone in the caprock. ▪ Low-angle faults and horizontal hydraulic fracturing is mostly possible in lower part of the caprock without likelihood of propagation upward.

(1) Roest and Kuilman, 1994 (2) Samier et al., 2006 (3) Zweigel and Heil, 2003 (4) NASCENT, 2005 (5) Jimenez, 2006 (6) Rutqvist et al., 2002

Further to the site-specific numerical modeling summarized in Table 2.3 several more general studies of production-/injection-induced stress change have been conducted using numerical models, as follows:

A numerical study on the behaviour of a reservoir (2000 m radius, 50 m thickness) during depletion has been carried out by Gambolati et al. (1999). They considered the reservoir to behave elastically and isotropically. Their study indicates that induced stresses for a laterally constrained, cylinderical reservoir embedded in a half space, stresses are quite uniform throughout the reservoir except in a small region on the boundary of the reservoir. In the interior portion of the reservoir, shear stress is zero but close to the edges of the reservoir large shear stresses develop with a magnitude roughly equal to the horizontal stresses. Using this model, it is concluded that an odeometer test is the most appropriate test for assessing a hydrocarbon field's compressibility. The main shortcoming of the study is the very specific geometry for the reservoir that was considered (i.e, a very small aspect ratio, $e = 0.025$). For a reservoir with such a low aspect ratio, some of the results, such as independency of induced stresses on the reservoir depth (see Table 2.2), are not surprising considering the fact that $e = 0.025$ is not significantly different from a laterally infinite reservoir (i.e., $e = 0$).

Morita et al. (1989) used a finite element model of a general disk-shape reservoir for a sensitivity study on the effects of reservoir geometry, burial depth, and material properties contrast with surrounding rock on reservoir compaction, subsidence, and induced stress change within the reservoir. Studying the contrast between the reservoir and the confining formation showed that, if the contrast is small, the change in the overburden stress is insignificant, although it increases slightly towards the flanks of the reservoir. The stress in the caprock significantly increases if the reservoir is weak compared with the surrounding rock. Their study for thin reservoirs showed significant vertical effective stress change but trivial horizontal effective stress change within the reservoir.

Khan et al. (2000) developed a geomechanical model to determine the effects of geological and geomechanical factors that control the reservoir stress path within a

reservoir during production. A production well was placed at the center of the reservoir. The effects of reservoir geometry of lenticular reservoirs and contrasts in elastic properties between the reservoir, and surrounding rock were evaluated. A specific depth was considered for the reservoir and reservoir geometry was changed by varying the aspect ratio. The effects of elastic properties and the contrast between the reservoir and surrounding rock, anisotropy, and plasticity were considered in this study. They concluded that uniaxial deformation is only a reasonable approximation if, simultaneously, the ratio of the shear modulus of the reservoir to surrounding rock is between 0.2 and 1.5, the depth of the reservoir is more than its half-width, and the aspect ratio of the reservoir is less than 0.05.

Mulders (2003) studied the stress change within and outside of reservoirs when the pore pressure change distribution is constant throughout the entire reservoir. This study gives an overview of stress development during depletion of ellipsoidal and disk-shaped hydrocarbon reservoirs which shows that the calculated stress change in the disk-shaped reservoir is not constant within the reservoir as it is within the ellipsoidal reservoir (Figure 2.2). There is significant variation of stress change near the lateral edges of disk-shaped reservoirs which is considerably influenced by the surrounding rock. However, there is a roughly constant stress change distribution within the central part of the disk-shaped reservoir (consistent with the results of Gambolati et al., 1999), meaning that near the edges stresses are arched away from the reservoir. In addition, a sensitivity analysis was carried out to find the influence of several parameters, including reservoir rock properties, surrounding rock properties, reservoir geometry (depth and aspect ratio) and reservoir tilting, on the stress development within and around reservoirs (see Table 2.2). The study shows that the numerically calculated values of arching ratios at the center of both ellipsoidal and disk-shaped reservoir for reservoirs with small aspect ratio ($e = 0.05$) match with the analytical values for uniaxial reservoir compaction conditions. In the surrounding rock just above and below the reservoir's centre, there is an increase in horizontal in-situ stress and a decrease in vertical in-situ stress.
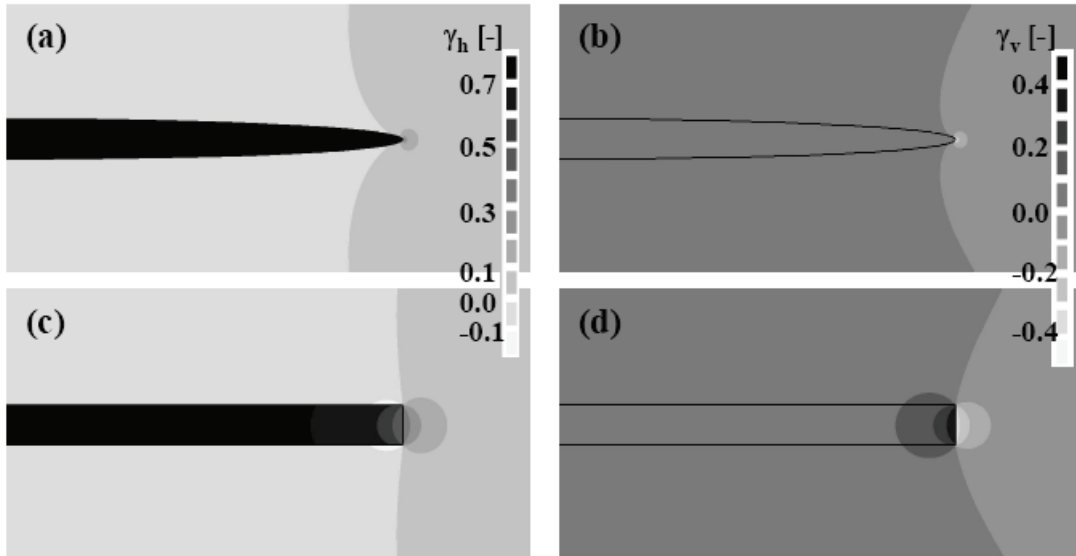
Figure 2.2. Comparison of numerically calculated arching ratios in (a) and (b) an ellipsoidal reservoir and (c) and (d) a disk-shaped reservoir (from Mulders, 2003).

Chapter 3

Induced stress change modelling

3.1. Introduction

Closed-form and semi-analytical solutions for induced poroelastic stresses and strains are extremely useful for the design of subsurface fluid storage in reservoirs because of their relative ease of implementation and their suitability for parameter sensitivity analyses. It is possible to model production and injection-induced stress changes using the theory of inclusions. Semi-analytical solutions are presented in this chapter for reservoirs with different geometries for both horizontal reservoirs, and for those that are inclined in the cross-sectional plane. In addition, Eshelby's theory of inhomogeneities is used to derive equations that can be implemented to predict the induced stresses and strains for reservoirs with ellipsoidal shape and possessing different material properties from the surrounding rocks. Stress change parameters calculated using these equations are charted for different reservoir geometries and depths using dimensionless parameters. These charts can be used to estimate induced stress changes for reservoirs of any depth or dimensions, provided their geometries are similar to the idealized geometries used for these models. Sensitivity analyses are conducted to study the effects of different parameters such as reservoir geometry (e.g., shape, depth, and tilt) and material properties on induced stress changes. It is important to note that most of modelss developed in this chapter have been verified using numerical

modelling applications (e.g., FLAC) by the author or by comparing to results presented in the literature (e.g., Mulders, 2005; Jimenez, 2006 – as presented in section 6.6 of this thesis).

The following assumptions have been made in the development of new models presented in this chapter and used in the subsequent chapters of this thesis:

- Reservoirs and their surrounding rocks are assumed to behave as homogeneous, isotropic linear-elastic continua.
- The model domains considered assume idealized reservoir geometries (2D plane strain or axisymmetric) embedded within either a full-space (i.e., the surrounding rock extends to infinity in all directions) or a half-space (i.e., accounting for the presence of ground surface, which is assumed to be planar and stress-free).
- Given the adopted assumption of continuum mechanics material behavior, the effects of displacements on and propagation of newly-induced or existing faults and fractures have not been considered. The intent of the models developed in this work is to assess if induced stresses will induce fractures or reactivate existing ones; NOT to assess how these features will behave once formed or reactivated.
- Pore pressure and temperature changes are considered to be uniform within the reservoir (although this is not necessarily a requirement for some of the models).
- The interaction of fluid flow and temperature change with rock deformation is neglected. A drained response is assumed in the rock surrounding the reservoir; i.e., it is assumed that no pressure change occurs in the surrounding rock during fluid injection into or withdrawal from the reservoir. Similarly, a condition of zero temperature change in the surrounding rock is assumed for thermoelastic problems.
- Processes of fluid migration through faults and fractures are not considered.

3.2. Elasticity field equations

The equilibrium equations for a continuous medium are:

$$\sigma_{ij,j} + b_i = 0 \tag{3.1}$$

31

where σ_{ij} is the stress tensor and b_i represents body forces. In these equations, and those that follow, Einstein's index notation has been used. More information on index notations, which are commonly used to simplify the presentation of equations involving vector or tensor fields, can be found in most continuum mechanics textbooks (e.g., Mase, 1970). For a thermo-poroelastic medium, the relationship between the stress tensor and strain tensor (ε_{ij}) can be written as follows:

$$\sigma_{ij} = C_{ijkl}\varepsilon_{kl} - \alpha P\delta_{ij} - \beta_{ij}\Delta T \qquad (3.2)$$

where C_{ijkl} is the elastic stiffness tensor, α is Biot's coefficient, P is pore pressure, δ_{ij} is the Kronecker delta, β_{ij} is the thermoelastic modulus tensor, and ΔT is the temperature change. For small strains, the relation between displacements (u_i) and strains is:

$$\varepsilon_{ij} = (u_{i,j} + u_{j,i})/2 \qquad (3.3)$$

Substituting equations (3.2) and (3.3) in equation (3.1) and using the symmetrical property of elastic stiffness tensor (i.e., $C_{ijkl}=C_{klij}=C_{ijlk}$) results in the poroelasticity displacement field equation, as follows:

$$C_{ijkl}u_{k,li} - \alpha P_{,i} - \beta_{ij}\Delta T_{,j} + b_i = 0 \qquad (3.4)$$

This equation can be written as the following general form:

$$C_{ijkl}u_{k,li} + f_i = 0 \qquad (3.5)$$

where f_i is considered to be an equivalent force which, based on superposition, is defined as a linear combination of any or all of the following: body force (b_i), pore pressure effect ($-\alpha P_{,i}$), and thermal effect ($-\beta\Delta T_{,i}$).

In the case of isotropic linear elasticity, the stiffness tensor C_{ijkl} and thermoelastic modulus tensor β_{ij} are expressed as:

$$C_{ijkl} = \frac{2\mu v}{1 - 2v} \delta_{ij} \delta_{kl} + \mu(\delta_{ik}\delta_{jl} + \delta_{il}\delta_{jk}) \tag{3.6}$$

$$\beta_{ij} = 3K\eta\delta_{ij} = \frac{2\mu(1+v)}{1-2v}\eta\delta_{ij} \tag{3.7}$$

where K, μ, and v, respectively, are bulk modulus, shear modulus and Poisson's ratio, and η is linear thermal expansion coefficient. Using equations (3.6) and (3.7), equation (3.5) will reduce to the following form for an isotropic poroelastic material which is a general form of equation (2.6):

$$\mu\nabla^2 u_i + \frac{\mu}{1-2v}u_{j,i}u_{j,j} - \frac{2\mu(1+v)}{1-2v}\eta\Delta T_{,i} - \alpha P_{,i} + b_i = 0 \tag{3.8}$$

3.3. Stress arching ratios

Stress arching ratios are defined as the ratio of induced stress change to pore pressure change within a reservoir (e.g., Mulders, 2005) and their values are constant for a poroelastic medium during fluid injection or production. In this work, a more general form of these factors is defined as the ratio of induced stress change to effective pore pressure change within the reservoir (i.e., $\alpha\Delta P$ where α is Biot's coefficient and ΔP is reservoir pressure change, which is positive during injection and negative during production), as follows:

$$\gamma_{\alpha(H_1)} = \Delta\sigma_{H_1}/(\alpha\Delta P) \; ; \; \gamma_{\alpha(H_2)} = \Delta\sigma_{H_2}/(\alpha\Delta P) \; ; \; \gamma_{\alpha(V)} = \Delta\sigma_V/(\alpha\Delta P) \tag{3.9}$$

where $\gamma_{\alpha(H_1)}$, $\gamma_{\alpha(H_2)}$, and $\gamma_{\alpha(V)}$, respectively, are poroelastic normalized horizontal and vertical stress arching ratios; $\Delta\sigma_{H_1}$, $\Delta\sigma_{H_2}$, and $\Delta\sigma_V$, respectively, are horizontal and vertical stress changes. H_1 and H_2 denote directions for two assumed perpendicular horizontal stresses (e.g., minimum and maximum in-situ horizontal stresses). Assuming that the poroelastic stress arching ratios for a given reservoir have been determined, the effective stress changes within the reservoir can be calculated as follows:

$$\Delta\sigma'_{H_1} = -(1-\gamma_{\alpha(H_1)})(\alpha\Delta P) \; ; \; \Delta\sigma'_{H_2} = -(1-\gamma_{\alpha(H_2)})(\alpha\Delta P) \; ; \; \Delta\sigma'_V = -(1-\gamma_{\alpha(V)})(\alpha\Delta P) \tag{3.10}$$

Note: Biot's coefficient, which is used in the preceding equations (and throughout this thesis), is a function of matrix stiffness (K_m) and solid mineral grain stiffness (K_s). For a monomineralic rock, it is defined as $\alpha = 1 - K_m / K_s$. This coefficient has been defined to be used in porous media and it has being widely used for poroelastic analysis of rocks (e.g., Segall et al., 1994). When the rock has a high porosity or a highly fractured structure, this coefficient will have a value close to one due to the reduced stiffness of the matrix (e.g., Ekofisk's reservoir, see Chapter 6). For cemented or over-compacted rocks, the value of Biot's coefficient might be significantly less than one (e.g., Lacq gas reservoir, see Chapter 6).

For the sake of solving the problem for thermoelasticity, horizontal and vertical thermoelastic stress arching ratios (i.e., respectively $\gamma_{T(H_1)}$, $\gamma_{T(H_2)}$, and $\gamma_{T(V)}$) are defined as follows:

$$\gamma_{T(H_1)} = \Delta\sigma_{H_1} / \Delta T, \ \gamma_{T(H_2)} = \Delta\sigma_{H_2} / \Delta T, \ \gamma_{T(V)} = \Delta\sigma_V / \Delta T \tag{3.11}$$

Due to the similar, dilatational nature of pore pressure change and temperature change effects, the thermoelastic solution can be considered as an analogous case for the poroelastic solution. As will be shown later in this chapter, the thermoelastic stress arching ratios can be evaluated by transformation of the poroelastic stress arching ratios. It should be noted, however, that the definition given in equation (3.11) is such that these thermoelastic arching ratios are not dimensionless.

3.4. Theory of strain nuclei

The theory of strain nuclei was essentially developed to solve the field equations in an elastic medium for point loading conditions, also called singularities, such as point forces, concentrated moments, and centers of dilatation (or compression). However, by integration, this methodology was extended to solve problems of distributed loading conditions (Love, 1944).

The simplest form of such a solution is for a point force in an infinite medium, which is known as Kelvin's problem. Imagine a force with unit magnitude in any direction acting on any point $\mathbf{x'}$ within an infinite medium. Since f_i in equation (3.5) has a body force nature,

to imply the effect of this unit point force in this equation, as an equivalent, we might use the Dirac delta function. The Dirac delta function is defined as follows, for a point $\mathbf{x}$ in an arbitrary volume V:

$$\begin{cases} \delta(\mathbf{x} - \mathbf{x'}) = 0 & \text{if } \mathbf{x} \neq \mathbf{x'} \\ \int_V \delta(\mathbf{x} - \mathbf{x'}) dV = 1 & \text{if } \mathbf{x} = \mathbf{x'} \end{cases} \tag{3.12}$$

In this case, equation (3.4) can be written as:

$$C_{knim} G_{ij,mn}(\mathbf{x}, \mathbf{x'}) + \delta(\mathbf{x} - \mathbf{x'})\delta_{jk} = 0 \tag{3.13}$$

$G_{ij}(\mathbf{x}, \mathbf{x'})$, which are known as Green's functions, are defined in this equation as the magnitude of displacement of point $\mathbf{x}$ in the i-direction, when a unit body force in the j-direction is applied at point $\mathbf{x'}$ in an elastic medium.

If, instead of a unit point load, a point force of F_j acts on point $\mathbf{x'}$, the displacement at point $\mathbf{x}$ can be found as:

$$u_i = F_j G_{ij}(\mathbf{x}, \mathbf{x'}) \tag{3.14}$$

If a distributed load f_j is applied on the volume Ω, the following solution can be used to solve for the displacement at point $\mathbf{x}$:

$$u_i = \int_\Omega f_j G_{ij}(\mathbf{x}, \mathbf{x'}) d\mathbf{x'} \tag{3.15}$$

Returning to the context of thermo-poroelasticity, f_j in equation (3.5) might be a consequence of loading conditions such as pressure or thermal changes. Since all deformations in these cases are volumetric, they are known as dilatational (or compressional) problems. For instance, in the case of pore pressure change, equation (3.15) can be written as:

$$u_i = \int_\Omega -\alpha P_{,j} G_{ij}(\mathbf{x}, \mathbf{x'}) d\mathbf{x'} \tag{3.16}$$

Integration of this equation by parts results in the following equation (Segall, 1992):

$$u_i = \int_\Omega \alpha \Delta P G_i^D(\mathbf{x}, \mathbf{x'}) d\mathbf{x'} \tag{3.17}$$

where $G_i^D(\mathbf{x}, \mathbf{x'})$ are called influence functions for dilatation and they are functions of Green's functions, as follows:

$$G_i^D(\mathbf{x}, \mathbf{x'}) = G_{ij,j}(\mathbf{x}, \mathbf{x'}) \tag{3.18}$$

Knowing u_i, equations (3.2) and (3.3) can be used to find induced stresses in the medium. These result in the following equation:

$$\Delta \sigma_{ij}(\mathbf{x}) = -\oint_\Omega \alpha \Delta P G_{ij}^S(\mathbf{x}, \mathbf{x'}) d\mathbf{x'} - \alpha \Delta P \delta_{ij} \tag{3.19}$$

where $G_{ij}^S(\mathbf{x}, \mathbf{x'})$, which are referred to as stress functions, are a function of Green's functions as follows:

$$G_{ij}^S(\mathbf{x}, \mathbf{x'}) = \mu(G_{ip,pj}(\mathbf{x}, \mathbf{x'}) + G_{jp,pi}(\mathbf{x}, \mathbf{x'})) + \frac{2\mu\nu}{1-2\nu} G_{kp,pk}(\mathbf{x}, \mathbf{x'}) \delta_{ij} \tag{3.20}$$

Green's functions for a full space can be derived by solving equation (3.13) using partial differential equation solutions such as a Fourier transform. Using the process of superposition, differentiation, and integration, and starting from the solution of the elasticity equations for a single force in a full space, the solution for influence functions for several different strain nuclei in an infinite medium or a semi-infinite medium can be derived (e.g., Mindlin, 1936; Mindlin and Cheng, 1950). An extensive list of Green's functions and influence functions was given by Seremet (2003).

3.5. Theory of inclusions

An inclusion Ω is a region in a homogeneous isotropic elastic medium D that would undergo an arbitrary strain if it was unbounded, but due to the constraint imposed by the matrix $D - \Omega$ that surrounds it, the strain field within it is modified. The arbitrary strain is referred to as an "eigenstrain". Eigenstrains can be thought of as internal strains that would be caused by various mechanisms, including poroelastic, plastic, and thermal changes, in a body free from external force and surface constraint. In his well-known papers on this subject, Eshelby (1957, 1959) showed that the inclusion problem is equivalent to solving for the equations of elastic equilibrium for a homogeneous body with a known body force distribution. For such bodies, the equations of elastic equilibrium are solved using the elastic Green's functions. Using the Green's function method, the displacement components u_i and stress field σ_{ij} due to eigenstrain ε_{ij}^* in the inclusion Ω can be written as (Mura, 1982, p. 33):

$$u_i(\mathbf{x}) = -\oint_{\Omega} C_{jlmn} \varepsilon_{mn}^*(\mathbf{x'}) G_{ij,l}(\mathbf{x},\mathbf{x'}) d\mathbf{x'} \qquad (3.21)$$

$$\sigma_{ij}(\mathbf{x}) = -C_{ijkl} \left\{ \oint_{\Omega} C_{pqmn} \varepsilon_{mn}^*(\mathbf{x'}) G_{kp,ql}(\mathbf{x},\mathbf{x'}) d\mathbf{x'} + \varepsilon_{kl}^*(\mathbf{x}) \right\} \qquad (3.22)$$

where $\varepsilon_{ij}^*(\mathbf{x}) = 0$ for $x \in D - \Omega$.

In the case of "dilatational" eigenstrain (i.e., the tendency of the inclusion would be to expand or contract isotropically, as would be the case for poroelastic or thermoelastic strains in an isotropic medium), $\varepsilon_{ij}^*(\mathbf{x}) = \varepsilon^C(\mathbf{x})\delta_{ij}$ and equations (3.21) and (3.22) reduce to:

$$u_i(\mathbf{x}) = -\frac{2\mu(1+v)}{1-2v} \oint_{\Omega} \varepsilon^C(\mathbf{x'}) G_i^D(\mathbf{x},\mathbf{x'}) d\mathbf{x'} \qquad (3.23)$$

$$\sigma_{ij}(\mathbf{x}) = -\frac{2\mu(1+v)}{1-2v} \oint_{\Omega} \varepsilon^C(\mathbf{x'}) G_{ij}^S(\mathbf{x},\mathbf{x'}) d\mathbf{x'} - \sigma_{ij}^*(\mathbf{x}) \qquad (3.24)$$

where $\sigma_{ij}^*(\mathbf{x}) = \dfrac{2\mu(1+\nu)}{1-2\nu}\delta_{ij}\varepsilon^C(\mathbf{x})$ is the eigenstress at point $\mathbf{x}$.

The theory of inclusions can be applied to a wide variety of problems in elasticity for different types of eigenstrains. However, in reservoir engineering, we are interested in dilatational eigenstrains resulting from pore pressure or temperature changes; the values of dilatational eigenstrain (ε_C^*) for these conditions, respectively, are:

$$\varepsilon_C^* = \frac{1}{3}\left(\frac{\alpha\Delta P}{K_b}\right) = \frac{(1-2\nu)}{2\mu(1+\nu)}(\alpha\Delta P) \tag{3.25}$$

and

$$\varepsilon_C^* = \eta\Delta T \tag{3.26}$$

where K_b is bulk modulus and η is the linear coefficient of thermal expansion.

The treatment of a reservoir as an inclusion also requires the assumption that no pressure or temperature change occurs in the surrounding rocks; i.e., there is no hydraulically-driven flow, no heat transfer, and fully-drained loading occurs. Inclusion theory allows the consideration of reservoirs of arbitrary shape. A useful result of inclusion theory, which will be exploited in the dimensionless parameterization described in section 3.5.1, is the fact that induced stress changes depend on an inclusion's shape (e.g., thickness/width ratio) and relative depth (i.e., width/depth ratio), but *not* on its absolute dimensions.

3.5.1. Theory of inclusions applied to elliptical reservoirs in a full-space

Eshelby (1957) showed that, for an ellipsoidal inclusion in a full-space, the strain and stress field are uniform for all interior points. Eshelby (1961) further speculated that ellipsoidal inclusions are the only ones to have this remarkable property. This hypothesis was reinforced when Rodin (1996) showed that constant stresses are impossible in inclusions

with corners. In such cases, the following relation exists between induced strain (ε_{ij}) and stress change ($\Delta\sigma_{ij}$) fields and eigenstrain vector:

$$\varepsilon_{ij} = S_{ijkl}\varepsilon_{kl}^{*} \tag{3.27}$$

$$\Delta\sigma_{ij} = C_{ijkl}(\varepsilon_{kl} - \varepsilon_{kl}^{*}) \tag{3.28}$$

where S_{ijkl} is Eshelby's tensor. This unique character for ellipsoidal inclusions can be used to derive an analytical solution for induced stress change within a reservoir. Segall and Fitzgerald (1998) proposed using the theory of inclusions to find stress changes within and adjacent to an axisymmetric ellipsoidally shaped reservoir in a full-space. Following, this theory is applied to derive closed-form solutions for stress arching ratios within reservoirs with different variations of ellipsoidal geometries in a full-space. Various sub-classes of an ellipsoidal inclusion geometry are considered, including: oblate spheroid, prolate spheroid, sphere, and penny-shaped. Further, by allowing one or two axes to extend to infinity, an ellipsoidal geometry can be used to consider an inclusion that is either an elliptic cylinder or a layer of infinite lateral extent. The dilatational components of Eshelby's tensors for these different geometries are listed in Table 3.1.

For an isotropic elastic medium, induced stress changes, hence poroelastic and thermoelastic stress arching ratios, can be found by using equations (3.25) to (3.28). Following, arching ratios are given for the above-noted classes of an ellipsoidal inclusion. A summary of these solutions is given in Table 3.2.

For a prolate spheroid (i.e., an axisymmetric ellipsoid with an axis of symmetry dimension greater than the diametrical dimension) with a vertical axis of symmetry, the poroelastic normalized stress arching ratios induced by pore pressure change can be determined as:

39

Table 3.1. Dilatational components of Eshelby's tensor for different geometrical variations of an ellipsoidal inclusion (after Mura, 1982)
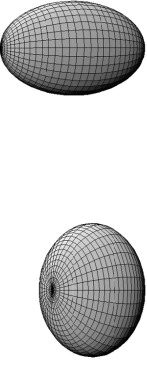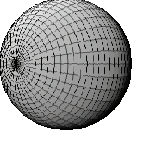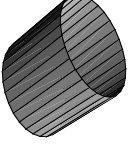
Eshelby's Tensor	Spheroid	Sphere	Penny-shape	Elliptic cylinder
S_{1111}	$\dfrac{3}{8(1-\nu)}\left[1-\dfrac{1+3F}{2(e^2-1)}\right]+\dfrac{1-2\nu}{4(1-\nu)}(1+F)$	$\dfrac{7-5\nu}{15(1-\nu)}$	$\dfrac{13-8\nu}{32(1-\nu)}\pi e$	$\dfrac{1}{2(1-\nu)}\left[\dfrac{e^2+2e}{(1+e)^2}+(1-2\nu)\dfrac{e}{1+e}\right]$
S_{1122}	$\dfrac{1}{8(1-\nu)}\left[1-\dfrac{1+3F}{2(e^2-1)}\right]-\dfrac{1-2\nu}{4(1-\nu)}(1+F)$	$\dfrac{5\nu-1}{15(1-\nu)}$	$\dfrac{8\nu-1}{32(1-\nu)}\pi e$	$\dfrac{1}{2(1-\nu)}\left[\dfrac{e^2}{(1+e)^2}-(1-2\nu)\dfrac{e}{1+e}\right]$
S_{1133}	$\dfrac{1}{4(1-\nu)}\dfrac{e^2(1+3M)}{e^2-1}-\dfrac{1-2\nu}{4(1-\nu)}(1+F)$	S_{1122}	$\dfrac{2\nu-1}{8(1-\nu)}\pi e$	$\dfrac{\nu}{1-\nu}\dfrac{e}{1+e}$
S_{2211}	S_{1122}	S_{1122}	S_{1122}	$\dfrac{1}{2(1-\nu)}\left[\dfrac{1}{(1+e)^2}-(1-2\nu)\dfrac{1}{1+e}\right]$
S_{2222}	S_{1111}	S_{1111}	S_{1111}	$\dfrac{1}{2(1-\nu)}\left[\dfrac{1+2e}{(1+e)^2}+(1-2\nu)\dfrac{1}{1+e}\right]$
S_{2233}	S_{1133}	S_{1122}	S_{1133}	$\dfrac{\nu}{1-\nu}\dfrac{1}{1+e}$
S_{3311}	$\dfrac{1}{4(1-\nu)}\dfrac{1+3F}{e^2-1}+\dfrac{1-2\nu}{2(1-\nu)}F$	S_{1122}	$\dfrac{\nu}{1-\nu}\left(1-\dfrac{4\nu+1}{8\nu}\pi e\right)$	0
S_{3322}	S_{3311}	S_{1122}	S_{3311}	0
S_{3333}	$\dfrac{1}{2(1-\nu)}\left[1-\dfrac{e^2(1+3F)}{e^2-1}\right]-\dfrac{1-2\nu}{2(1-\nu)}F$	S_{1111}	$1-\dfrac{1-2\nu}{1-\nu}\dfrac{\pi e}{4}$	0

40

Table 3.1(Continued). Dilatational components of Eshelby's tensor for different geometrical variations of an ellipsoidal inclusion (after Mura, 1982)
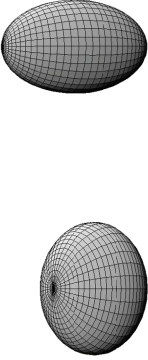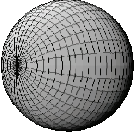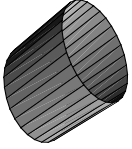
Eshelby's Tensor	**Spheroid**	**Sphere**	**Penny-shape**	**Elliptic cylinder**
Comments	For $e>1$ (i.e., a prolate spheroid): $$F = 1/(e^2-1) - (e\cosh^{-1} e)/(e^2-1)^{3/2}$$ For $e<1$ (i.e., an oblate spheroid): $$F = 1/(e^2-1) + (e\cos^{-1} e)/(1-e^2)^{3/2}$$	$e=1$	$e\leq 0.2$	Plane strain geometry

41

Table 3.2. Poroelastic normalized stress arching ratios for different geometrical variations of an ellipsoidal reservoir derived using the theories of inclusions and inhomogeneities.
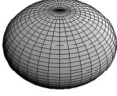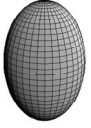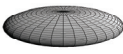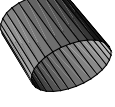
Shape	Inclusion (Reservoir and surrounding rock have identical elastic properties)	Inhomogeneity (Elastic properties of reservoir are different from the surrounding rock)
Oblate spheroid	$\gamma_{\alpha(H_1)} = \gamma_{\alpha(H_2)} = \frac{1}{2}\frac{1-2\nu}{1-\nu}\left[1+\frac{1}{1-e^2}-\frac{e\cos^{-1}e}{(1-e^2)^{3/2}}\right]$ $\gamma_{\alpha(V)} = \frac{1-2\nu}{1-\nu}\left[\frac{e\cos^{-1}e}{(1-e^2)^{3/2}}-\frac{e^2}{1-e^2}\right]$	Numerical solution can be found from equations (3.62). For a simplified inhomogeneity (i.e., $\nu=\nu^*$), a closed form solution can be found as: $\gamma_{\alpha(H_1)} = \gamma_{\alpha(H_2)} = B_1/B_3$, $\gamma_{\alpha(V)} = B_2/B_3$
Prolate spheroid	$\gamma_{\alpha(H_1)} = \gamma_{\alpha(H_2)} = \frac{1}{2}\frac{1-2\nu}{1-\nu}\left[1-\frac{1}{e^2-1}+\frac{e\cosh^{-1}e}{(e^2-1)^{3/2}}\right]$ $\gamma_{\alpha(V)} = \frac{1-2\nu}{1-\nu}\left[\frac{e^2}{e^2-1}-\frac{e\cosh^{-1}e}{(e^2-1)^{3/2}}\right]$	$B_1 = (1+\nu)(1-X_2+(1-R_\mu)X_1)+R_\mu(X_3+\nu X_4)$ $B_2 = (1+\nu)[1-(R_\mu-1)X_1-X_2]+R_\mu[(1-\nu)X_4+2\nu X_3]$ $B_3 = (1+\nu)[(R_\mu-1)^2 X_1+(R_\mu-1)X_2+1]$ where: $X_1 = (S_{1111}+S_{1122})S_{3333}-2S_{3311}S_{1133}$ $X_2 = S_{1111}+S_{1122}+S_{3333}$; $X_3 = S_{3333}-S_{1133}$ $X_4 = S_{1111}+S_{1122}-2S_{3311}$
Sphere	$\gamma_{\alpha(H_1)} = \gamma_{\alpha(H_2)} = \gamma_{\alpha(V)} = \frac{2}{3}\frac{1-2\nu}{1-\nu}$	$\gamma_{\alpha(H_1)} = \gamma_{\alpha(H_2)} = \gamma_{\alpha(V)} = \frac{2(1-2\nu^*)}{R_\mu(1+\nu^*)+2(1-2\nu^*)}$
Penny-shape	$\gamma_{\alpha(H)} = \gamma_{\alpha(h)} = \frac{1-2\nu}{1-\nu}\left(1-\frac{\pi e}{4}\right)$ $\gamma_{\alpha(V)} = \frac{1-2\nu}{1-\nu}\frac{\pi e}{2}$	Numerical solution can be found from equations (3.62). For a simplified inhomogeneity (i.e., $\nu=\nu^*$), a closed form solution can be found as: $\gamma_{\alpha(H_1)} = \gamma_{\alpha(H_2)} = C_1/C_3$, $\gamma_{\alpha(V)} = C_2/C_3$ where: $C_1 = (1-2\nu)\{\pi^2 e^2(1-R_\mu)(1+\nu)-8R_\mu(1-\nu)-2\pi e[R_\mu(\nu-2)+1]\}$ $C_2 = \pi e(1-2\nu)[\pi e(1-R_\mu)(1+\nu)-2R_\mu(1-2\nu)-2]$ $C_3 = (m-1)\pi e$ $\{(1-2\nu)[2-\pi e(1-R_\mu)(1+\nu)]-R_\mu(3-4\nu)(1+\nu)\}-8R_\mu(1-\nu)^2$

Table 3.2. (Continued) Poroelastic normalized stress arching ratios for different geometrical variations of an ellipsoidal reservoir derived using the theories of inclusions and inhomogeneities.

Shape	Inclusion (Reservoir and surrounding rock have identical elastic properties)	Inhomogeneity (Elastic properties of reservoir are different from the surrounding rock)
Elliptic cylinder	$\gamma_{\alpha(H_1)} = \dfrac{1-2\nu}{1-\nu}\dfrac{1}{1+e}$ $\gamma_{\alpha(H_2)} = \dfrac{1-2\nu}{1-\nu}$ $\gamma_{\alpha(V)} = \dfrac{1-2\nu}{1-\nu}\dfrac{e}{1+e}$	$\gamma_{\alpha(H_1)} = A_1/A_4, \gamma_{\alpha(H_2)} = A_2/A_4, \gamma_{\alpha(V)} = A_3/A_4$ $A_1 = (1-2\nu^*)[R_\mu[e(1-2\nu)+2(1-\nu)]+e]$ $A_2 = (1-2\nu^*)[R_\mu[R_\mu e(3-4\nu)+2(1+e^2)(1-\nu)]+e]$ $A_3 = (1-2\nu^*)[R_\mu[2e(1-\nu)+1-2\nu]+1]e$ $A_4 = R_\mu[2(1+e)^2(1-\nu)(1-\nu^*)$ $\quad -2e\nu^*(1-2\nu)+R_\mu e(3-4\nu)]+e(1-2\nu^*)$
Circular cylinder	$\gamma_{\alpha(H_1)} = \gamma_{\alpha(V)} = \dfrac{1}{2}\dfrac{1-2\nu}{1-\nu}; \gamma_{\alpha(H_2)} = \dfrac{1-2\nu}{1-\nu}$	$\gamma_{\alpha(H_1)} = \gamma_{\alpha(V)} = \dfrac{1-2\nu^*}{R_\mu+1-2\nu^*}, \gamma_{\alpha(H_2)} = \dfrac{(1+R_\mu)(1-2\nu^*)}{R_\mu+1-2\nu^*}$
Infinite layer	$\gamma_{\alpha(H_1)} = \gamma_{\alpha(H_2)} = \dfrac{1-2\nu}{1-\nu}; \gamma_{\alpha(V)} = 0$	$\gamma_{\alpha(H_1)} = \gamma_{\alpha(H_2)} = \dfrac{1-2\nu^*}{1-\nu^*}, \gamma_{\alpha(V)} = 0$

$$\gamma_{\alpha(H_1)} = \gamma_{\alpha(H_2)} = \frac{1}{2}\frac{1-2\nu}{1-\nu}\left[1 - \frac{1}{e^2-1} + \frac{e\cosh^{-1}e}{(e^2-1)^{3/2}}\right]$$

$$\gamma_{\alpha(V)} = \frac{1-2\nu}{1-\nu}\left[\frac{e^2}{e^2-1} - \frac{e\cosh^{-1}e}{(e^2-1)^{3/2}}\right]$$

(3.29)

where *e* is the aspect ratio of the prolate spheroid (the ratio of the vertical semi-axis to the horizontal semi-axes), which, by definition is always greater than one. [Note: Due to the fact that this axisymmetric solution has been derived for a full-space, by interchanging the axis indices, these equations could also be used for reservoirs with symmetry axes that are horizontal or inclined.]

For an oblate spheroid (i.e., an axisymmetric ellipsoid with aspect ratio (*e*) less than one) with a vertical axis of symmetry, the poroelastic normalized stress arching ratios (as shown previously by Fjær et al., 2008, p. 397) are calculated as follows:

$$\gamma_{\alpha(H_1)} = \gamma_{\alpha(H_2)} = \frac{1}{2}\frac{1-2\nu}{1-\nu}\left[1 + \frac{1}{1-e^2} - \frac{e\cos^{-1}e}{(1-e^2)^{3/2}}\right]$$

$$\gamma_{\alpha(V)} = \frac{1-2\nu}{1-\nu}\left[\frac{e\cos^{-1}e}{(1-e^2)^{3/2}} - \frac{e^2}{1-e^2}\right]$$

(3.30)

Poroelastic normalized stress arching ratios for a sphere (i.e., $e = 1$) can be found as:

$$\gamma_{\alpha(H_1)} = \gamma_{\alpha(H_2)} = \gamma_{\alpha(V)} = \frac{2}{3}\frac{1-2\nu}{1-\nu}$$

(3.31)

In the special case of an oblate spheroid when aspect ratio is very small ($e \leq 0.2$), which is the case for many reservoirs, the inclusion shape can be approximated by a penny-shaped geometry with a maximum absolute error of 0.065. This maximum error occurs for the smallest possible value of Poisson's ratio; i.e., zero. For the penny-shaped case, poroelastic normalized stress arching ratios (as shown previously by Segall and Fitzgerald, 1998) can be derived as:

$$\gamma_{\alpha(H_1)} = \gamma_{\alpha(H_2)} = \frac{1-2\nu}{1-\nu}(1 - \frac{\pi e}{4}) \; ; \; \gamma_{\alpha(V)} = \frac{1-2\nu}{1-\nu}\frac{\pi e}{2}$$

(3.32)

In the limiting case where aspect ratio (e) approaches zero, the ellipsoid resembles a horizontal layer with a very small thickness compared to its lateral extent. In such a case, the poroelastic normalized stress arching ratios are:

$$\gamma_{\alpha(H_1)} = \gamma_{\alpha(H_2)} = \frac{1-2\nu}{1-\nu} \; ; \quad \gamma_{\alpha(V)} = 0$$

(3.33)

These simple equations have been traditionally used for stress analysis in reservoir geomechanics (e.g., Zoback and Zinke, 2002; Hawkes et al., 2005).

All the solutions given above have been developed for reservoirs with axisymmetric geometries. In cases where the reservoir has an elongated geometry, an elliptic cylinder geometry can be used. This case gives a plane strain solution for the problem, as follows:

$$\gamma_{\alpha(H_1)} = \frac{1-2\nu}{1-\nu}\frac{1}{1+e}; \quad \gamma_{\alpha(H_2)} = \frac{1-2\nu}{1-\nu}; \quad \gamma_{\alpha(V)} = \frac{1-2\nu}{1-\nu}\frac{e}{1+e} \tag{3.34}$$

For the special case of a circular cylinder (i.e., $e = 1$) these equations reduce to:

$$\gamma_{\alpha(H_1)} = \gamma_{\alpha(V)} = \frac{1-2\nu}{2(1-\nu)}; \quad \gamma_{\alpha(H_2)} = \frac{1-2\nu}{1-\nu} \tag{3.35}$$

It is interesting to note that, for all of the geometries considered above, the following relationship between poroelastic normalized stress arching ratios holds true (Fjær et al., 2008, p. 398):

$$\gamma_{\alpha(H_1)} + \gamma_{\alpha(H_2)} + \gamma_{\alpha(V)} = \frac{2(1-2\nu)}{1-\nu} \tag{3.36}$$

Figure 3.1 shows the variation of horizontal and vertical normalized poroelastic stress arching ratios as a function of aspect ratio for different geometries, calculated using a value of 0.2 for Poisson's ratio (ν). Based on this figure, the maximum difference between results from a plane strain solution for an elliptic cylinder and an axisymmetric solution for a prolate spheroid is 0.13; this occurs when $e = 1$, where the geometries are a circular cylinder and a sphere, respectively. For aspect ratios less than 0.2, the maximum difference is 0.06. This shows that, for many reservoirs, either a plane strain or an axisymmetric solution might be considered without a significant error. Dilatational eigenstrains in equations (3.25) and (3.26) and equations (3.27) and (3.28) can be used to find the relationship between thermoelastic and poroelastic stress arching ratios, as follows:

$$\gamma_{T(ij)} = \frac{2\mu\eta(1+\nu)}{1-2\nu}\gamma_{\alpha(ij)} \tag{3.37}$$
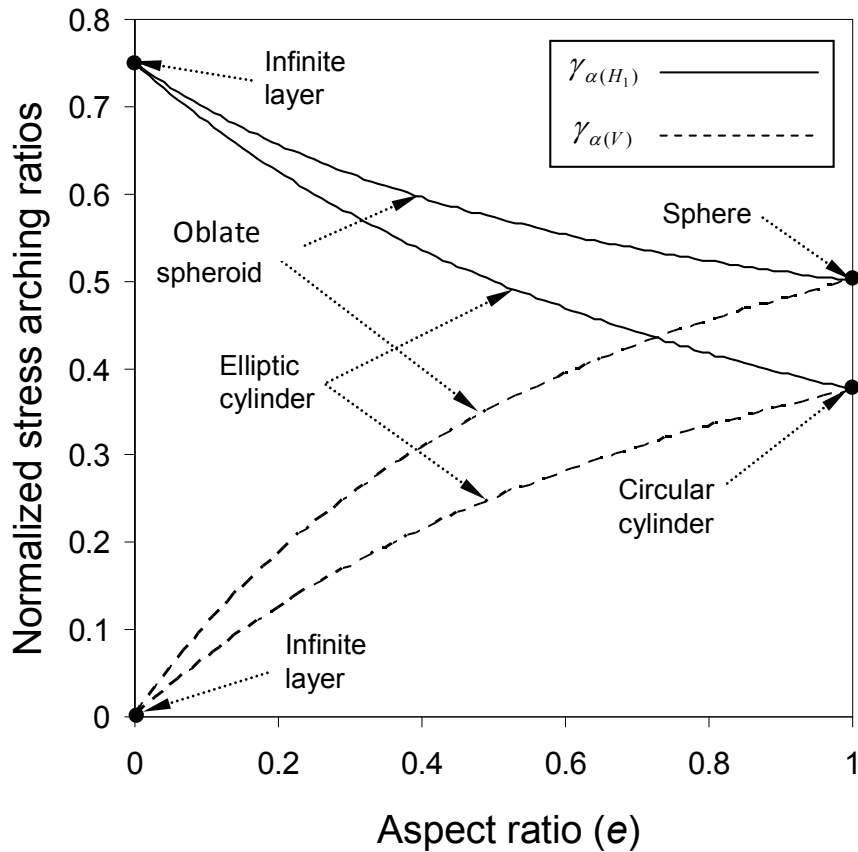
Figure 3.1. Poroelastic normalized horizontal ($\gamma_{\alpha(H1)}$) and vertical ($\gamma_{\alpha(V)}$) stress arching ratios versus aspect ratio (*e*) for an elliptic cylinder (i.e., plane strain solution) and an oblate spheroid (i.e., an axisymmetric solution) for a Poisson's ratio of 0.2 when the material properties of the reservoir are identical to the surrounding rock. [Note: For the axisymmetric solution, $\gamma_{\alpha(H1)} = \gamma_{\alpha(H2)}$. For the plane strain solution, $\gamma_{\alpha(H1)}$ represents the arching ratio in the cross-sectional plane, and $\gamma_{\alpha(H2)}$ (the out-of-plane arching ratio) has a constant value of 0.75.]

Using the principle of superposition in elasticity, thermoelastic and poroelastic stress arching ratios can be applied in combination to find the induced stress changes in cases where both temperature and pore pressure changes have occurred.

3.5.2. Theory of inclusions applied to reservoirs in a half-space

The theory of inclusions might also be applied when an inclusion is embedded in a matrix with different boundary conditions such as a half-space, which resembles a reservoir buried at a finite depth. However, in this case Eshelby's rule for ellipsoidal inclusions is no longer applicable, hence semi-analytical approaches must be applied to determine induced

stresses and strains within reservoirs. To do so, it is necessary to use Green's functions that have been derived for such a half-space. One advantage of using semi-analytical models is the fact that they provide an opportunity to consider other geometries for the reservoir. The following section provides such solutions and also studies the effects of reservoir depth, shape, and "tilting" (i.e., dip) on induced stress change within the reservoir and in the surrounding rocks.

Inclusion theory applied to horizontal reservoirs

Consider a reservoir under plane strain conditions with elliptical or rectangular cross-section, its center at depth D, having thickness T, width $2a$ and dipping at an angle β in the cross-sectional plane (see Figure 3.2). Given the independency of stress change on inclusion size, the results of production or injection-induced stress change analyses can be used in a very general sense if the solutions are cast in terms of dimensionless reservoir geometry parameters. For this reason, reservoir aspect ratio (e) and depth number (n) are defined as:

$$x = \frac{x_1}{D}; \quad y = \frac{x_2}{D}; \quad x' = \frac{x'_1}{D}; \quad y' = \frac{x'_2}{D} \tag{3.39}$$

$$e = \frac{T}{2a}; \quad n = \frac{a}{D} \tag{3.38}$$

and dimensionless coordinates (x, y) and (x', y') are defined as:

When the reservoir is horizontal, with an elliptical cross-section, equations (3.9) and (3.24) can be used to solve for normalized arching ratios as follows:

$$\gamma_{\alpha(ij)}(x, y) = -\int_{-n}^{n} \int_{1-e \times n \sqrt{1-(y'/n)^2}}^{1+e \times n \sqrt{1-(y'/n)^2}} G_{ij}^{S}(x, y, x', y') dx' dy' \quad , \quad i, j = 1, 2 \tag{3.40}$$
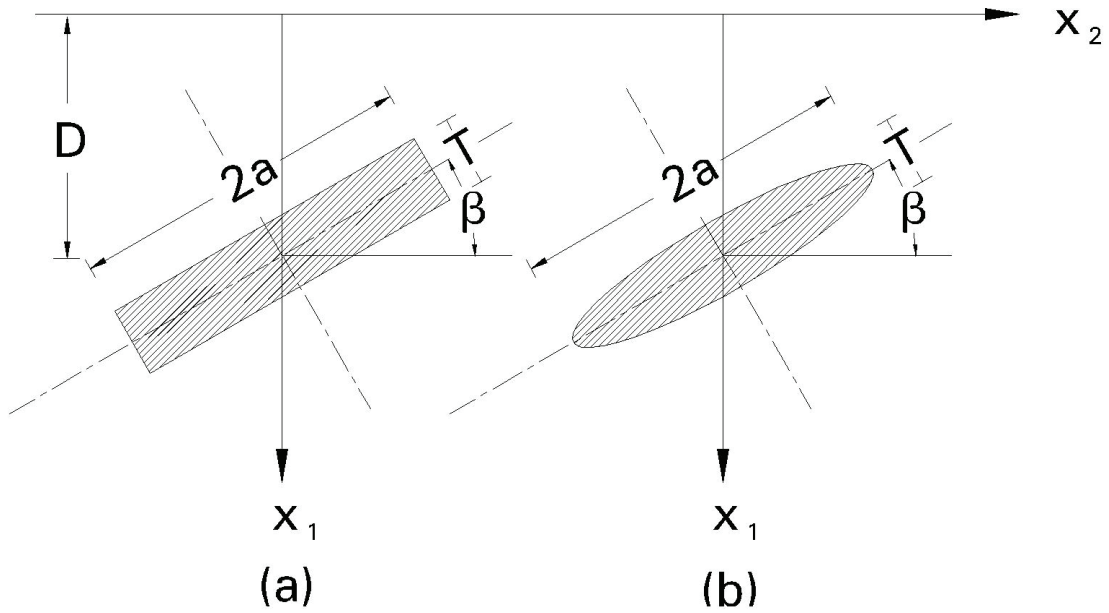
Figure 3.2. Geometries used for poroelastic analysis of (a) elliptical and (b) rectangular reservoirs.

The corresponding equation for a horizontal rectangular reservoir is:

$$\gamma_{\alpha(ij)}(x,y) = -\int_{-n}^{n}\int_{1-e\times n}^{1+e\times n} G_{ij}^{S}(x,y,x',y')dx'dy' \qquad (3.41)$$

Green's functions for a plane strain semi-infinite medium with a stress-free boundary (i.e., ground surface) are (Seremet , 2003, pp. 358-361):

$$\mathbf{x} = x_1\mathbf{i} + x_2\mathbf{j} \qquad (3.42)$$

$$\mathbf{x}' = x_1'\mathbf{i} + x_2'\mathbf{j} \qquad (3.43)$$

$$R_1 = \left[(x_1 - x_1')^2 + (x_2 - x_2')^2\right]^{1/2} \qquad (3.44)$$

$$R_2 = \left[(x_1 + x_1')^2 + (x_2 - x_2')^2\right]^{1/2} \qquad (3.45)$$

48

$$G_{11}(\mathbf{x}, \mathbf{x'}) = \frac{1}{8\pi\mu(1-v)} \left[-(3-4v)\ln(R_1 \times R_2) - 2(1-2v)^2 \ln R_2 + \frac{(x_1 - x_1')^2}{R_1^2} \right.$$

$$\left. + \frac{(3-4v)(x_1^2 + x_1'^2) + 4(1-2v)x_1 x_1'}{R_2^2} + \frac{4x_1 x_1'(x_1 + x_1')^2}{R_2^4} \right] \tag{3.46}$$

$$G_{12}(\mathbf{x}, \mathbf{x'}) = \frac{1}{8\pi\mu(1-v)} \left[\frac{(x_1 - x_1')(x_2 - x_2')}{R_1^2} + \frac{(3-4v)(x_1 - x_1')(x_2 - x_2')}{R_2^2} \right.$$

$$\left. - \frac{4x_1 x_1'(x_1 + x_1')(x_2 - x_2')}{R_2^4} - 4(1-v)(1-2v)\arctan\left(\frac{x_1 + x_1'}{x_2 - x_2'}\right) \right] \tag{3.47}$$

$$G_{21}(\mathbf{x}, \mathbf{x'}) = \frac{1}{8\pi\mu(1-v)} \left[\frac{(x_1 - x_1')(x_2 - x_2')}{R_1^2} + \frac{(3-4v)(x_1 - x_1')(x_2 - x_2')}{R_2^2} \right.$$

$$\left. + \frac{4x_1 x_1'(x_1 + x_1')(x_2 - x_2')}{R_2^4} + 4(1-v)(1-2v)\arctan\left(\frac{x_1 + x_1'}{x_2 - x_2'}\right) \right] \tag{3.48}$$

$$G_{22}(\mathbf{x}, \mathbf{x'}) = \frac{1}{8\pi\mu(1-v)} \left[-(3-4v)\ln(R_1 \times R_2) - 2(1-2v)^2 \ln R_2 + \frac{(x_2 - x_2')^2}{R_1^2} \right.$$

$$\left. + \frac{(x_2 - x_2')^2 - 2(1-2v)(x_1 + x_1')^2 - 2x_1 x_1'}{R_2^2} + \frac{4x_1 x_1'(x_1 + x_1')^2}{R_2^4} \right] \tag{3.49}$$

These Green's function can be reduced to their corresponding forms in a full-space, plane strain problem by eliminating all terms containing $x_1 + x_1'$. This term accounts for the existence of the free surface in a half-space. As such, Green's functions for an isotropic full plane can be written as:

$$G_{ij}(\mathbf{x}, \mathbf{x'}) = \frac{1}{8\pi\mu(1-v)} \left\{ l_i l_j - (3-4v)\delta_{ij} \ln R_1 \right\}, \quad i = 1,2 \tag{3.50}$$

where $l_i = (x_i - x_i')/R$, and $R = |\mathbf{x} - \mathbf{x}'|$.

Evaluation of integrals in equations (3.40) and (3.41), and all others that follow in this chapter, can be conducted using any of a number of commercially available mathematical software applications. Mathcad version 11 (Mathsoft, 2002) was used for the work presented in this thesis.

Figures 3.3 to 3.5 show induced stress changes calculated for a horizontal reservoir with rectangular cross-section and dimensionless geometric parameters $n = 0.5$ and $e = 0.05$. The identification of regions of tensile or compressive stress change is accomplished by considering the sign of ΔP within the reservoir. For example, in the case of production (i.e., $\Delta P < 0$), tensile horizontal stress changes and compressive vertical stress changes are predicted in the rocks laterally adjacent to the reservoir. Above and below the reservoir, compressive horizontal stress changes and tensile vertical stress changes are predicted.

Figure 3.6 demonstrates the variation of arching values along the horizontal center-line of reservoirs with rectangular and elliptical cross-sections under plane strain conditions. For the rectangular case, the horizontal arching value reaches a maximum near the center of the reservoir and decreases towards the edge of the reservoir. For the elliptical geometry, in relatively deep reservoirs such as this example, the horizontal normalized arching ratio is virtually constant throughout the reservoir. The vertical arching value is variable within the rectangular reservoir, reaching a minimum at its center, whereas it is virtually constant throughout the elliptical reservoir. For both reservoir geometries, there is a discontinuity in the vertical arching value at the lateral boundaries. The magnitude of this theoretical discontinuity is given as (Goodier, 1937; Segall and Fitzgerald, 1998):

$$\gamma_{\alpha(V)}^{Inside} - \gamma_{\alpha(V)}^{Outside} = \frac{1 - 2\nu}{1 - \nu} \tag{3.51}$$

The right-hand side of equation (3.51) has been used as a normalization parameter in Figures 3.3 through 3.8. A similar discontinuity also exists in the horizontal normalized stress arching ratio at the top and bottom reservoir boundaries. As a practical point, it should
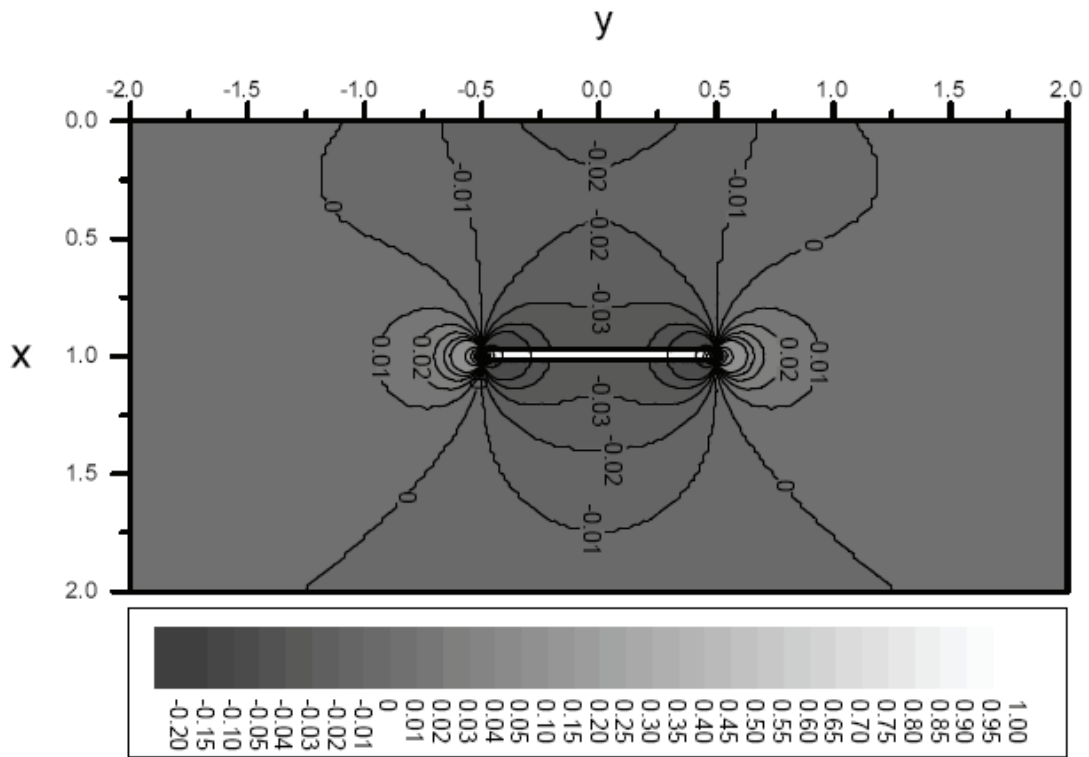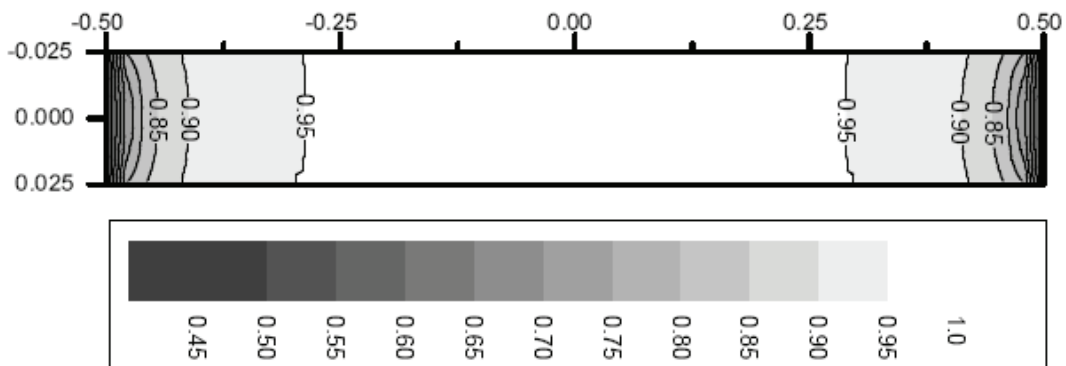
Figure 3.3. Contours of horizontal normalized stress arching ratios for a rectangular reservoir with $n = 0.5$ and $e = 0.05$ (a) for the surrounding rock and (b) within the reservoir. All of the values are normalized by $(1 - 2v)/(1 - v)$.
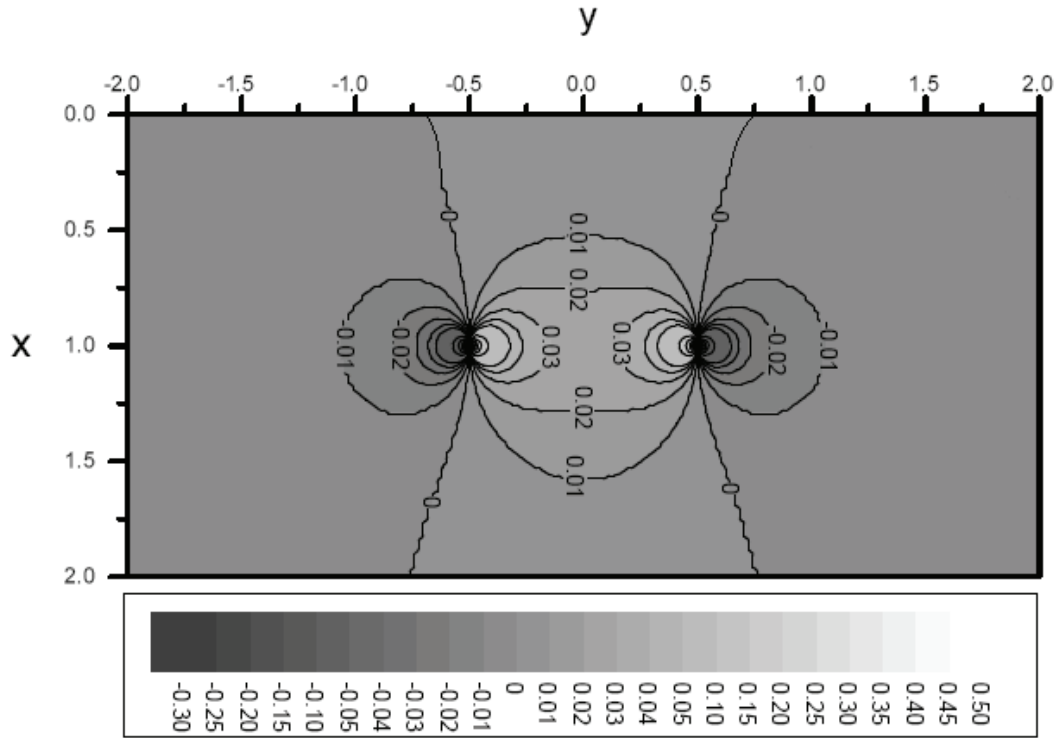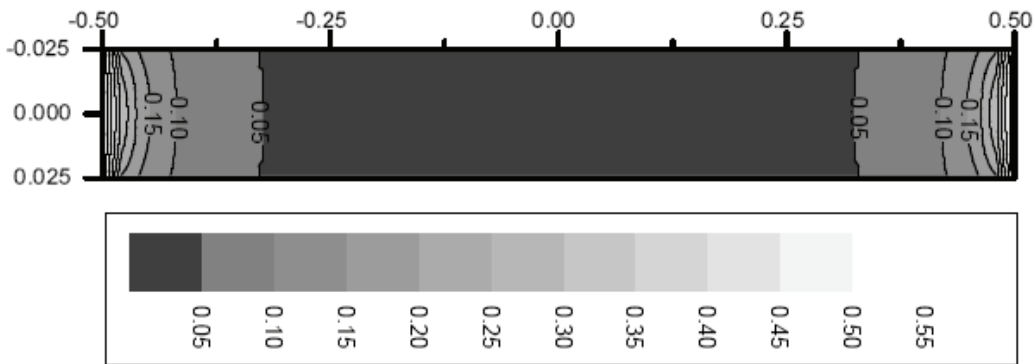
Figure 3.4. Contours of vertical normalized stress arching ratios for a rectangular reservoir with $n = 0.5$ and $e = 0.05$ (a) for the surrounding rock and (b) within the reservoir. All of the values are normalized by $(1-2v)/(1-v)$.
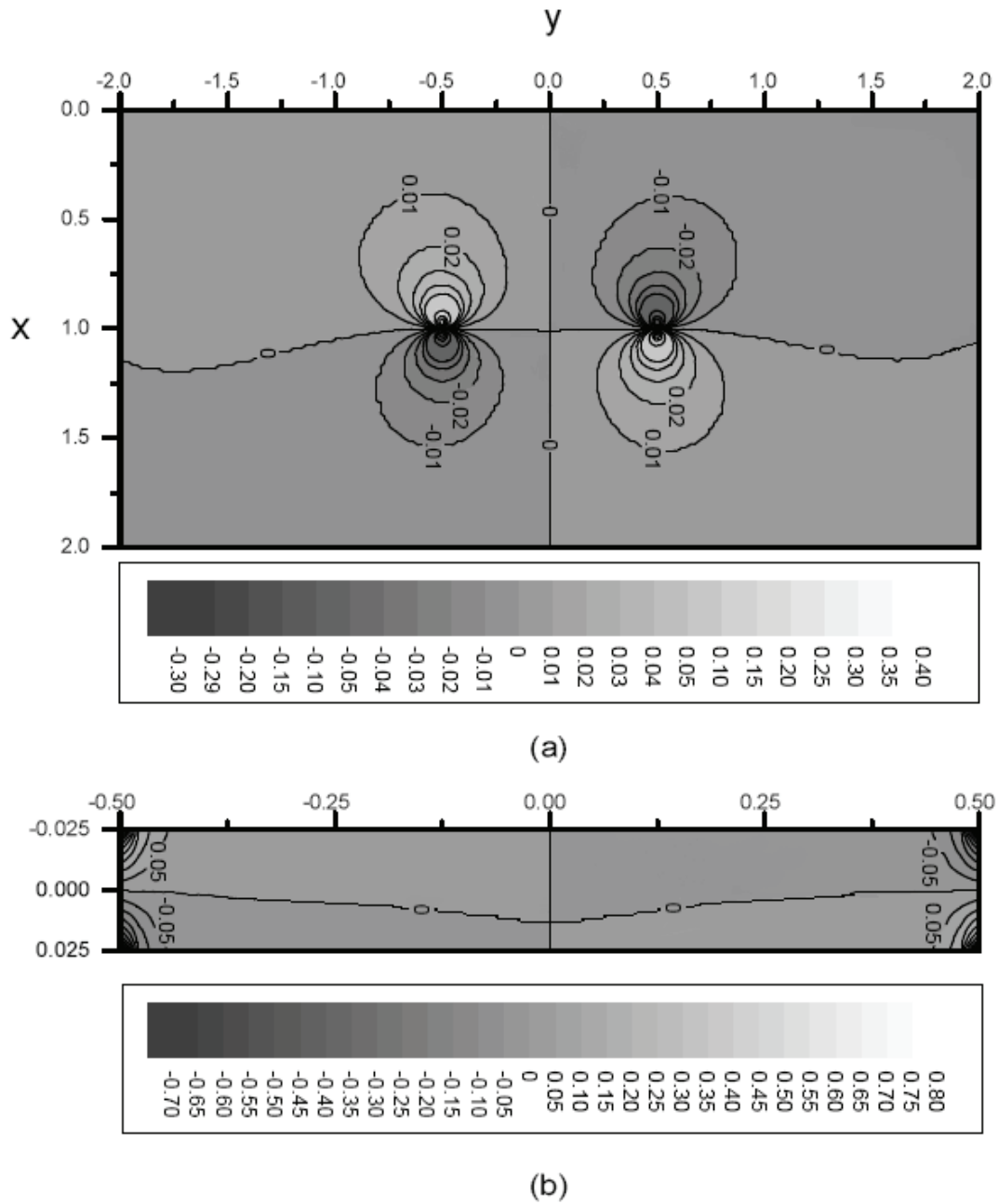
Figure 3.5. Contours of shear normalized stress arching ratios for a rectangular reservoir with $n = 0.5$ and $e = 0.05$ (a) for the surrounding rock and (b) within the reservoir. All of the values are normalized by $(1-2v)/(1-v)$.
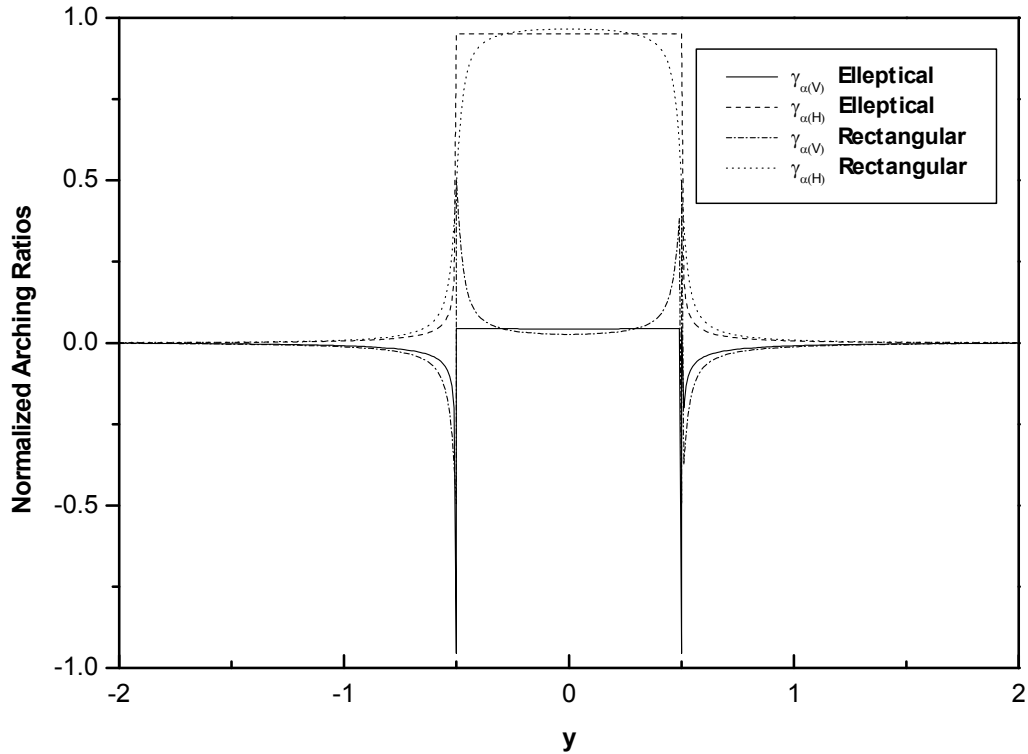
Figure 3.6. Variation of horizontal and vertical normalized stress arching ratios along the horizontal centerline of horizontal rectangular and elliptical reservoirs with $n = 0.5$ and $e = 0.05$. All of the values are normalized by $(1-2\nu)/(1-\nu)$.

be noted that factors such as non-linear or plastic deformation, and gradual pore pressure transitions between the reservoir and surrounding rocks, would likely act to diminish the magnitude and alter the character of these discontinuities. In fault reactivation and induced fracturing analysis, this assumption can be on the conservative side or non-conservative side depending upon the location in the surrounding rock and reservoir pressure change scenario (i.e., injection or production).

Figure 3.7(a) shows the normalized arching ratios at the center of horizontal, rectangular reservoirs as a function of aspect ratio and depth number. Figure 3.7(b) shows analogous results for elliptical reservoirs. It can be seen that with increasing aspect ratio (*e*), the vertical arching ratio increases while the horizontal arching ratio decreases. As expected, at the limiting value $e = 0$ (i.e., a reservoir of infinite lateral extent) the vertical arching ratio is zero and the horizontal arching ratio is $(1-2\nu)/(1-\nu)$, which is independent of depth.

When the reservoir is deep enough, the results shown for an elliptical reservoir in a half-space are the same as the results for a full-space, as previously shown in equation (3.34).
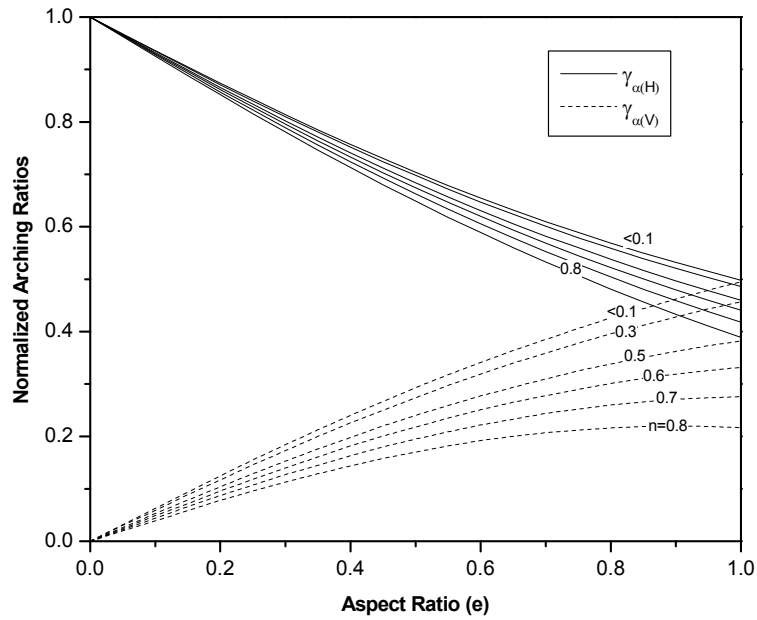
(a)
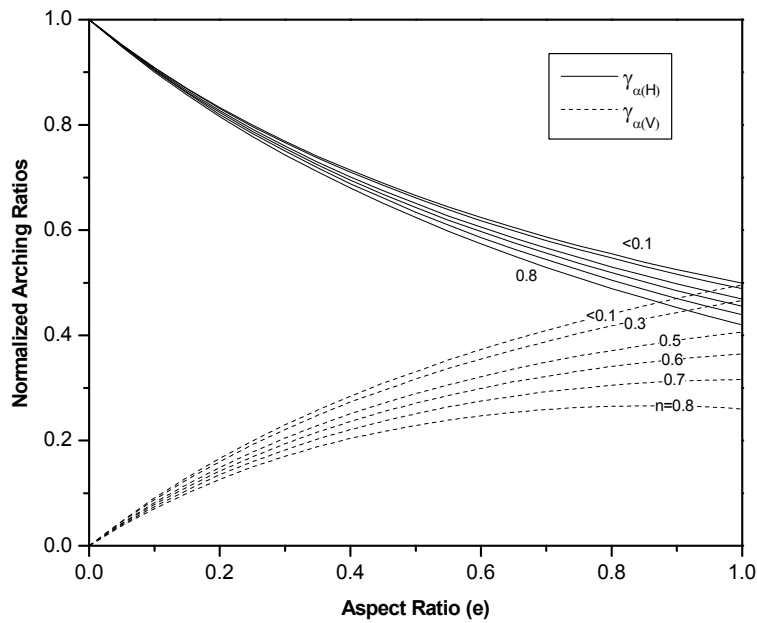
(b)

Figure 3.7. Variation of normalized arching ratios with aspect ratio (e) and depth number (n) in the center of (a) a horizontal rectangular reservoir and (b) a horizontal elliptical reservoir. All of the values are normalized by $(1-2\nu)/(1-\nu)$.

The full-space plane strain solution is reasonably accurate in settings where reservoir depth and lateral extent are similar in magnitude (i.e., $n < 0.5$), especially for reservoirs that are relatively thin (i.e., with an aspect ratio less than 0.2). Further, regardless of reservoir thickness, the full-space plane strain solution is virtually exact when reservoir depth is at least five times greater than lateral extent (i.e., $n < 0.1$).

Inclusion theory applied to tilted reservoirs

For the case of a plane strain reservoir with an elliptical cross-section that is dipping by an angle β from horizontal, the following equation for arching values has been derived during this research:

$$\gamma_{\alpha(ij)}(x,y) = -\int_{-y'_{max}}^{y'_{max}} \int_{1+(Cy'-\sqrt{(C^2-4AB)y'^2+4A})/(2A)}^{1+(Cy'+\sqrt{(C^2-4AB)y'^2+4A})/(2A)} G_{ij}^S(x,y,x',y')dx'dy' \qquad (3.52)$$

where

$$y'_{max} = (e \times n)\cos[\arctan(\cot\beta/e)]\sin\beta + n\sin[\arctan(\cot\beta/e)]\cos\beta$$

$$A = (\sin^2\beta + \cos^2\beta/e^2)/n^2$$

$$B = (\cos^2\beta + \sin^2\beta/e^2)/n^2$$

$$C = (1-1/e^2)\sin 2\beta/n^2 \qquad (3.53)$$

Similarly, for a plane strain reservoir with rectangular cross-section that is dipping by an angle β from horizontal:

$$\gamma_{\alpha(ij)}(x,y) = -\left[\int_{-y'_1}^{y'_1} \int_{1-y'\tan\beta-e\times n/\cos\beta}^{1-y'\tan\beta+e\times n/\cos\beta} G_{ij}^S(x,y,x',y')dx'dy' \right.$$

$$\left. + \int_{y'_1}^{y'_2} \int_{1-(y'-n\cos\beta)/\tan\beta-n\sin\beta}^{1-y'\tan\beta+e\times n/\cos\beta} G_{ij}^S(x,y,x',y')dx'dy' \right.$$

$$+ \int_{-y_2'}^{-y_1'} \int_{1-y'\tan\beta - e\times n/\cos\beta}^{1+(y'+n\cos\beta)/\tan\beta + n\sin\beta} G_{ij}^S(x,y,x',y')dx'dy' \Bigg] \tag{3.54}$$

where:

$$y_1' = n(\cos\beta - e\sin\beta) \tag{3.55}$$

$$y_2' = n(\cos\beta + e\sin\beta) \tag{3.56}$$

Using these equations for dipping reservoirs in a half-space, it is found that the induced stress field for a reservoir with a dip angle less than $30°$ only deviates slightly from a simple rotation of the stress field induced for a horizontal reservoir, provided that the reservoir's width is not more than twice its depth (i.e., $n \leq 1$) and its aspect ratio is not very high $(e \leq 0.7)$. Parameter sensitivity analyses conducted during this research have shown that, if these conditions are satisfied, the maximum error obtained using a simple horizontal stress field rotation is roughly 20%. This error significantly decreases for smaller dip angles, aspect ratios and depth numbers. In fact, rotation of the stress field obtained with the horizontal reservoir solution will provide virtually exact results in cases where the reservoir is so deep that the ground surface has negligible impact on the induced stress field (i.e., a full-space problem). In such cases, it is possible to use a Mohr circle construction to find the arching values in the center of a "tilted" or dipping reservoir, based on the values for a horizontal reservoir with the same geometry and center point, as follows:

$$(\gamma_{\alpha(H)})_{Tilted} = \frac{(\gamma_{\alpha(H)})_{Horizontal} + (\gamma_{\alpha(V)})_{Horizontal}}{2} + \frac{(\gamma_{\alpha(H)})_{Horizontal} - (\gamma_{\alpha(V)})_{Horizontal}}{2}\cos 2\beta$$

$$\tag{3.57}$$

$$(\gamma_{\alpha(V)})_{Tilted} = \frac{(\gamma_{\alpha(H)})_{Horizontal} + (\gamma_{\alpha(V)})_{Horizontal}}{2} - \frac{(\gamma_{\alpha(H)})_{Horizontal} - (\gamma_{\alpha(V)})_{Horizontal}}{2}\cos 2\beta$$

$$\tag{3.58}$$

$$(\gamma_{\alpha(HV)})_{Tilted} = -\frac{(\gamma_{\alpha(H)})_{Horizontal} - (\gamma_{\alpha(V)})_{Horizontal}}{2}\sin 2\beta \tag{3.59}$$

Figures 3.8(a) and 3.8(b) show the normalized stress arching ratios at the center of plane strain reservoirs with rectangular and elliptical cross-sections, respectively, when the cross-sectional dip angle is 30 degrees. Comparing these results with the results for a horizontal reservoir in Figure 3.7 clearly indicates that the effect of dip on normalized stress arching ratios is significant.

3.6. Theory of Inhomogeneities

In the case when the inclusion (i.e., reservoir) and matrix (i.e., surrounding rock) have different elastic properties, the inclusion is referred to as an inhomogeneity. Consider the case of an infinite elastic matrix with the elastic moduli C_{ijkl}, containing an ellipsoidal domain with the elastic moduli C^*_{ijkl} as shown in Figure 3.9. If constant eigenstrain ε^*_{ij} in the inhomogeneity causes the strain field ε_{ij}, the induced stress $\Delta\sigma_{ij}$ in the inhomogeneity can be found as:

$$\Delta\sigma_{ij} = C^*_{ijkl}(\varepsilon_{kl} - \varepsilon^*_{kl})$$
(3.60)

Eshelby (1957) showed that the problem of an ellipsoidal inhomogeneity with constant eigenstrains can be transformed into an equivalent inclusion problem. As such, it is useful to simulate the inhomogeneity as an inclusion in a homogeneous material with eigenstrain ε^{**}_{ij}. By doing this, the stress within the inhomogeneity can be written as:

$$\Delta\sigma_{ij} = C_{ijkl}(\varepsilon_{kl} - \varepsilon^{**}_{kl})$$
(3.61)

Here, the eigenstrain ε^{**}_{ij} is a fictitious one which is introduced for the purpose of this simulation.

Using equation (3.27) and (3.28), and the equivalency between equations (3.60) and (3.61), we find the following:
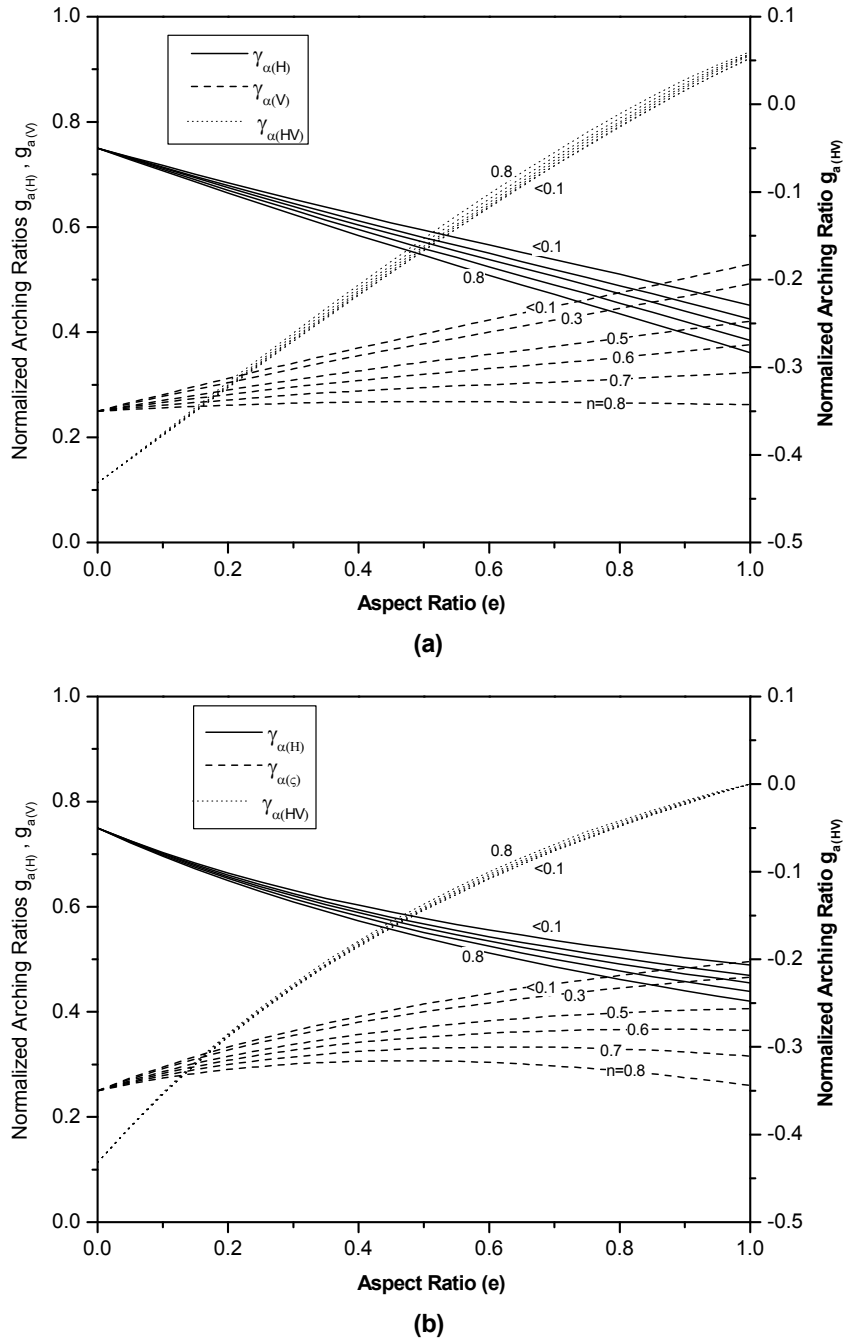
Figure 3.8. Variation of normalized arching ratios with aspect ratio in the center of (a) a rectangular reservoir dipping at 30° and (b) an elliptical reservoir dipping at 30° from horizontal in the cross-sectional plane. All of the values are normalized by $(1-2\nu)/(1-\nu)$.
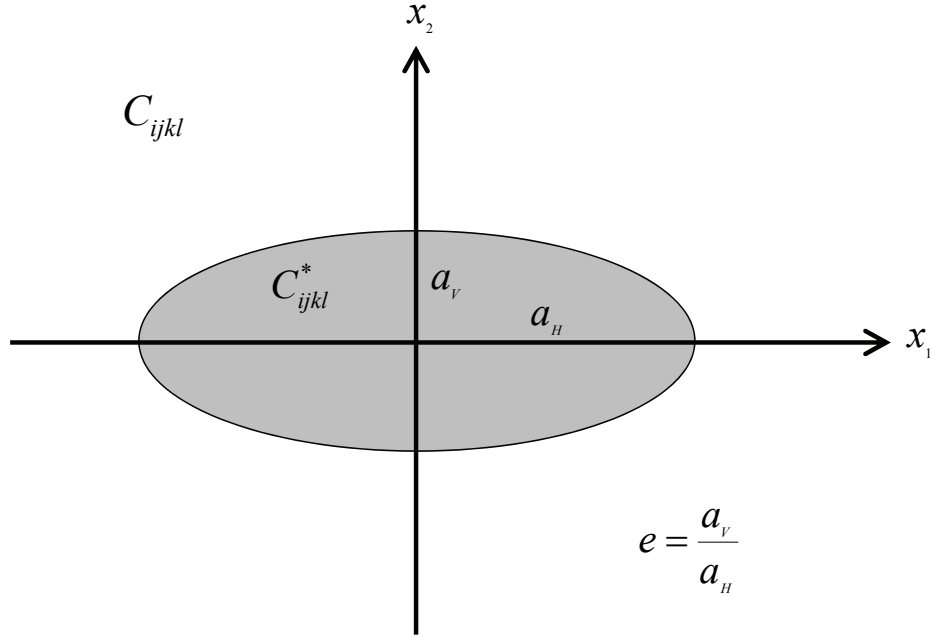
Figure 3.9. Elliptical inhomogeneity in a full plane

$$\left[(C^*_{ijkl} - C_{ijkl})S_{klmn} + C_{klmn}\right]\varepsilon^{**}_{mn} = C^*_{ijkl}\varepsilon^*_{kl} \tag{3.62}$$

Poroelastic eigenstrains are similar to thermoelastic ones in that the eigenstrain inside the inclusion is dilatational, hence no shear strain components exist. As such, for a poroelastic problem under plane strain conditions, we have:

$$\boldsymbol{\varepsilon}^*_{ij} = \varepsilon^*_C \delta_{ij} \qquad\qquad i, j = 1,2 \tag{3.63}$$

ΔP is pore pressure change, μ^* is shear modulus, and ν^* is Poisson's ratio in the inhomogeneity.

The isotropic elastic moduli for the matrix and inhomogeneity, respectively, can be written as:

$$C_{ijkl} = \mu C_{\nu(ijkl)} \tag{3.64}$$

$$C^*_{ijkl} = \mu^* C^*_{\nu(ijkl)} \tag{3.65}$$

where

$$C_{v(ijkl)} = \frac{2v}{1-2v}\delta_{ij}\delta_{kl} + \delta_{ik}\delta_{jl} + \delta_{il}\delta_{jk} \qquad (3.66)$$

and

$$C^*_{v(ijkl)} = \frac{2v^*}{1-2v^*}\delta_{ij}\delta_{kl} + \delta_{ik}\delta_{jl} + \delta_{il}\delta_{jk} \qquad (3.67)$$

Substituting equations (3.63) to (3.66) into equation (3.62) we find:

$$\left[\left(R_\mu C^*_{v(ijkl)} - C_{v(ijkl)}\right)S_{klmm} + C_{v(klmm)}\right]\varepsilon^{**}_{N(mm)} = \delta_{ij} \qquad (3.68)$$

where $R_\mu = \mu^*/\mu$ is the ratio of shear moduli in the inhomogeneity and matrix, and $\varepsilon^{**}_{N(ij)}$ will be referred to as the "normalized fictitious eigenstrain":

$$\varepsilon^{**}_{N(ij)} = \frac{\varepsilon^{**}_{ij}}{-(\alpha\Delta P/\mu)} \qquad (3.69)$$

The values of equivalent eigenstrains $\left(\varepsilon^{**}_{ij}\right)$ can be found using equations (3.68) and (3.69). They can then be used in equations (3.60) and (3.61) for an equivalent inclusion, to solve for the stress and strain fields within and surrounding the inhomogeneity. Following, as an example, this methodology is applied to determine induced in-plane stress changes for an infinitely long inclusion of elliptical cross-section within a full-space. Then, this methodology will be applied to determine induced stress change within different variations of ellipsoidal reservoir in three-dimensional full space.

3.6.1. Application of the theory of inhomogeneities for a plane strain reservoir

For the case of an infinitely long inclusion of elliptical cross-section within a full-space (as shown in Figure 3.9), the values of S_{ijkl} can be found from Mura's (1982) equations for an elliptical cylinder in a full-space as (see Table 3.1):

$$S_{1111} = \frac{1}{2(1-v)}\left[\frac{e^2+2e}{(1+e)^2}+(1-2v)\frac{e}{1+e}\right] \quad , \quad S_{1122} = \frac{1}{2(1-v)}\left[\frac{e^2}{(1+e)^2}-(1-2v)\frac{e}{1+e}\right]$$

$$S_{2211} = \frac{1}{2(1-v)}\left[\frac{1}{(1+e)^2}-(1-2v)\frac{1}{1+e}\right] \quad , \quad S_{2222} = \frac{1}{2(1-v)}\left[\frac{1+2e}{(1+e)^2}+(1-2v)\frac{1}{1+e}\right] \quad (3.70)$$

where e is the aspect ratio of the elliptical reservoir.

Fictitious eigenstrains for a plane strain condition

Using these expressions for S_{ijkl} in equation (3.68) it is possible to find the poroelastic normalized fictitious eigenstrains in closed form as:

$$\varepsilon_{N(H)}^{**} = \frac{E_1}{E_4} \ , \ \varepsilon_{N(V)}^{**} = \frac{E_2}{E_4} \qquad\qquad (3.71)$$

where:

$\varepsilon_{N(H)}^{**}$ = in-plane horizontal component of the normalized fictitious eigenstrain

$\varepsilon_{N(V)}^{**}$ = vertical component of the normalized fictitious eigenstrain

$$E_1 = [R_\mu[(1+e)^2(1-v)-e^2]+e^2](1-2v^*)(1-v) \qquad\qquad (3.72)$$

$$E_2 = [R_\mu[(1+e)^2(1-v)-1]+1](1-2v^*)(1-v) \qquad\qquad (3.73)$$

$$E_4 = R_\mu[2(1+e)^2(1-v)(1-v^*)-2ev^*(1-2v)+R_\mu e(3-4v^*)]+e(1-2v^*) \qquad\qquad (3.74)$$

Special cases

In the case of a homogeneous material (i.e., $R_\mu = 1$ and $v = v^*$):

$$\varepsilon_{N(H)}^{**} = \varepsilon_{N(V)}^{**} = \frac{1-2v}{2} \qquad\qquad (3.75)$$

For two limiting cases of R_μ, equation (3.71) can be greatly simplified. In the case of $R_\mu = 0$ (i.e., the inhomogeneity is a cavity), the following expressions are found:

$$\varepsilon_{N(H)}^{**} = e(1-\nu) \ , \varepsilon_{N(V)}^{**} = \frac{1-\nu}{e} \tag{3.76}$$

In the case of $R_\mu \rightarrow \infty$, we find that

$$\varepsilon_{N(H)}^{**} = \varepsilon_{N(V)}^{**} = 0 \tag{3.77}$$

This agrees with the intuitive expectation of no induced fictitious eigenstrains in a perfectly rigid body.

In the special case of an inhomogeneity of infinite lateral extent (i.e., $e = 0$), equations (3.71) reduce to:

$$\varepsilon_{N(H)}^{**} = \frac{1-2\nu^*}{2(1-\nu^*)}(1-\nu), \ \varepsilon_{N(V)}^{**} = \frac{1-2\nu^*}{2(1-\nu^*)}(\frac{1}{R_\mu} - \nu) \tag{3.78}$$

In the case of a circular inhomogeneity ($e = 1$), we find that:

$$\varepsilon_{N(H)}^{**} = \varepsilon_{N(V)}^{**} = \frac{1-2\nu^*}{1-2\nu^* + R_\mu}(1-\nu) \tag{3.79}$$

Stress change within an inhomogeneity

The induced total stress change within an inhomogeneity can be found using equations (3.61) and (3.27) as:

$$\Delta\sigma_{ij} = C_{ijkl}(S_{klmn}\varepsilon_{mn}^{**} - \varepsilon_{kl}^{**}) \tag{3.80}$$

In the case of poroelastic eigenstrains, this can be expressed using equations (3.9), (3.64), and (3.69) as:

$$\gamma_{\alpha(ij)} = C_{v(ijkl)}(\delta_{km}\delta_{lm} - S_{klmn})\varepsilon_{N(mm)}^{**}$$ (3.81)

For plane strain conditions, the solution of these equations can be written in closed form as:

$$\gamma_{\alpha(H)} = \frac{A_1}{E_4}, \ \gamma_{\alpha(V)} = \frac{A_3}{E_4}$$ (3.82)

where

$$A_1 = (1-2v^*)[R_\mu[e(1-2v)+2(1-v)]+e]$$ (3.83)

$$A_3 = (1-2v^*)[R_\mu[2e(1-v)+1-2v]+1]e$$ (3.84)

Sensitivity analyses

This section demonstrates the effects of reservoir aspect ratio and rock properties on induced stress changes within a reservoir.

Values of normalized arching ratios, in most conditions, have a weak dependency on Poisson's ratio of the matrix. This is shown in Figure 3.10, which graphs the maximum absolute error incurred if the matrix is assumed to have a Poisson's ratio identical to the inhomogeneity's. This maximum error was calculated as follows:

1. For a given shear modulus ratio, exact solutions for vertical and horizontal arching ratios were calculated over the full range of reservoir aspect ratios ($0 \le e \le 1.0$) and matrix Poisson's ratios ($0 \le v \le 0.5$).
2. The maximum error obtained for all of these cases was recorded, and its absolute value plotted on the graph shown in Figure 3.10.
3. Steps 1 and 2 were repeated for various values of the shear modulus ratio, ranging from 0.001 to 1000.
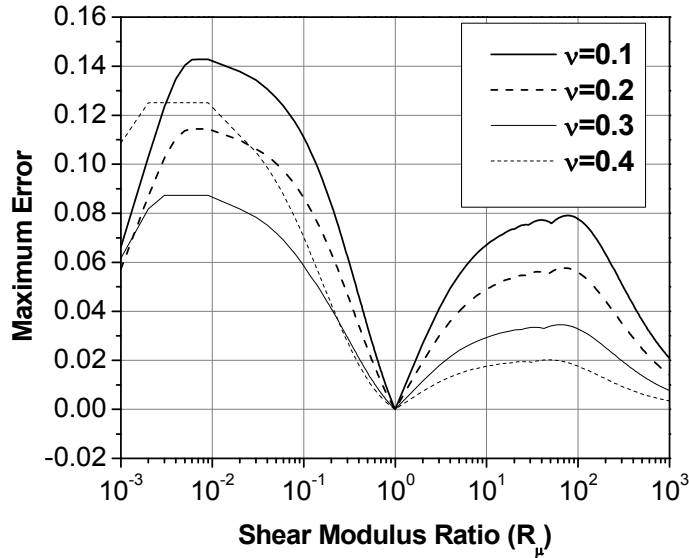
Figure 3.10. Maximum error in the calculated normalized stress arching ratio when Poisson's ratio of the matrix and inhomogeneity are assumed to be equal.

The maximum error in the normalized arching ratio is less than 0.15. This means that, using the simplifying assumption of a uniform Poisson's ratio throughout the entire full-plane, the maximum error in calculating the induced stress changes will be less than 15 percent of the effective change in pore pressure ($\alpha \Delta P$). In many of the cases evaluated, especially for shear modulus ratios close to 1, the error will be much smaller. In a practical sense, then, it will often be acceptable to make the simplifying assumption of uniform Poisson's ratio.

As shown, values of normalized stress arching ratios within reservoirs have a weak dependence on Poisson's ratio of the matrix, for most conditions. As such, the simplifying assumption of uniform Poisson's ratio throughout the full-space has been made in the examples that follow.

Figures 3.11(a) and 3.11(b) show the variation of normalized horizontal and vertical arching ratios with aspect ratio and shear modulus ratio for two different scenarios with uniform Poisson's ratios ($\nu = \nu^* = 0.2$ and $\nu = \nu^* = 0.4$). Some general observations pertaining to these figures are:

- Vertical arching ratio increases monotonically with increasing aspect ratio.

65
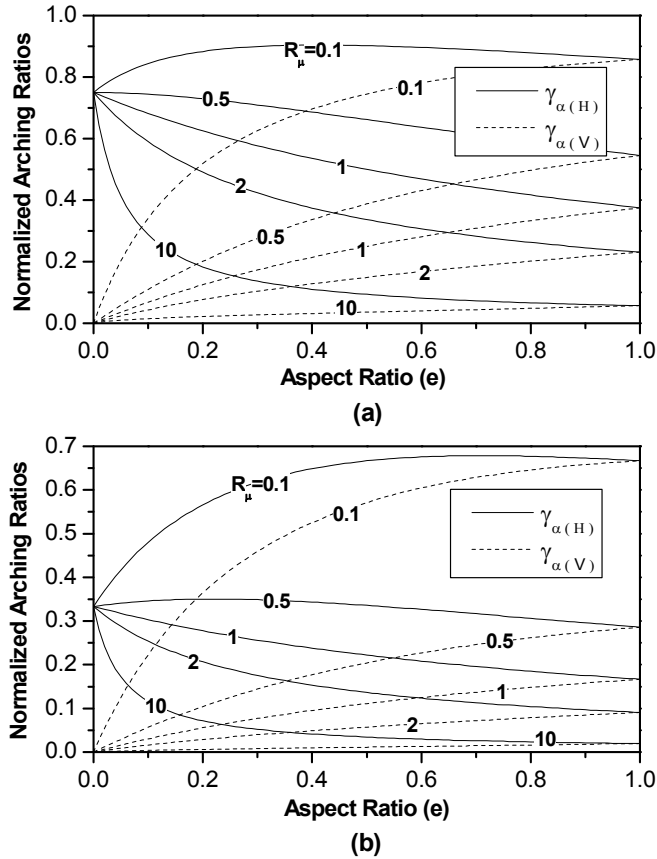
Figure 3.11. Normalized horizontal and vertical stress arching ratios ($\gamma_{\alpha(H)}$ and $\gamma_{\alpha(V)}$) as a function of elliptical inhomogeneity aspect ratio (e) for different values of the shear modulus ratio (R_μ): (a) Uniform Poisson's ratio ($v = v^*$) of 0.2. (b) Uniform Poisson's ratio ($v = v^*$) of 0.4.

- Horizontal arching ratio decreases monotonically with increasing aspect ratio only if shear modulus ratio is close to or greater than 1.

- Both vertical and horizontal arching ratios decrease monotonically with increasing shear modulus ratio.

- Both vertical and horizontal arching ratios are larger for the case with smaller Poisson's ratio.

The variation of normalized arching ratios with shear modulus ratio is shown in Figure 3.12 for an inhomogeneity with an aspect ratio of 0.5 for cases in which Poisson's ratio of the matrix and inhomogeneity are identical and equal to 0.2 and 0.4, respectively. Once again, it is observed that the arching ratios are larger for the case of smaller Poisson's ratio.

66
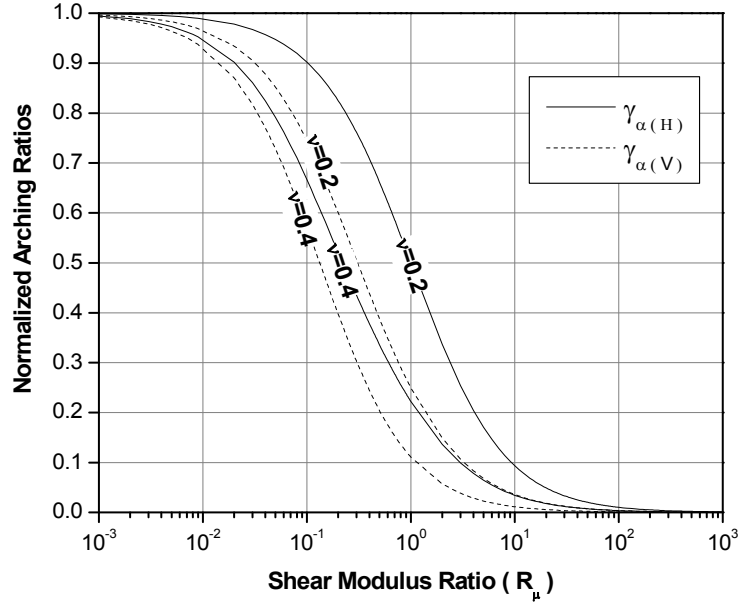
Figure 3.12. Normalized horizontal and vertical stress arching ratios ($\gamma_{\alpha(H)}$ and $\gamma_{\alpha(V)}$) for different values of the shear modulus ratio (R_μ) for an elliptical inhomogneity with an aspect ratio (e) of 0.5 and uniform Poisson's ratio throughout the problem domain (i.e., $v = v^*$).

Special cases

In the case of a homogeneous material (i.e., $R_\mu = 1$ and $v = v^*$), the new model provides results that are equivalent to those that would be generated using models based on the theory of inclusions or the theory of strain nuclei. For example, equation (3.82) reduces to the following form in such a case, which corresponds to the solutions derived for homogeneous media (see equation (3.34)):

$$\gamma_{\alpha(H)} = \frac{1-2v}{1-v}\frac{1}{1+e}, \; \gamma_{\alpha(V)} = \frac{1-2v}{1-v}\frac{e}{1+e} \tag{3.85}$$

Further to the sensitivity analyses discussed previously, Figure 3.12 also shows the two limiting behaviours for shear modulus ratio. For $R_\mu = 0$, which implies that the materials of the inhomogeneity are significantly softer than matrix (e.g., a cavity), $\gamma_{\alpha(H)} = \gamma_{\alpha(V)} = 1$. This means that all of the pore pressure change is transferred to the matrix as a stress change. For very large values of R_μ, which means that inhomogeneity is

67

considerably more rigid than the matrix, the expected result $\gamma_{\alpha(H)} = \gamma_{\alpha(V)} = 0$ is obtained. This means that all of the effect of pore pressure change is sustained by the inhomogeneity itself.

In the case of an inhomogeneity of infinite lateral extent (i.e., $e = 0$), equation (3.82) reduces to the familiar equation [e.g., Segall and Fitzgerald (1998)]:

$$\gamma_{\alpha(H)} = \frac{1 - 2v^*}{1 - v^*}, \gamma_{\alpha(V)} = 0 \tag{3.86}$$

In the case of a circular inhomogeneity ($e = 1$) we find that:

$$\gamma_{\alpha(H)} = \gamma_{\alpha(V)} = \frac{1 - 2v^*}{R_\mu + 1 - 2v^*} \tag{3.87}$$

Stress field within the matrix

For cases such as poroelastic dilation, for which there are no shear eigenstrains ($\varepsilon_{ij}^* = 0$ when $i \neq j$), equation (3.22) can be re-written as:

$$\Delta\sigma_{ij}(\mathbf{x}) = -\oint_\Omega \left[\lambda(3\lambda + 2\mu)G_{ks,sk}(\mathbf{x},\mathbf{x}')\varepsilon_{rr}(\mathbf{x}') + 2\mu(3\lambda G_{km,mk}(\mathbf{x},\mathbf{x}') + 2\mu G_{im,mi}(\mathbf{x},\mathbf{x}'))\varepsilon_{mm}(\mathbf{x}') \right] d\mathbf{x}' \tag{3.88}$$

The first derivatives of Green's functions in equation (3.50) are found as:

$$G_{ij,k} = \frac{1}{8\pi\mu(1 - v)} \frac{2l_i l_j l_k + (3 - 4v)l_k\delta_{ij} - l_i\delta_{jk} - l_j\delta_{ik}}{R} \tag{3.89}$$

The second derivatives of Green's functions are found as:

$$G_{ij,kp}(\mathbf{x},\mathbf{x}') = \frac{1}{8\pi\mu(1 - v)} \frac{1}{R^2} [8l_i l_j l_k l_p - 2l_j l_k\delta_{ip} - 2l_i l_k\delta_{jp} - 2l_i l_j\delta_{kp} - 2l_i l_p\delta_{jk} - 2l_j l_p\delta_{ik} +$$
$$2(3 - 4v)l_k l_p\delta_{ij} + \delta_{ip}\delta_{jk} + \delta_{ik}\delta_{jp} - (3 - 4v)\delta_{ij}\delta_{kp}]$$
$$\tag{3.90}$$

Using equations (3.9) and (3.69), and derivatives of Green's functions, equation (3.88) can be written as:

$$\gamma_{ij} = N_{ijkk} \varepsilon_{N(kk)}^{**} \tag{3.91}$$

$$N_{ijkk}(\mathbf{x}) = \frac{1}{2\pi(1-\nu)} \oint_{\Omega} \frac{8 l_i l_j l_k l_k - 4 l_k^2 \delta_{ik} \delta_{ij} - 2 l_1 l_2 (1 - \delta_{ij}) - \delta_{ij}}{R^2} d\mathbf{x}' \tag{3.92}$$

Specific forms of these equations, for horizontal and vertical stress arching ratios, can be written as follows:

$$\gamma_{\alpha(H)} = N_{HH} \varepsilon_{N(H)}^{**} + N_{HV} \varepsilon_{N(V)}^{**} \tag{3.93}$$

$$\gamma_{\alpha(V)} = N_{VH} \varepsilon_{N(H)}^{**} + N_{VV} \varepsilon_{N(V)}^{**} \tag{3.94}$$

where the coefficients N_{HH}, N_{HV}, N_{VH} and N_{VV} are given by:

$$N_{HH} = \frac{1}{2\pi(1-\nu)} \int_{-1}^{1} \int_{-e\sqrt{1-(x_1')^2}}^{e\sqrt{1-(x_1')^2}} \left[8 \frac{(x_1 - x_1')^4}{R^6} - 4 \frac{(x_1 - x_1')^2}{R^4} - \frac{1}{R^2} \right] dx_2' dx_1' \tag{3.95}$$

$$N_{HV} = N_{VH} = \frac{1}{2\pi(1-\nu)} \int_{-1}^{1} \int_{-e\sqrt{1-(x_1')^2}}^{e\sqrt{1-(x_1')^2}} \left[8 \frac{(x_1 - x_1')^2 (x_2 - x_2')^2}{R^6} - \frac{1}{R^2} \right] dx_2' dx_1' \tag{3.96}$$

$$N_{VV} = \frac{1}{2\pi(1-\nu)} \int_{-1}^{1} \int_{-e\sqrt{1-(x_1')^2}}^{e\sqrt{1-(x_1')^2}} \left[8 \frac{(x_2 - x_2')^4}{R^6} - 4 \frac{(x_2 - x_2')^2}{R^4} - \frac{1}{R^2} \right] dx_2' dx_1' \tag{3.97}$$

Figure 3.13 shows the spatial variation of these coefficients for an inhomogeneity having an elliptical cross-section with an aspect ratio of 0.5, under plane strain conditions. Figures 3.14(a) and 3.14(b) show the variation of these coefficients along the horizontal and vertical centerlines of the same inhomogeneity. Using equations (3.93) and (3.94) and these figures, it is possible to calculate the normalized stress arching ratios at any point in the matrix using only basic arithmetic operations. [Note: This is a significant point. Although the numerical integration required to generate Figures 3.13 and 3.14 is relatively straightforward

using available applied mathematics software applications, it is nevertheless a time-consuming process. As such, a set of contour plots for N_{HH}, N_{HV} and N_{VV} need only be generated once for a given reservoir aspect ratio, and normalized stress arching ratios can then be easily calculated for any combination of inhomogeneity and matrix properties. As a case in point, all of the stress arching ratio plots discussed in the following section were generated directly from Figures 3.13 and 3.14.]
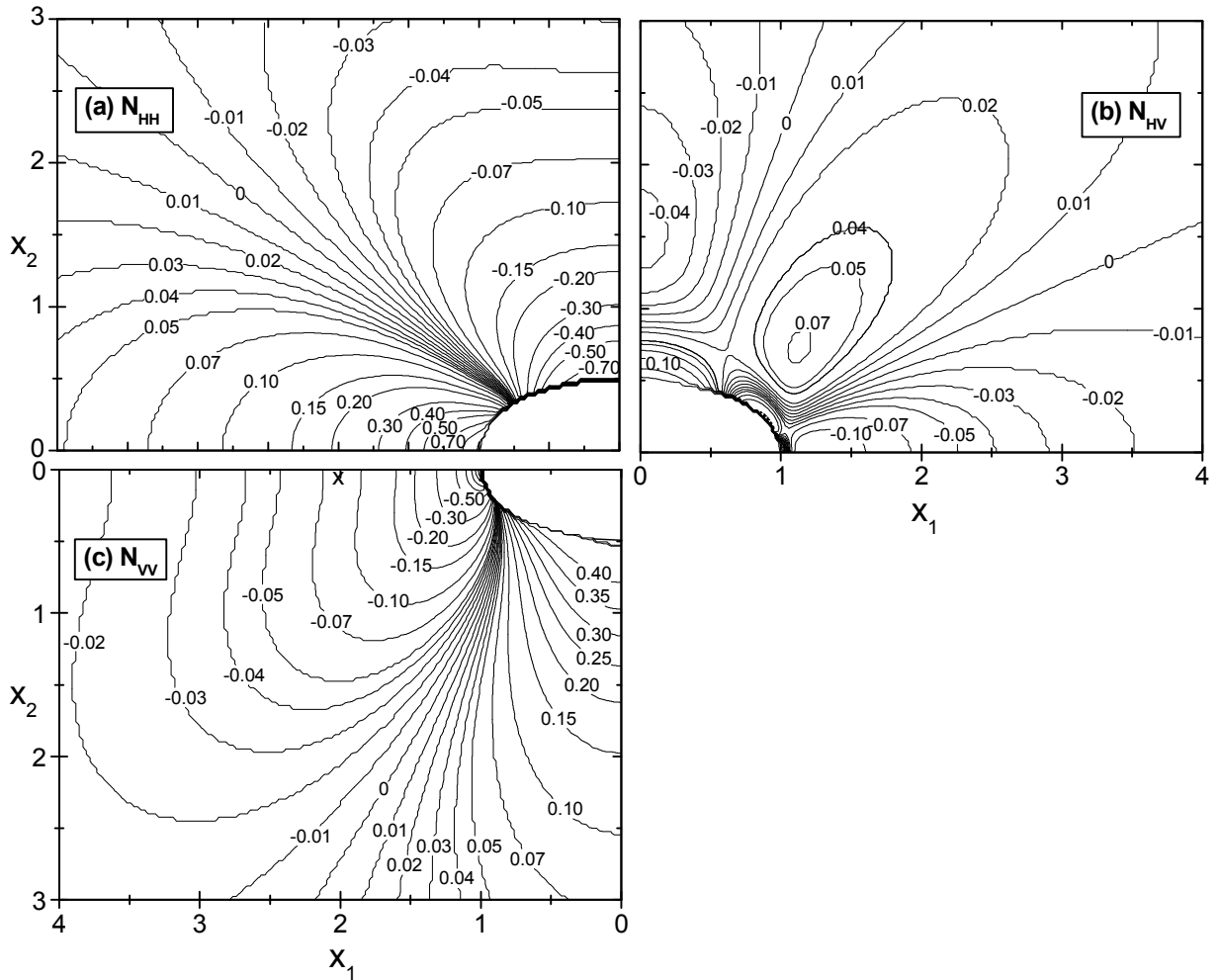
Figure 3.13. Contour plots of coefficients (a) N_{HH}, (b) N_{HV}, and (c) N_{VV} for an elliptical inhomogeneity with aspect ratio $e = 0.5$. All of the values are normalized by $1/(1-v)$.
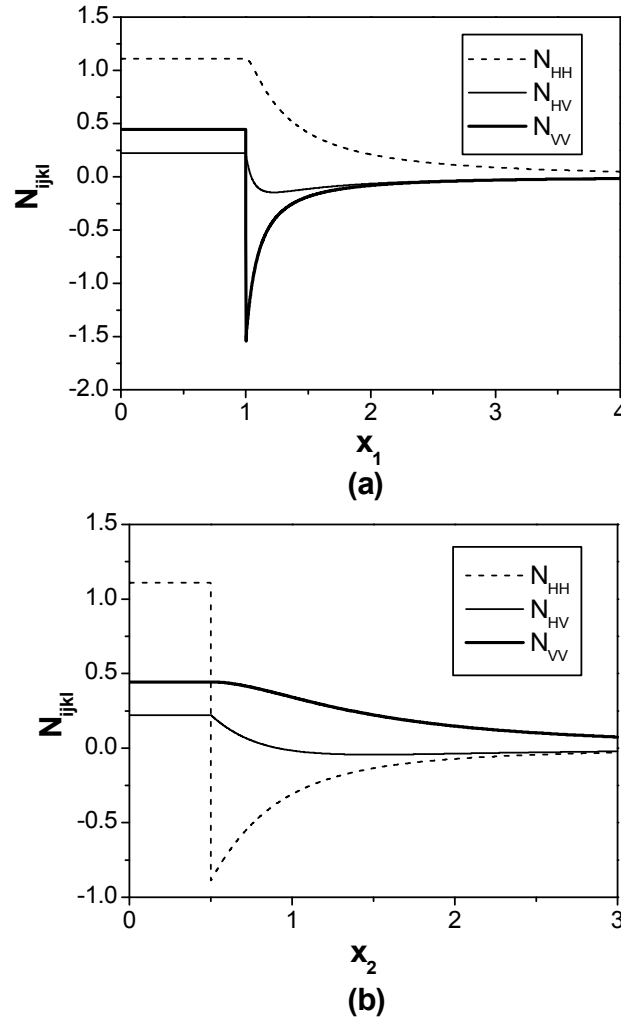
Figure 3.14. Coefficients N_{HH}, N_{HV} and N_{VV} for an elliptical inhomogeneity with aspect ratio $e = 0.5$, (a) along the horizontal centerline (b) along the vertical centerline. All of the values are normalized by $1/(1-v)$.

Example calculations

Figures 3.15 and 3.16 are contour plots showing normalized horizontal and vertical stress arching ratios, respectively, for an infinitely long inhomogeneity of elliptical cross-section, with an aspect ratio of 0.5 and Poisson's ratio of 0.2 for both the matrix and the inhomogeneity. Results are shown for shear modulus ratios of 1, 0.5, 2 and 0. Figures 3.17 and 3.18 show analogous output for the same calculations, repeated using a uniform Poisson's ratio of 0.4.

The general form of the horizontal arching ratio field is similar for the three reservoir cases shown, and slightly different for the cavity case. Common to all cases, though, is the fact that the normalized values of these arching ratios are negative above and beneath the inhomogeneity, and positive beyond its lateral flanks. This means that, for the example of a depleted reservoir (i.e., $\Delta P < 0$) or a depressurized cavity, compressive stress changes will occur above and below the reservoir, while tensile stress changes will occur beyond its lateral flanks.

The general form of the vertical arching ratio field is similar for all cases shown. The normalized values of these arching ratios are positive above and beneath the inhomogeneity, and negative beyond its lateral flanks. This means that, for the example of a depleted reservoir, tensile stress changes will occur above and below the reservoir, while compressive stress changes will occur outside of its lateral flanks. From a comparison of Figures 3.15 and 3.16 to Figures 3.17 and 3.18, it is apparent that the region of influence of pore pressure change is greater for smaller values of Poisson's ratio. In other words, during pore pressure change within the inhomogeneity, the stress change front propagates deeper into the matrix as Poisson's ratio decreases.

The results indicate that, with decreasing rigidity of the inhomogeneity, a greater proportion of the pore pressure change is transferred to the matrix. In the limiting case of a cavity ($R_\mu = 0$), all of the pore pressure will be transferred to the matrix as a stress change, resulting in significant stress changes in the vicinity of the inhomogeneity. As can be seen from equations (3.76) and (3.93) and (3.94) the stress field in the matrix for a cavity is independent of Poisson's ratio of the matrix.
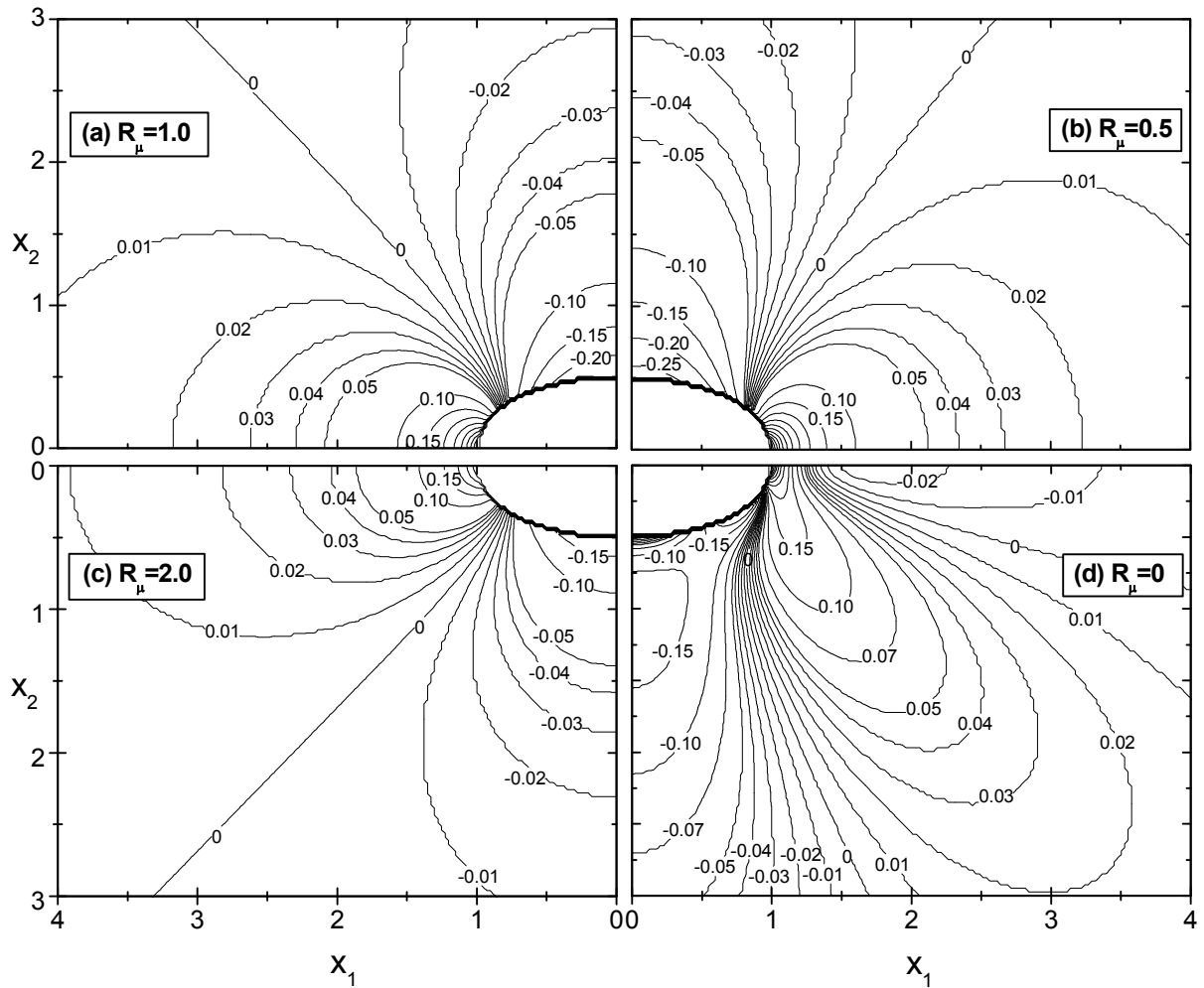
Figure 3.15. Normalized horizontal stress arching ratio $\gamma_{\alpha(H)}$ field for an elliptical inhomogeneity with an aspect ratio of 0.5 and Poisson's ratio of 0.2 for both the inhomogenity and the matrix. Results for different shear modulus ratios are shown, as follows: (a) R_μ=1.0 (i.e., homogenous inclusion), (b) R_μ=0.5, (c) R_μ=2.0 and (d) R_μ=0 (i.e., the inhomogeneity is a cavity).

Figure 3.16. Normalized vertical stress arching ratio $\gamma_{\alpha(V)}$ field for an elliptical inhomogeneity with an aspect ratio of 0.5 and Poisson's ratio of 0.2 for both the inhomogenity and the matrix. Results for different shear modulus ratios are shown, as follows: (a) $R_\mu=1.0$ (i.e., homogenous inclusion), (b) $R_\mu=0.5$, (c) $R_\mu=2.0$ and (d) $R_\mu=0$ (i.e., the inhomogeneity is a cavity).
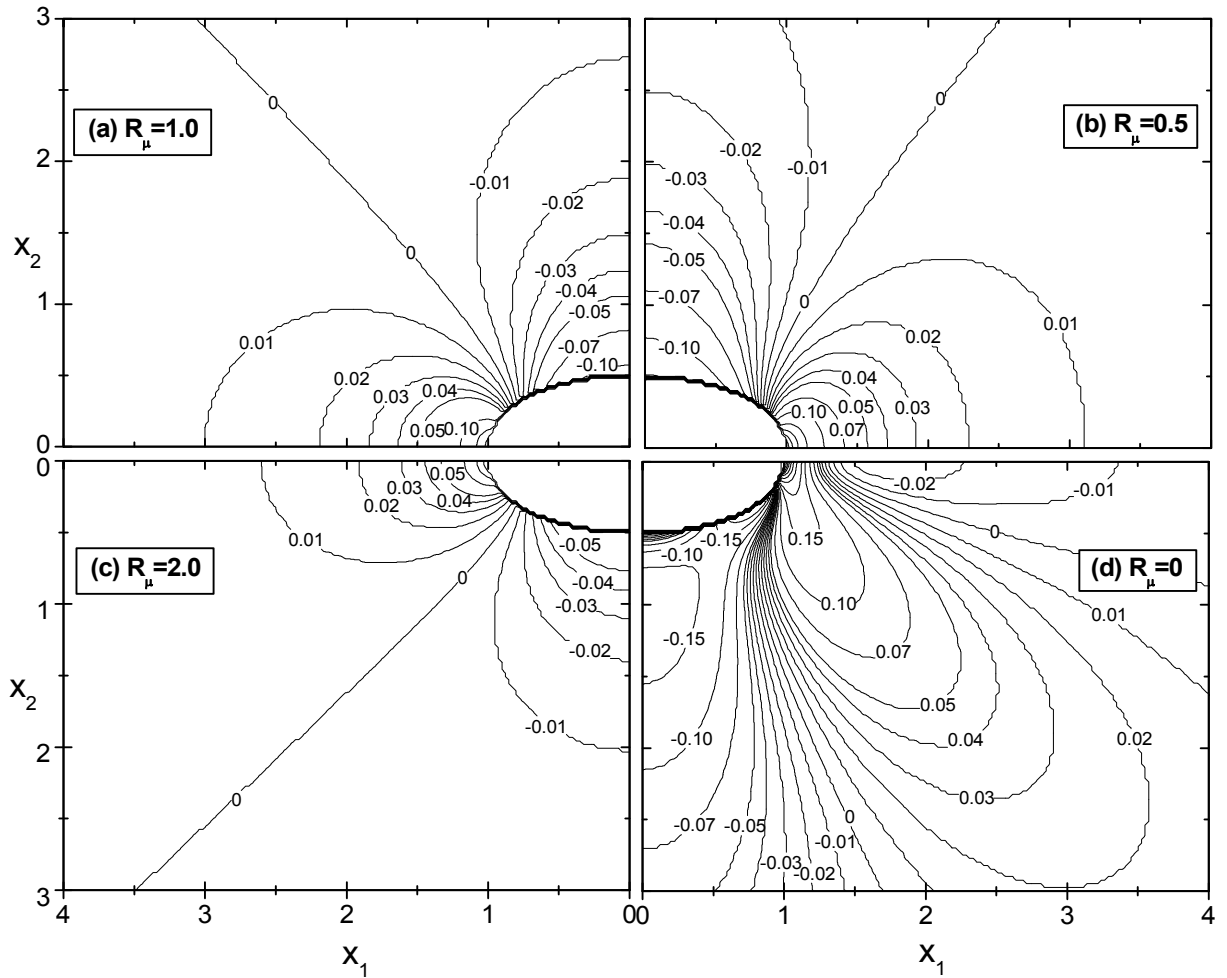
Figure 3.17. Normalized horizontal stress arching ratio $\gamma_{\alpha(H)}$ field for an elliptical inhomogeneity with an aspect ratio of 0.5 and Poisson's ratio of 0.4 for both the inhomogenity and the matrix. Results for different shear modulus ratios are shown, as follows: (a) R_μ=1.0 (i.e., homogenous inclusion), (b) R_μ=0.5, (c) R_μ=2.0 and (d) R_μ=0 (i.e., the inhomogeneity is a cavity).
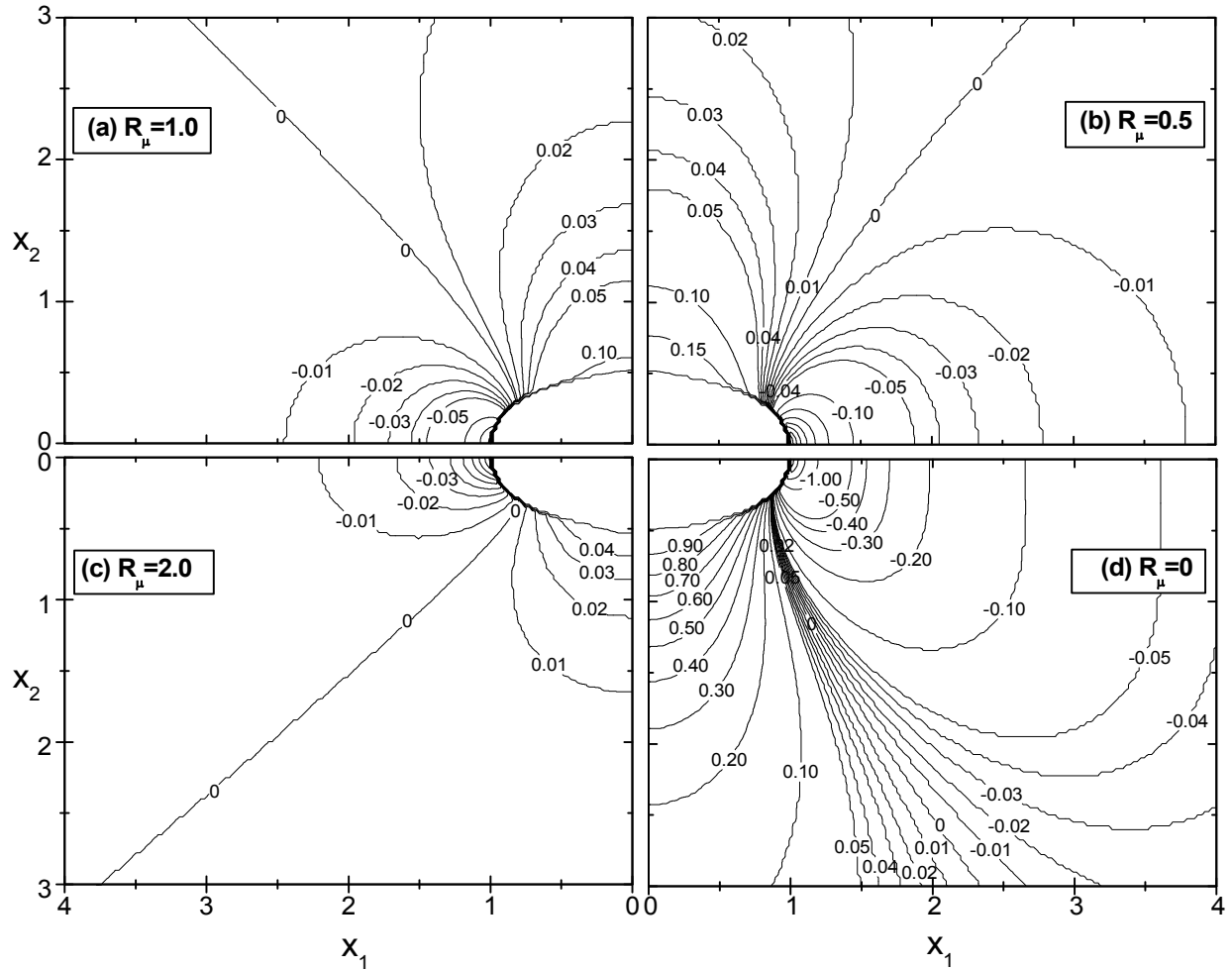
Figure 3.18. Normalized vertical stress arching ratio $\gamma_{\alpha(V)}$ field for an elliptical inhomogeneity with an aspect ratio of 0.5 and Poisson's ratio of 0.4 for both the inhomogenity and the matrix. Results for different shear modulus ratios are shown, as follows: (a) R_μ=1.0 (i.e., homogenous inclusion), (b) R_μ=0.5, (c) R_μ=2.0 and (d) R_μ=0 (i.e., the inhomogeneity is a cavity).

Stress field discontinuities

In Figures 3.19(a) to 3.19(d), the variation of normalized stress arching ratios along the horizontal centerline of an inhomogeneity of elliptical cross-section with an aspect ratio of 0.5 is shown. Similarly, Figures 3.20(a) to 3.20(d) show the variation of normalized arching ratios along the vertical centerline of such an inhomogeneity. Examination of these figures reveals that there are discontinuities in the vertical stress arching ratio ($\gamma_{\alpha(V)}$) at the lateral boundaries of the inhomogeneity, and discontinuities in the horizontal stress arching

76
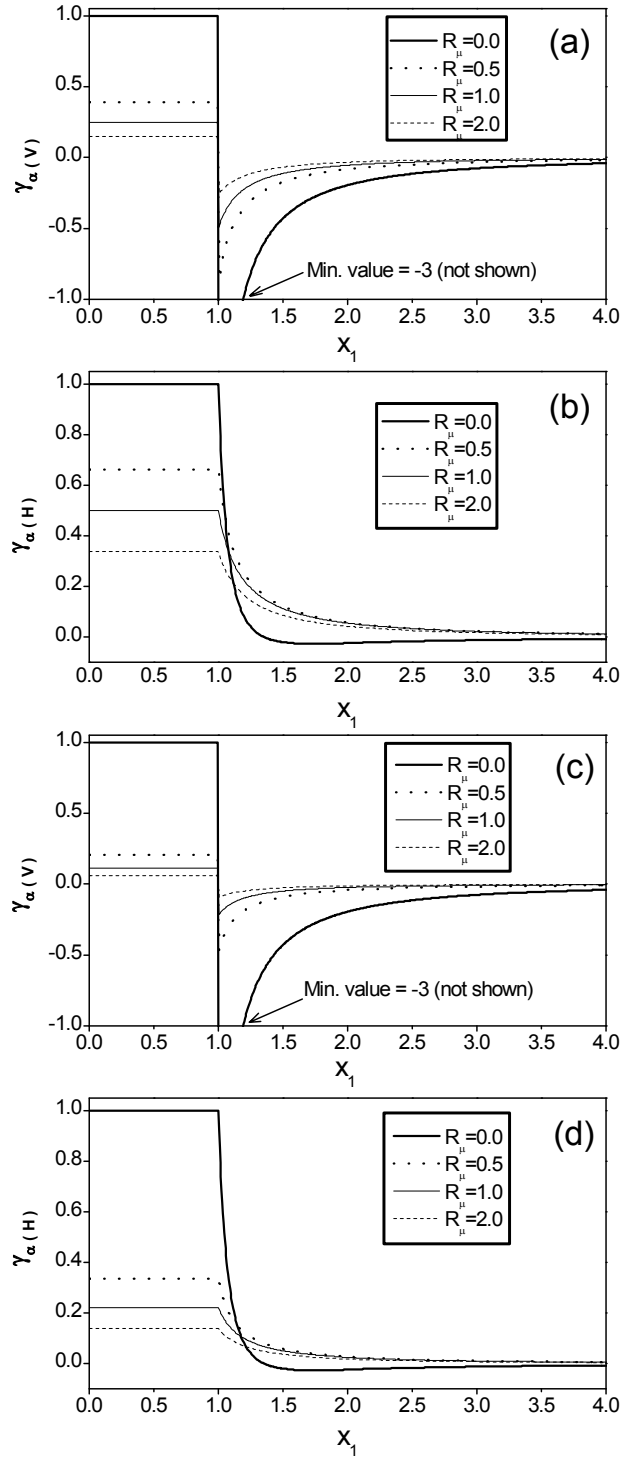
Figure 3.19. Variation of normalized stress arching ratios along the horizontal centerline of an elliptical inhomogeneity with an aspect ratio of 0.5 and uniform Poisson's ratio throughout the matrix and the inhomogenity. (a) Vertical stress arching ratio for $v = 0.2$, (b) horizontal stress arching ratio for $v = 0.2$, (c) vertical stress arching ratio for $v = 0.4$ and (d) horizontal stress arching ratio for $v = 0.4$.
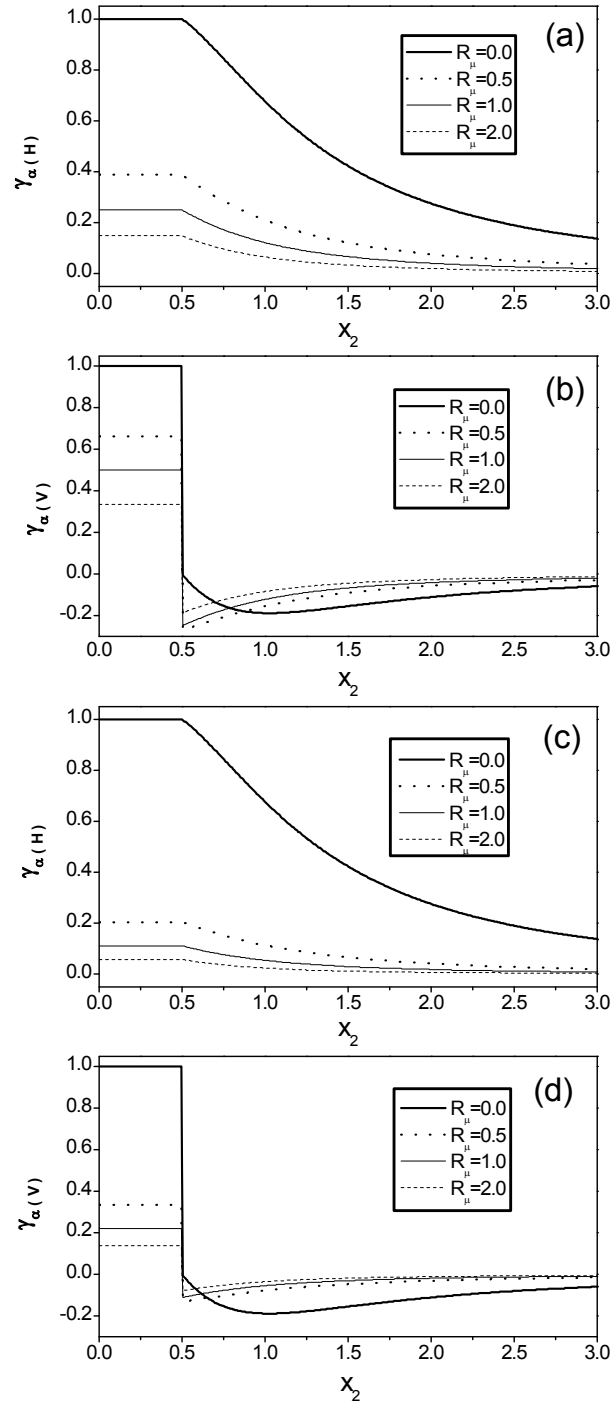
Figure 3.20. Variation of normalized stress arching ratios along the vertical centerline of an elliptical inhomogeneity with an aspect ratio of 0.5 and uniform Poisson's ratio throughout the matrix and the inhomogenity. (a) Vertical stress arching ratio for $v = 0.2$, (b) horizontal stress arching ratio for $v = 0.2$, (c) vertical stress arching ratio for $v = 0.4$ and (d) horizontal stress arching ratio for $v = 0.4$.

ratio ($\gamma_{\alpha(H)}$) at the top and bottom boundaries of the inhomogeneity. This behaviour is expected, given that there is a step change in pore pressure at the reservoir-matrix interface. In essence, induced stress components tangent to this interface will be discontinuous, whereas components normal to the interface will be continuous.

These stress arching ratio discontinuities are controlled by the coefficients presented in equations (3.93) and (3.94). As shown in Figure 3.14, N_{HH} is discontinuous along the vertical centerline, N_{VV} is discontinuous along the horizontal centerline, and there is no discontinuity in N_{HV}. Figures 3.14 further shows that the magnitudes of these discontinuities in N_{HH} and N_{VV} are equal to $2/(1-v)$. Additional analyses have indicated that this result is independent of reservoir aspect ratio. As such, using equations (3.93) and (3.94), the magnitude of the discontinuities in normalized stress arching ratios can be written as:

$$Dis(\gamma_{\alpha(H)}) = \frac{2}{1-v} \varepsilon_{N(V)}^{**}$$

$$Dis(\gamma_{\alpha(V)}) = \frac{2}{1-v} \varepsilon_{N(H)}^{**} \qquad (3.98)$$

In general cases, $\varepsilon_{N(H)}^{**}$ and $\varepsilon_{N(V)}^{**}$ can be found from equations (3.71). In the special case of a homogenous medium (i.e., $R_{\mu} = 1$, $v^* = v$), using equation (3.75) we find the familiar expression (e.g., Goodier 1937):

$$Dis(\gamma_{\alpha(H)}) = Dis(\gamma_{\alpha(V)}) = \frac{1-2v}{1-v} \qquad (3.99)$$

In the case of a cavity (i.e., $R_{\mu} = 0$), using equation (3.76) we find:

$$Dis(\gamma_{\alpha(H)}) = \frac{2}{e}$$

$$Dis(\gamma_{\alpha(V)}) = 2e \qquad (3.100)$$

As a practical point, as mentioned before, it should be noted that factors such as non-linear or plastic deformation, and gradual pore pressure transitions between the reservoir and surrounding rocks, would likely act to diminish the magnitude and alter the characteristics of these discontinuities.

3.6.2. Application of theory of inhomogeneities for ellipsoidal reservoirs in three dimensions

The previously described methodology can be extended to find induced stress change for different variations of an ellipsoidal reservoir with different material properties from the surrounding rock. Below, arching ratios are given for the different variations of an ellipsoidal inhomogeneity. A summary of these solutions is given in Table 3.2.

The generalized form of the results for a poroelastical elliptical reservoir with different material properties from its surrounding rock, under plane strain conditions (i.e., an inhomogeneity that is an elliptic cylinder) can be written as follows:

$$\gamma_{\alpha(H_1)} = A_1 / A_4 \; ; \; \gamma_{\alpha(H_2)} = A_2 / A_4 \; ; \; \gamma_{\alpha(V)} = A_3 / A_4 \tag{3.101}$$

where $\gamma_{\alpha(H_1)}$ and $\gamma_{\alpha(H_2)}$ denote the in-plane and out-of-plane poroelastic normalized stress arching ratios, respectively, and:

$$A_2 = (1 - 2v^*)[R_\mu[R_\mu e(3 - 4v) + 2(1 + e^2)(1 - v)] + e] \tag{3.102}$$

For the case of a circular cylinder (i.e., $e = 1$), these equations reduce to the following:

$$\gamma_{\alpha(H_1)} = \gamma_{\alpha(V)} = \frac{1 - 2v^*}{R_\mu + 1 - 2v^*} \; ; \; \gamma_{\alpha(H_2)} = \frac{(1 + R_\mu)(1 - 2v^*)}{R_\mu + 1 - 2v^*} \tag{3.103}$$

In the case of a sphere, the results are (as shown previously by Rudnicki, 1999)

$$\gamma_{\alpha(H_1)} = \gamma_{\alpha(H_2)} = \gamma_{\alpha(V)} = \frac{2(1 - 2v^*)}{R_\mu(1 + v^*) + 2(1 - 2v^*)} \tag{3.104}$$

And for an infinite layer:

$$\gamma_{\alpha(H_1)} = \gamma_{\alpha(H_2)} = \frac{1-2v^*}{1-v^*} \quad ; \quad \gamma_{\alpha(V)} = 0 \tag{3.105}$$

Unfortunately, deriving such simple closed-form solutions is not easy for all different ellipsoidal geometries. However, it is possible to find solutions with some simplifications in modelling assumptions. Previously conducted sensitivity analyses (see section 3.6.1) have shown that the values of stress arching ratios within reservoirs have only a weak dependency on Poisson's ratio of the matrix. Therefore, an assumption of identical Poisson's ratios in the inhomogeneity and the matrix (i.e., $v = v^*$) can be used, without incurring a significant error. By considering this simplification, for any axisymmetric ellipsoidal inhomogeneity including an oblate or prolate geometry, the following closed-form solutions can be found for poroelastic normalized stress arching ratios:

$$\gamma_{\alpha(H_1)} = \gamma_{\alpha(H_2)} = B_1 / B_3, \ \gamma_{\alpha(V)} = B_2 / B_3 \tag{3.106}$$

where:

$$B_1 = (1+v)(1 - X_2 + (1 - R_\mu)X_1) + R_\mu(X_3 + vX_4) \tag{3.107}$$

$$B_2 = (1+v)[1 - (R_\mu - 1)X_1 - X_2] + R_\mu[(1-v)X_4 + 2vX_3] \tag{3.108}$$

$$B_3 = (1+v)[(R_\mu - 1)^2 X_1 + (R_\mu - 1)X_2 + 1] \tag{3.109}$$

where X_1, X_2, and X_3 are auxiliary variables which are functions of Eshelby tensor (see Table 3.1), as follows:

$$X_1 = (S_{1111} + S_{1122})S_{3333} - 2S_{3311}S_{1133} \tag{3.110}$$

$$X_2 = S_{1111} + S_{1122} + S_{3333} \tag{3.111}$$

$$X_3 = S_{3333} - S_{1133} \tag{3.112}$$

$$X_4 = S_{1111} + S_{1122} - 2S_{3311} \tag{3.113}$$

The relationships in equations (3.110) to (3.113) reduce to a more simplified form for a penny-shaped reservoir:

$$\gamma_{\alpha(H_1)} = \gamma_{\alpha(H_2)} = C_1 / C_3 , \; \gamma_{\alpha(V)} = C_2 / C_3 \tag{3.114}$$

where:

$$C_1 = (1 - 2v)\left\{\pi^2 e^2 (1 - R_\mu)(1 + v) - 8R_\mu(1 - v) - 2\pi e[R_\mu(v - 2) + 1]\right\} \tag{3.115}$$

$$C_2 = \pi e(1 - 2v)[\pi e(1 - R_\mu)(1 + v) - 2R_\mu(1 - 2v) - 2] \tag{3.116}$$

$$C_3 = (R_\mu - 1)\pi e\left\{(1 - 2v)[2 - \pi e(1 - R_\mu)(1 + v)] - R_\mu(3 - 4v)(1 + v)\right\} - 8R_\mu(1 - v)^2 \tag{3.117}$$

Figure 3.21 shows the variation of normalized poroelastic horizontal and vertical stress arching ratios with respect to aspect ratio and shear modulus ratio for a reservoir shaped like an elliptical cylinder, and possessing the same Poisson's ratio (0.2 in this case) as the surrounding rock. Figure 3.22 shows the same parameters for a reservoir with a prolate spheroid geometry. These figures show that the vertical stress arching ratio increases monotonically with increasing aspect ratio, whereas the horizontal stress arching ratio decreases monotonically with increasing aspect ratio only if shear modulus ratio is close to or greater than 1. In addition, it shows that both vertical and horizontal stress arching ratios decrease with increasing shear modulus ratio. An interesting fact in Figure 3.21 is the variation of the out-of-plane stress arching ratio ($\gamma_{\alpha(H_2)}$) with respect to aspect ratio. From this figure, for a very small aspect ratio, $\gamma_{\alpha(H_2)}$ tends to be close to the value from equation (3.105) for an infinite layer, while with increasing aspect ratio it reaches a constant value which can be find from the formulation for a circular cylinder in equation (3.103).

Similar to the theory of inclusions, equation (3.37) can be applied to transform poroelastic stress arching ratios to their analogous thermoelastic arching ratios.
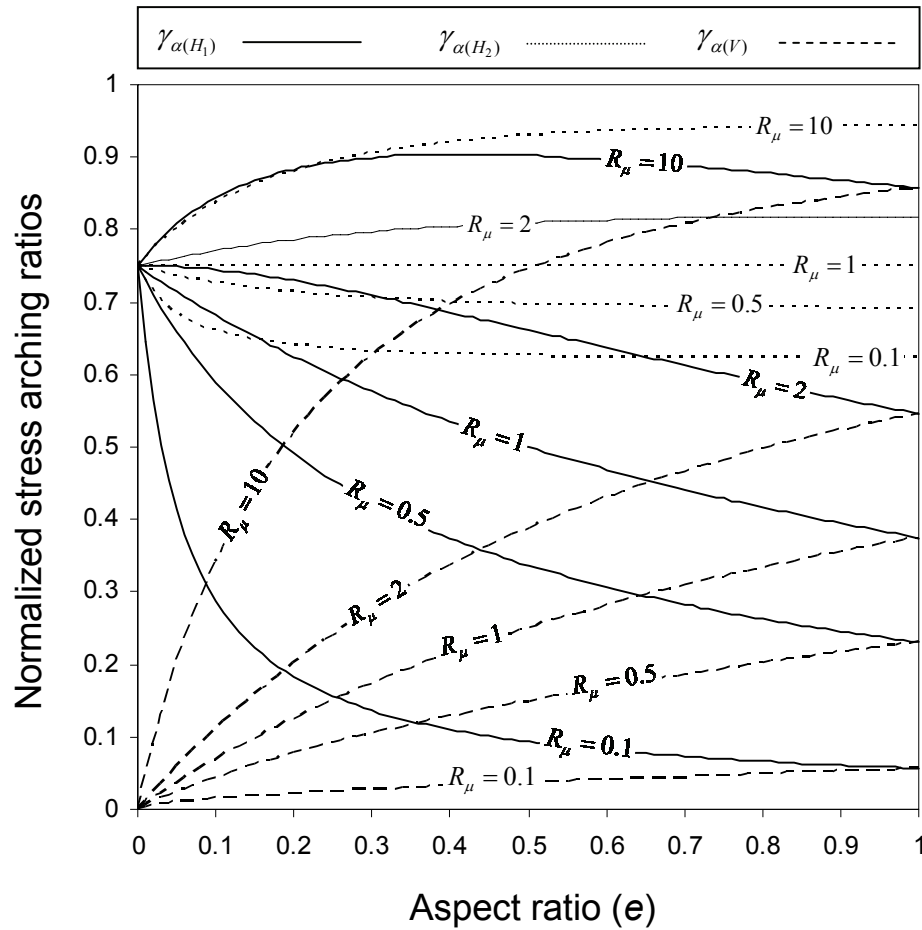
Figure 3.21. Normalized poroelastic in-plane horizontal ($\gamma_{\alpha(H1)}$), out-of-plane horizontal ($\gamma_{\alpha(H2)}$) and vertical ($\gamma_{\alpha(V)}$) stress arching ratios versus aspect ratio (e) for an elliptic cylinder (i.e., plane strain conditions). Poisson's ratios of the reservoir and the matrix are both 0.2 for this case.
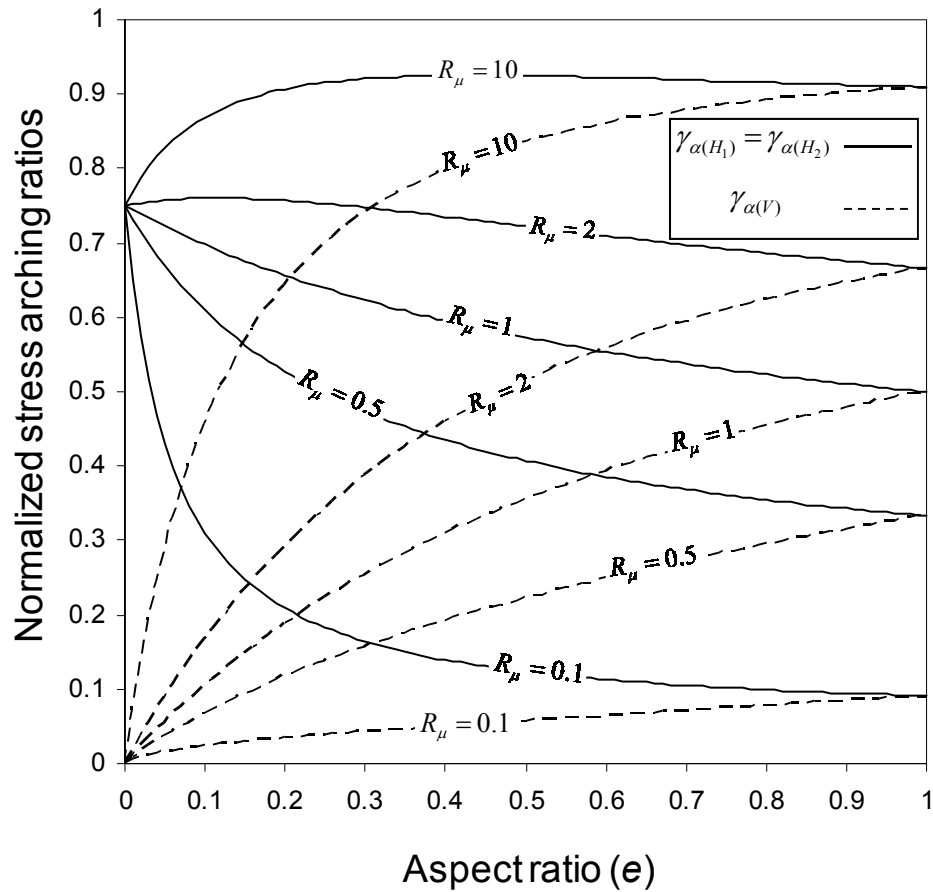
Figure 3.22. Normalized poroelastic horizontal ($\gamma_{\alpha(H1)}=\gamma_{\alpha(H2)}$) and vertical ($\gamma_{\alpha(V)}$) stress arching ratios versus aspect ratio (e) for an oblate spheroid (i.e., axisymmetric solution) for a Poisson's ratio ($v=v^*$) of 0.2 when the material properties of the reservoir is different from the surrounding rock.

3.7. Summary and Conclusion

A review of semi-analytical models for predicting induced stress changes in a poroelastic medium, including the theory of strain nuclei, the theory of inclusions, and theory of inhomgeneites has been presented. A definition of normalized poroelastic stress arching ratios has been introduced, and a simple relationship between thermoelastic and poroelastic stress changes has been presented, which enables the calculation of thermally induced stress changes using the formulations presented in this chapter for normalized poroelastic stress arching ratios.

Applying the theory of inclusions, semi-analytical solutions have been developed for induced stress changes in various classes of ellipsoidal reservoir geometries in a homogeneous, poroelastic full-space. New equations have been derived in this research for reservoirs with rectangular and elliptical cross-sections in a half-space under plane strain conditions. The equations given include solutions for reservoirs that are both horizontal and inclined (dipping) in the plane of the cross-section. Normalized stress arching ratios calculated using these equations have been charted for different reservoir geometries and depths using dimensionless parameters.

Using Eshelby's theory of inhomogeneities, the problem of a poroelastic inhomogeneity of elliptical cross-section under plane strain conditions in an infinite matrix has been solved explicitly. Closed-form expressions for the induced stress field within a reservoir have been derived. The values of stress arching ratios in the rock surrounding a reservoir have been found by numerical integration. Furthermore, Eshelby's theory of inhomogeneities has been used to develop closed-form solutions for various classes of ellipsoidal reservoir geometries in a homogeneous, poroelastic full-space.

It has been shown that induced stress changes within a reservoir are sensitive to its aspect ratio (height/width), but not its absolute size. Sensitivity analyses indicate that induced vertical stresses increase as the reservoir becomes more equi-dimensional in cross-section. Induced horizontal stresses decrease as the reservoir becomes more equi-dimensional in cross-section, except for cases where the shear modulus of the reservoir is less than the surrounding rock. Vertical and horizontal induced stresses both decrease as the reservoir:matrix shear modulus ratio increases. Vertical and horizontal induced stresses increase as the Poisson's ratio of the reservoir decreases. The Poisson's ratio of the matrix has limited effect on induced stresses. As such, it will usually be acceptable to make use of the simplifying assumption that the matrix and the inhomogeneity have identical Poisson's ratios.

It has been shown that the full-space plane strain solution is reasonably accurate in settings where reservoir depth and lateral extent are similar in magnitude, especially for reservoirs that are relatively thin (i.e., with an aspect ratio less than 0.2). Further, regardless

of reservoir thickness, the full-space plane strain solution is virtually exact when reservoir depth is at least five times greater than lateral extent.

Compressive and tensile stress changes can occur in either the vertical or horizontal directions above, below and to the sides of the reservoir depending on the sign of the pore pressure change. With decreasing rigidity of the reservoir, the magnitude of induced stress changes in the matrix increases.

The solutions presented in this chapter will be useful for analyses of fault reactivation and induced shear fracturing in caprocks, borehole instability and sand production risks, well casing failures and hydraulic fracturing operations in reservoirs affected by fluid extraction or injection. Also, these solutions could easily be modified to predict both poroelastic and thermally-induced stresses around reservoirs or cavities, which would prove useful for applications such as nuclear waste disposal, subsurface fluid disposal, greenhouse gas sequestration and enhanced recovery of oil by thermal methods. The following chapters will focus on fault reactivation and induced fracturing due to pore pressure change.

Chapter 4

Fault reactivation due to reservoir pressure change

4.1. Introduction

To safely and effectively design, operate and monitor injection or production projects in porous reservoirs, it is essential to assess the likelihood of fault reactivation which may lead to leakage from the reservoir, earthquakes or ground movements. This chapter investigates the assessment of fault reactivation tendency within and surrounding reservoirs during fluid injection or production. Induced stress analysis is performed using Eshelby's theories of inclusions and inhomogeneities for a poroelastic material (as explained in Chapter 3), and the concept of Coulomb Failure Stress Change is implemented as a criterion for fault reactivation tendency. The intention of this chapter is to provide relatively straight-forward solutions to be applied either for studying the general patterns of fault reactivation, or site-specific fault reactivation studies in the cases where reservoir geometry is reasonably approximated by the idealized geometries underlying these solutions. Different methodologies are developed to study fault reactivation, including identifying the likely regions for reactivation for a specific fault in a field, the range of fault dip angles that tend towards reactivation, and the critical pressure change for fault reactivation. The critical pressure change for fault reactivation is calculated for the entire field while induced stress change was calculated using a plane strain solution. In addition, critical pressure change for fault reactivation within a reservoir is calculated when a 3D induced stress change solution is available. Sensitivity analyses are performed which investigate the effect of different parameters such as the geometry and material properties and fault characteristics on fault

reactivation. A detailed study is conducted to study fault reactivation within reservoirs. Results are given in the forms of tables and graphs for different in-situ stress regimes. The solutions have been cast in dimensionless form, and are useful thus for a broad range of conditions.

In this chapter, fault reactivation is studied only in a shear failure mode, with the conservative assumption of zero cohesion (i.e., the possibility that the mineralization of fault gouge may result in fault rock with non-zero cohesion has been neglected). Figure 4.1 shows a comparison of a zero-cohesion failure criterion for a fault and a failure criterion for intact rock (i.e., a criterion possessing components of cohesive and frictional strength). The failure criterion for intact rock represents the upper limit on permissible stress states in a given rock. If the rock contains a fault that is optimally oriented for failure, the lower bound on permissible stress states is governed by the fault's failure criterion. For a non-optimally oriented fault with dip angle θ, the stress state at failure (i.e, shown in Figure 4.1 as the intersection of the fault's failure criterion and the radius of Mohr circle which is oriented as angle of 2θ from the σ' axis) will be intermediated between aforementioned limits.

As a final point on this topic, it is worth noting that Biot's coefficient may have different values in intact rock and fault rock, though this scenario has not been pursued in this research.
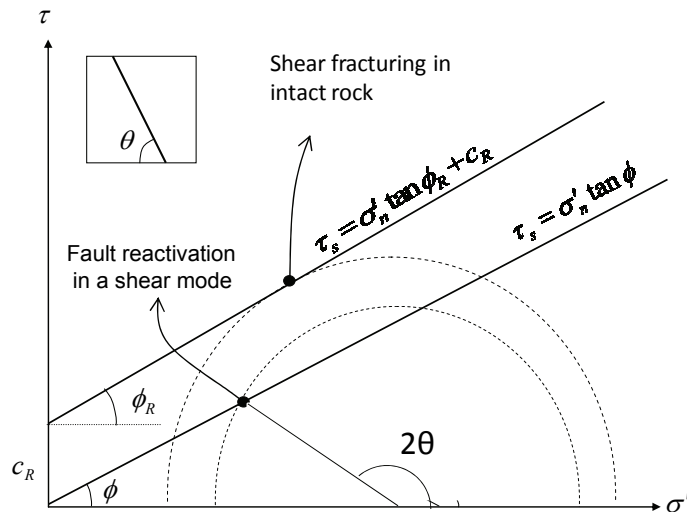
Figure 4.1. Different modes of shear failure fault reactivation and induced fracturing of intact rock. ϕ_R and c_R, respectively, are friction angle and cohesion of intact rock and ϕ is the friction angle of the fault surface.

4.2. Coulomb Failure Stress concept

In order to facilitate assessment of fault reactivation for a general range of scenarios (e.g., for faults of varying dip that are located both within and outside of the reservoir), the Coulomb Failure Stress Change method has been developed. The Coulomb Failure Stress *(CFS)* is defined as follows (e.g., King et al., 1994):

$$CFS = \tau - \mu_s \sigma'_n \qquad (4.1)$$

where τ and σ_n, respectively, are shear and effective normal stress on the fault plane and μ_s is the coefficient of friction in the fault plane (i.e., $= \tan \phi$). A fault plane is believed to be activated when *CFS* is equal to or greater than zero (Figure 4.2).

In a production or injection scenario, wherein stress changes have been induced, the change in Coulomb Failure Stress can be evaluated as (Figure 4.2):

$$\Delta CFS = \Delta \tau - \mu_s \Delta \sigma'_n \qquad (4.2)$$

where $\Delta \tau$ and $\Delta \sigma'_n$, respectively, are induced changes of shear and effective normal stress on the fault plane. The sign of $\Delta \tau$ is positive when it points in the same direction as the initial shear stress on the plane. The sign of $\Delta \sigma'_n$ is positive for an increase in compressive stress. As such, a positive ΔCFS indicates a tendency towards fault reactivation. ΔCFS values as small as 0.1 MPa have been found to induce seismic activity in faulted settings where initial *CFS* values are close to zero (e.g., King et al., 1994).
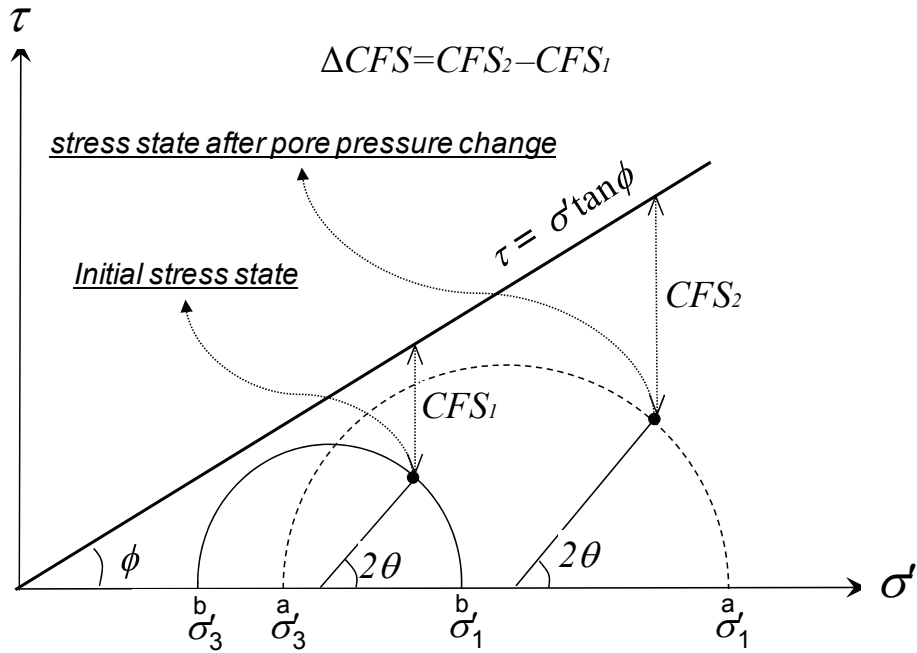
Figure 4.2. Definition of the concept of Coulomb Failure Stress change

In order to achieve a more general, dimensionless characterization of fault reactivation risk, a new parameter called "fault reactivation factor" (λ) is defined here as follows:

$$\lambda = \frac{\Delta CFS}{\alpha \Delta P} \tag{4.3}$$

To derive specific forms of λ for normal and thrust fault stress regimes, we start by considering an element of rock which is in a state of static equilibrium, subject to induced horizontal and vertical effective stress changes $\Delta\sigma'_H$ and $\Delta\sigma'_V$ under plane strain conditions. To make this derivation completely general, the presence of an induced shear stress change $\Delta\tau_{HV}$ is also considered. Using stress equilibrium equations to calculate the shear stress change ($\Delta\tau$) and effective normal stress change ($\Delta\sigma'_n$) on a fault plane dipping at an angle θ from horizontal (see Figure 4.3), and substituting into equations (4.2), (4.3), the following general expressions are found for a normal and thrust fault stress regime for plane strain stress conditions:
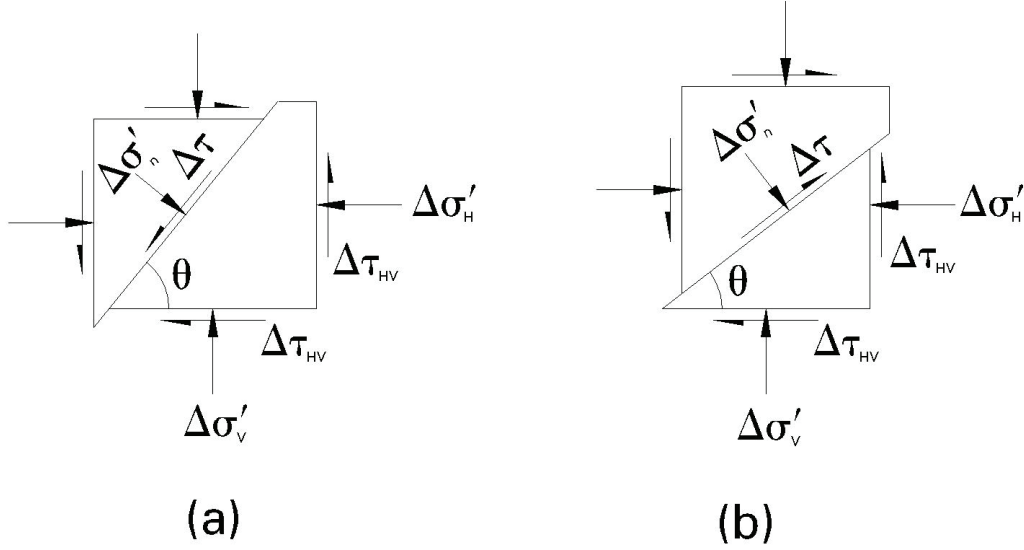
Figure 4.3. Induced stress changes in a reservoir resolved on a fault plane (a) in a normal fault stress regime, and (b) in a thrust fault stress regime. Shear stress arrows on the fault planes denote the direction of positive shear stress change for each fault type.

$$\lambda = (\delta_L - \gamma_{\alpha(H)})\sin\theta(\delta_F \cos\theta + \mu_s \sin\theta)$$
$$- (\delta_L - \gamma_{\alpha(V)})\cos\theta(\delta_F \sin\theta - \mu_s \cos\theta) \tag{4.4}$$
$$+ \delta_D \gamma_{\alpha(HV)}((\sin^2\theta - \cos^2\theta)\delta_F - 2\mu_s \sin\theta\cos\theta)$$

where:

θ = fault dip angle

$\gamma_{\alpha(H)}$ = normalized horizontal stress arching ratio

$\gamma_{\alpha(V)}$ = normalized vertical stress arching ratio

$\gamma_{\alpha(HV)}$ = normalized shear stress arching ratio

δ_F = stress regime index;

= 1 for a normal fault stress regime

= -1 for a thrust fault stress regime

δ_D = fault dip direction index;

= 1 for faults dipping towards to the bottom left corner of the cross-sectional analysis plane

= -1 for faults dipping towards to the bottom right corner

δ_L = location index

= 1 within the reservoir

= 0 within the surrounding rock.

4.3. Patterns of fault reactivation tendency in the entire field

The change in fault reactivation potential for a reservoir during depletion or injection can be assessed by evaluating the fault reactivation parameter (λ) using equation (4.4). This procedure is demonstrated here for two cases: (1) a horizontal rectangular reservoir, and (2) a "tilted" (i.e., dipping) rectangular reservoir. For both cases, the following reservoir geometry was used: centre-depth (D) = 4 km; reservoir width ($2a$) = 4 km; and thickness (T) = 200 m. As such, the depth number (n) is 0.50, and the aspect ratio (e) is 0.05. Further, Poisson's ratio and Biot's coefficient of the rock were set at 0.2 and 1.0, respectively. The theory of inclusions, as described in the previous chapter, was used for induced stress change analysis and determination of stress arching ratios.

4.3.1. Fault reactivation tendency for a horizontal reservoir

Figures 4.4 and 4.5 show contour plots of λ for the horizontal reservoir case, for two different stress regimes. For the output shown in Figure 4.4, a normal fault stress regime was considered, with faults dipping by 60° from horizontal and having a friction coefficient (μ_s) of 0.6 (i.e., a friction angle of roughly $30°$). It can be seen in Figure 4.4(a) that, during depletion, there is a tendency towards normal fault reactivation in the rock near the lateral flanks of the reservoir. [Note: Recall that ΔP is negative for depletion. So, according to equation (4.3), a negative value for λ during depletion corresponds to a positive ΔCFS.] Figure 4.4(b) shows that there is a tendency towards fault reactivation with depletion within the central portion of a horizontal, rectangular reservoir. For the output shown in Figure 4.5, a thrust fault stress regime was considered, with faults dipping by 30° from horizontal and
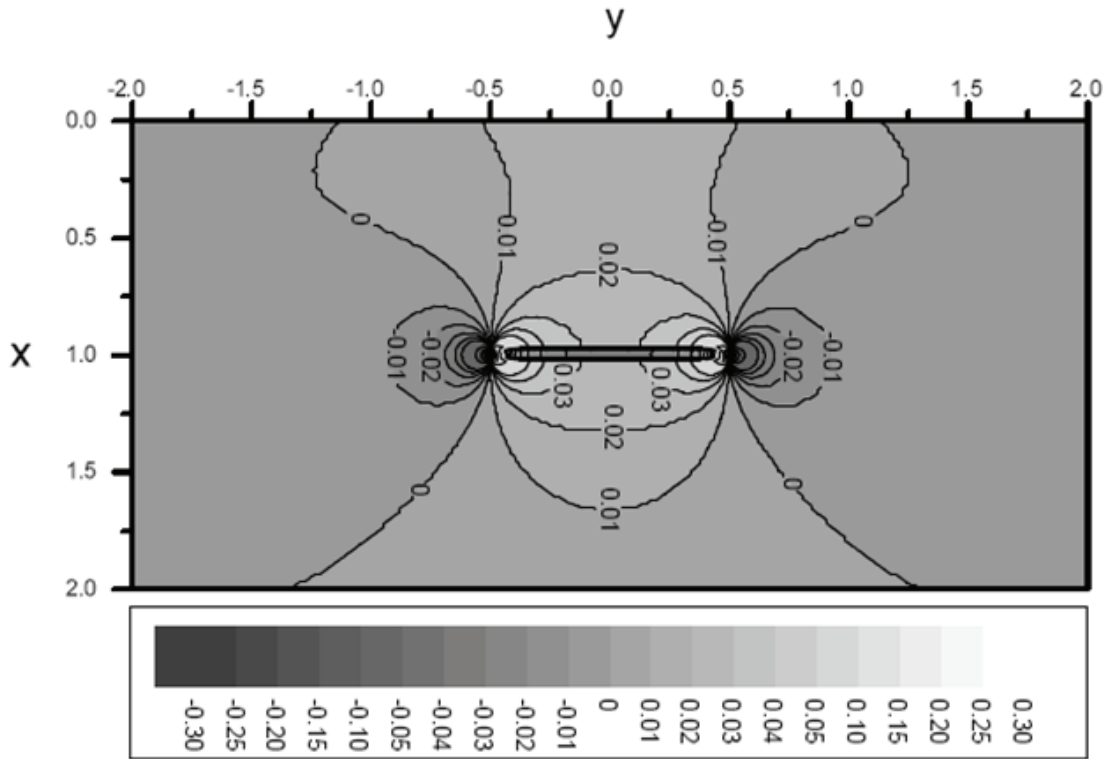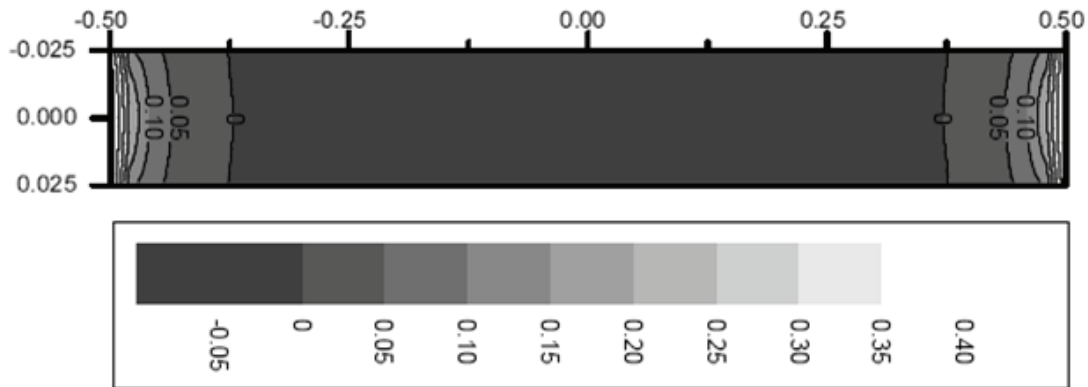
Figure 4.4. Distribution of fault reactivation factor in a normal fault regime (λ_{Normal}) for a horizontal rectangular reservoir with a fault dip angle of 60° (a) for the entire field, and (b) within the reservoir. ($n = 0.5$; $e = 0.05$; $\nu = 0.2$)
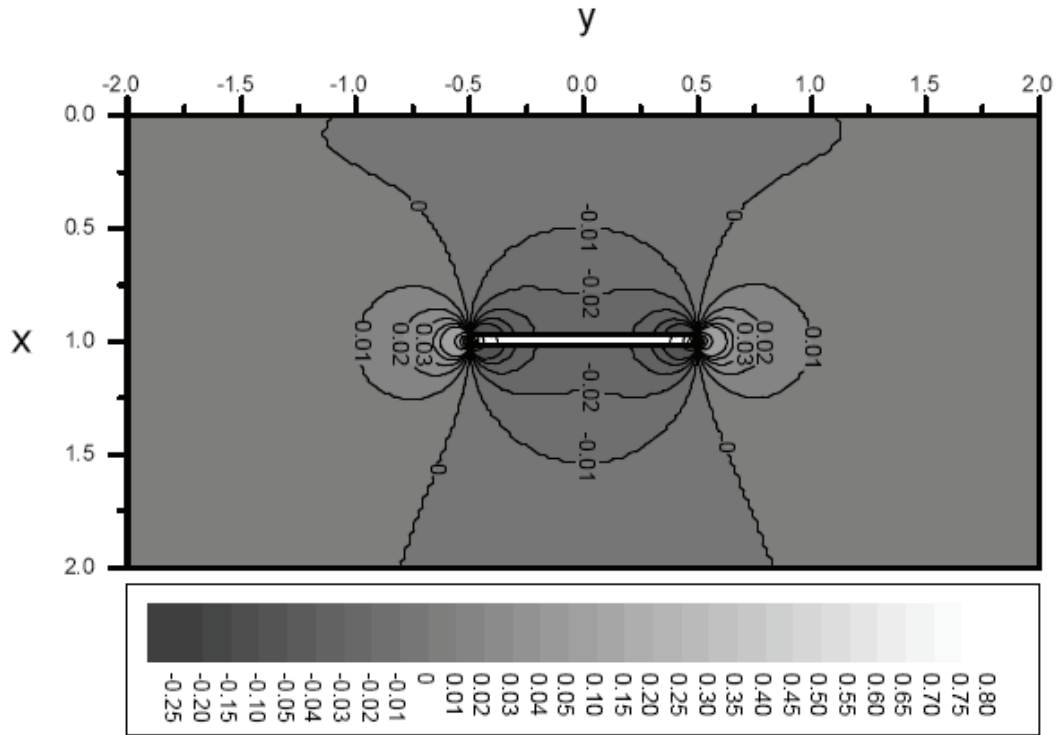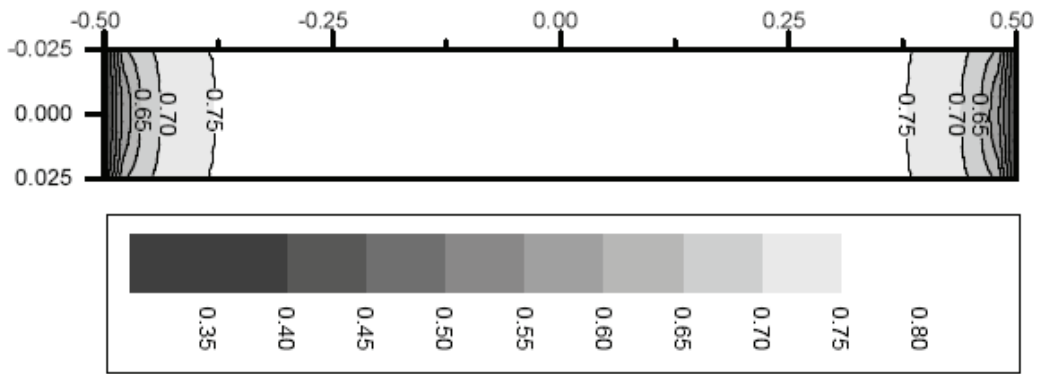
Figure 4.5. Distribution of fault reactivation factor in a thrust fault regime (λ_{Thrust}) for a horizontal rectangular reservoir with a fault dip angle of 30° (a) for the entire field, and (b) within the reservoir. ($n = 0.5$; $e = 0.05$; $v = 0.2$)

having a friction coefficient of 0.6. It can be seen in Figure 4.5(a) that, during depletion, there is a tendency towards thrust fault reactivation in the rocks above and below the reservoir. Figure 4.5(b) shows that there is no tendency towards fault reactivation with depletion anywhere within the reservoir. [Note: If the same reservoir was considered for an injection scenario (i.e., positive ΔP), Figure 4.5(b) would indicate a tendency towards fault reactivation everywhere within the reservoir.]

4.3.2. Fault reactivation tendency for a tilted reservoir

Results for a reservoir with a 30° dip angle are shown in Figures 4.6 and 4.7 for normal and thrust fault stress regimes, respectively, with the same fault orientations and friction coefficient as the previous examples. Clearly, the dip of the reservoir has a significant impact on the location of faults that are most prone to reactivation. For the normal fault stress regime, the increase in fault reactivation potential with depletion is most acute above the left end and below the right end of the reservoir. No depletion-induced increase in fault reactivation potential is predicted within the reservoir. For the thrust fault stress regime, the depletion-induced increase in fault reactivation potential is most acute above the right end and below the left end of the reservoir. No depletion-induced increase in fault reactivation potential is predicted within the reservoir.

These results demonstrate the importance of accounting for the actual reservoir geometry when assessing fault reactivation location and potential. Previous induced seismicity analyses have often been conducted using idealized geometries such as laterally infinite or axisymmetric reservoirs (e.g., Segal et al., 1994; Zoback and Zinke, 2002), even though the reservoirs are often anticlinal structures or tilted fault blocks. In the assessment of caprock integrity in depleted reservoirs, or the selection of safe upper limits on injection pressure during enhanced recovery or sequestration operations, it is important to account for the real geometry of the reservoir.
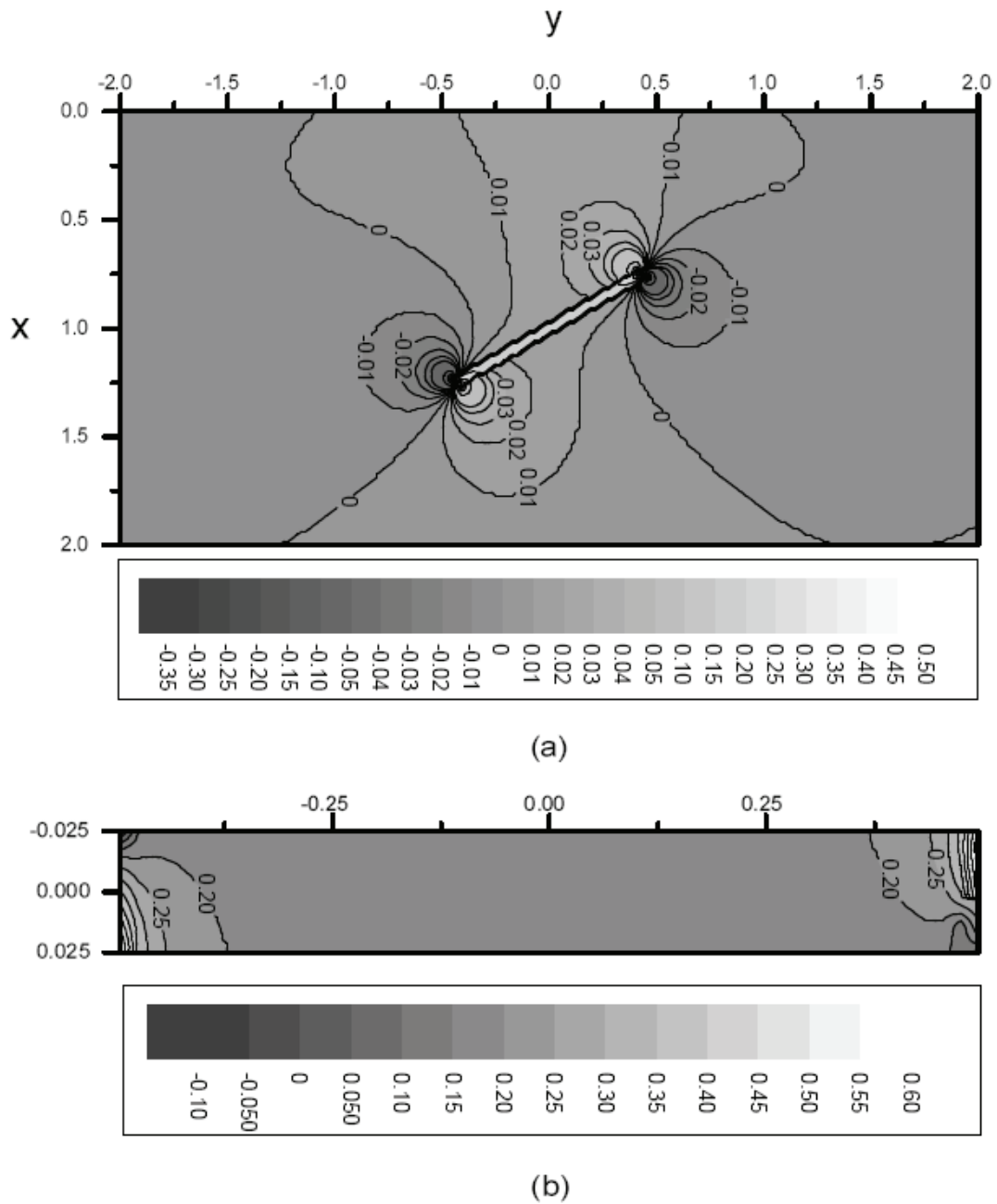
Figure 4.6. Distribution of fault reactivation factor in a normal fault regime for a rectangular reservoir dipping by 30°, calculated for a fault dip angle of 60° (a) for the entire field, and (b) within the reservoir. ($n = 0.5$; $e = 0.05$; $v = 0.2$)
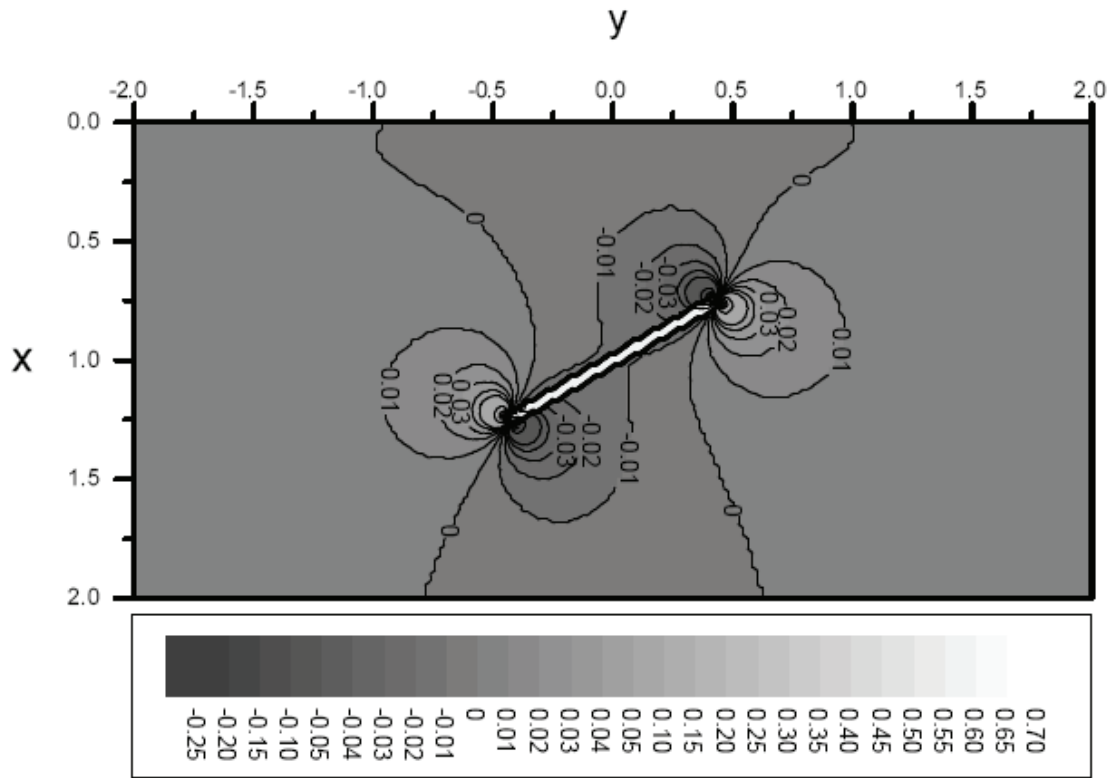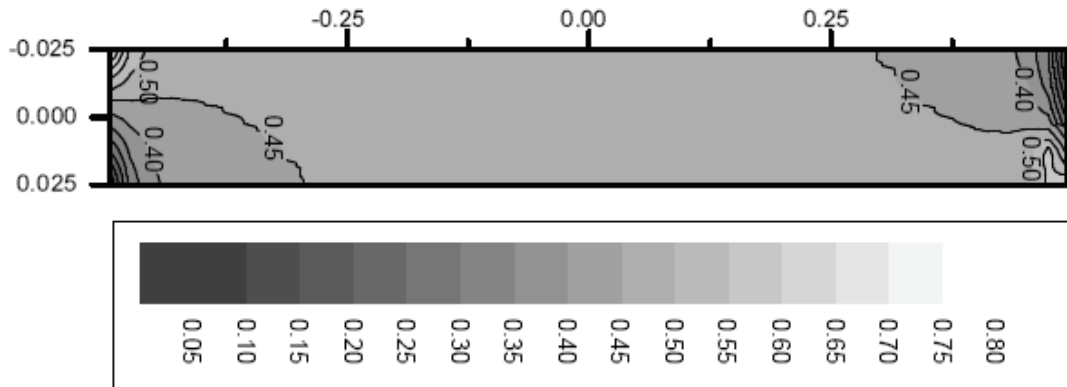
Figure 4.7. Distribution of fault reactivation factor in a thrust fault regime for a rectangular reservoir dipping by 30°, calculated for a fault dip angle of 30° (a) for the entire field, and (b) within the reservoir. ($n = 0.5$; $e = 0.05$; $v = 0.2$)

4.4. Effect of friction coefficient on potential regions for fault reactivation

The precise value of a fault surface's friction coefficient (μ_s) is one of the uncertainties in fault reactivation analysis. One useful application of the methodology described above is to study the sensitivity of the potential regions for fault reactivation to the value of μ_s. Byerlee (1978) suggests that values of the friction coefficient vary between 0.65 to 0.8 for natural sliding surfaces in a broad range of rocks; however, there are known to be some faults with lower frictional strengths (e.g., Morrow et al., 1992). For the sake of generality, a broad range of friction coefficients, between 0.4 to 0.8 (as used by Hawkes et al., 2005) is considered for the sensitivity analyses presented in this paper. Figures 4.8(a) and 4.8(b) show the positions of the boundary lines which separate the likely regions for reactivation and stabilization (i.e., the $\lambda = 0$ contour lines) for μ_s values of 0.4, 0.6 and 0.8. Figures 4.8(a) and 4.8(b) were generated for the same reservoir geometry, fault dip angles and dip directions, and material properties as Figures 4.4 and 4.5, respectively.

The shaded areas in Figures 4.8(a) and 4.8(b) denote the region within which this boundary position varies as the friction coefficient varies from 0.4 to 0.8. Compared to the dimensions of the reservoir and the cross-sectional plane of interest, the friction coefficient has a relatively modest effect on the boundaries of regions tending towards reactivation. Therefore, assuming an average μ_s value of 0.6 may be suitable for the purpose of identifying likely regions for fault reactivation with reasonable accuracy for most faults. It is important to note, however, that the friction coefficient is a very sensitive parameter when predicting the magnitude of critical pressure (hence stress) change required to reactivate a fault.

4.5. Identifying critical fault dip angles within and surrounding a reservoir

The methodology presented above for identifying the regions tending towards fault reactivation for a prescribed dip angle may be extended to a more general methodology that accounts for all dip angles using the criterion $\lambda = 0$ (i.e., $\Delta CFS = 0$) to identify the boundary between regions of fault reactivation and stabilization. It is thus possible to predict the range of fault dip angles at any point in the cross-sectional plane of analysis that tend towards
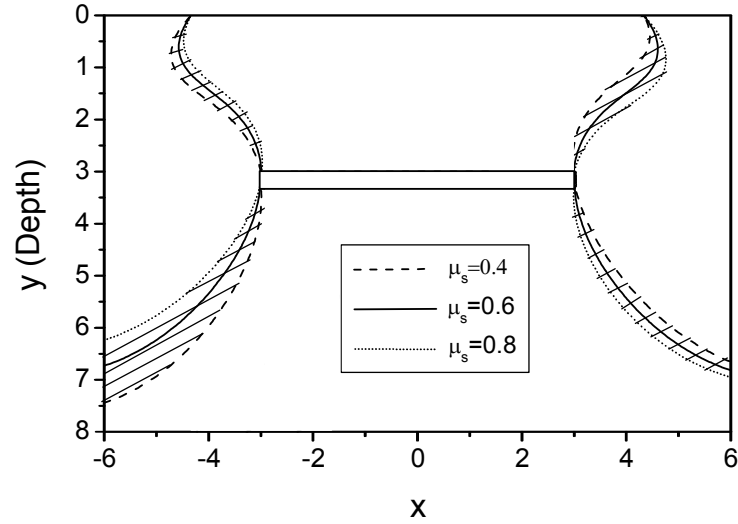
(a)
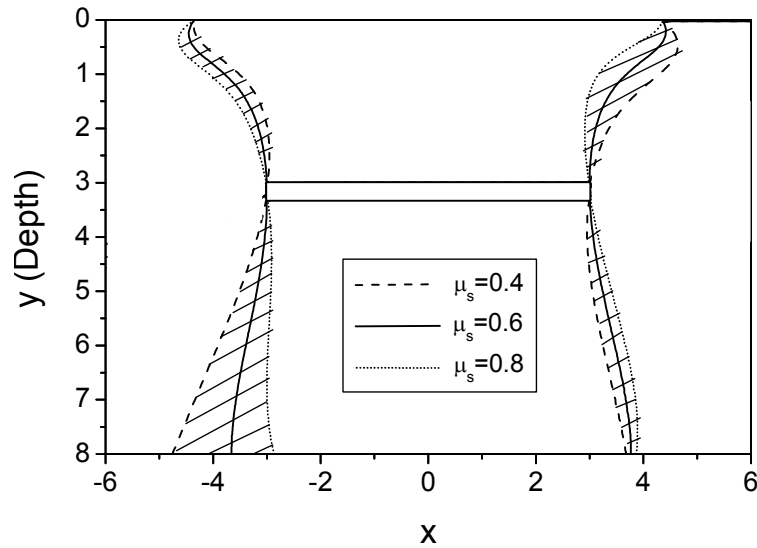
(b)

Figure 4.8. Variation in the position of fault reactivation boundary line ($\lambda = 0$) due to the change in friction coefficient (μ_s) for the rectangular reservoir analyzed in Figure 4.4 and 4.5 for (a) faults dipping at 60° in a normal fault stress regime, and (b) faults dipping at 30° in a thrust stress regime. For both figures, faults are dipping towards to the bottom left corner of the cross section.

reactivation. Solving equation (4.4) for $\lambda = 0$ results in the following equation for critical fault dip angle (θ):

$$M \tan^2 \theta + N \tan \theta + Q = 0 \tag{4.5}$$

where:

$$M = \mu_s R_\sigma + \delta_D \delta_F R_\tau$$
$$N = \delta_F (R_\sigma - 1) - 2\mu_s \delta_D R_\tau \qquad\qquad (4.6)$$
$$Q = \mu_s - \delta_F \delta_D R_\tau$$

In this equation, R_σ is the stress path ratio which has been defined previously (Khan et al., 2000; Schutjens et al., 2001) as the ratio of the horizontal effective stress change to the vertical effective stress change (see equations (2.5) and (3.9)):

$$R_\sigma = \frac{\Delta\sigma'_H}{\Delta\sigma'_V} = \frac{\delta_L - \gamma_{\alpha(H)}}{\delta_L - \gamma_{\alpha(V)}} \qquad\qquad (4.7)$$

and R_τ is the shear stress path ratio, which is defined here as the ratio of shear stress change to the vertical effective stress change:

$$R_\tau = \frac{\Delta\tau_{HV}}{\Delta\sigma'_V} = \frac{\gamma_{\alpha(HV)}}{\delta_L - \gamma_{\alpha(V)}} \qquad\qquad (4.8)$$

The roots of equation (4.5) can be used to verify the sign of λ (or ΔCFS) as shown by a flowchart given in Figure 4.9. This flowchart provides the range of fault dip angles (i.e., $\theta_{min} < \theta < \theta_{max}$) where fault reactivation factor (λ) is negative. λ is positive for fault dip angles outside of this range. Therefore, any fault with a dip angle within this range has a tendency towards reactivation during production and towards stabilization during injection. In contrast, any fault with a dip angle outside of this range has a tendency towards stabilization during production and towards reactivation during injection. There is one special case (which is denoted by the bottom right box in Figure 4.9) for which the fault reactivation factor is negative over two ranges of dip angle. For this case, these two ranges are denoted θ_{min} - θ_{max} and θ'_{min} - θ'_{max}. The occurrence of this special case is rare for analyses of the type presented in this chapter, in which induced stress changes have been predicted using the theory of inclusions.

Finding roots by solving the following equation:
$M \tan^2\theta + N \tan\theta + Q = 0$
If there is no root, both roots are considered to be zero, if any root is less than zero it must be considered zero. As a result we have two roots: θ_1 and θ_2 where $\theta_1 < \theta_2$. If $M=0$, there is just one root: θ_0
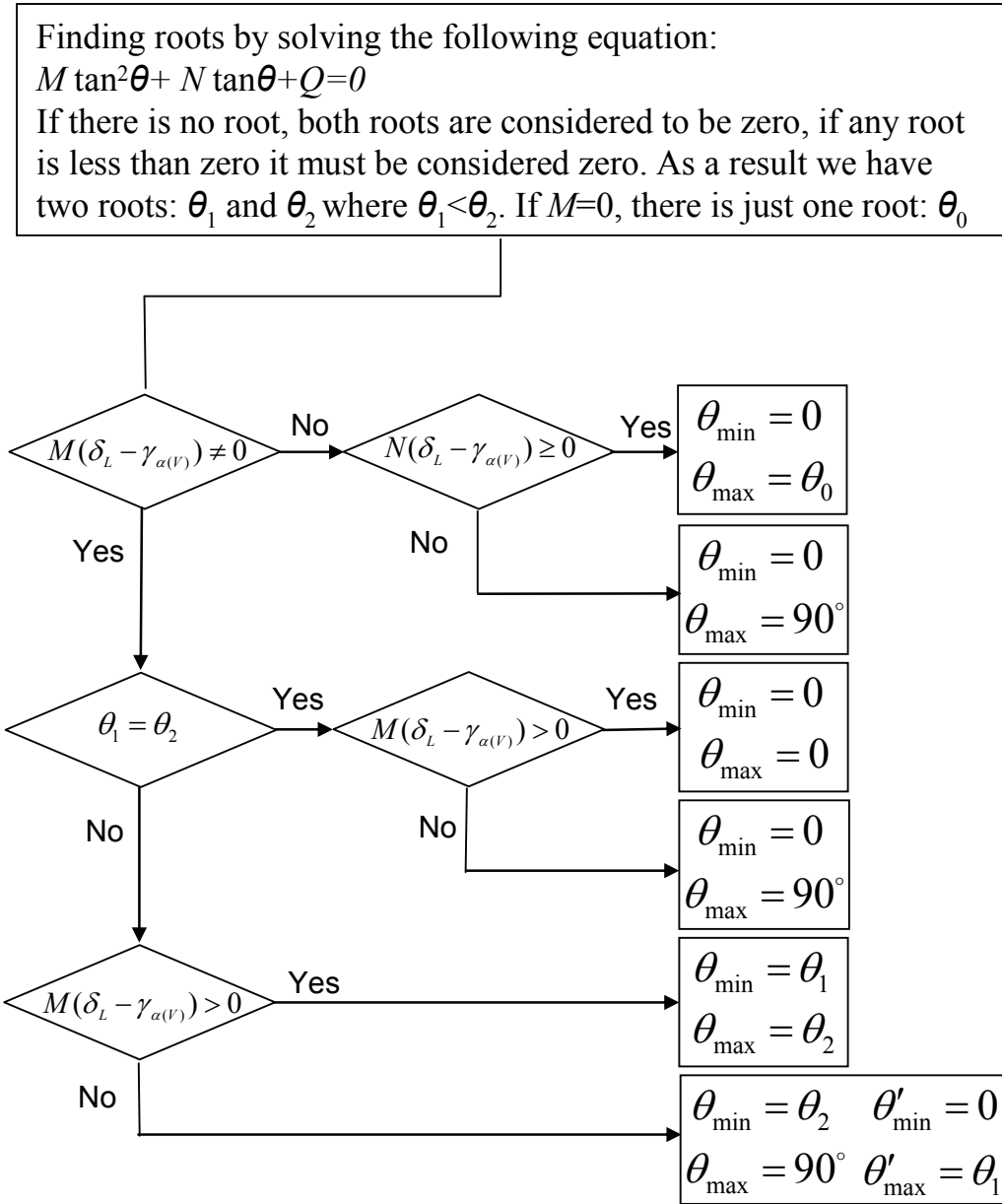
Figure 4.9. Procedure for the sign determination of the fault reactivation factor (λ).

Figures 4.10 and 4.11 demonstrate applications of this method for the rectangular reservoir analysed in Figures 4.4 and 4.5. These figures show the values of θ_{min} and θ_{max} as contour maps, respectively, for normal and thrust fault stress regimes. For both examples, faults are considered to be dipping towards to the bottom left corner of the cross section (i.e., $\delta_D = 1$).
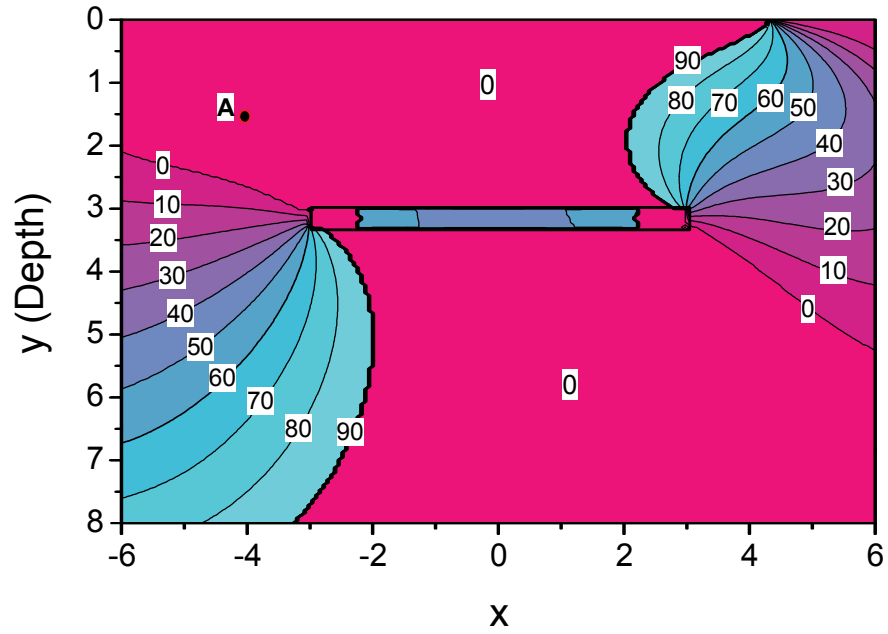
(a)
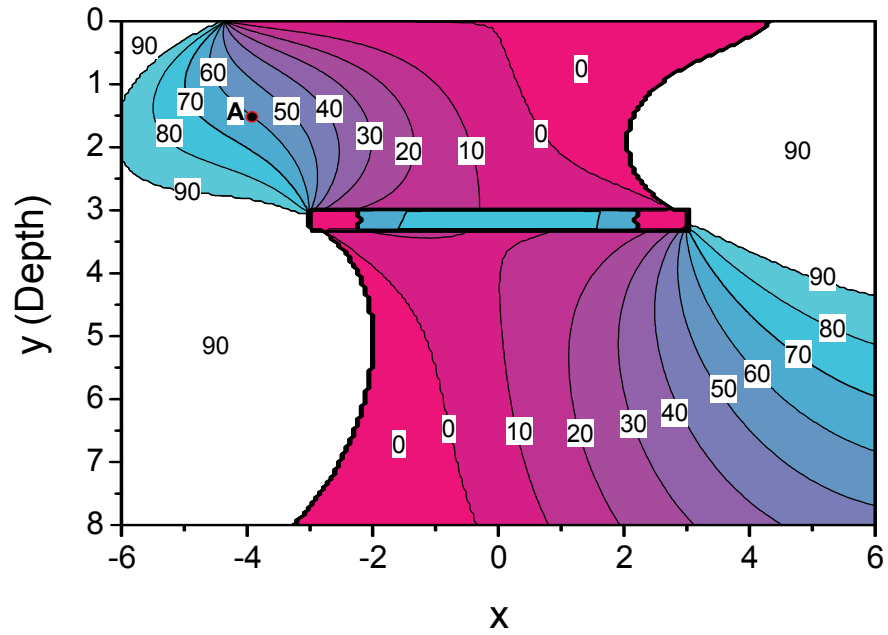
(b)

Figure 4.10. Contour maps for (a) θ_{min} and (b) θ_{max} for the rectangular reservoir analyzed in Figures 4.4 to 4.7, in a normal fault stress regime for faults which are dipping towards to the bottom left corner of the cross section
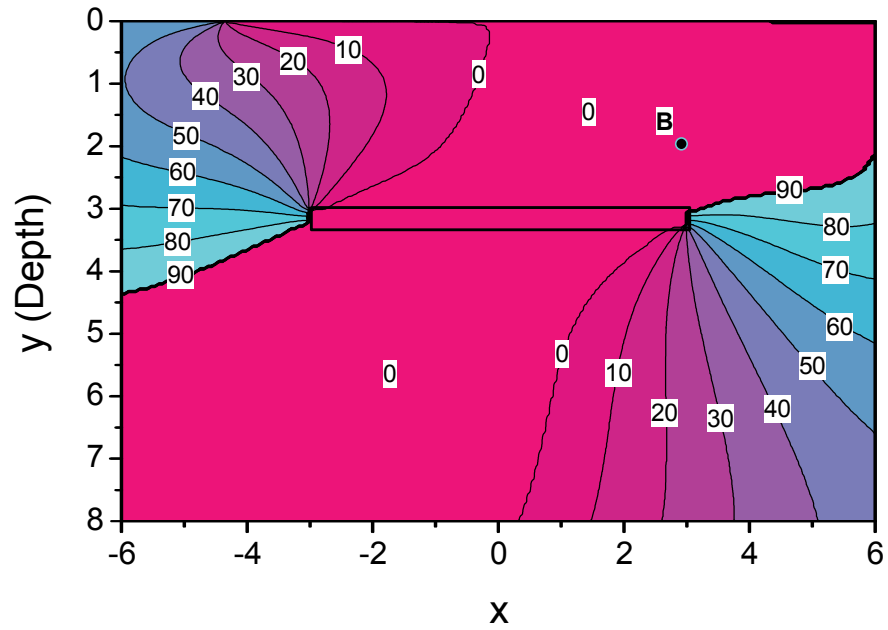
(a)
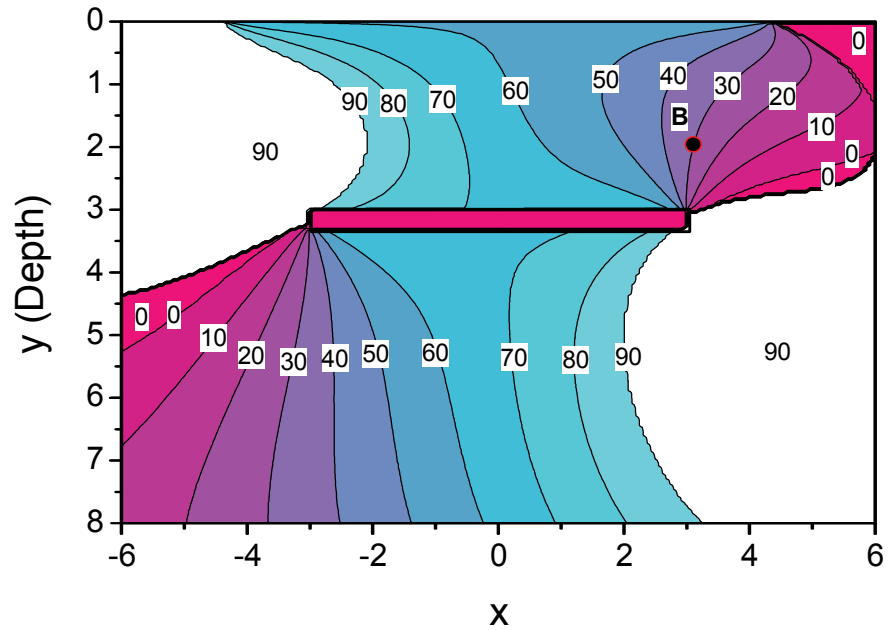
(b)

Figure 4.11. Contour maps for (a) θ_{min} and (b) θ_{max} for the rectangular reservoir analyzed in Figures 4.4 to 4.7, in a thrust fault stress regime, for faults which are dipping towards to the bottom left corner of the cross section.

Figures 4.10 and 4.11 can be used to identify the range of fault dip angles which tend towards reactivation at any location throughout the cross section. For instance, for a normal fault stress regime, at point A (Figures 4.10(a) and 4.10(b)), θ_{min} =0 and θ_{max}=60°. This means that faults passing through this point and having dip angles between 0 and 60° will tend towards reactivation during production, while faults with dip angles more than 60° tend towards stabilization. Similarly, at point B (Figures 4.11(a) and 4.12(b)), θ_{min} =0 and θ_{max}=30°. Therefore, in a thrust fault stress regime, faults with dip angles in the range of 0 to 30 ° tend towards reactivation during production, while faults with dip angles more than 30° tend towards stabilization. In both cases, the faults behave in the exact opposite sense during injection.

4.6. Fault reactivation within a reservoir

In this section, methodologies are developed to study fault reactivation tendency within reservoirs. Similar to the previously discussed solutions for the entire field, using a Coulomb failure criterion for fault surfaces and poroelastic models for induced stress changes, fault reactivation within reservoirs is investigated to: (1) identify the reactivation tendency of a fault of known dip angle; and (2) determine the range of fault dip angles which are likely to reactivate during production or injection.

To illustrate the use of effective stress changes on fault reactivation potential, consider the case of a reservoir in which the initial and induced stress changes in the vertical and horizontal directions are principal stresses. Figures 4.12(a) and 4.12(b) demonstrate the process of induced stress change leading to fault reactivation in a normal and in a thrust stress regime, respectively. The induced shear stress change within the reservoir has been considered as zero. This assumption is consistent with the induced stress models presented in the previous chapter.

For a setting with a normal fault stress regime (i.e., $\sigma_V > \sigma_H$), Figure 4.12(a) illustrates a plausible effective stress path within a reservoir that has been pressure depleted. Due to the large increase in vertical effective stress relative to the effective horizontal stress
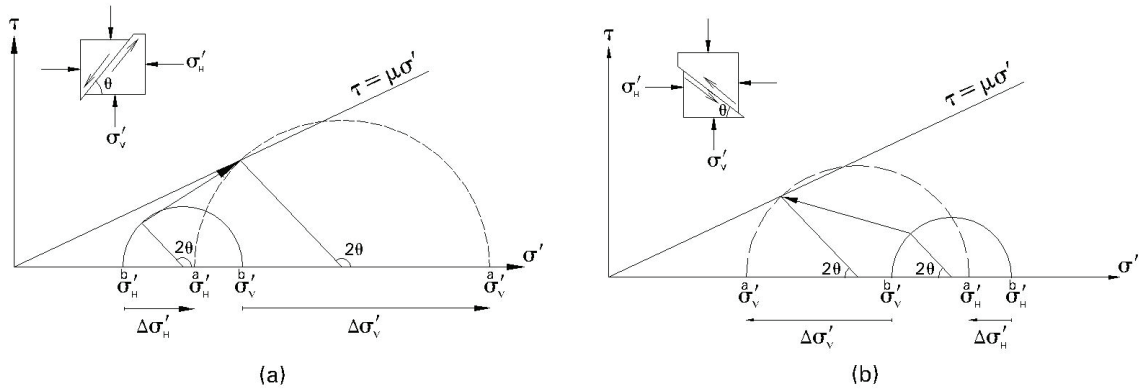
Figure 4.12. Mohr-circle representation of stress changes resulting in fault reactivation for (a) a normal fault within a reservoir during depletion, and (b) a thrust fault within a reservoir during injection. Index *a* denotes "after change in pore pressure" and index *b* denotes "before change in pore pressure". θ denotes fault dip angle.

change, the Mohr circle for the resultant effective stress state exceeds the fault's failure criterion. For the normal fault illustrated in this example, reactivation would occur.

For a setting with a thrust fault stress regime (i.e., $\sigma_V < \sigma_H$), Figure 4.12(b) illustrates a plausible effective stress path within a reservoir that is undergoing injection. Due to the large decrease in vertical effective stress relative to the effective horizontal stress change, the Mohr circle for the resultant effective stress state exceeds the fault's failure criterion, and fault reactivation would occur.

4.6.1. Likelihood of reactivation tendency for a fault of known dip angle

The mechanics of fault reactivation can be depicted graphically in a coordinate system with effective vertical stress (σ'_V) on the x-axis and effective horizontal stress (σ'_H) on the y-axis (Figure 4.13).

The slope of a Coulomb failure criterion in a σ'_H- σ'_V coordinate system for a fault with dip angle θ can be derived from the traditional representation of such a problem in a Mohr coordinate system (σ'-τ). The stress state when a fault in a normal fault stress regime is reactivated is shown in Figure 4.14. With reference to this figure, the values of shear and normal stresses in the fault plane at failure can be calculated as:
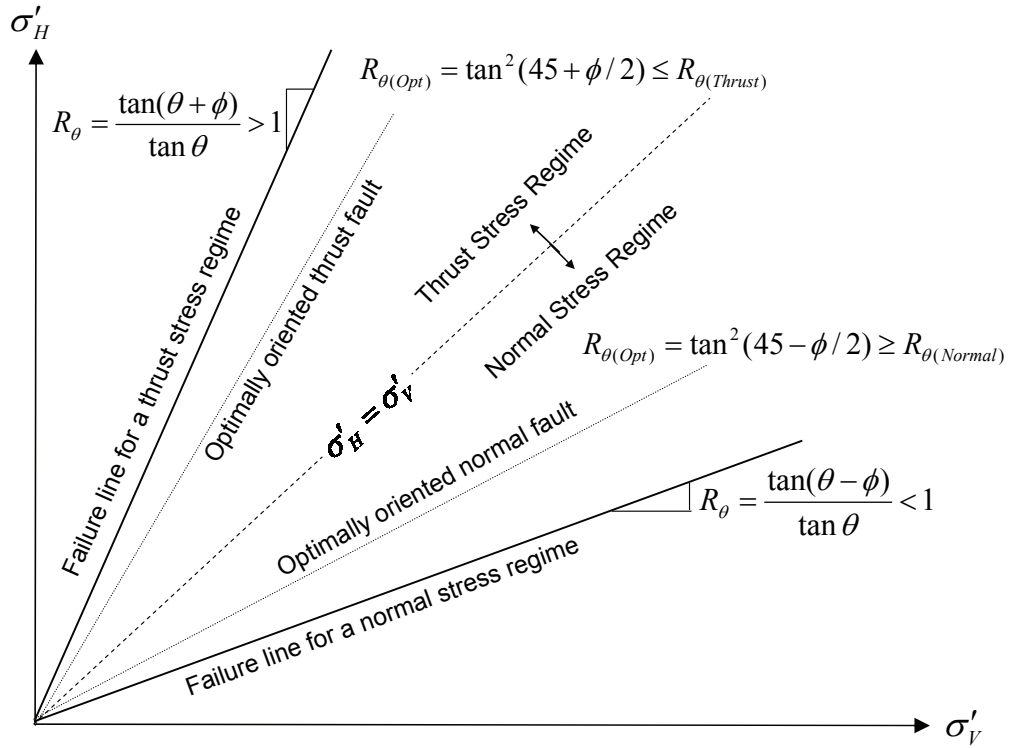
Figure 4.13. Coulomb shear failure envelopes for thrust and normal fault stress regimes in a $\sigma_H{'}$- $\sigma_V{'}$ coordinate system.
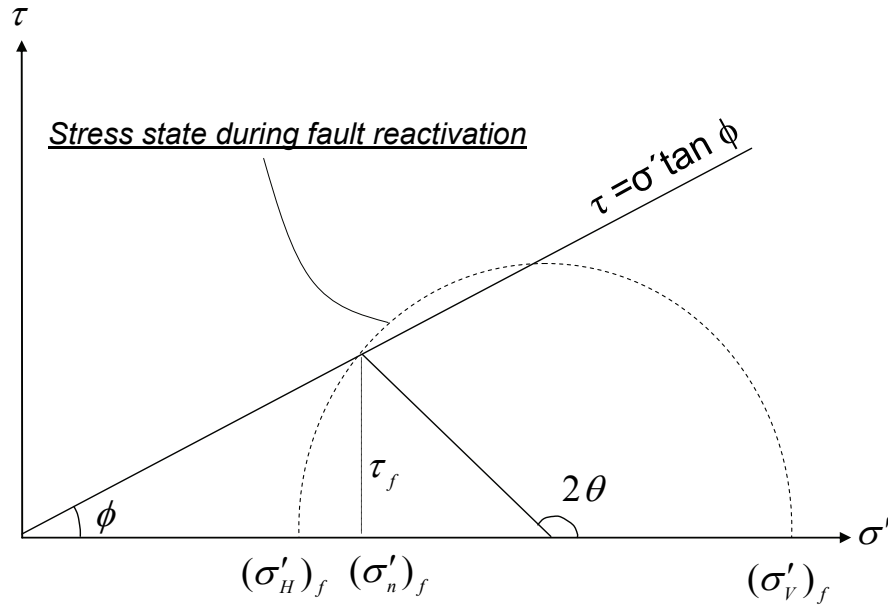
Figure 4.14. Mohr circle representation of stress state of a reactivated fault within a reservoir with a normal fault stress regime.

106

$$(\tau)_f = (1/2)[(\sigma'_V)_f - (\sigma'_H)_f]\sin 2\theta \tag{4.9}$$

$$(\sigma'_n)_f = (1/2)[(\sigma'_V)_f + (\sigma'_H)_f] + (1/2)[(\sigma'_V)_f - (\sigma'_H)_f]\cos 2\theta \tag{4.10}$$

Substituting these values in cohesionless Coulomb failure criterion (i.e., $\tau = \mu_s \sigma'$), after a series of mathematical manipulations it can be shown that:

$$(\sigma'_H)_f / (\sigma'_V)_f = (1/\tan\theta)(\tan\theta - \mu_s)/(1 + \mu_s \tan\theta) \tag{4.11}$$

A simpler form of this equation may be derived using the definition of internal friction angle (i.e., $\tan\phi = \mu_s$) and the trigonometric formula for the tangent of reduction of two angles (i.e., $\tan(\alpha - \beta) = (\tan\alpha - \tan\beta)/(1 + \tan\alpha \cdot \tan\beta)$), as follows:

$$(\sigma'_H)_f / (\sigma'_V)_f = \tan(\theta - \phi)/\tan\theta \tag{4.12}$$

A similar derivation may be used to obtain the analogous equation for a thrust fault stress regime:

$$(\sigma'_H)_f / (\sigma'_V)_f = \tan(\theta + \phi)/\tan\theta \tag{4.13}$$

Using stress regime index (δ_F), both of equations (4.12) and (4.13) may be written as a single equation, as follows:

$$R_\theta = (\sigma'_H)_f / (\sigma'_V)_f = \tan(\theta - \delta_F\phi)/\tan\theta \tag{4.14}$$

Figure 4.13 illustrates this concept for both normal and thrust fault stress regimes and explains how the most critical failure envelope occurs when the fault is optimally oriented with respect to the in-situ stresses and the fault friction angle. In this case, the fault dip angle is equal to $45° + \delta_F \cdot \phi / 2$ with respect to the horizontal axis and equation (4.14) reduces to:

$$R_{\theta(Opt)} = \tan^2(45 - \delta_F\phi/2) \tag{4.15}$$

The evolution of the stress state in a σ'_H- σ'_V coordinate system can be expressed using the stress path ratio (R_σ, see equation (4.7)). Stress path ratio can be interpreted as an indicator for the change in absolute value of the deviatoric stress (i.e., $(\Delta\sigma'_V$- $\Delta\sigma'_H)\delta_F$) within a reservoir. In fact, by increasing R_σ the absolute value of change in deviatoric stress decreases, because the change in stress state becomes less anisotropic, while by increasing R_σ it becomes more anisotropic. Mathematical models (provided in the previous chapter) confirm the intuitive expectation that, for production/injection within hydrocarbon reservoirs, the change in horizontal total stress is always greater than the change in vertical total stress (i.e., $\gamma_{\alpha(H)} > \gamma_{\alpha(V)}$). Therefore, the stress path ratio is limited to a range between zero and one.

Figure 4.15 illustrates all of the plausible scenarios of stress change paths for both normal and thrust fault stress regimes. Apparently, given that the inequality $R_\sigma < 1 < R_\theta$ always holds true for a thrust fault stress regime, injection will always favour fault reactivation, while production will favour fault stabilization, independent of fault dip angle. This condition will hold true, unless the magnitude of reservoir pressure depletion is high enough to change the stress regime from thrust to normal.

For a normal fault stress regime, two scenarios are possible. 1. When $R_\sigma > R_\theta$, production will favour the stabilization of a fault, while injection will favour reactivation. 2. However, when $R_\sigma < R_\theta$, production will favour reactivation of a fault, while injection will favour stabilization, unless the reservoir pressure increase during injection is large enough to change the stress regime from a normal to thrust.

The described methodology can be easily used to determine the tendency towards reactivation (or stabilization) for faults of known dip angle during production or injection in either thrust or normal fault stress regimes.
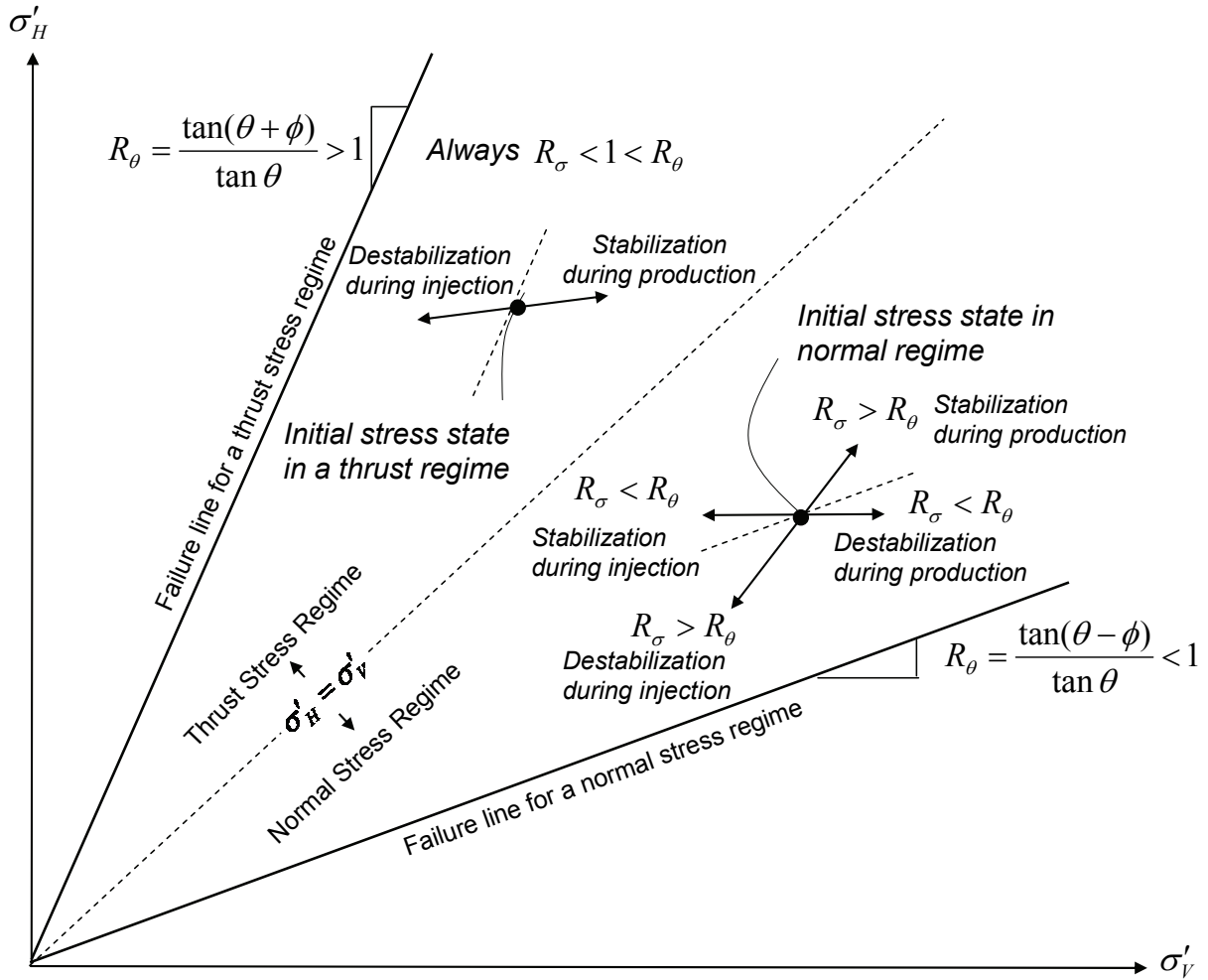
Figure 4.15. Portrayal of different plausible stress paths during injection and production for normal and thrust fault stress regimes.

4.6.2. Estimation of the range of fault dip angles that tend towards reactivation

In a case where induced shear stress change within a reservoir is zero, equation (4.4) can be rewritten as:

$$\lambda = \delta_F (1 - \gamma_{\alpha(H)}) \sin\theta (\cos\theta + \delta_F \mu_s \sin\theta) - \delta_F (1 - \gamma_{\alpha(V)}) \cos\theta (\sin\theta - \delta_F \mu_s \cos\theta) \quad (4.16)$$

Solving equation (4.16) for $\lambda=0$, we find the following equation for identifying this threshold for fault reactivation tendency:

$$\mu_s R_\sigma \tan^2 \theta - \delta_F (1 - R_\sigma) \tan \theta + \mu_s = 0 \qquad (4.17)$$

Once the values of the stress path ratio have been determined, whether using the models provided in Chapter 3 or some other stress change model, equation (4.17) can be used to evaluate the range of dip angles over which there is a tendency towards (or away from) fault reactivation.

Figure 4.16 shows the solution of equation (4.21) for different values of stress path ratio and fault friction coefficient, for a normal fault stress regime. In Figure 4.16, for a given stress path ratio, the upper and lower curves bound the range of fault dip angles for which the fault reactivation factor is negative. Outside this range, the fault reactivation factor is positive. Using the convention that pore pressure change during production is negative, faults with dip angles within this range will tend towards reactivation during production. Similarly, faults with dip angles outside of this range will tend towards fault reactivation during injection. Stating these results in terms consistent
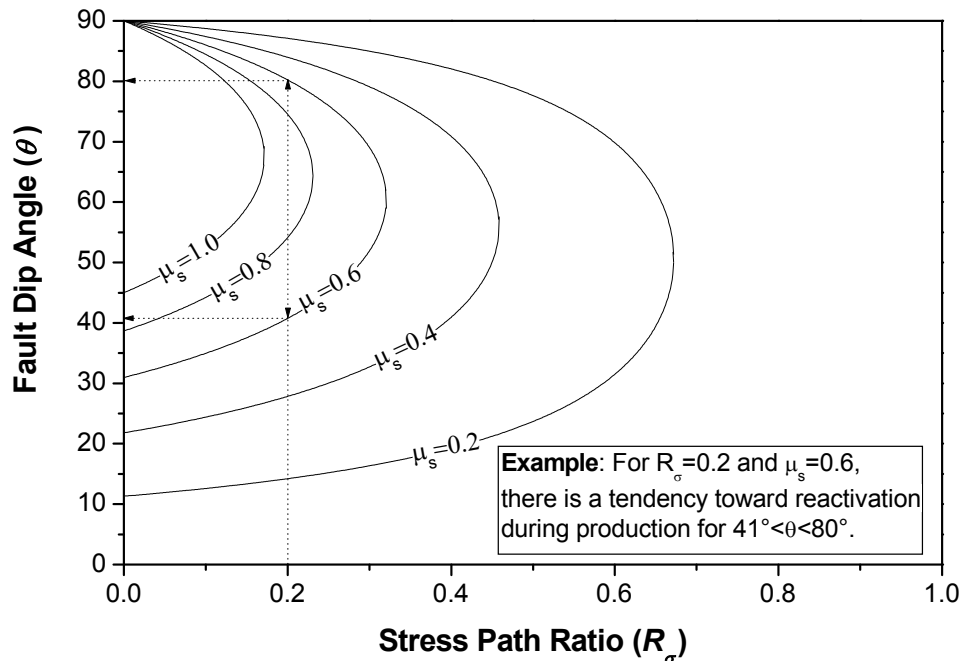
Figure 4.16. Range of fault dip angles which tend towards reactivation as a function of stress path ratio, for different fault friction coefficients, in a normal fault stress regime.

with the previous section, $R_\sigma < R_\theta$ for the dip angles within the appropriate curve in Figure 4.16, and $R_\sigma \geq R_\theta$ outside of this range.

Figure 4.16 also shows that an increase in stress path ratio indicates a reduced tendency towards fault reactivation for a normal fault stress regime. This might be physically interpreted based on the relationship between stress path ratio and the deviatoric stress change. Increasing R_σ indicates a decrease in deviatoric stress change, and as expected, less deviatoric stress change (which means less shear stress on the fault plane) leads to a decrease in tendency towards fault reactivation.

Solving equation (4.17) for the sensible values of R_σ (i.e., between zero and one) in a thrust fault stress regime gives no real roots, which indicates that the value of the fault reactivation factor is always positive for faults in a thrust fault stress regime independent of their dip angles. Therefore, there is a tendency towards reactivation during injection and towards stabilization during production for any fault within a reservoir with such a stress regime. This is consistent with the results discussed in the previous section; i.e., the inequality $R_\sigma < 1 < R_\theta$ always holds true in a thrust fault stress regime.

4.6.3. Determination of stress path ratio

The preceding sections demonstrated the significant role played by stress path ratio in determining the reactivation tendency of a fault during pore pressure change. From equations (4.7), this parameter is a function of induced horizontal and vertical stress changes within the reservoir.

In the following sections, expressions for stress path ratio will be proposed for two different poroelastic models, both of which are based on a reservoir of elliptical cross section under plane strain condition.

Homogeneous half-space

As shown in the previous chapter, normalized stress arching ratios in homogeneous half-space are functions of aspect ratio (e = maximum reservoir thickness/reservoir width),

111

reservoir depth (parameterized as depth number n = reservoir half-width/reservoir depth) and Poisson's ratio. The arching ratios were further shown to be constant throughout such a reservoir, provided it is sufficiently deep (i.e., $n \leq 0.1$) or thin (i.e., $e \leq 0.2$), and pore pressure change is uniform throughout it. By virtue of being a direct function of horizontal and vertical arching ratios, the stress path ratio (R_σ) would be also constant throughout such a reservoir.

Using the results of induced stress change analysis in a half-space, the variation of R_σ with reservoir aspect ratio is shown in Figure 4.17 for different values of depth number and Poisson's ratio. Clearly there is limited sensitivity to depth number for small values of the reservoir aspect ratios ($e \leq 0.4$), which are relatively common for reservoirs.
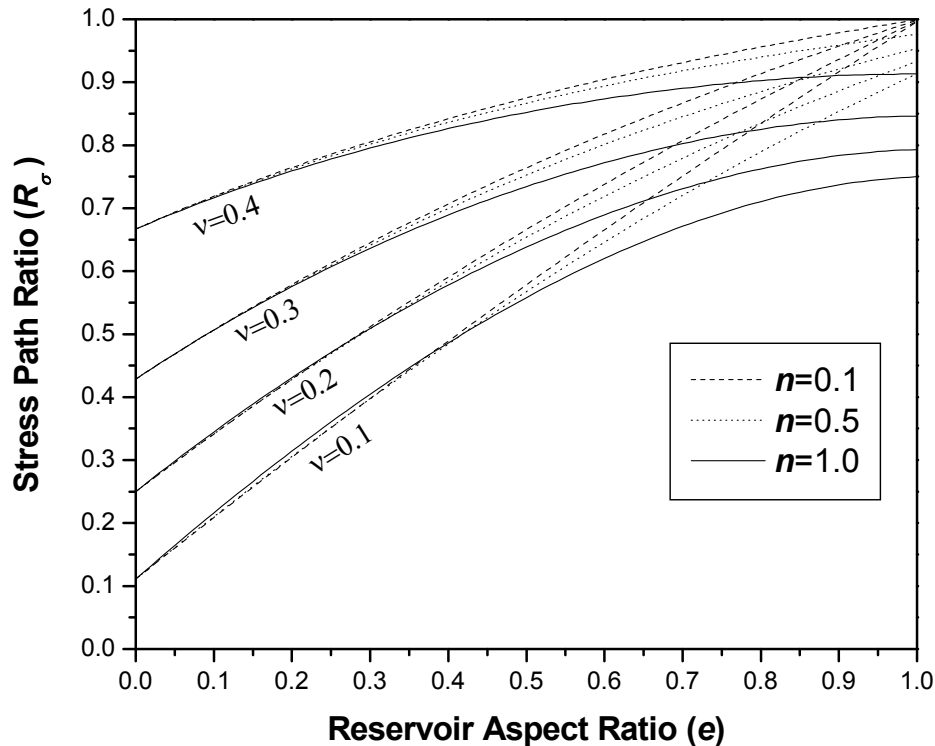
Figure 4.17. Variation of stress path ratio (R_σ) with reservoir aspect ratio (e) for different depth numbers (n) and different Poisson's ratios (v) for an infinitely long reservoir of elliptical cross section in a homogenous half-space.

Hence, it will often be possible to evaluate R_σ using the relatively simple stress arching ratio solutions that have been derived for plane strain reservoirs in a full-space. Using equation (3.34), R_σ can be calculated as:

$$R_\sigma = (e + v - ve)/(1 - v + ve) \tag{4.18}$$

Based on equation (4.18) or Figure 4.17, the value of R_σ increases (i.e., the deviatoric stress change decreases) with increasing reservoir aspect ratio (e), which leads to an decrease in the likelihood of fault reactivation. Therefore, during production, there is a greater tendency towards reactivation for a given fault within a thin reservoir (i.e., with small aspect ratio) compared to the same fault in a thick reservoir (i.e., with high aspect ratio).

Inhomogeneous full-space

Explicit solutions for ellipsoidal inhomogeneities derived in the previous chapter for a full-space are reasonably accurate for reservoirs of finite depth (in a similar fashion to the homogeneous reservoir solution, as demonstrated in the previous section). For a plane strain solution, using equations (3-82), the value of R_σ within the reservoir can be written as:

$$R_\sigma = (A_4 - A_1)/(A_4 - A_3) \tag{4.19}$$

The upper bound for R_σ corresponds to the special case of a laterally infinite reservoir. In such a case, R_σ is independent of R_μ and it can be found as:

$$R_\sigma = v^*/(1 - v^*) \tag{4.20}$$

The lower bound corresponds to the case of a circular reservoir, for which $R_\sigma = 1.0$.

To simplify analyses, it is useful to take advantage of the fact that Poisson's ratio of the rock surrounding the reservoir does not have a significant effect on the stress arching ratios. Hence, it is acceptable to proceed using the assumption that $v = v^*$.

Figure 4.18 shows the variation of stress path ratio as a function of shear modulus ratio and aspect ratio for a value of Poisson's ratio equal to 0.2. These results indicate that
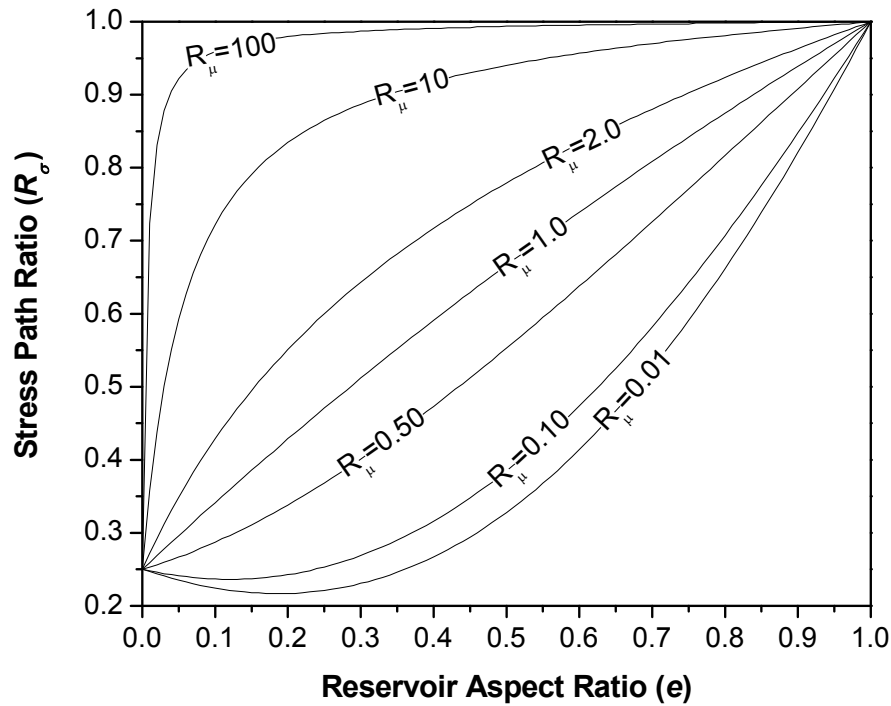
Figure 4.18. Variation of stress path ratio (R_σ) as a function of aspect ratio (e) and shear modulus ratio (R_μ) for Poisson's ratio: $v = v^* = 0.2$.

the stress path ratio increases (i.e., deviatoric stress change decreases) with increasing shear modulus ratio. Therefore, reactivation is less likely within relatively rigid reservoirs during production in comparison with softer reservoirs.

A significant point related to the effect of modulus ratio on induced stress change and fault reactivation tendency is the fact that reservoir stiffness may vary over the operating life of a reservoir. For example, as a reservoir consolidates during depletion its rigidity may increase, especially for high porosity reservoirs. In such cases, the stress path ratio, and the rate at which a fault approaches reactivation or stabilization, will change during pressure depletion. Furthermore, depending on the pre-consolidation history of a reservoir, it's stiffness during injection may be notably larger that its stiffness during production.

Special case: Fault reactivation within a laterally infinite reservoir

To simplify analyses of reservoir stress-depletion response and fault reactivation risk, it is common to consider reservoirs as laterally infinite in extent; i.e., $e = 0$ (e.g., Streit and

Hillis, 2002; Zoback and Zinke, 2002; Hawkes et al., 2005). Analysis of this special case is demonstrated here, in order to find the range of fault dip angles favourable for reactivation in normal and thrust fault stress regimes.

In this special case, R_σ can be found from equation (4.20), and then substituted into equation (4.17) to evaluate the range of fault dip angles that tend towards reactivation. Figure 4.19 illustrates the solution of equation (4.17) for a normal fault stress regime, for several values of Poisson's ratio. An important general result that is demonstrated in Figure 4.19 is the following: For smaller values of Poisson' ratio there is a wider range for fault dips that tend towards reactivation during production in a normal fault stress regime. This is expected. In essence, the horizontal effective stress decreases more rapidly as Poisson's ratio decreases. Given that the vertical effective stress is insensitive to Poisson's ratio, a smaller Poisson's ratio results in a larger deviatoric stress.

In the case of a thrust fault stress regime for the idealized reservoir analyzed above, there are no real roots for equation (4.17), so the sign of fault reactivation factor (λ) is always positive. Consequently, for all possible fault dip angles, there is a tendency towards fault reactivation during injection. Conversely, no faults will tend towards reactivation during production.

4.7. Critical reservoir pressure change for fault reactivation

To ensure safe production from and injection into a reservoir, it is important to know the critical pressure changes (i.e., maximum pressure change during depletion or injection) which may lead to reactivation of existing faults in the field. This section introduces methodologies to identify critical pressure change for reactivation of faults in a field with poroelastic material behaviour.

Based on the Coulomb failure criterion shear on a fault plane occurs when:

$$\left| \frac{\tau_s}{\sigma'_n} \right| = \mu_s \ \text{ or } \ \tau_s \pm \mu_s \sigma'_n = 0 \tag{4.21}$$

115
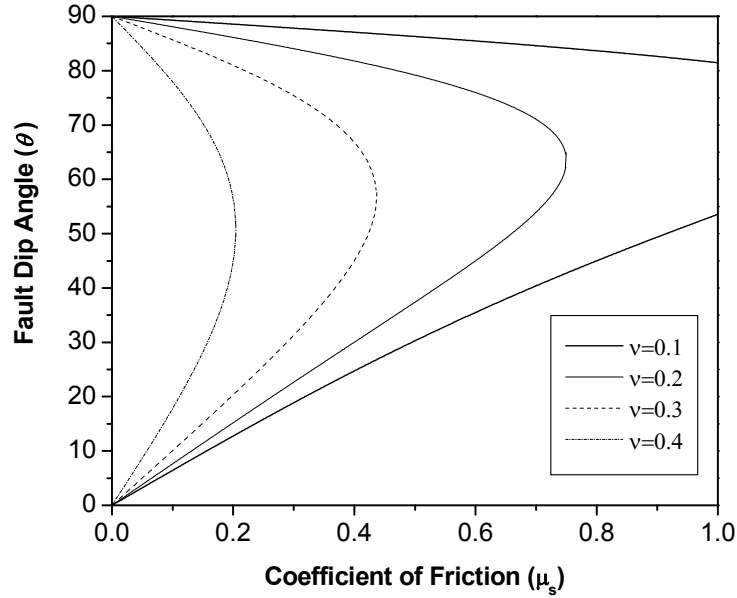
Figure 4.19. Range of fault dip angles that tend towards reactivation during depletion of a laterally infinite reservoir in a normal fault stress regime.

where τ_s and σ'_n are shear stress, effective normal stress, on the fault plane, respectively. In terms of induced stress changes, where the ambient shear and normal effective stresses, respectively, are τ_{s0} and σ'_{n0} and the changes in these stresses during reservoir pressure change, respectively, are $\Delta\tau_s$ and $\Delta\sigma'_n$, equation (4.21) can be written as:

$$(\tau_{s0} \pm \mu_s \sigma'_{n0}) + (\Delta\tau_s \pm \mu_s \Delta\sigma'_n) = 0 \qquad (4.22)$$

Following, equations (4.22) are solved to find critical pressure change for: (1) faults in the entire field with a plane-strain induced stress solution and either a normal or a thrust fault stress regime; and (2) faults within the reservoir with a three-dimensional stress solution and an arbitrary stress regime

4.7.1. Critical pressure change for fault reactivation in the entire field with a plane strain solution

In practice, the vertical stress in most reservoir settings is a principal stress component; this means that there is no shear stress acting on the horizontal plane (and vice versa). As such, $\tau_{HV} = 0$. Under such conditions, for a fault with a dip angle of θ, the initial

shear and normal stresses on the fault plane can be written using stress transform formulations as follows:

$$\tau_{s0} = -\delta_D \left(\frac{\sigma'_{H0} - \sigma'_{V0}}{2} \right) \sin 2\theta \tag{4.23}$$

$$\sigma_{n0} = \frac{\sigma'_{H0} + \sigma'_{V0}}{2} - \left(\frac{\sigma'_{H0} - \sigma'_{V0}}{2} \right) \cos 2\theta \tag{4.24}$$

where σ'_{H0} and σ'_{V0}, respectively, are horizontal and vertical ambient stresses. The sign convention for shear stresses used here specifies that shear stress is positive when the couple of shear stresses affecting on opposite sides of a rectangular element tend to rotate it in a counterclockwise direction. The normal stress is assumed to be positive if it is compressive and negative if it is tensile.

In a general form equations (4.23) and (4.24) can be written as:

$$\tau_{s0} = \Psi_s P_0 \tag{4.25}$$

$$\sigma_{n0} = \Psi_n P_0 \tag{4.26}$$

where P_0 is ambient pore pressure and Ψ_s and Ψ_n are dimensionless parameters, defined as follows:

$$\Psi_s = \delta_D (1 - K_0) \sin 2\theta / (2\lambda_p) \tag{4.27}$$

$$\Psi_n = (1/(2\lambda_p))[(1 + K_0) + (1 - K_0) \cos 2\theta] - 1 \tag{4.28}$$

where K_0 is the lateral pressure coefficient (i.e., =Ambient horizontal total stress/Ambient vertical total stress) and λ_p is an over-pressuring degree ratio which is defined as follows (e.g., Zoback, 2007):

$$\lambda_p = P_0 / \sigma_{V0} \tag{4.29}$$

In a homogenous field with a rock bulk density of G_s, the value of λ_p simply equals $1/G_s$ when the pore pressure regime is hydrostatic.

Using stress transform formulations, the changes in shear and normal stresses (i.e., $\Delta\tau_s$ and $\Delta\sigma'_n$) can be written as:

$$\Delta\tau_s = -\delta_D \left(\frac{\Delta\sigma'_H - \Delta\sigma'_V}{2} \right) \sin 2\theta - \Delta\tau_{HV} \cos 2\theta \tag{4.30}$$

$$\Delta\sigma'_n = \frac{\Delta\sigma'_H + \Delta\sigma'_V}{2} - \left(\frac{\Delta\sigma'_H - \Delta\sigma'_V}{2} \right) \cos 2\theta + \delta_D \Delta\tau_{HV} \sin 2\theta \tag{4.31}$$

where $\Delta\sigma'_H$, $\Delta\sigma'_V$ and $\Delta\tau_{HV}$, respectively, indicate changes in horizontal effective, vertical effective and shear stresses. By some mathematical manipulation of equations (4.30) and (4.31), changes in shear and normal stresses can also be written in the following form:

$$\Delta\tau_s = \gamma_{\alpha(s)}(\alpha\Delta P) \tag{4.32}$$

$$\Delta\sigma'_n = \gamma_{\alpha(n)}(\alpha\Delta P) \tag{4.33}$$

where:

$$\gamma_{\alpha(s)} = -\delta_D \left(\frac{\gamma_{\alpha(H)} - \gamma_{\alpha(V)}}{2} \right) \sin 2\theta - \gamma_{\alpha(HV)} \cos 2\theta \tag{4.34}$$

$$\gamma_{\alpha(n)} = -\left(\delta_L - \frac{\gamma_{\alpha(H)} + \gamma_{\alpha(V)}}{2} \right) - \left(\frac{\gamma_{\alpha(H)} - \gamma_{\alpha(V)}}{2} \right) \cos 2\theta + \delta_D \gamma_{\alpha(HV)} \sin 2\theta \tag{4.35}$$

Using equations (4.22) and (4.25) to (4.31) the critical reservoir pressure change (ΔP_C) to reactivate a fault can be derived as:

$$\Delta P_C / P_0 = -\frac{\Psi_s \pm \mu_s \Psi_n}{\gamma_{\alpha(s)} \pm \mu_s \gamma_{\alpha(n)}} \tag{4.36}$$

The ratio $\Delta P/P_0$ will be called as relative pressure change and denoted by δP in this research. In a similar way, the ratio $\delta P_C=\Delta P_C/P_0$ will be referred to as the critical relative pressure change.

4.7.2. Critical pressure change for faults within a reservoir: three-dimensional stress solution and an arbitrary stress regime

Consider a three-dimensional Cartesian coordinate system oriented in such a way that axes 1,2, and 3 are coincident with the principal total stresses of σ_1, σ_2, and σ_3 within the reservoir. The field behaves poroelastically and shear induced stresses are assumed to be zero within the reservoir. Therefore, stress changes induced by pressure change can be determined using normalized stress arching ratios of $\gamma_{\alpha(1)}$, $\gamma_{\alpha(2)}$, and $\gamma_{\alpha(3)}$ (see sections 3.5.1 and 3.6.2). Critical pressure change for a certain fault passing through this reservoir can be found by using the criteria for reactivation in equation (4.21), which requires calculation of the values of normal effective stress (σ'_n) and shear stress (τ_s) on the fault surface. If the normal direction of the fault surface can be represented by the unit vector of (n_1, n_2, n_3), these stresses can be found by the following formulae:

$$\sigma'_n = \sum \sigma'_i n_i{}^2 \tag{4.37}$$

$$\tau_s{}^2 = (\sum \sigma'^2_i n_i{}^2)^2 - \sigma'^2_n \tag{4.38}$$

where σ'_i represents principal effective stresses, and can be written as a function of in-situ total stresses (σ_{i0}), in-situ pore pressure (P_0), normalized stress arching ratios ($\gamma_{\alpha(i)}$), and pore pressure change (ΔP), in the following form:

$$\sigma'_i / \alpha P_0 = L_i - (1 - \gamma_{\alpha(i)}) \delta P \tag{4.39}$$

where L_i is:

$$L_i = \frac{\sigma_{i0}}{\alpha P_0} - 1 \tag{4.40}$$

By substituting equations (4.39) and (4.40) and after some mathematical manipulation, equations (4.37) and (4.38) can be written in the following form which, respectively, give σ'_n and τ_s as functions of relative pressure change (i.e., $\delta P = \Delta P / P_0$):

$$\sigma'_n / \alpha P_0 = \Sigma \big\{ [(1-\gamma_{\alpha(i)})^2 (n_i)^4 + 2(1-\gamma_{\alpha(i)})(1-\gamma_{\alpha(j)})(n_i n_j)^2](\delta P_C)^2$$
$$+ 2\Sigma[(L_i(1-\gamma_{\alpha(j)}) + L_j(1-\gamma_{\alpha(i)}))(n_i n_j)^2 + L_i(1-\gamma_{\alpha(i)})(n_i)^4]\delta P_C + \Sigma[2L_i L_j (n_i n_j)^2 + L_i^2 (n_i)^4] \big\}^{1/2}$$

(4.41)

$$\tau_S / \alpha P_0 = \big\{ \Sigma[(1-\gamma_{\alpha(i)})^2 n_i^2 (1-n_i^2) - 2(1-\gamma_{\alpha(i)})(1-\gamma_{\alpha(j)})(n_i n_j)^2](\delta P_C)^2$$
$$+ \Sigma[-2L_i(1-\gamma_{\alpha(i)})n_i^2(1-n_i^2) + 2(L_j(1-\gamma_{\alpha(i)}) + L_i(1-\gamma_{\alpha(j)}))(n_i n_j)^2]\delta P_C$$
$$+ \Sigma L_i^2 n_i^2(1-n_i^2) - 2L_i L_j (n_i n_j)^2 \big\}^{1/2}$$

(4.42)

These two expressions for σ'_n and τ_s can be used in equation (4.21) to find the critical pressure change for fault reactivation. This will lead to the following second-order equation which can be solved for the relative critical pressure change:

$$A\delta P_C^2 + B\delta P_C + C = 0$$

(4.43)

where:

$$A = \Sigma[(1-\gamma_{\alpha(i)})^2 n_i^2 (1-n_i^2) - 2(1-\gamma_{\alpha(i)})(1-\gamma_{\alpha(j)})(n_i n_j)^2]$$
$$- \mu^2[\Sigma(1-\gamma_{\alpha(i)})^2 (n_i)^4 + 2\Sigma(1-\gamma_{\alpha(i)})(1-\gamma_{\alpha(j)})(n_i n_j)^2]$$

(4.44)

$$B = \Sigma[-2L_i(1-\gamma_{\alpha(i)})n_i^2(1-n_i^2) + 2(L_j(1-\gamma_{\alpha(i)}) + L_i(1-\gamma_{\alpha(j)}))(n_i n_j)^2]$$
$$- 2\mu^2[\Sigma(L_i(1-\gamma_{\alpha(j)}) + L_j(1-\gamma_{\alpha(i)}))(n_i n_j)^2 + \Sigma L_i(1-\gamma_{\alpha(i)})(n_i)^4]$$

(4.45)

$$C = \Sigma L_i^2 n_i^2(1-n_i^2) - 2\Sigma L_i L_j (n_i n_j)^2 - \mu^2 \Sigma[2L_i L_j (n_i n_j)^2 + L_i^2 (n_i)^4]$$

(4.46)

For a reservoir where axes 1, 2, and 3 are oriented to be coincided with the maximum horizontal, minimum horizontal , and vertical in-situ stresses (i.e., σ_{Hmax}, σ_{Hmin}, and σ_V, respectively) the values of the dimensionless parameters L_i can be rewritten as:

$$L_1 = \frac{\sigma_{H\,max}}{\alpha P_0} - 1 = \frac{K_{0(max)}}{\alpha \lambda_P} - 1 \tag{4.47}$$

$$L_2 = \frac{\sigma_{H\,min}}{\alpha P_0} - 1 = \frac{K_{0(min)}}{\alpha \lambda_P} - 1 \tag{4.48}$$

$$L_3 = \frac{1}{\alpha \lambda_P} - 1 \tag{4.49}$$

where $K_{0(max)}$ and $K_{0(min)}$ are lateral pressure coefficients, respectively, in the maximum and minimum horizontal in-situ stresses orientations.

If the fault has a dip angle of θ and a strike angle of β and the azimuth of the maximum horizontal in-situ stress (σ_{Hmax}) is ζ, the unit normal vector of the fault surface (n_i) can be written as:

$$n_1 = -\sin(\theta)\sin(\beta - \xi) \tag{4.50}$$

$$n_2 = \sin(\theta)\cos(\beta - \xi) \tag{4.51}$$

$$n_3 = -\cos(\theta) \tag{4.52}$$

4.7.3. Limitations on calculated values of critical pressure change

Although, in a theoretical sense, it is possible to find any value for critical pressure change, the value might have no practical significance. For instance, it is unreasonable to consider values of ΔP_C during production that exceed the ambient reservoir pressure (P_0). In addition, an upper limit on ΔP_C would be imposed by the tensile fracturing limit of the reservoir – beyond this limit additional fluid injection would be accommodated more-so by fracture propagation than pressure increase. For the sake of simplicity, in this research, the maximum practical pressure change during injection is considered to be same as the ambient reservoir pressure. In summary, the modified critical pore pressure ((ΔP_C) $_{Modified}$) in the reservoir must be in the following range to be considered as a reasonable value in this work:

$$-P_0 < (\Delta P_C)_{Modified} < P_0 \tag{4.53}$$

4.7.4. Tendency factor

When a certain maximum pore pressure change (i.e., ΔP_{Max}) during the exploitation life of the reservoir is applied, the degree of confidence in preventing fault reactivation can be evaluated by defining a tendency factor, as follows:

$$T_F = \Delta P_{Max} / \Delta P_C \tag{4.54}$$

This tendency factor can be used for quantitative assessment of fault reactivation. In theory, a tendency factor of 1.0 represents the onset of reactivation, and values less than 1.0 represent a stable state (i.e., no reactivation). In practice, depending on risk tolerance thresholds and the degree of input data uncertainty, it may be advisable to use a critical tendency factor threshold somewhat smaller than 1.0; in other words, designing to allow a safety margin.

4.8. Summary and conclusion

The stress changes induced within and around a porous reservoir during fluid production or injection can affect the hydraulic integrity of the reservoir through various mechanisms, including fault reactivation. In this chapter, a method for assessing fault reactivation tendency based on the Coulomb Failure Stress Change (ΔCFS) concept has been presented. While the ΔCFS method can be used in conjunction with any induced stress change model, its use has been demonstrated in this chapter in conjunction with semi-analytical, poroelastic models based on the theories of inclusions and inhomogeneities. It has been shown that fault reactivation potential is dependent on reservoir geometry and dip angle, hence it is important to consider the real reservoir geometry in the analysis of induced seismicity and caprock integrity.

The general pattern of fault reactivation in a normal fault stress regime shows that, during production, the regions within and near the lateral flanks of the reservoir tend towards reactivation, while during injection, the underlying and overlying regions of the reservoir

tend towards reactivation. For a thrust fault stress regime, the overlying and underlying rocks tend towards reactivation during production while, during injection, the reservoir and rocks near the lateral flanks of the reservoir tend towards reactivation.

A sensitivity analysis has shown that the position of the boundary between regions tending towards reactivation and stabilization is relatively insensitive to the value of the friction coefficient. As such, the assumption of an average value of 0.6 for this parameter will likely give a reasonable estimate of this boundary's position for most friction coefficients typically encountered. It should be noted, however, that a tendency towards reactivation will not necessarily result in a significant risk of fault reactivation in settings where the shear stresses on existing faults are relatively low. In such cases, it is more useful to use an induced stress change model of the type used in this work in conjunction with a methodology that assesses the critical conditions required for fault reactivation in an absolute sense. In such analyses, the results are indeed very sensitive to the friction coefficient.

A new methodology was developed to find the ranges of fault dip angles that tend towards reactivation throughout the entire cross-sectional plane of analysis. The results have been presented using pairs of contour maps which, for any chosen point, allow the reader to determine the minimum and maximum fault dip angles that will tend towards reactivation.

Similar methodologies were presented for assessing the effect of induced stress changes on faults passing through reservoirs. These can either predict the range of dip angles which tend towards reactivation during a given pore pressure change, or the reactivation tendency of a fault of known dip angle. Reactivation tendency has been shown to be a function of stress path ratio (R_σ), identified in this work as the ratio of horizontal effective stress change to vertical effective stress change. Theories of inclusions and inhomogeneities have been used for predicting R_σ, both of which are valid for reservoirs of elliptical cross section under plane strain conditions. It has been shown that induced stress analysis solutions for a full-space can be used with confidence for most reservoirs and conditions where the full-space solution is appropriate have been identified.

It has been demonstrated that, within a reservoir located in a setting with a thrust fault stress regime, all fault dip angles tend towards reactivation during injection and stabilization during production (unless a stress regime change occurs). For normal fault stress regimes, faults with moderate angles around the optimum dip angle tend towards reactivation during production and stabilization during injection, while the opposite response is predicted for other dip angles. Stress path ratio has a significant role in the determination of fault dip angles tending most strongly towards reactivation.

The results show that there is a significant effect of elastic property contrast between a reservoir and its surrounding rocks on the stress path, and consequently on fault reactivation tendency. Specifically, for a normal fault stress regime, fault reactivation is less likely within relatively rigid reservoirs during production. In addition, results show that, for a normal fault stress regime, faults in reservoirs with large lateral extents relative to their thicknesses, are more likely to reactivate during production.

A solution was presented to identify the critical pressure change for fault reactivation in the entire field for either thrust or normal stress regime and a plane-strain solution for induced stress change. Similarly, a formulation has been derived to assess critical pressure change for faults within reservoirs in a three-dimensional coordinate system which allows considering different in-situ stress regimes, fault geometries, and reservoir geomechanical response to pore pressure change.

Chapter 5

Induced fracturing due to reservoir pressure change

5.1. Introduction

Induced shear and tensile fracturing of a reservoir and the surrounding rock during production has been considered responsible for induced seismicity recorded in many reservoirs around the world. In addition, it is categorized as a main risk which might threaten the integrity of the reservoir and caprock during fluid injection for carbon dioxide storage. In this chapter, the problem of induced fracturing within a reservoir and surrounding rock during production/injection is studied. For a plane strain solution, the concept of arching ratios for a poroelastic material is used in conjunction with the Coulomb failure criterion to study the likelihood towards fracturing within reservoirs and also to calculate the critical pressure change for fracturing within reservoirs and their surrounding rock. In addition, a three dimensional stress analysis is merged with the Drucker-Prager failure criterion to calculate the critical pressure change for fracturing within reservoirs.

5.2. Induced fracturing within reservoirs analysed in plane strain

As mentioned in Chapter 3, induced stress analysis shows that shear stresses in the central part of horizontal reservoirs are negligible. This section takes the advantage of this fact to study the likelihood of fracturing and critical pressure change for fracturing within reservoirs in a plane strain condition. This section only discusses induced fractures whose surfaces strike normal to the studied cross-section of the plane strain analysis.

Due to the plane strain character of induced stress change analysis and the inability of the Coulomb failure criterion to account for the effect of intermediate principal stress, the proposed methodology in this section is only able to predict induced fracturing for fractures with a surface plane perpendicular to the analysed cross-section. Therefore, strike-slip fault stress regime is not discussed in this section. However, the methodology could be extended to be used for a strike-slip regime by the use of a horizontal cross-section (i.e., by analyzing the reservoir in plan view).

5.2.1. Failure criterion for fracturing within reservoirs

One of the most common failure criteria in rock mechanics is the Coulomb failure criterion. Values of strength properties in this criterion can be determined using direct shear tests or triaxial compression tests. In a Mohr coordinate system (Figure 5.1), for a thrust or a normal fault stress regime, the Coulomb failure criterion can be written as follows:
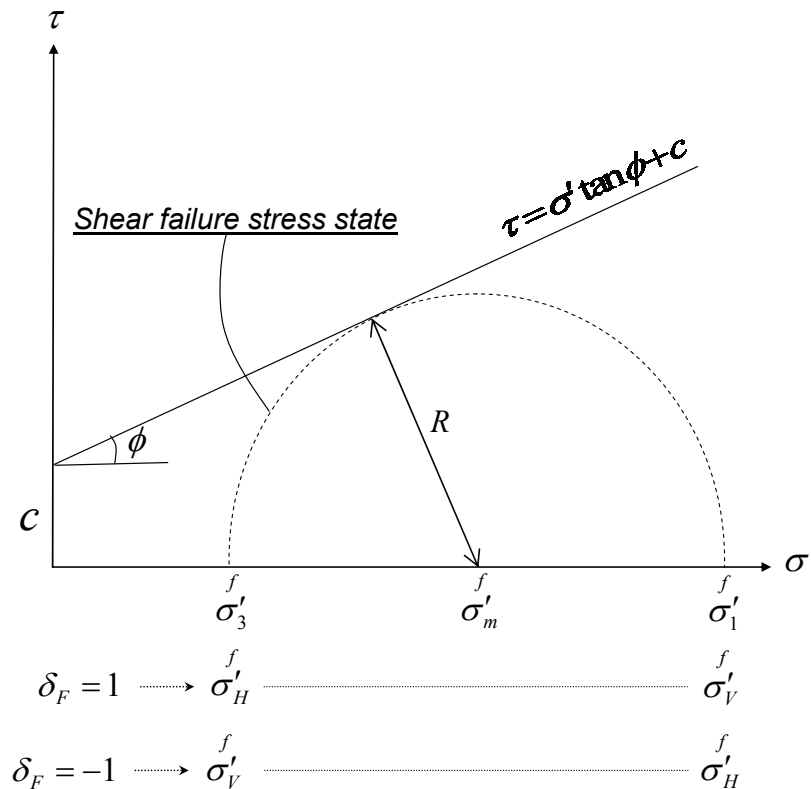
Figure 5.1. Stress state at the point of failure in a Mohr coordinate system for a normal fault stress regime ($\delta_F=1$) and a thrust fault stress regime ($\delta_F=-1$).

$$\left(\frac{\overset{f}{\sigma'}_V + \overset{f}{\sigma'}_H}{2}\right)\sin\phi - \left(\frac{\overset{f}{\sigma'}_V - \overset{f}{\sigma'}_H}{2}\right)\delta_F + c\cos\phi = 0 \qquad (5.1)$$

In this equation, $\overset{f}{\sigma'}_H$ and $\overset{f}{\sigma'}_V$, respectively, are horizontal and vertical effective stresses in the failure state; c and ϕ, respectively, are cohesion and internal friction angle of the reservoir rock. To develop equation (5.1) it is assumed that there is no change in shear stress within the central part of the reservoir. By manipulation of equation (5.1), the Coulomb failure envelope in a σ'_H-σ'_V coordinate system can be represented as a line with the following equation (Figure 5.2):

$$\overset{f}{\sigma'}_H = \overset{f}{\sigma'}_V R_\phi - 2c\delta_F\sqrt{R_\phi} \qquad (5.2)$$

Where R_ϕ is the slope of the linear failure envelope:
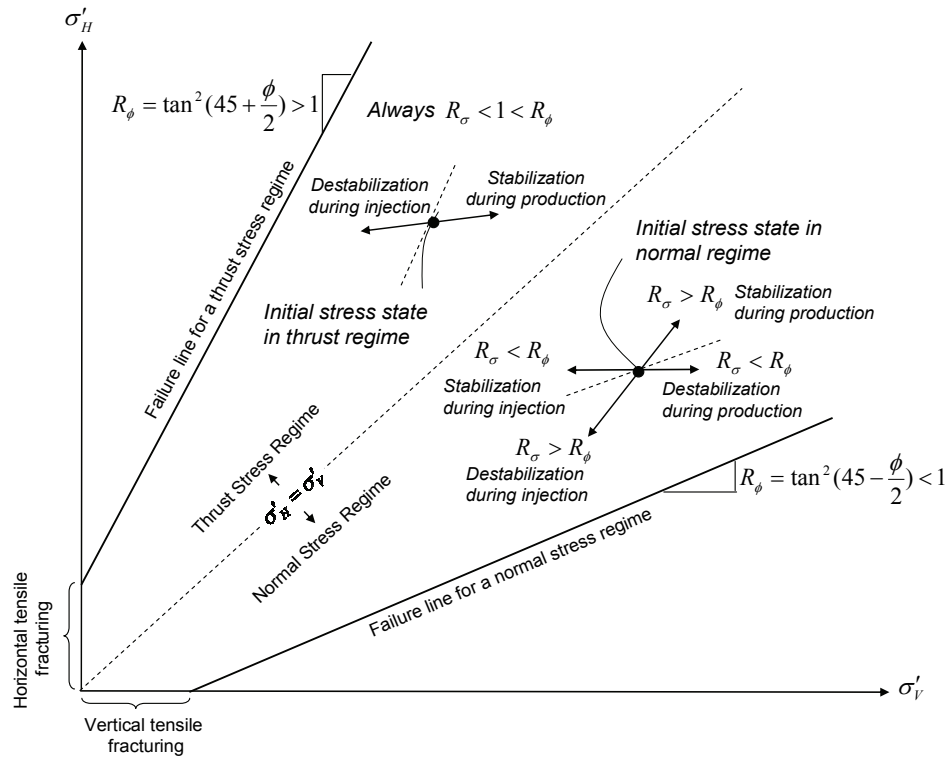
Figure 5.2. Portrayal of different plausible stress change paths during injection and production for normal and thrust fault stress regimes.

$$R_\phi = \tan^2(45 - \delta_F \phi / 2)$$

<div align="right">(5.3)</div>

5.2.2. Different modes of fracturing

Referring to Figure 5.2, there are four different plausible modes of fracturing during reservoir pressure change: (1) horizontal tensile fracturing (i.e., where $\sigma'_V = 0$); (2) vertical tensile fracturing (i.e., where $\sigma'_H = 0$); (3) shear failure in a thrust fault stress regime (i.e., sub-horizontal fractures) which is referred to in this thesis as the thrust mode of fracturing, and (4) shear failure in a normal fault stress regime (i.e., sub-vertical fractures) which is referred to in this thesis as the normal mode of fracturing.

5.2.3. Likelihood of fracturing within reservoirs

Figure 5.2 may be used to develop a straightforward approach to determine the tendency towards fracturing (or stabilization) within a reservoir in either a thrust or a normal fault stress regime during reservoir pressure change. Consider a point in the reservoir with initial horizontal and vertical in-situ stresses σ_{H0} and σ_{V0}, and the corresponding effective stresses denoted σ'_{H0} and σ'_{V0}. By stress evolution during reservoir pressure change, this point moves along a line with a slope of R_σ (see equation (4.7)). As shown in Figure 5.2, based on the relative values of R_ϕ and R_σ, a number of different scenarios pertaining to intact rock failure (or stabilization) are possible, as follows.

In a normal fault stress regime (i.e., the lower-right half of the graph), when R_σ is greater than R_ϕ, the stress state moves further away from the failure line during production (i.e., stabilization occurs), but towards it during injection (i.e., destabilization occurs). When $R_\sigma < R_\phi$, however, the opposite occurs. For a thrust fault stress regime, the relation $R_\sigma < 1 < R_\phi$ always holds true. Therefore, in a thrust fault stress regime, the stress state always moves away from the failure line (i.e., stabilization) during production, while it always moves towards it (i.e., destabilization) during injection.

These scenarios are summarized in Table 5.1. The key words of stabilization and destabilization in Table 5.1 are only appropriate if the initial stress regime remains

unchanged during reservoir pressure change. As Figure 5.3 shows, when $R_\sigma < R_\phi$, for sufficiently large values of reservoir pressure change, a normal fault stress regime might change to a thrust fault regime during injection. This might result in shear fracturing in a thrust fault stress regime, or horizontal or vertical tensile fracturing depending on the initial stress state (i.e., σ'_{H0} and σ'_{V0}) and the stress path ratio (R_σ). In a similar manner, a thrust fault stress regime might change to a normal fault stress regime during injection, and the rock failure mode might be changed as a consequence.
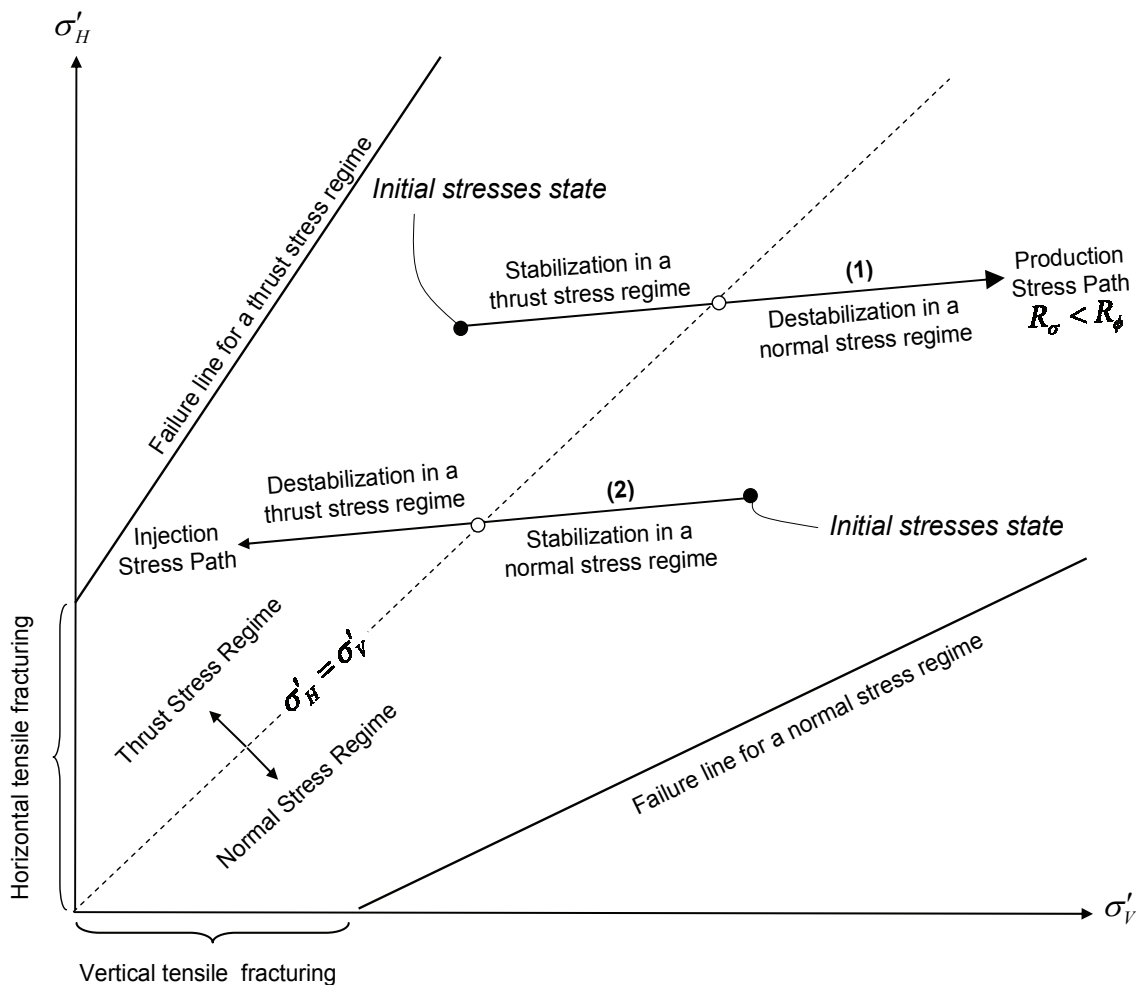
Figure 5.3. Occurrence of stress regime change, and consequent failure mode change, for sufficiently high values of reservoir pressure change during: (1) production from a reservoir with an initially thrust fault stress regime; and (2) injection in a reservoir with an initially normal fault stress regime.

Table 5.1. Rock failure tendency within a reservoir during production or injection in normal or thrust fault stress regimes.

Pressure Change Scenario	Normal fault Stress Regime		Thrust fault Stress Regime
	$R_\phi > R_\sigma$	$R_\phi < R_\sigma$	
Injection	**_Stabilization_** (Although Tensile fracturing modes or shear fracturing are plausible for sufficiently high values of ΔP)	**_Destabilization_**	**_Destabilization_**
Production	**_Destabilization_**	**_Stabilization_**	**Stabilization** (Although shear fracturing is plausible for sufficiently high values of ΔP)

5.2.4. Critical pore pressure change for induced fracturing within reservoirs

Further to analyzing the failure (or stabilization) tendency resulting from pore pressure change in a relative sense, it is useful to estimate, in an absolute sense, the critical pore pressure change at which shear or tensile fracturing will be induced within a reservoir (ΔP_f). This critical value can be used to establish the lower limit on reservoir pressure during production, and the upper limit on reservoir pressure during enhanced recovery or greenhouse gas sequestration operations.

The critical pore pressure change to induce shear fracturing ((ΔP_f)$_S$) within a reservoir can be calculated by substituting changes in effective stresses from equation (3.10) into equation (5.2), leading to the following equation:

$$(\Delta P_f)_S / P_0 = \frac{[(K_0 - \lambda_p)] - [1 - \lambda_p]R_\phi + 2c^* \lambda_p \delta_F \sqrt{R_\phi}}{\alpha \lambda_p (1 - \gamma_{\alpha(V)})[R_\sigma - R_\phi]} \qquad (5.4)$$

where P_0 is the ambient reservoir (pore) pressure, c^* is a normalized form of the reservoir rock's cohesion (c) with respect to the ambient reservoir pressure (i.e., $c^* = c/P_0$);

K_0 is the lateral pressure coefficient in the in-situ stress state (i.e., $K_0 = \sigma_{H0}/\sigma_{V0}$) and λ_p is as defined in equation (4.29). With an assumption of negligible tensile strength for the reservoir rock, which is fairly common for sedimentary rocks (e.g., Zoback, 2007), the value of λ_p must satisfy the following condition to ensure that the both of horizontal and vertical effective in-situ stresses are compressive (i.e., $\sigma'_{H0} > 0$ and $\sigma'_{V0} > 0$).

$$\alpha\lambda_P < \min\{1, K_0\} \tag{5.5}$$

Equation (5.4) provides two different values of the critical pressure change in either a normal (i.e, $\delta_F = 1$) or a thrust fault stress regime (i.e, $\delta_F = -1$). Either or both of these values might not be realistic, depending on the specific characteristics of the problem. To filter out the unrealistic values, first, the pore pressure change during production (ΔP_f) must not be greater than the ambient reservoir pressure (P_0). Second, the maximum pressure change during injection must be less than the critical pressure change for tensile fracturing. By assuming a zero tensile strength for the reservoir, the critical pressure changes to induce horizontal and vertical tensile fractures (i.e., $(\Delta P_f)_{T(H)}$ and $(\Delta P_f)_{T(V)}$), can be determined as follows:

$$(\Delta P_f)_{T(H)} / P_0 = (1 - \lambda_p)/[\alpha\lambda_p(1 - \gamma_{\alpha(V)})] \tag{5.6}$$

$$(\Delta P_f)_{T(V)} / P_0 = (K_0 - \lambda_p)/[\alpha\lambda_p(1 - \gamma_{\alpha(H)})] \tag{5.7}$$

To sum up, any normalized reservoir pressure change must satisfy the following inequality:

$$-P_0 < \Delta P_f < \min\{(\Delta P_f)_{T(H)}, (\Delta P_f)_{T(V)}\} \tag{5.8}$$

5.3. Induced fracturing in the entire field by implementing a plane strain stress change analysis

Following, a methodology is developed to model induced fracturing-faulting in the entire field during pressure change within a reservoir. The methodology is designed to calculate the critical pressure changes for the both cases of shear and tensile fracturing. The

developed methodology uses the poroelastic methods described previously to determine induced stress change and a Coulomb failure criterion to define the onset of fracturing.

5.3.1. Critical pressure change for shear fracturing

The condition corresponding to shear failure in intact rock is demonstrated in Figure 5.4, which shows a Mohr circle representing the failure stress state. This failure state develops when the critical reservoir pressure change ($\Delta P_{C(S)}$) occurs within the reservoir. This pressure change might be a result of either injection or production. At this critical condition, when shear is occurring in the rock, using the trigonometry of Figure 5.4, the following equation between different stresses can be written:

$$(\frac{\sigma'_H + \sigma'_V}{2}) \sin\phi + c\cos\phi = \left[(\frac{\sigma'_H - \sigma'_V}{2})^2 + \sigma_{HV}^2 \right]^{1/2} \tag{5.9}$$

where σ'_H and σ'_V, and σ_{HV}, respectively, are horizontal effective stress, vertical effective stress, and shear stress that exist when the critical pressure change for shear fracturing within the reservoir ($\Delta P_{C(S)}$) is reached. By using equations (3.10) and (4.29), and after some mathematical manipulation, the following equation can be derived from equation (5.9):

$$A(\Delta P_{C(S)} / P_0)^2 +' B(\Delta P_{C(S)} / P_0) + C = 0 \tag{5.10}$$

where

$$
\begin{aligned}
A &= \gamma_{\alpha(m)}^2 \mu^2 - (\gamma_{\alpha(d)}^2 / 4 + \gamma_{\alpha(HV)}^2)(1 + \mu^2) \\
B &= 2\gamma_{\alpha(m)} \mu(m\mu + c^*) - d\gamma_{\alpha(d)}(1 + \mu^2) \\
C &= m^2 \mu^2 - d^2(1 + \mu^2) + 2c^* m\mu + c^{*2}
\end{aligned}
\tag{5.11}
$$

and $\gamma_{\alpha(m)}$ and $\gamma_{\alpha(d)}$ are average and deviatoric normalized stress arching ratios:

132

$$\gamma_{\alpha(m)} = \frac{\gamma_{\alpha(H)} + \gamma_{\alpha(V)}}{2} - \delta_L$$

$$\gamma_{\alpha(d)} = \gamma_{\alpha(H)} - \gamma_{\alpha(V)}$$

(5.12)

and,

$$c^* = c/(\alpha P_0)$$

$$d = [1/(2\alpha\lambda_p)](1 - K_0)$$

$$m = [1/(2\alpha\lambda_P)](1 + K_0) - 1$$

(5.13)

Equation (5.10) may be used in a relatively straight-forward manner to find the value of critical pressure change for shear fracturing at any point in the entire field.

As can be seen in Figure 5.4, the orientation of induced shear fractures can be easily found if the orientations of critical principal effective stresses are known. As shown, shear fractures make an angle of 45° - ϕ/2 with the direction of maximum principal effective stress (i.e., σ'_1) which can be determined from the Mohr circle.

5.3.2. Critical pressure change for tensile fracturing

In addition to shear fracturing, there is also a condition in which of tensile fracturing may occur. As shown in Figure 5.4, for a tensile strength of zero, this happens if the critical pressure change of $\Delta P_{C(T)}$ is such that the minimum principal effective stress (σ'_3) becomes zero or less. This condition leads to the following equation:

$$\sigma'_3 = \left(\frac{\sigma'_H + \sigma'_V}{2}\right) - R = 0$$

(5.14)

Using equations (3.10) and (4.29) this equation can be written as follows:

$$A'(\Delta P_{C(T)}/P_0)^2 +' B'(\Delta P_{C(T)}/P_0) + C' = 0$$

(5.15)
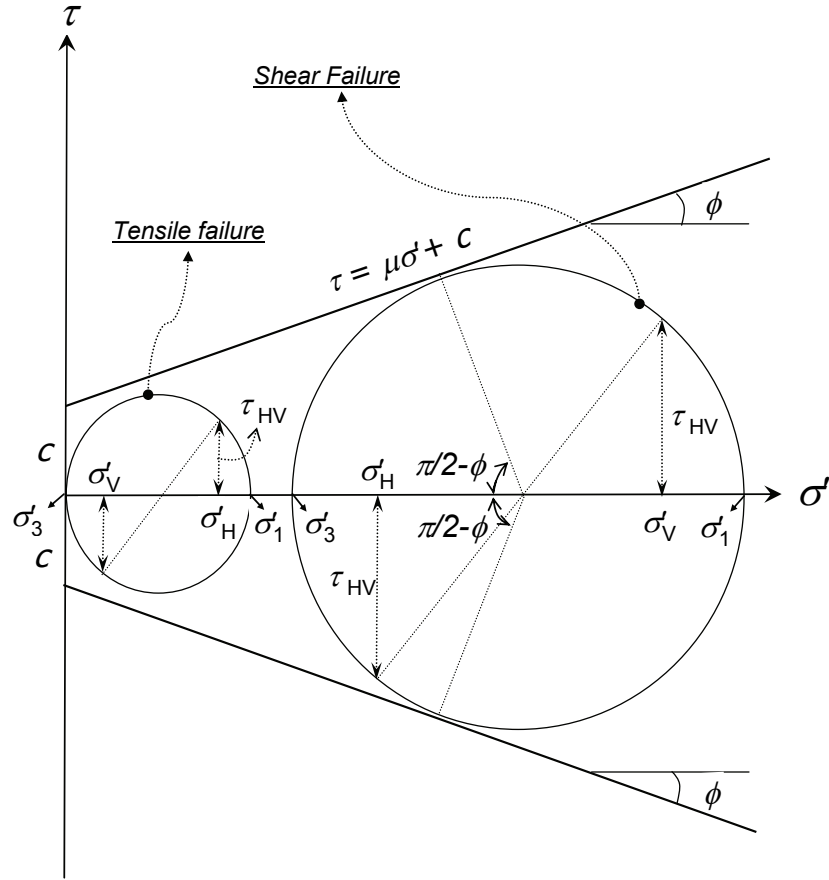
Figure 5.4. Demonstration of shear failure and tensile failure induced by reservoir pressure change

where:

$$A' = \gamma_{\alpha(m)}^2 - \gamma_{\alpha(d)}^2 - \gamma_{\alpha(HV)}^2$$
$$B' = 2(m\gamma_{\alpha(m)} - d\gamma_{\alpha(d)}) \qquad\qquad (5.16)$$
$$C' = m^2 - d^2$$

Using equation (5.15) gives the critical pressure change ($\Delta P_{C(T)}$) for tensile induced fracturing. The orientation of tensile fractures will be normal to the direction of the minimum principal stress, which can be determined from the Mohr circle.

The critical pressure change for fracturing is determined by comparing the tensile critical pressure change ($\Delta P_{C(T)}$) and shear critical pressure change ($\Delta P_{C(S)}$) and the direction of failure surface must be determined based on this fact.

5.4. Induced fracturing within the reservoir by implementing a three-dimensional stress change analysis

The previous methodology, which was developed for calculation of critical pressure change for induced shear fracturing within reservoirs in a plane strain condition, can be extended to a three dimensional solution. This can be done by considering all three possible fracturing planes in the field and finding the most vulnerable one for fracturing (i.e., the minimum critical pressure change). However, the Coulomb failure criterion does not consider the effect of intermediate stress. The Drucker-Prager criterion is able to consider this effect, is mathematically conducive to the development of closed-form solutions, and is sometimes used for rocks (e.g., Zoback, 2007). As will be shown here, using the Drucker-Prager failure criterion, it is possible to derive a single equation to calculate the critical pressure change for shear fracturing for a three-dimensional condition. The Drucker-Prager failure criterion can be stated as:

$$J_2^{1/2} = Q_1 + Q_2 I_1 \tag{5.17}$$

Where Q_1 and Q_2 are material strength constants and I_1 and J_2, respectively, are the first variant of stresses and the second variants of the deviatoric part of stresses, and can be written as:

$$J_2 = (1/6)\Sigma(\sigma_i' - \sigma_j')^2 \tag{5.18}$$

$$I_1 = (1/3)\Sigma\sigma_i' \tag{5.19}$$

where σ_i are principal stresses. By substituting equations (4.39) and (4.40) in equations (5.17) through (5.19), the following equation can be derived to calculate the relative critical pressure change required for shear fracturing:

$$A\delta P_C^2 + B\delta P_C + C = 0 \tag{5.20}$$

where,

$$A = 3\Sigma(\gamma_{\alpha(i)} - \gamma_{\alpha(j)})^2 - 2Q_2^2(3 - \Sigma\gamma_{\alpha(i)})^2 \tag{5.21}$$

$$B = 6\Sigma(L_i - L_j)(\gamma_{\alpha(i)} - \gamma_{\alpha(j)}) + 4Q_2^2(\Sigma L_i)(3 - \Sigma\gamma_{\alpha(i)}) + 12Q_1'Q_2(3 - \Sigma\gamma_{\alpha(i)}) \tag{5.22}$$

$$C = 3\Sigma(L_i - L_j)^2 - 18Q_1'^2 - 2Q_2^2(\Sigma L_i)^2 - 12Q_1'Q_2\Sigma L_{i\,i} \tag{5.23}$$

and,

$$Q_1' = \frac{Q_1}{\alpha P_{0\,i}} \tag{5.24}$$

Material strength parameters (i.e., Q_1 and Q_2) can be related to the Coulomb failure criterion parameters (i.e., c and ϕ) using the following formulations (Zoback, 2007):

1. When the Drucker-Prager failure criterion surface circumscribes the Coulomb failure criterion surface:

$$Q_1 = \frac{6c\cos\phi}{\sqrt{3}(3 + \sin\phi)} \qquad Q_2 = \frac{2\sin\phi}{\sqrt{3}(3 + \sin\phi)} \tag{5.25}$$

2. When the Drucker-Prager failure criterion surface inscribes the Coulomb failure criterion surface:

$$Q_1 = \frac{6c\cos\phi}{\sqrt{3}(3 - \sin\phi)} \qquad Q_2 = \frac{2\sin\phi}{\sqrt{3}(3 - \sin\phi)} \tag{5.26}$$

In a similar manner to the plane strain solution, the critical pressure change for fracturing in three-dimensional case can be written as follows for the induced tensile fractures within a plane normal to the vertical, minimum horizontal, and maximum horizontal in-situ stresses, respectively:

$$(\Delta P_f)_{T(H1)}/P_0 = (1 - \lambda_p)/[\alpha\lambda_p(1 - \gamma_{\alpha(V)})] \tag{5.27}$$

$$(\Delta P_f)_{T(V1)} / P_0 = (K_{0(\max)} - \lambda_p) / [\alpha \lambda_p (1 - \gamma_{\alpha(H\max)})] \tag{5.28}$$

$$(\Delta P_f)_{T(V2)} / P_0 = (K_{0(\min)} - \lambda_p) / [\alpha \lambda_p (1 - \gamma_{\alpha(H\min)})] \tag{5.29}$$

And the minimum critical pressure change to induce fracturing is:

$$(\Delta P_f)_T < \min\{(\Delta P_f)_{T(H)}, (\Delta P_f)_{T(V1)}, (\Delta P_f)_{T(V2)}\} \tag{5.30}$$

5.5. Summary and Conclusion

A framework has been developed to study the potential for induced fracturing within a reservoir and the surrounding rock during fluid injection or production. Depending on the initial stress state, the reservoir rock's strength parameters, and the stress change path during production or injection, four different modes of fracturing were recognized: horizontal tensile fracturing, vertical tensile fracturing, shear fracturing in a thrust mode (i.e., sub-horizontal fractures), and shear fracturing in a normal mode (i.e., sub-vertical fractures). A straightforward approach has been suggested to determine the tendency of the reservoir towards either of fracturing or stabilization during reservoir pressure change. In addition, a series of formulations has been developed to determine the critical reservoir pressure change for induced fracturing for the both a plane strain stress analysis model (for both within reservoirs and in the entire field) and a three-dimensional stress analysis model (for within reservoirs).

Chapter 6

Case Studies

6.1. Introduction

The objective of this chapter is to use different case studies to demonstrate the application of the developed methodologies for induced fracturing and fault reactivation analysis. In addition, sensitivity analyses are carried out to show the effects of parameter uncertainty on patterns of induced stress change, stress evolution, fracturing and fault reactivation.

The following case studies are studied in this chapter:

- Fault reactivation analysis for a synthetic case study
- Studying general patterns of stress evolution, and fracturing using a synthetic case study
- Fault reactivation in the Lacq gas field, France
- Fault reactivation and induced fracturing analyses within the Ekofisk oil and gas reservoir, North Sea
- Fault reactivation and induced fracturing analyses in the Weyburn oil field, Saskatchewan, Canada
- Fault reactivation and induced fracturing analyses for the Zama Acid Gas Injection Project, Alberta

6.2. Fault reactivation analysis for a synthetic case study

This synthetic case study considers a field containing a reservoir of rectangular cross-section, having a depth (to the reservoir top) of 3 km, a width of 6 km, and a thickness of 300 m embedded in rock possessing the same material properties as the reservoir under plane strain condition. As shown in Figure 6.1, there are 14 faults with different dip angles and dip directions throughout the cross section to be analyzed. All faults strike normal to the cross-section plane. The coefficient of friction for all the faults is considered to be 0.6. The homogeneous isotropic rock of the field has a Poisson's ratio (v) of 0.2, and a specific gravity (G_s) of 2.05 which is representative of high-porosity (e.g., under-consolidated) sedimentary rocks, the lateral pressure coefficient (K_0) is 0.85, which indicates a normal fault stress regime as the ambient condition. Pore pressure is considered to be hydrostatic outside of the reservoir, and an over-pressuring ratio (λ_p) of 0.76 is considered for the reservoir. The Biot's coefficient is considered to be 1.0. The objective of this study is analysing the likelihood for reactivation, the critical pressure change, and the tendency factor for reactivation for the existing faults.
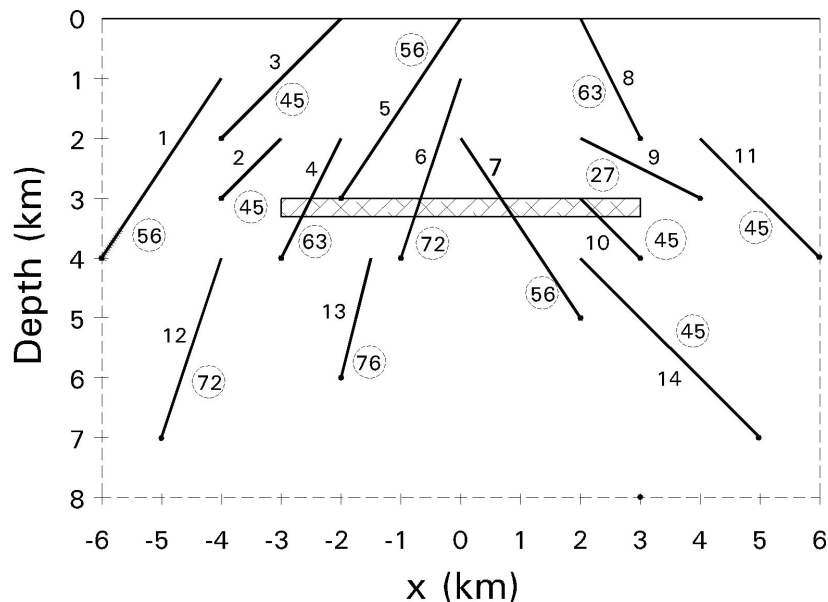
Figure 6.1. (a) Cross-sectional geometry of the synthetic case study for fault reactivation tendency in a normal fault stress regime under plane strain conditions. Each fault is labeled with a reference number (i.e., 1 through 14), and a dip angle (which is circled).

6.2.1. Stress change analysis

The values of the normalized stress arching ratios are primarily dependent on the mechanical properties and geometry of a reservoir and its surrounding rock. For the special case of a homogeneous, linear elastic reservoir with the same elastic properties as the surrounding rock, the stress arching ratios can be found using the theory of inclusions. Output for a plane strain stress analysis of this field using the theory of inclusions was shown and discussed in section 3.5.2. It is important to remember that a continuum mechanics modelling approach has been used, hence the effects of post-reactivation fault plane displacements have not been considered.

In addition to calculation of arching ratios for the entire field, arching ratios also were determined directly along the faults to calculate the critical pressure change for reactivation. Figure 6.2 shows how arching ratios vary along fault 7. Horizontal normalized arching ratios ($\gamma_{\alpha(H)}$) along this fault are negative except for a segment located within the reservoir. During injection (i.e., $\Delta P > 0$), then, the fault is under compressive horizontal stress change within the reservoir (i.e., $\Delta\sigma_H > 0$) and under tensile horizontal stress change in the overburden and underburden (i.e., $\Delta\sigma_H < 0$).
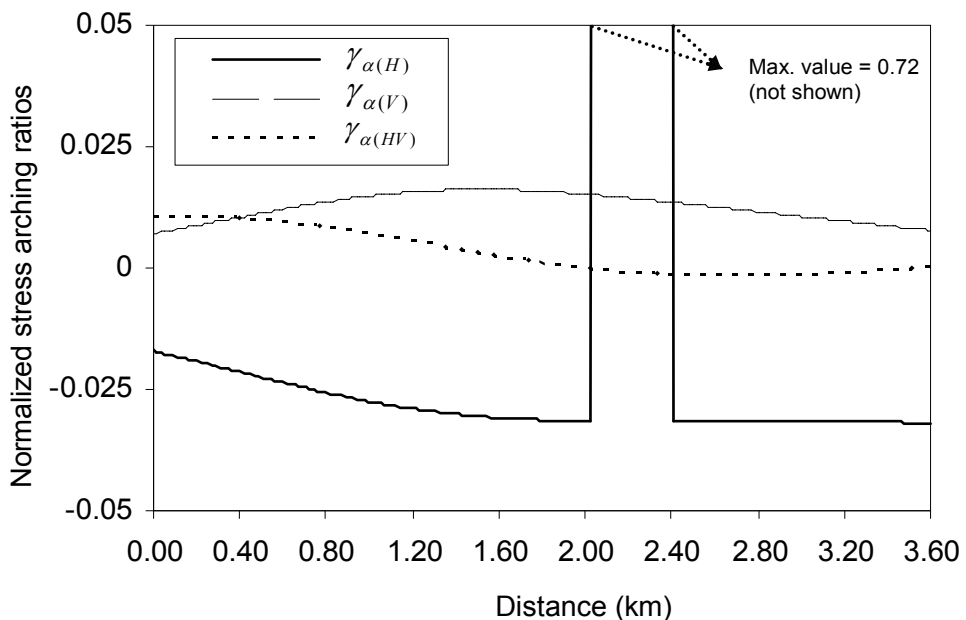
Figure 6.2. Variation of normalized arching ratios along Fault 7

Further, the magnitude of total stress change is considerable within the reservoir relative to the surrounding rock. The normalized vertical arching ratio ($\gamma_{\alpha(V)}$) is positive along the entire length of the fault, which indicates that the entire fault is under compressive vertical stress change ($\Delta\sigma_V > 0$) during injection. The opposite of these results occur for the case of production.

6.2.2. Fault reactivation tendency analysis

Due to the similarities in geometry and material properties, Figures 4.10a and 4.10b can be used to identify the tendency towards reactivation for the faults in this case study. These figures show the values of θ_{min} and θ_{max} as contour maps, for a normal stress regime. Although in these figures, faults are considered to be dipping towards to the bottom left corner of the cross section (i.e., $\delta_D = 1$), due to the symmetrical nature of the problem, the results for the analogous case in which the faults dip towards to the bottom right corner of the cross section (i.e., $\delta_D = -1$) can be generated by mirroring the contours along the $x = 0$ line. The final results are shown in Figure 6.3, in which the faults that tend towards reactivation during production are identified using fat grey lines, and the faults that tend towards reactivation during injection are identified as thin black lines.

As shown in Fig. 6.3, there are 7 faults that tend towards reactivation during production, either fully or partly. These faults can be categorized into two main groups: Firstly, faults 1, 2, 9, 11 and a segment of fault 3, which are located near the lateral flanks of the reservoir; secondly, the segment of fault 7 which is located within the reservoir.

The mechanisms of fault reactivation in these two groups are different. Faults in the first group tend towards reactivation due to the effective horizontal stress relaxation (tensile stress change) and vertical effective stress increase (compressive stress change). These stress changes apparently accentuate the existing normal fault stress regime (i.e., increase the deviatoric stress), hence the tendency towards reactivation. Fault 7, on the other hand, tends towards reactivation because the increase in vertical effective stress is larger than the increase in the effective horizontal stress. Even though both stress
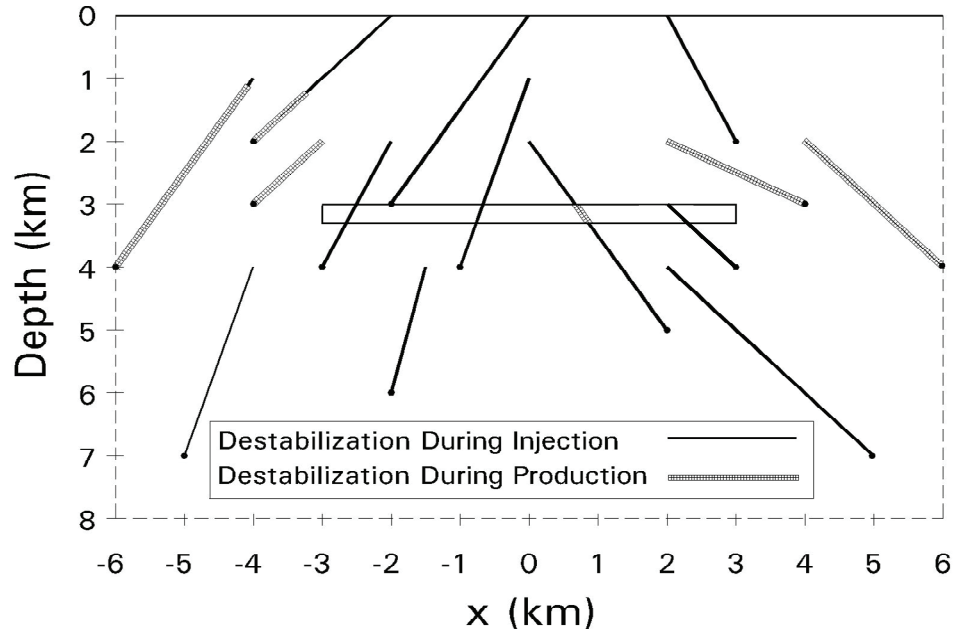
Figure 6.3. Tendency towards reactivation during fluid injection and production.

changes are compressive, the induced deviatoric stress is sufficient to force the stress state on the fault towards failure. However, depending on the amount of stress change within the reservoir, only a certain range of fault dip angles (i.e., moderate dip angles) tend towards reactivation. For example, because the dip angle of fault 6 is relatively steep, the component of induced shear stress resolved on its surface is small, hence it does not tend towards reactivation.

According to Fig. 6.3, the faults above and below the reservoir stabilize during production due to a stress state change that works to counter-act the deviatoric stress in the existing normal fault stress regime. As also shown in Fig. 6.3, fault behaviour during injection is the exact opposite of the case discussed for production.

6.2.3. Critical pressure change for fault reactivation

Equation (4.36) was used to calculate the theoretical critical pressure changes (ΔP_C) for fault reactivation for both injection and production. The results for fault number 7 are shown in Figure 6.4a. Clearly, some of the calculated critical pressure changes are impractically high. Figure 6.4b shows the results after applying the filtering
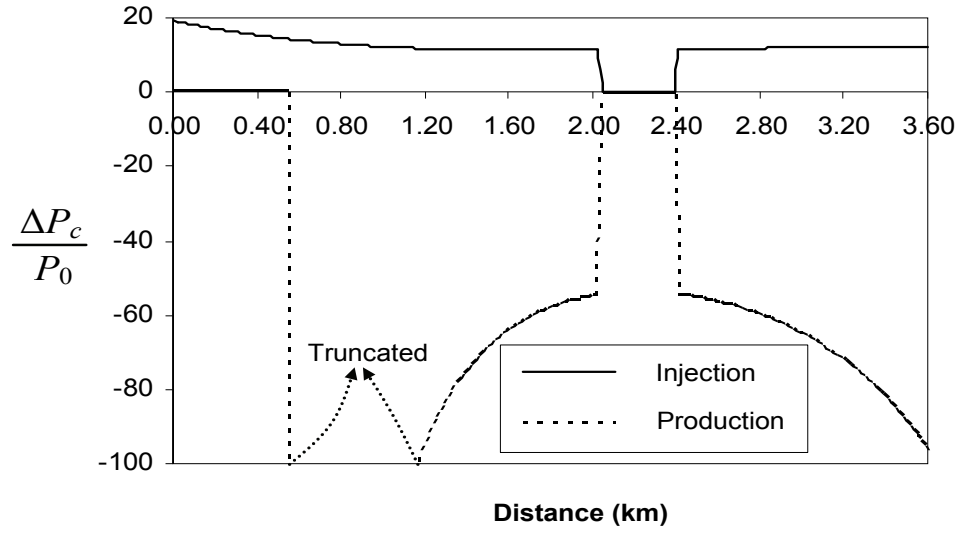
(a)
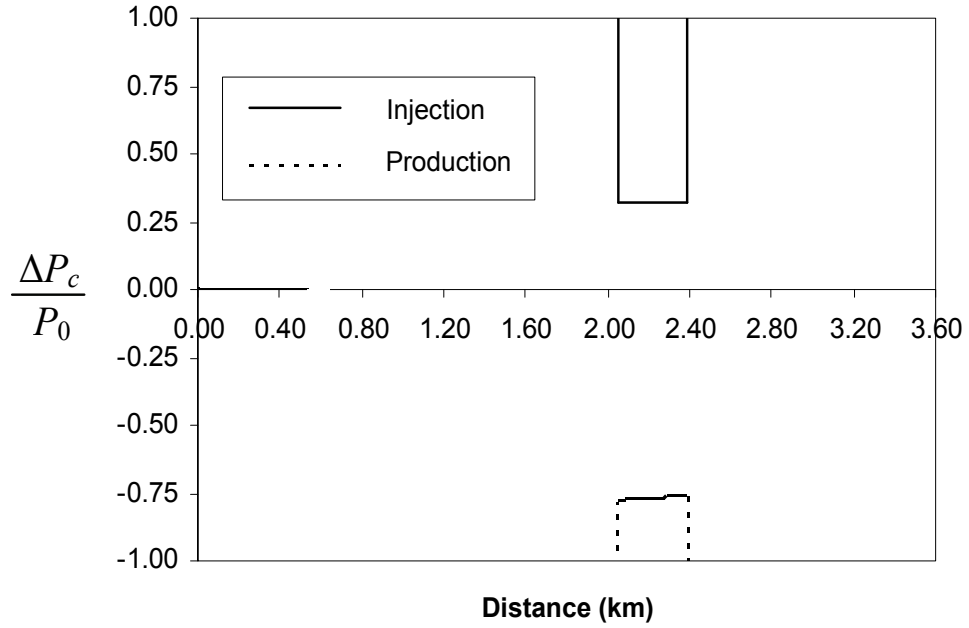
(b)

Figure 6.4. Critical pressure change analysis along fault 7: (a) variation of normalized arching ratios; (b) the critical pressure change; (c) modified critical pressure change; and (d) tendency factor for a reservoir pressure change of -29 *MPa*.

143
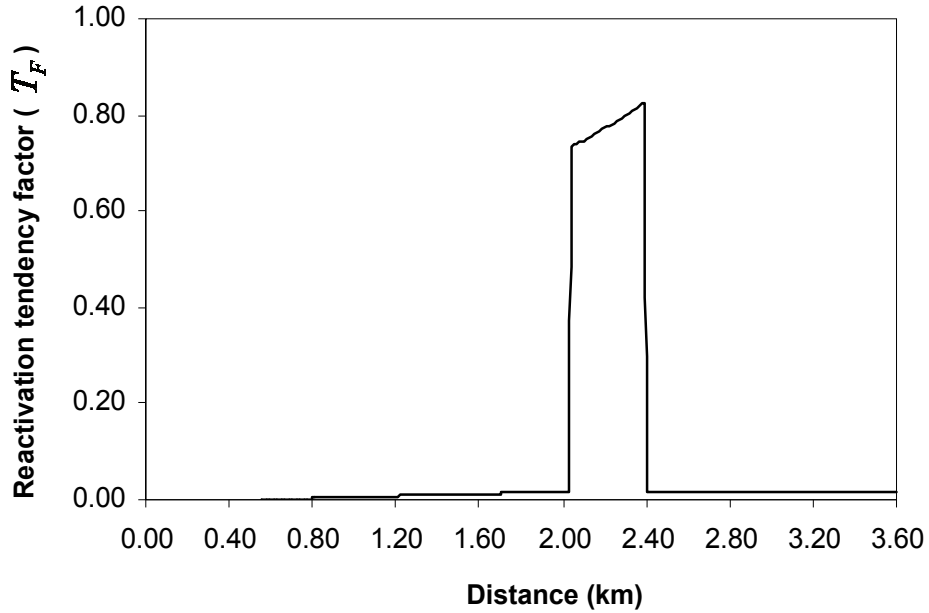
(c)

Figure 6.4 (Continued). Critical pressure change analysis along fault 7: (a) variation of normalized arching ratios; (b) the critical pressure change; (c) modified critical pressure change; and (d) tendency factor for a reservoir pressure change of -29 *MPa*.

criteria given in equation (4.53). Based on these results, for either injection or production scenarios, the only possibility for reactivation of fault 7 is for a segment which is located within the reservoir. During production, the reactivation occurs when the pressure decreases by 78% of its ambient value (i.e., a decrease of roughly 38 MPa). During injection, it occurs when the ambient pressure of the reservoir increases by 33% (i.e. an increase of roughly 16 MPa)

In Figure 6.4c, the tendency factor (T_F) calculated using equation (4.54) along fault 7 is shown for a hypothetical production scenario in which the reservoir pressure is reduced by of 29 MPa (i.e., 60% of the ambient reservoir pressure). This figure shows that the maximum reactivation tendency factor (i.e., T_F=0.82) occurs for a point on fault 7 near the top boundary of the reservoir. The reactivation tendency factors for the segments of fault located in the surrounding rock are negligible (less than .02), which suggests that there is no reactivation potential for fault 7 in this region.

144

To illustrate the mechanism of reactivation for both production and injection scenarios for fault 7, the ambient stress state and the induced stress states in these two cases, for a point at mid-height in the reservoir, are projected in a Mohr coordinate system (see Figure 6.5). Figure 6.5b shows that production, as predicted in Figure 4.15, accentuates the existing normal fault stress regime (Figure 6.5a) and moves the stress state on the fault surface towards the failure criterion. Figure 6.5c shows that, during injection, fault reactivation is only possible if the failure occurs in a thrust fault stress regime. This means that, during the earlier stages of injection (i.e., up to $\Delta P \cong 14$ MPa), the stress regime becomes more isotropic. This gives rise to a reduced likelihood of fault reactivation (i.e., stabilization). Conversely, for $\Delta P > 14$ MPa, the stress regime switches from normal to thrust fault. Beyond this transition point, further increases in pressure increases the tendency towards fault reactivation – in theory, at least (Figure 6.5c). It is significant to note that, at these elevated pressures, the magnitude of the normal effective stress on the fault surface is very small (0.2 to 1.2 *MPa*), hence the potential for tensile failure becomes high. This specific scenario is referred to as a pseudo-tensile failure mode by this author which, in fact, represents a specific type of shear failure mode.

Following a similar procedure to fault 7 for all faults in the field, it has been determined that none of the faults are at risk of reactivation when they are located in the surrounding rock. However, within the reservoir, fault 7 is the only one which – within reasonable bounds of pressure change - can be reactivated during production. During injection, in addition to fault 7, those segments of faults 4, 6 and 10 which are located within the reservoir tend towards reactivation. The amounts of critical pressure change for these faults are almost the same as for fault 7; i.e., roughly 33% of ambient reservoir pressure ($\cong 16$ *MPa*). This equivalency of critical pressure change can be understood by realizing that the mechanism of reactivation for all these faults follows a pseudo-tensile failure mode.

To summarize, the results of this analysis show that, without considering any margin of safety, fault reactivation is predicted when the reservoir pressure is decreased by 38 MPa or increased by 16 MPa.
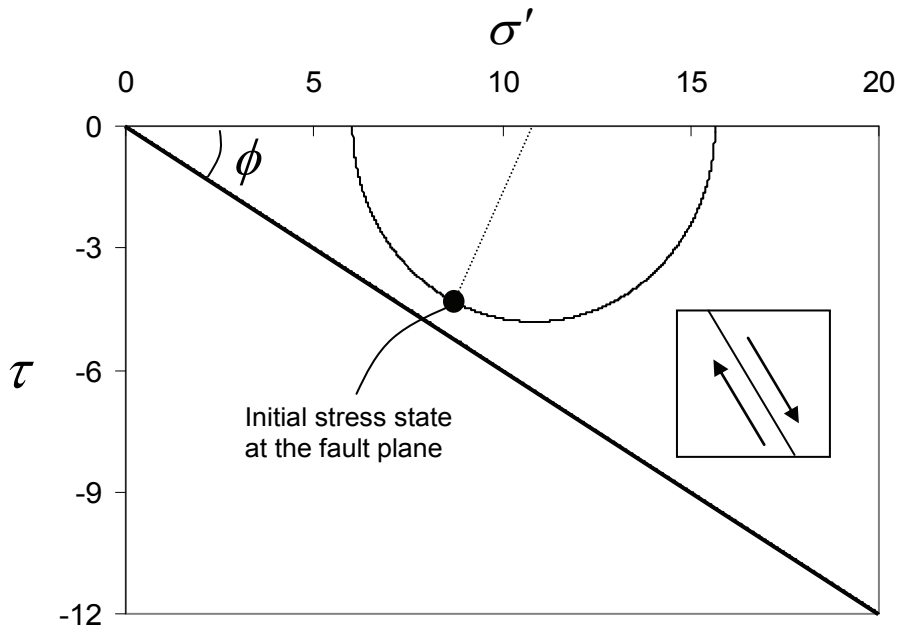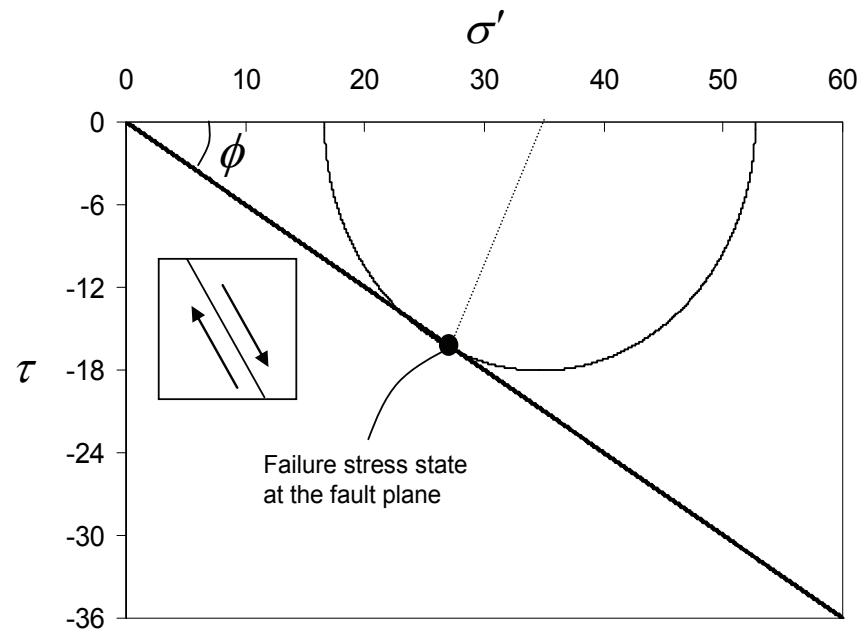
Figure 6.5. Mohr circles corresponding to stress state in a point on fault 7 located in the middle of the reservoir: (a) initial stress state; (b) stress state at the time of failure during production; and (c) stress state at the time of failure during injection.

(c)
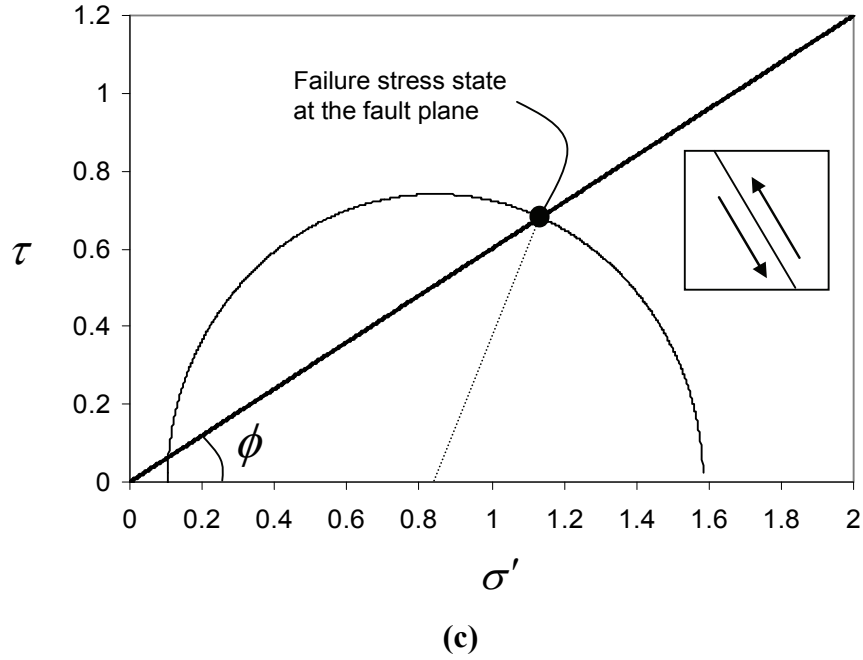
Figure 6.5. (Continued) Mohr circles corresponding to stress state in a point on fault 7 located in the middle of the reservoir: (a) initial stress state; (b) stress state at the time of failure during production; and (c) stress state at the time of failure during injection.

6.2.4. Sensitivity analysis

One useful application of the methodology described in section 4.6.1 is to study the sensitivity of critical pressure change to important parameters which are often poorly constrained; a notable example being the coefficient of friction (μ_s). The objective of this sensitivity analysis is to show the effect of varying the friction coefficient on the critical pressure change for reactivation of fault 7 in the middle part of the reservoir. Mechanistically, with respect to the initial stress state, the value of the friction coefficient cannot be smaller than the boundary value of μ_{s0}, stated as:

$$\left| \frac{\tau_{s0}}{\sigma'_{n0}} \right| \leq \mu_{s0} \tag{6.1}$$

where τ_{s0} and σ'_{n0}, respectively, are ambient shear and normal effective stresses resolved on the fault surface plane. At the point of interest, μ_{s0} is calculated as 0.5. Thus, a range of $0.5 < \mu_s < 1.0$ was considered in this sensitivity analysis.

Figure 6.6 demonstrates the results of this analysis. For $0.5 < \mu_s < 0.65$, reactivation is possible in either cases of production or injection, while for $\mu_s > 0.65$, it is only possible during injection. For values of μ_s more than 0.6, the critical pressure change for reactivation during production is too high to be practical. Also, this figure shows that, for the entire range of change in μ_s, the critical pressure change during injection is roughly constant.

The mechanisms leading to these results can be interpreted by the methodology proposed in section 4.7.1 for fault reactivation tendency analysis within reservoirs. According to this methodology, when shear stress is negligibly small, the mechanics of fault reactivation can be depicted graphically in a coordinate system with effective vertical stress (σ'_V) on the x-axis and effective horizontal stress (σ'_H) on the y-axis (Figure 6.7). In such a coordinate system, for a fault with dip angle of θ, a cohesionless Coulomb failure criterion can be displayed as a straight line with a slope of R_θ.
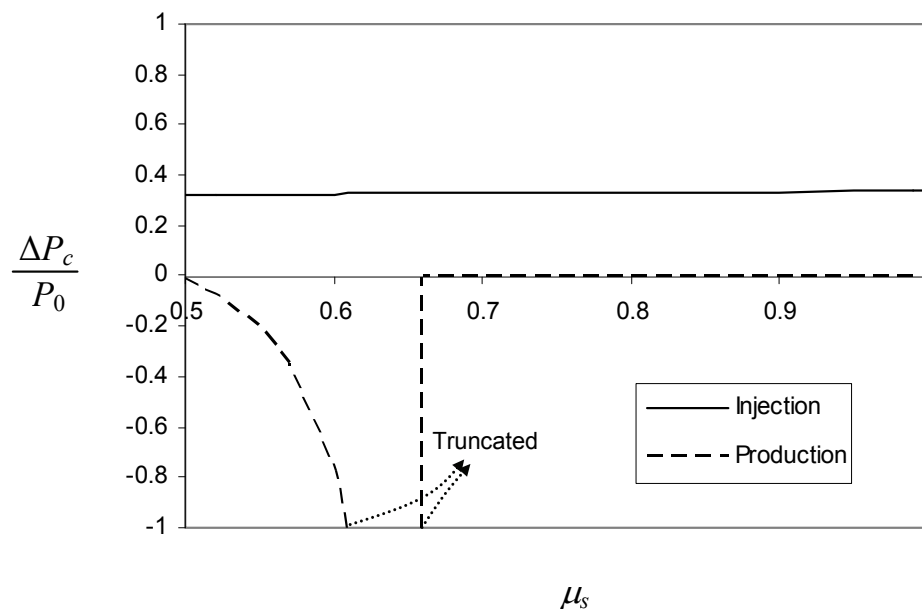
Figure 6.6. Variation of critical pressure versus friction coefficient at a point on fault 7 located in the middle of the reservoir.
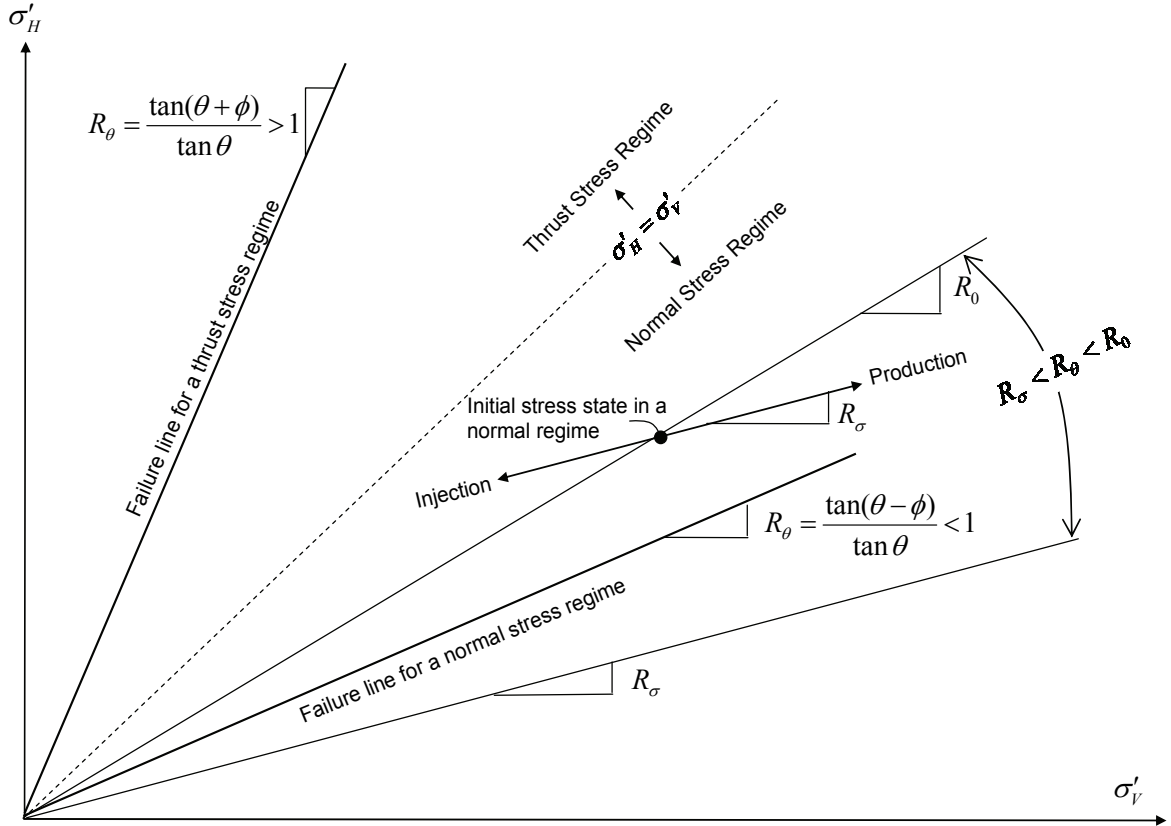
Figure 6.7. Portrayal of different plausible reactivation paths during injection and production for a normal stress regime in a σ'_H-σ'_V coordinate system.

The evolution of the stress state in a σ'_H- σ'_V coordinate system can be expressed using the stress path ratio (R_σ) in equation (4.7), and the initial stress slope (R_0) which is defined as follows:

$$R_0 = \frac{\sigma'_{H0}}{\sigma'_{V0}} = \frac{K_0 - \lambda_p}{1 - \lambda_p} \tag{6.2}$$

where $\Delta\sigma'_H$ and $\Delta\sigma'_V$, respectively, are horizontal and vertical effective stress changes.

Apparently, it is not mechanically acceptable to have $R_\theta > R_0$, which indicates an over-failure condition (Figure 6.7). Therefore, the inequality $R_\theta \leq R_0$ must always hold true. [Note: This is merely a re-statement of the inequality expressed in equation (6.1).] Figure 6.7 also demonstrates that, for a normal fault stress regime, only when R_θ is

smaller that R_σ is production potentially able to reactivate a fault. These conditions, in combination, state that production is likely to reactivate a fault within a reservoir only if $R_0 < R_\theta < R_\sigma$.

Regarding the fact that, for the problem under investigation, shear stress change at the point of interest is negligible (i.e., $\gamma_{\alpha(HV)}$=-0.001), the described methodology can be efficiently applied for interpretation of the sensitivity analysis results in Figure 6.8. To do so, the stress state of the point of interest (σ'_{H0}=15.7; σ'_{V0}=6) is projected in a σ'_{H}-σ'_{V} coordinate system (Figure 6.8). The initial stress slope (R_0) corresponding to this initial stress state is 0.38, and the stress path ratio (R_σ) for this point is found using equation (4.7) as 0.29 (by knowing $\gamma_{\alpha(H)}$= 0.72 and $\gamma_{\alpha(V)}$= 0.015).

Based on the rationale presented above, fault reactivation during production is only likely if $0.29 < R_\sigma < 0.38$. Using equation (4.7), this corresponds to $0.5 < \mu_s < 0.65$, which is consistent with the sensitivity analysis results shown in Figure 6.6. Figure 6.8 also explains why a very high pressure change is required as the friction coefficient approaches 0.65. In fact, in this case, the failure line (i.e., R_θ) becomes more parallel to the stress change path (i.e., R_σ), and crossover of these two lines requires an exceedingly high magnitude of reservoir pressure change during production.

Figure 6.8 shows that, during injection, for values of $\mu_s > 0.5$, fault reactivation only occurs in a thrust fault stress regime and obviously the critical pressure change for fault reactivation does not significantly changes as μ_s increases. This is consistent with the results of the sensitivity analysis presented in Figure 6.6. In fact, as mentioned before, in this condition the normal stress on the fault surface is very small and fault reactivation occurs in a pseudo-tensile mode. So, as expected from a tensile mode, the critical pressure change is not essentially affected by friction coefficient (μ_s).
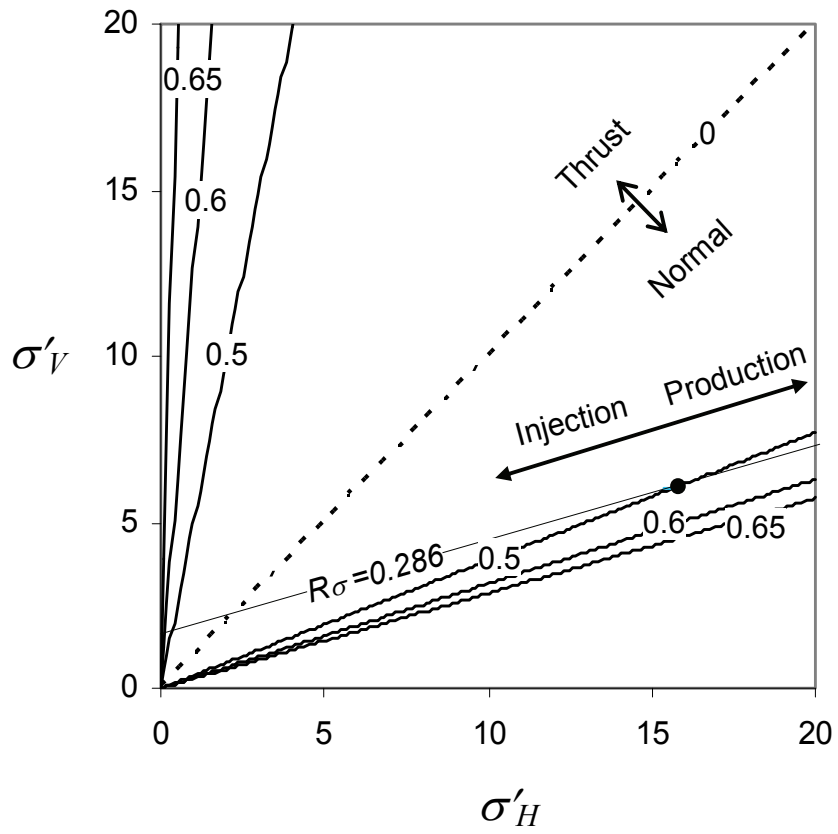
Figure 6.8. Portrayal of different plausible reactivation paths during injection and production for a point on fault 7 located in the middle of the reservoir. The values shown on the graphs are coefficient of friction (μ_s).

6.3. Studying general patterns of stress evolution, fracturing using a synthetic case study

This synthetic case study considers a field containing a reservoir of rectangular cross-section, having a depth (to the reservoir top) of 3 km, a width of 6 km, and a thickness of 300 m embedded in rock possessing the same material properties as the reservoir. The homogeneous isotropic rock of the field has a Poisson's ratio (v) of 0.2 and a specific gravity (G_s) of 2.05. Pore pressure is considered to be hydrostatic outside of the reservoir, and an over-pressuring ratio (λ_p) of 0.756 is considered for the reservoir. The Biot's coefficient is considered to be 1.0. The objective is to study patterns of evolution in in-situ stresses, and new fractures induced by reservoir pressure change in the entire field for both normal and thrust stress regimes with the lateral pressure coefficient (K_0) of 0.85 and 1.1, respectively.

6.3.1. Induced deformation and stress change analysis

A plane strain solution based on the theory of inclusions (see section 3.5.2) was used to calculate deformations and stresses in a homogeneous, linear elastic field embedding the porous reservoir described above. The output is shown in Figures 6.9 and 6.10. Figures 6.9a and 6.9b, respectively, show contour maps of horizontal and vertical deformations. Figure 6.9c shows the pattern of deformation in the field. Figure 6.9d demonstrates the ground surface horizontal and vertical deformations.

As shown in Figure 6.9, horizontal deformation is towards the central axis and vertical deformation is downward (subsiding) in the entire field during production. The surrounding rock can be roughly divided in two main regions: a central deformation region where, during production, the horizontal deformation is compressive and vertical deformation is tensile; and a peripheral deformation region where, during production, horizontal deformation is tensile and vertical deformation is compressive. Behavior of the field is exactly opposite during injection. Figure 6.9d shows that, on the ground surface,
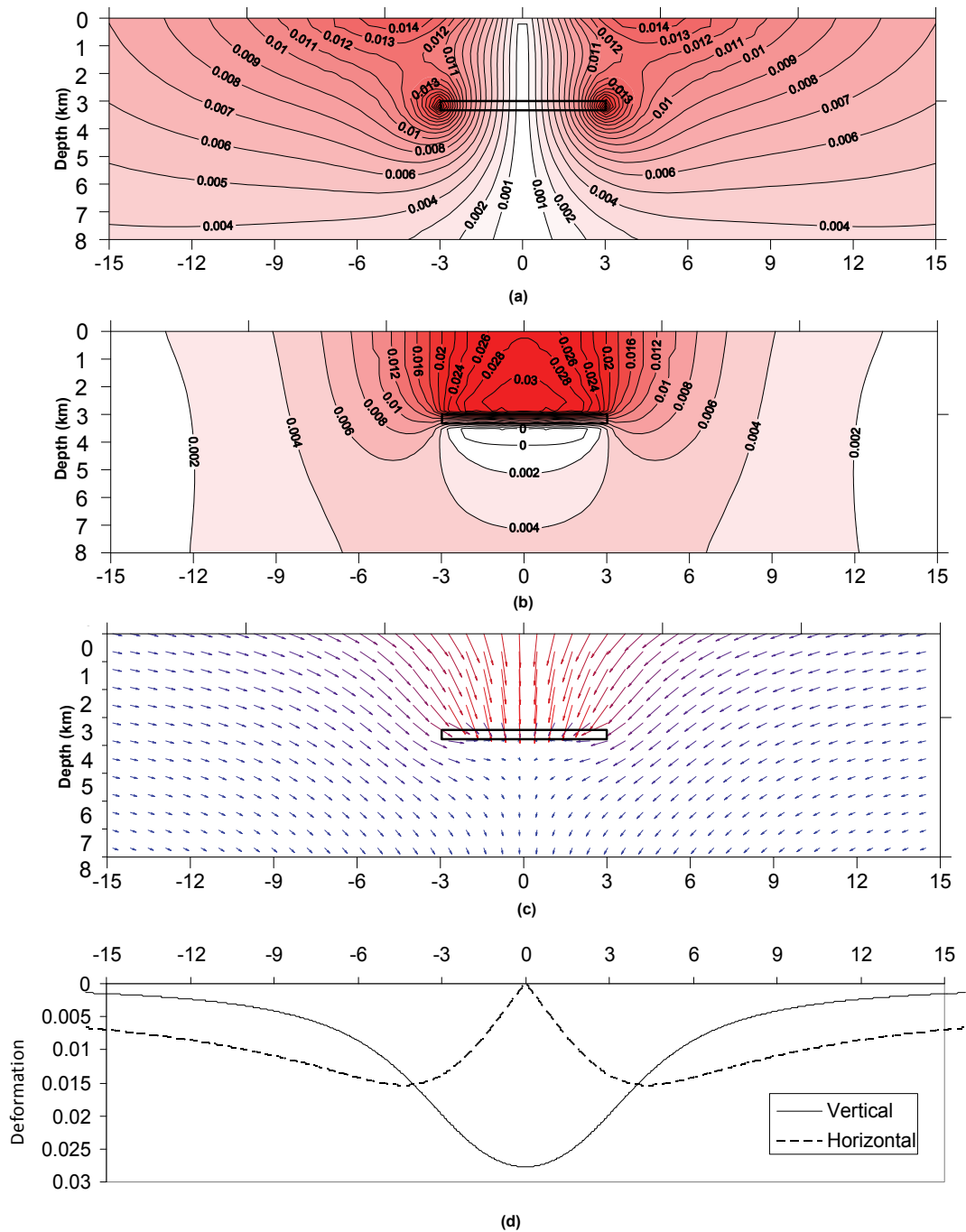
Figure 6.9. Results of deformation analysis for a rectangular reservoir with depth of 3 km, thickness of 300 m and width of 6 km. (a) Contour plots of horizontal deformation. Positive values of denote deformation towards the centre. (b) Contour plots of vertical deformation. Positive values denote deformation in a downward direction. (c) Vector map of deformation during production. Vectors directions would be reversed during injection. (d) Ground surface horizontal and vertical deformations. All values of deformations in these figures are normalized by $[\alpha\Delta P(1-2\nu)]/[\mu(1-\nu)]$, where μ is the shear modulus, ν is the Poisson's ratio of the field, α is Biot's coefficient, and ΔP is reservoir pressure change (positive during injection and negative during production).

maximum vertical deformation occurs above the centre of reservoir and maximum horizontal deformation occurs above the neighboring parts of the reservoir flanks (about 1.5 km beyond the reservoir sides). These results are qualitatively in agreement with field observations as Wilmington oil field, Texas Buena Vista and Inglewood oil fields in California (Yerkes and Castle, 1970).

Figures 6.10a-c show the results of induced stress change analysis for the same problem. These figures, respectively, show horizontal, vertical, and shear normalized stress arching ratios (i.e., $\gamma_{\alpha(H)}$, $\gamma_{\alpha(V)}$, and $\gamma_{\alpha(HV)}$). Figures 6.10a-b show that, similar to the deformation analysis presented in Figure 6.9, central and peripheral regions are recognizable for induced horizontal and vertical stress changes (i.e., respectively, $\Delta\sigma_H$ and $\Delta\sigma_V$). Figure 6.10c shows that shear stress change ($\Delta\sigma_{HV}$) is mainly concentrated on the edges of the reservoir.

6.3.2. Patterns of evolution in orientation and magnitude of in-situ stresses

In most studies on stress evolution during reservoir pressure change the focus has been on recognizing patterns and magnitudes of induced stress change in the field and there has been a less attention to deviation in orientation and magnitude of the in-situ stresses as a result of reservoir pressure change. In this work, to study the patterns of in-situ stress change during reservoir pressure change, the initial in-situ vertical and horizontal stresses were assumed to be principal stress components. Further, the stress regimes considered were normal fault (i.e., extensional) and thrust fault (i.e., compressive).

An example of in-situ stress evolution is shown in Figures 6.11a-d by considering $K_0=0.85$ (i.e., a normal stress regime), a hydrostatic pore pressure distribution in the surrounding rock (i.e., $\lambda_p=1/G_s=0.488$), and an over-pressured zone within the reservoir (i.e., $\lambda_p=0.756$). These figures show the evolution in orientation and magnitude of the maximum principal stress (σ_1) during the gradual depletion of the reservoir when the reservoir pressure change (ΔP) becomes, respectively, 25%, 50%, 75% and 100% of the average ambient reservoir pressure (i.e., P_0). Figures 6.11a-d

154

show that, during production from the reservoir, stress orientations within the reservoir and in the far sideburdens (where the shear stress is negligible, see Figure 6.10c) are unchanged, and the initial normal stress regime becomes accentuated (see Figures 6.10a-b).
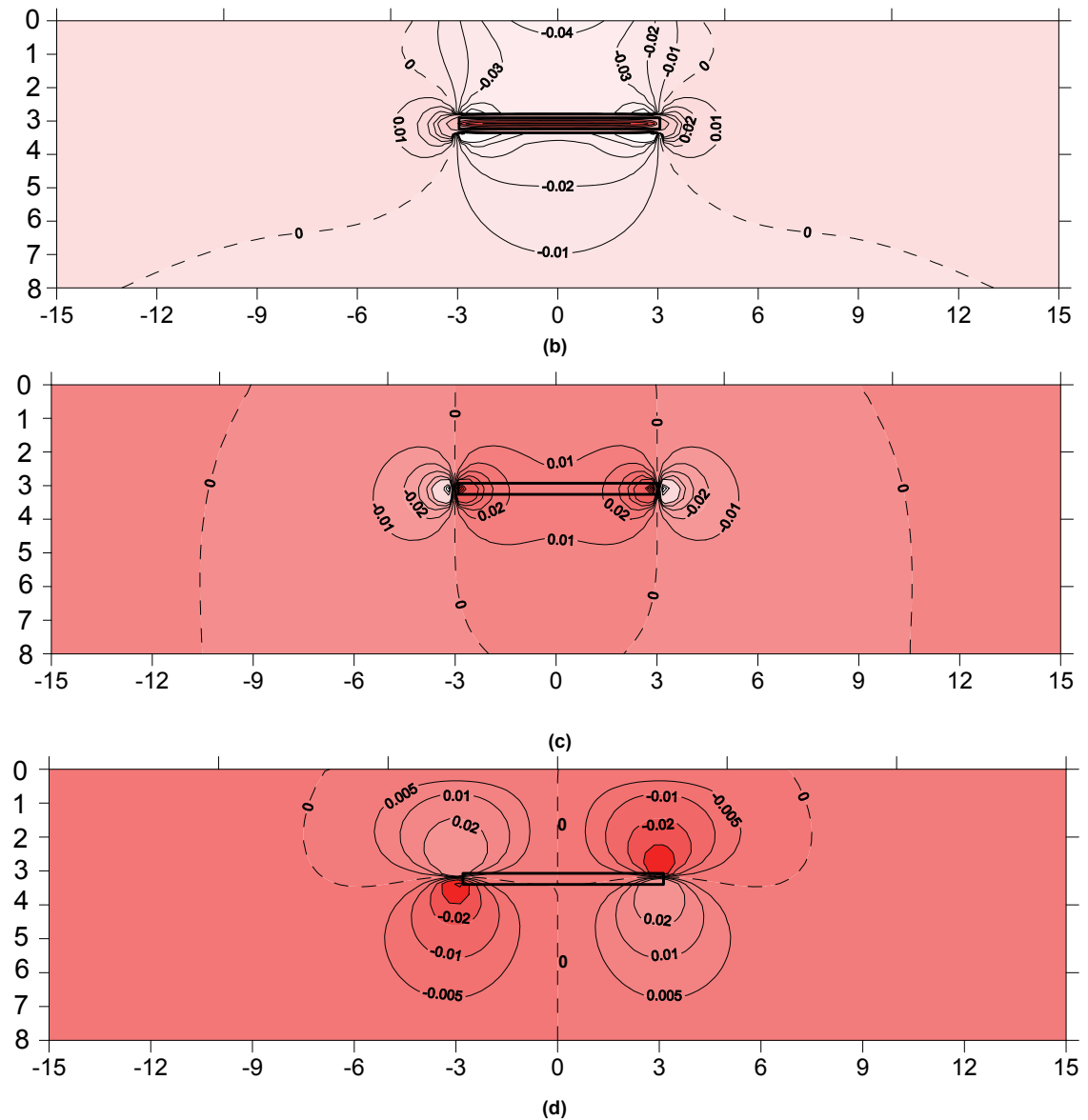
Figure 6.10. Contour maps for normalized stress arching ratios for a rectangular reservoir with the same geometry as the reservoir analyzed in Figure 1. (a) Normalized horizontal stress arching ratios ($\gamma_{\alpha(H)}$); (b) Normalized vertical stress arching ratios ($\gamma_{\alpha(V)}$); and (c) Normalized shear stress arching ratios ($\gamma_{\alpha(HV)}$). All values are normalized by $(1-2\nu)/(1-\nu)$. Horizontal and vertical scales are labeled in km.
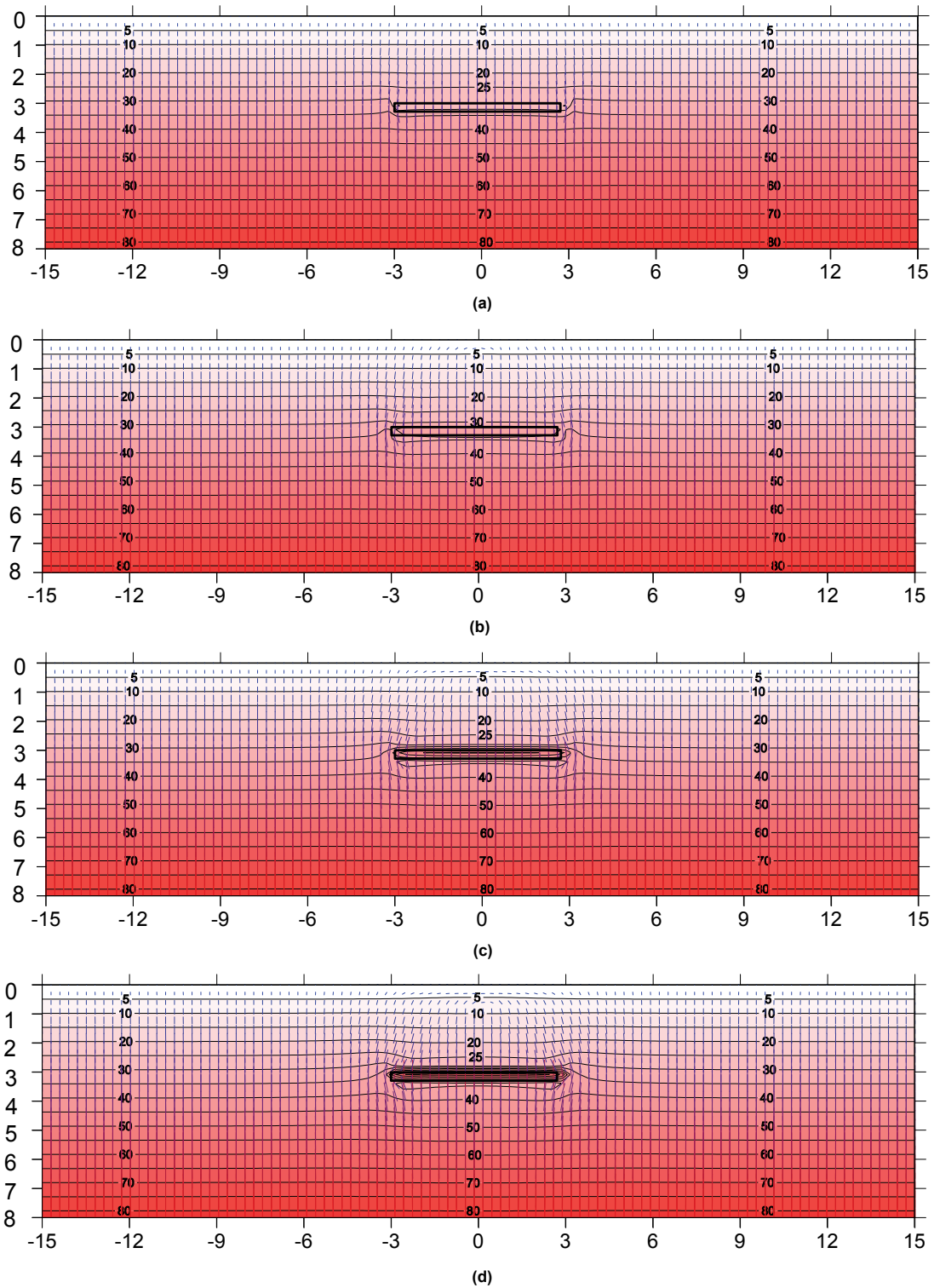
Figure 6.11. Results of stress evolution analysis (i.e., change in maximum principal stress magnitude and orientation) during production from a reservoir with an initially normal fault stress regime ($K_0 = 0.85$). (a) Initial stress state. Stress state after a reservoir pressure change (ΔP) of: (b) 25% of P_0; (c) 50% of P_0; (d) 75% of P_0; and (e) 100% of P_0. Horizontal and vertical scales are labeled in km.

156

In the overburden and underburden, the changes in stress orientation start from the corners of the reservoir (where shear stresses are maximum), and propagate upward and downward (almost along the boundary of the central deformation region) and laterally. The lateral spreading of the region of stress orientation change is mainly towards the central deformation region, where the initial normal fault stress regime is gradually changing to a thrust fault stress regime as a result of production induced stress changes which increase the horizontal in-situ stress and decrease the vertical in-situ stress (see Figures 6.10a-b). The stress orientation changes in the shallow overburden are greater due to the small magnitude of the in-situ stresses compared to the deeper overburden and underburden.

Figure 6.12a shows the result of stress evolution analysis of the same reservoir for the analogous case of injection within the reservoir while the increase in the reservoir pressure is 100% of the initial reservoir pressure. This figure shows that the general pattern of stress propagation might be explained in a similar manner as the case of production, by noticing that the lateral direction of propagation is mainly towards the sideburdens where the induced stresses intend to change the existing normal stress regime to a thrust fault stress regime (see Figure 6.10a-b). However, in the central part of the overburden and underburden, where injection accentuates the existing normal stress regime (see Figure 6.10a-b), stress orientation remains unchanged. Within the reservoir the initial stress regime changes from a normal fault stress regime to a thrust fault stress regime. Figures 6.12b and 6.12c show the results of the same analysis for a field with a thrust fault stress regime, respectively, during production and injection which can be interpreted in a very similar manner.

Assessment of all these different cases leads to a generalized pattern to predict and analyse the evolution of principal stress orientations and magnitudes in rocks surrounding a reservoir for different scenarios of initial stress regime and reservoir pressure change. A simple conceptual model (referred to in this work as a 'cavity pattern') is able to explain the stress evolution around a reservoir by analogy to stress change around a cavity (e.g., a prism in a plane strain scenario) during injection. Based on this model, during injection, the in-situ stress state in the surrounding rock tends to
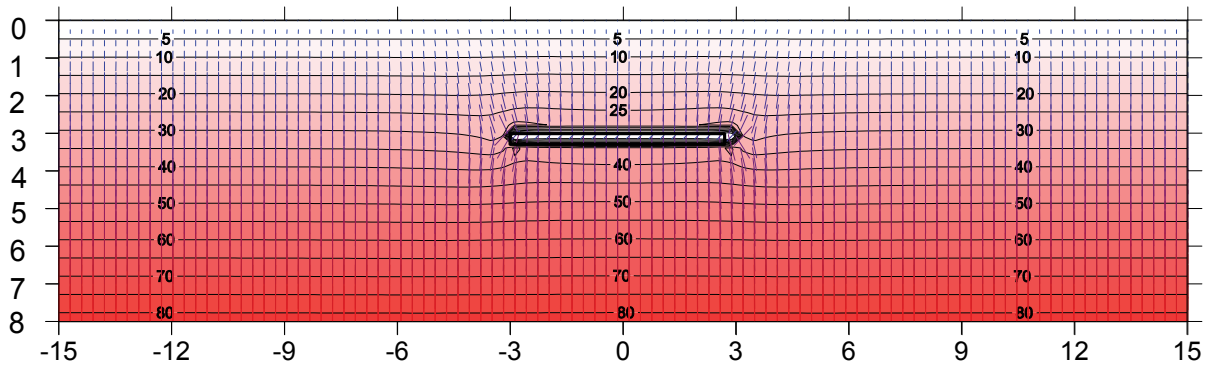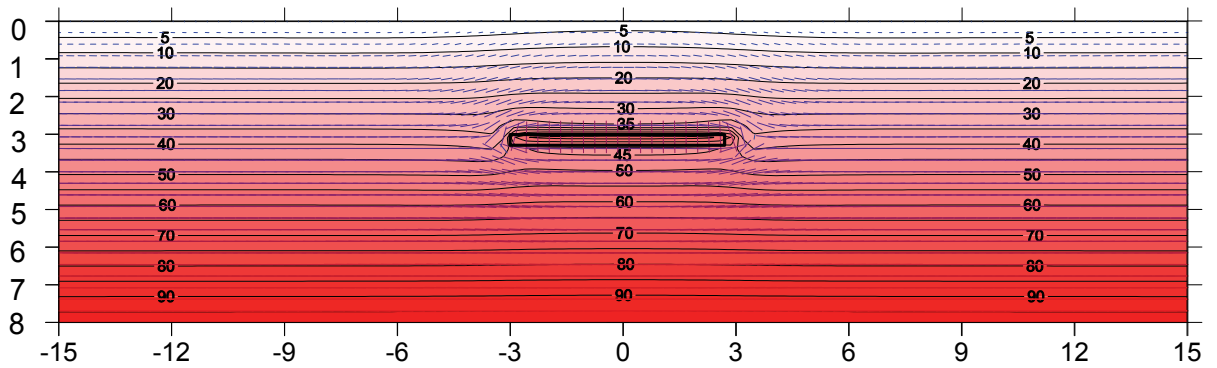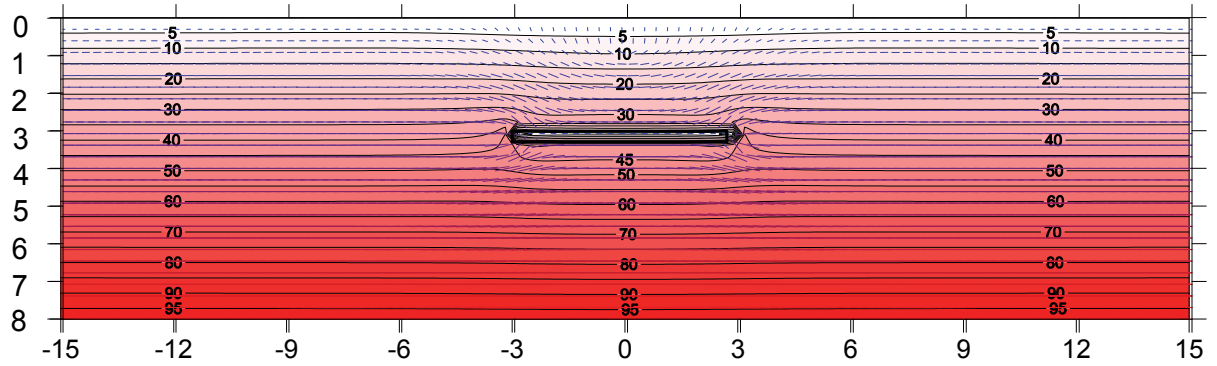
Figure 6.12. Results of stress evolution analysis (i.e., change in maximum principal stress magnitude and orientation) after reservoir pressure change (ΔP) of 100% of P_0: (a) During injection within a reservoir of initially normal fault stress regime ($K_0 = 0.85$); (b) During production from a reservoir of initially thrust fault stress regime ($K_0 = 1.1$); and (c) During injection in a reservoir of initially thrust fault stress regime ($K_0 = 1.1$).

evolve in magnitude and orientation to form a new stress state in which the maximum principal stresses become radially distributed around the cavity. For the analogous case of production, the in-situ stress state evolves in such a way that the maximum principal stress becomes tangential to the cavity surface. Later in this section, a very final stage of

158

such a stress evolution will be shown when the reservoir pressure change is high enough to bring the rock to its critical state.

6.3.3. Patterns of induced fracturing observed in hydrocarbon fields and physical models

Patterns of fracturing in hydrocarbon fields may be studied using field and experimental observations. These different sets of data can be integrated to determine a general pattern for induced fracturing/faulting in a field during reservoir pressure change. The developed patterns can be used to evaluate the results of mathematical models. In this section, the following sets of information have been used to study such patterns: surface and subsurface monitoring of faulting and fracturing, recordings of wellbore failure, and experimental modeling of fracturing/faulting. Following, these data are studied in details.

Induced fracturing/faulting has been observed in several production sites. Evidence of production-induced fracturing and faulting can be classified in four categories with respect to the fault type and location: The first category includes high-angle normal faults down dipping towards the reservoir which have been observed on the surficial parts of the peripheral deformation region (the so called 'periphery of subsidence bowl') during hydrocarbon production from the Wilmington oil field in Long Beach, California, Goose Creek and Mykawa oil fields in Texas, Inglewood and Kern Frent oil fields in California and during Frasch-process extraction of sulfur in the Texas Gulf Coast (Yerkes and Castle, 1970). The second category includes low-angle thrust faults in the central deformation region in the caprcock as observed in the Wilmington oil field, California (Dusseault et al., 2001), and the Buena Vista oil field in California (Yerkes and Castle, 1970; Segall, 1989). The third category includes high-angle thrust (reverse) faults within the central deformation region as observed during production from the Lacq gas reservoir in France (Feignier and Grasso, 1999). The fourth category includes low-angle thrust fault reactivation in the underburden, as observed immediately below the Strachan reservoir in Alberta, Canada (Wetmiller, 1986).

In general, casing shear is more common on the shoulders of the structure and it is more intense near the reservoir. For example, in the Ekofisk oil field, the concentration of well failures occurred 160m above the reservoir top (Dusseault et al., 2001). The vast majority of well damage at Wilmington was related to bedding-plane slip and low-angle faulting in the central deformation region and near the shoulders of the reservoir (Dusseault et al., 2001).

Experimental studies conducted by Odonne et al. (1999) and Papamichos et al. (2001) identified very useful information on fracturing in the surrounding rock during production. Odonne et al. (1999) experimentally modeled reservoir depletion using two different models: by deflation of a balloon, and by pumping air from an under-compacted ground sand volume. Results obtained using these two methods are shown in Figures 6.13a and 6.13b. Papamichos et al. (2001) used a trap door mechanism to investigate the problem of production from the reservoir as shown in Figure 6.13c. In all three of these experiments, a cohesionless sand with a coefficient of internal friction of 0.6 was used as the surrounding material. Different colouring agents were added to this sand to define the layers visible in Figures 6.13 to 6.14, in order to facilitate the identification of offsets along the induced fault surfaces. As shown in Figures 6.13a to 6.13c, the results of these three experiments are similar: shear failure slip lines form a cone-shaped volume which starts with steep slopes (about 70 °- 90°) from the reservoir boundaries and continues towards the surface while its slope reduces (about 30°).

6.3.4. Patterns of fracturing observed in mathematical modeling

Patterns of fracturing within a field may be studied using the mathematical approach developed in section 5.3.1. For this purpose, the rock in the field was considered to be cohesionless with a coefficient of internal friction of 0.6, similar to experimental modeling conducted by Odonne et al. (1999) and Papamichos et al. (2001). It is important to note that, due to the lack of cohesion, the dominant mode of fracturing is shear failure and no tensile failure is plausible. [It should be noted, however, that in a real field case with cohesive rock, during injection, especially within the reservoir, tensile fractures are likely to occur] Using this method, the critical pressure change for
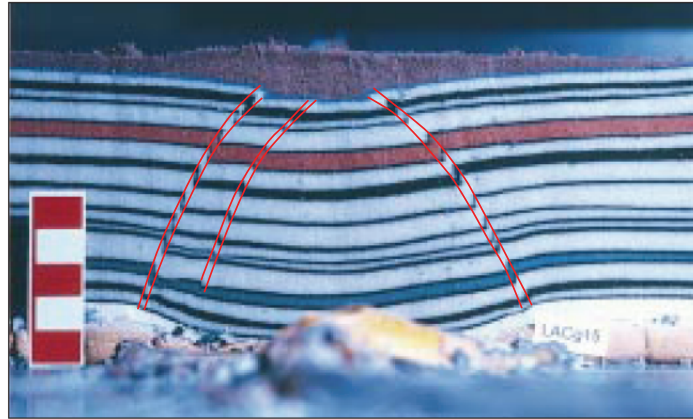
(a)
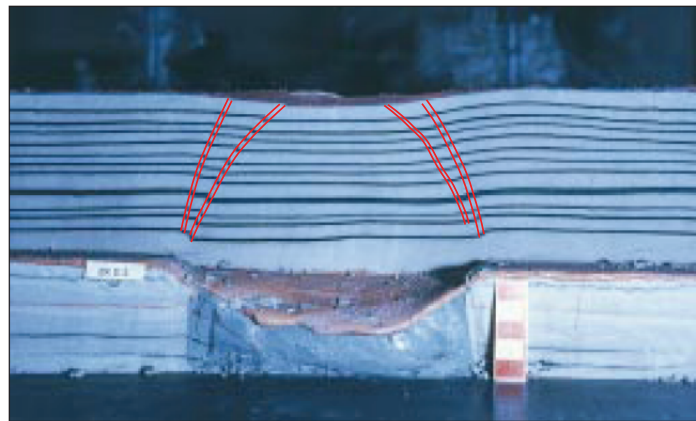
(b)
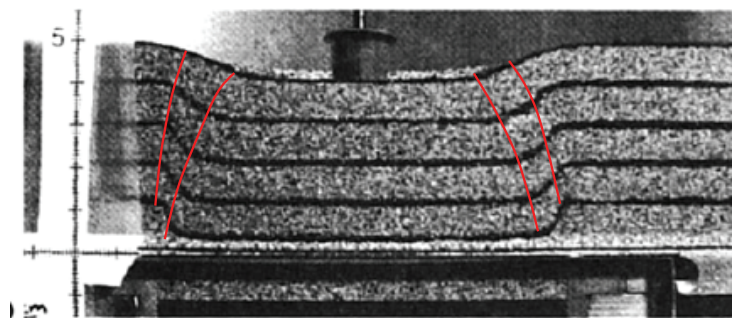
(c)

Figure 6.13. Depiction of slip-lines in experimental tests for modeling induced fracturing: (a) Reservoir has been modeled by a deflated balloon (after Odonne et al., 1999); (b) Reservoir has been modeled by pumping from under-compacted ground sand volum (after Odonne et al., 1999); and (c) reservoir has been modeled by a trap-door (after Papamichos et al., 2001)

fracturing can be determined in the entire field by using only equation (5.10). As with all of the induced fracturing analyses presented in this thesis, the effects of localized fracture displacements on the post-fracturing evolution of stress and strain fields is not considered.

Figures 6.14a-6.14d show the results of critical pressure change analysis and directions of slip lines for two different cases of normal fault stress regime (i.e., K_0=0.85) and thrust stress regime (i.e., $K_0 = 1.1$) during production and injection. In these figures, values of critical pressure change have been normalized by the average ambient reservoir pressure ($P_{0(reservoir)}$). Obviously, pressure changes with a magnitude more than this value are not practically possible during production from a real field case. In addition, it can be claimed that during injection this value might be an approximate upper-bound for reservoir pressure change to avoid tensile fractures. Therefore, the values based on these limitations have been shown in color. [Note, however, that for experiments conducted by Odonne et al. (1999) and Papamichos et al. (2001), due to considering a different mechanical system instead of a reservoir, which allows more deformation in the surrounding rock, failure might occur in conditions which are equivalent to higher pressure changes as shown with uncolored contours in Figure 6.14.]

Figures 6.14a and 6.14b demonstrate the critical pressure change during productionfor normal and thrust stress regimes, respectively. The patterns of fracturing in both cases are very similar. The only difference is the magnitude of critical pressure change for fracturing which varies depending on the initial magnitude of in-situ stresses. For example, induced fracturing in the surfacial part of the central deformation region is more plausible in a thrust fault stress regime than the case of a normal fault stress regime. This occurs because the initial value of the horizontal stress is larger than the vertical stress in the former case. In the latter case, it must first increase to the point where it exceeds the vertical stress before further pressure change migrates the stress state towards the critical state. These figures show that a less sensitive region forms in the overburden immediately above the reservoir and under it. In general, based on these figures, during production, there are four recognizable regions with high sensitivity to fracturing:
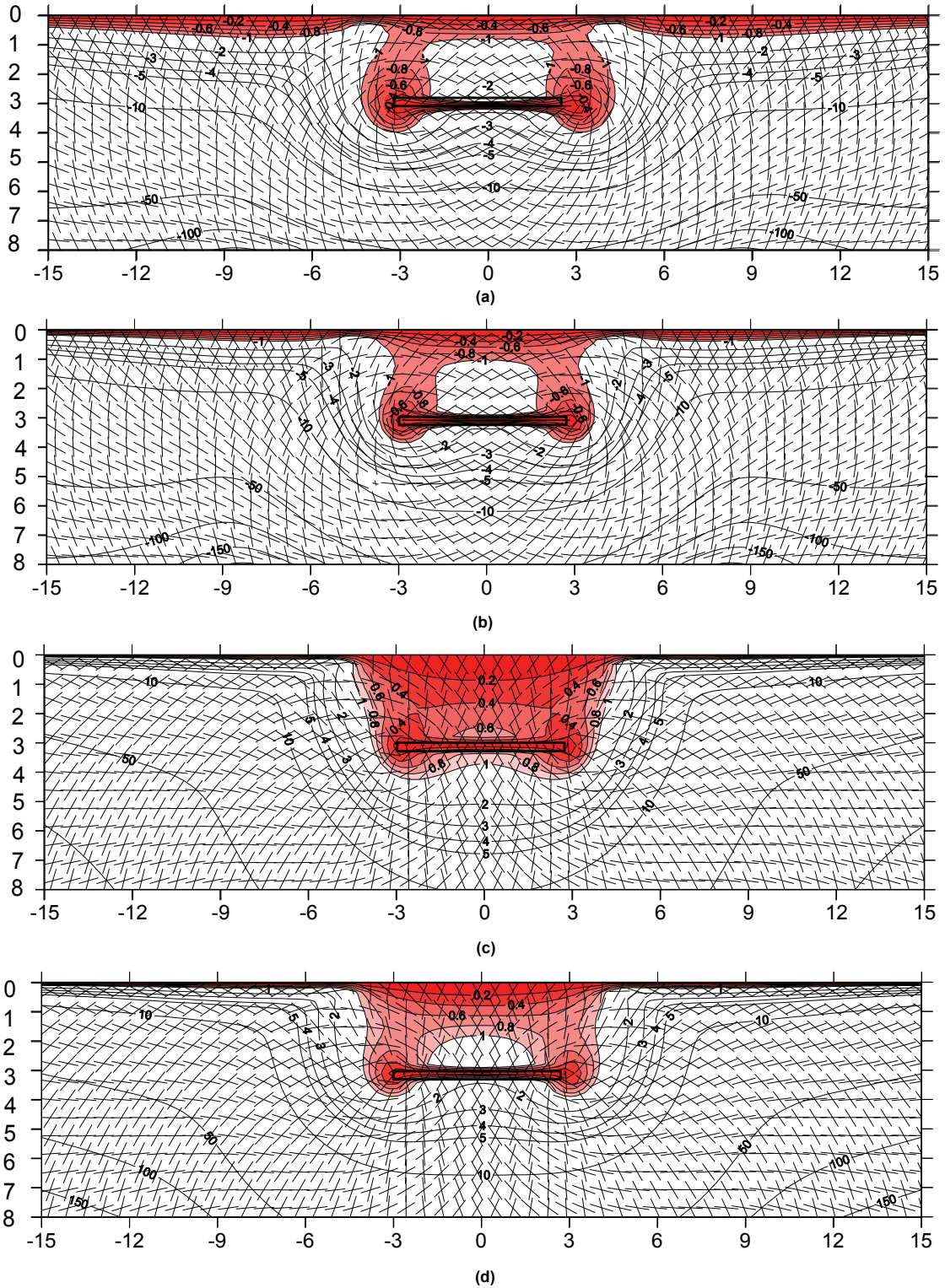
Figure 6.14. Contour map of critical pressure change and slip-line orientation for: (a) Production from a reservoir with an initially normal fault stress regime; (b) Production from a reservoir with an initially thrust fault stress regime; (c) Injection in a reservoir with an initially normal fault stress regime; and (d) Injection from a reservoir with an initially thrust fault stress regime.

163

1) Bubble–shaped regions located above the flanks and shoulders of the reservoir and around the zero-strain line (see Figure 6.9). The spatial extents of this region explain the occurrence of wellbore failures locations during production (e.g., Ekofisk and Wilmington oil fields (Dusseault et al., 2001)). The orientation of shear slip-lines in this region shows that the formation of slip lines (i.e., fracturing or faulting) starts from the corners of the reservoir with a high angle, and with increasing pressure depletion it grows upwards towards the surface while its slope decreases. This behavior is consistent with the experimental observations of induced fractures by Odonne et al. (1999) and Papamichos et al. (2001) (see Figures 6.13a-c), which shows that cone-shaped sliding volumes form above the reservoir during production.

2) Ground surface in the central deformation region where low-angle slip-lines form in a thrust fault stress regime. This pattern is very similar to field observation of thrust faults in Wilmington oil field in Wilmington oil field (Dusseault et al., 2001), Buena Vista oil field in California (Yerkes and Castle, 1970 and Segall, 1989);

3) Ground surface in the peripheral deformation region where high-angle slip-lines form in a normal stress regime. This pattern is similar to field observations in Wilmington oil field in Long Beach, California, Goose Creek and Mykawa oil fields in Texas, Inglewood and Kern Frent oil fields in California and in a sulfur field in Texas Gulf Coast (Yerkes and Castle, 1970);

4) Underburden, near the reservoir shoulders and flanks, where low-angle slip-lines form. This pattern was observed immediately below the Strachan reservoir in Alberta, Canada (Wetmiller, 1986).

These facts show that the results of the proposed methodology are consistent with the field and experimental observation of induced fracturing-faulting during production. These might be questioned from a practical perspective they do consider the effect of induced fracturing at any point on the subsequent stress state evolution and consequently on the critical pressure change in other points of the field. However, the

correlation between the field and experimental observations show that this methodology can be used with reasonable confidence to model stress evolution and induced stress change in a field, though its accuracy would be expected to diminish with increasing inelastic deformation.

Figures 6.14c and 6.14d demonstrate the patterns of fracturing for the analogous case of injection within the reservoir when the initial stress state is, respectively, a normal fault stress regime (K_0=0.85) and a thrust fault stress regime (K_0=1.1). These results show that the regions with high sensitivity to fracturing are: the central deformation region in the overburden where high-angle slip-lines form, and a region immediately below the reservoir where similarly normal high-angle slip-lines form. In the critical state, a normal fault stress regime forms in both regions, hence the case of initially normal fault stress regime is much more sensitive to pore pressure increase within the reservoir. From these figures, close to the flanks of the reservoir, where there is high sensitivity to the reservoir pressure change, the slip-lines are almost vertical. This shows that during injection, potentially, a slipping cylinder forms around the reservoir which later joins the sub-vertical fractures formed near the surface. Figures 6.14c and 6.14d show that low-angle thrust fault slip-lines form in small regions close to flank in the side-burdens.

Figures 6.15a and 6.15b show the orientation of maximum principal stress (σ_1) during production and injection, respectively, when a hypothetical stress state is reached in which stresses are critical throughout the entire field (i.e., the pressure change is critical in every point of the field). These figures show the occurrence of the previously introduced concept of a 'cavity pattern for the in-situ stress evolution resulting from pore pressure change within the reservoir.
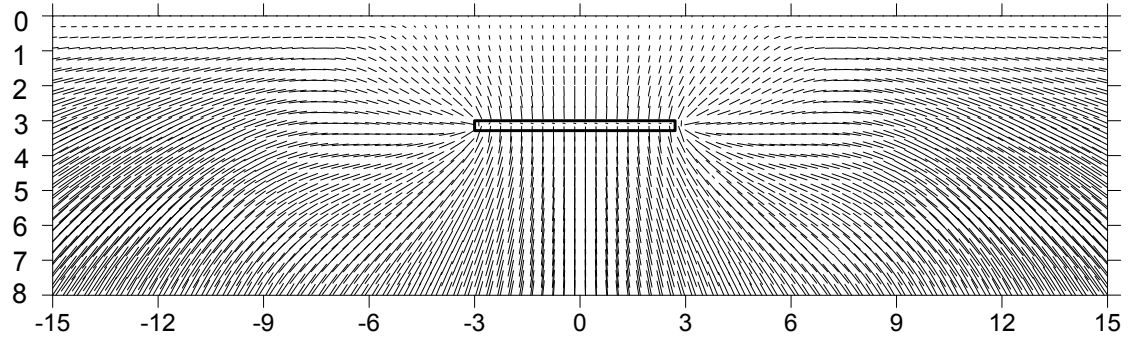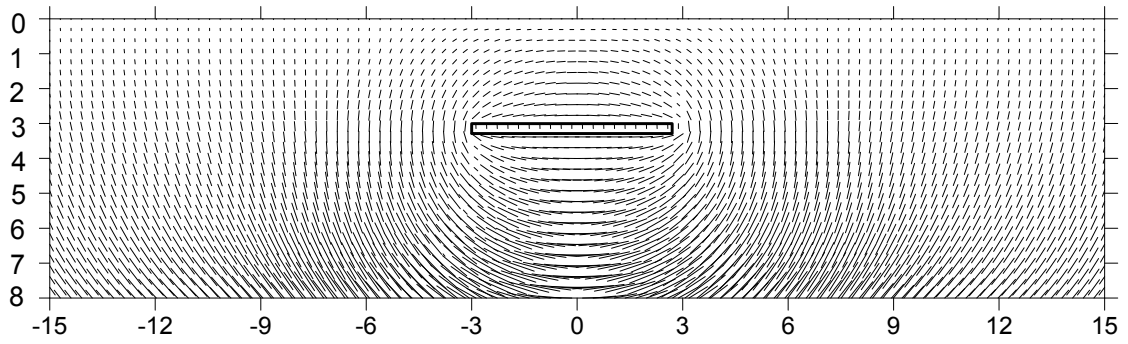
Figure 6.15. Direction of maximum principal stress when the entire field is in a critical state: (a) During injection; and (b) During production.

6.4. Fault reactivation analysis in the Lacq gas field, France

The Lacq gas field is located in the southwestern part of France. Fluid production started in 1959, and from 1969 to 2002 more than 1000 earthquakes (with magnitudes between 1 and 4.2) have been monitored (Bardainne et al., 2003). Before the onset of production neither historical nor instrumented monitoring program had revealed any seismic activity in this zone for several hundred years (Grasso and Wittlinger, 1990), and the nearest historical events were located on the North Pyrenean faults, some 30 km from the gas field (Lahaie and Grasso, 1999). In fact, the spatial distribution of these events in the region of the gas field is obviously different from regional seismicity observations (Feignier et al., 1990). It has been concluded that the events near the gas field are associated with reactivation of pre-existing faults and fractures (Guyoton et al., 1992). The objective of this case study is to determine the predicted reactivation tendencies of faults in this field, and to evaluate the developed methodologies for induced stress change and fault reactivation analyses this research by comparison to interpreted seismic event locations.

6.4.1. General characteristics of the reservoir

The depth of the gas field is from 3200 m to roughly 6000 m (Guyoton et al., 1992). The geological structure is an elongated dome, with its major axis in the northwest-southeast (120°N) direction (Feignier and Grasso, 1990). The gas-producing strata are within dolomitic sandstones and limestones of Portlandian to Barremian age. A 500 m thick, impermeable marly layer of lower Aptian age acts as the seal for the reservoir. A 2000 m thick Albo-Aptian calcareous reef lies above the marly layer. A small oil reservoir is located above this reef, and molassic Tertiary strata cap the oil field (Feignier and Grasso, 1990).

The gas reservoir consists of two zones. The upper zone level is made up of very low porosity (e.g., 0.1% to 6%) carbonate strata, while the lower zone consists of dolomites with porosities between 0.1 of 6%, decreasing to 0.1% at the base (Segall et al., 1994). The average porosity of the reservoir is 3.5% and its effective thickness is

between 250 to 450 m. Matrix permeability is very low throughout the reservoir, but a high density of natural fractures are present (Segall et al. 1994). As quoted by Segall et al. (1994), de Lanlay (1990) used numerical simulation and history matching to interpret reservoir permeabilities decreasing from 500 millidarcies near the crest of the structure to 0.035 millidarcies at the flanks (Note: an intrinsic permeability of 1 millidarcies is roughly equivalent to 1e-15 m^2 in S.I. units, which is roughly equivalent to hydraulic conductivity of 1e-8 m/s or 0.086 m/day).

6.4.2. In-situ stress state and pressure history

The present-day in-situ stress regime in the Lacq gas field is unclear (Segall et al., 1994). The results obtained using two different models for locating and characterizing seismic events have been contradictory. Using a velocity model interpreted by Grasso and Wittlinger (1990), the results are mainly consistent with a thrust fault stress regime. However, using a three-dimensional velocity model by Guyoton et al. (1992), interpreted focal points are significantly deeper and show different stress regimes for different periods of gas production from the field.

The initial gas pressure was 66 MPa at 3700 m depth below sea level in 1957, which indicates a highly overpressured state (Segall et al., 1994). During production, the pore pressure decreased to 7 MPa in 2002 (Bardainne et al., 2003). The pore pressure distribution over the central portion of the reservoir has been remarkably uniform during production (Segall et al., 1994).

6.3. Geomechanical properties

Grasso and Feignier (1990) reported the average values of elastic properties of different strata in the Lacq gas field based on laboratory tests on cores. Average values for Young's modulus of 54 GPa, 33 GPa and 60 GPa were interpreted for the reservoir, marls and calcareous reef, respectively. Average values for Poisson's of 0.25, 0.27-0.33 and 0.3 were interpreted for the reservoir, marls and calcareous reef, respectively. Based on these reported values, average shear moduli of 21 GPa for the reservoir, 12 GPa for the marl, and 23 GPa for the reef have been calculated. A Biot's coefficient value of

0.25 has been suggested by Segall et al. (1994) for the reservoir rock. For lack of directly-available measurements, a commonly accepted value of 0.6 (e.g., Chan and Zoback, 2002) has been assumed for the coefficient of friction (μ_s) for fault planes in the field.

6.4.4. Induced stress change analysis

A plane strain analysis of the northeast-southwest section of Lacq gas field (i.e., approximately perpendicular to the major axis of the elongated dome) with an effective reservoir thickness of 250 m (Feignier and Grasso, 1990) was undertaken in this work. The geometric context of the field is illustrated in Figure 6.16. Induced stress change analysis was conducted using the inclusion theory model discussed in Chapter 3. Because the model used is semi-analytical (i.e., numerical integration is required), it possesses more flexibility for the specification of reservoir shape than an analytical solution would. As such, the actual cross-sectional shape of the reservoir was input to the model, rather than an idealization such as a rectangle or ellipse. It should also be noted that, although the semi-analytical model is capable of accounting for non-uniform pore pressure changes within the reservoir, a uniform pressure change was used for this work. This simplifying assumption is consistent with the interpreted behaviour of the reservoir (Segall et al., 1994).

It might seem that the contrast in material properties between the reservoir and surrounding rocks should have an impact on induced stress change predictions.

However, the ratio of shear moduli in the reservoir to the surrounding rocks for Lacq would be between 0.9 and 1.75 (depending on whether the marly rocks or the calcareous reef dominate the "surrounding rock" behaviour). Results obtained using the theory of inhomogeneities show that for reservoirs that are elliptical in cross-section, the error incurred by neglecting the contrast between the reservoir and surrounding rock is at most a few percent for reservoirs with thicknesses much smaller than their widths, if the ratio of shear moduli is reasonably close to unity. Given that the Lacq reservoir satisfies both of these conditions, it is reasonable to proceed with the simplifying

assumption of uniform shear modulus throughout the field. Similarly, as shown by Rudnicki (1999) and also in Chapter 3 of this thesis, the effect of Poisson's ratio of the surrounding rock on induced stresses is negligible. Consequently, a value of 0.25 was used for Poisson's ratio of both the reservoir and the surrounding rock in this work.

(a)

(b)
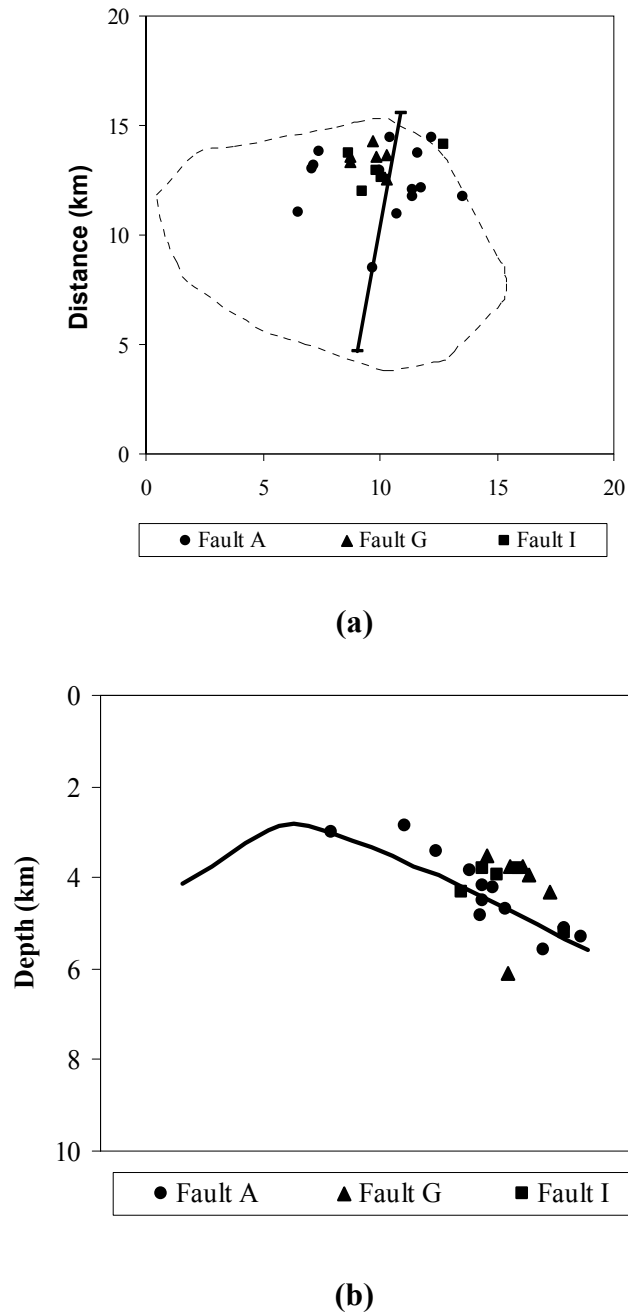
Figure 6.16. Distribution of seismic events corresponding to three fault planes, A, G and I, in the Lacq gas field (a) in plan view (b) in cross-section view (after Feignier and Grasso, 1990)

The results of induced stress analysis using the theory of inclusions (section 3.5.2) for the cross-section specified in Figure 6.16 are shown in Figure 6.17. The latter shows the distribution of horizontal, vertical and shear normalized stress arching ratios in the cross-section analyzed. Positive values of arching ratio in this figure indicate tensile stress changes, and negative values indicate compressive stress changes. [Recall that ΔP is negative during production and positive during injection.]

From Figure 6.17a, in the surrounding rock, compressive horizontal stresses are induced beneath and above the reservoir, whereas tensile horizontal stresses are induced on either side of the reservoir. This stress change pattern is consistent with the results for a planar reservoir (i.e., a very long reservoir with rectangular cross-section) computed in section 3.5.2. Figure 6.17b shows that, in the surrounding rock, compressive vertical stresses are induced on either side of the reservoir, whereas tensile vertical stresses are induced beneath the reservoir. These facts are consistent with the induced stress pattern for a planar reservoir (section 3.5.2.). However, during production in a planar reservoir, all the regions above the reservoir experience tensile stress changes in the vertical direction. In the case of this arched-shaped reservoir, induced vertical stress changes are predicted to be compressive above the crest of the reservoir. Figure 6.17c demonstrates that, similar to results for a planar reservoir, shear stresses are mainly concentrated on the corners of the reservoir - although there are some perturbations in the in-situ stresses near the crest of the reservoir.

6.4.5. Fault reactivation analysis

The geometries (e.g., strike, dip, slip direction) for the reactivated fault planes in the Lacq gas field interpreted by Feignier and Grasso (1990) were adopted for this work. By using the spatial distributions of monitored seismic events, they implemented composite mechanisms to localize these reactivated fault plane geometries. Fifteen fault planes were recognized in their work. The appropriate fault planes to use in this study were selected from these fault planes based on two major criteria:
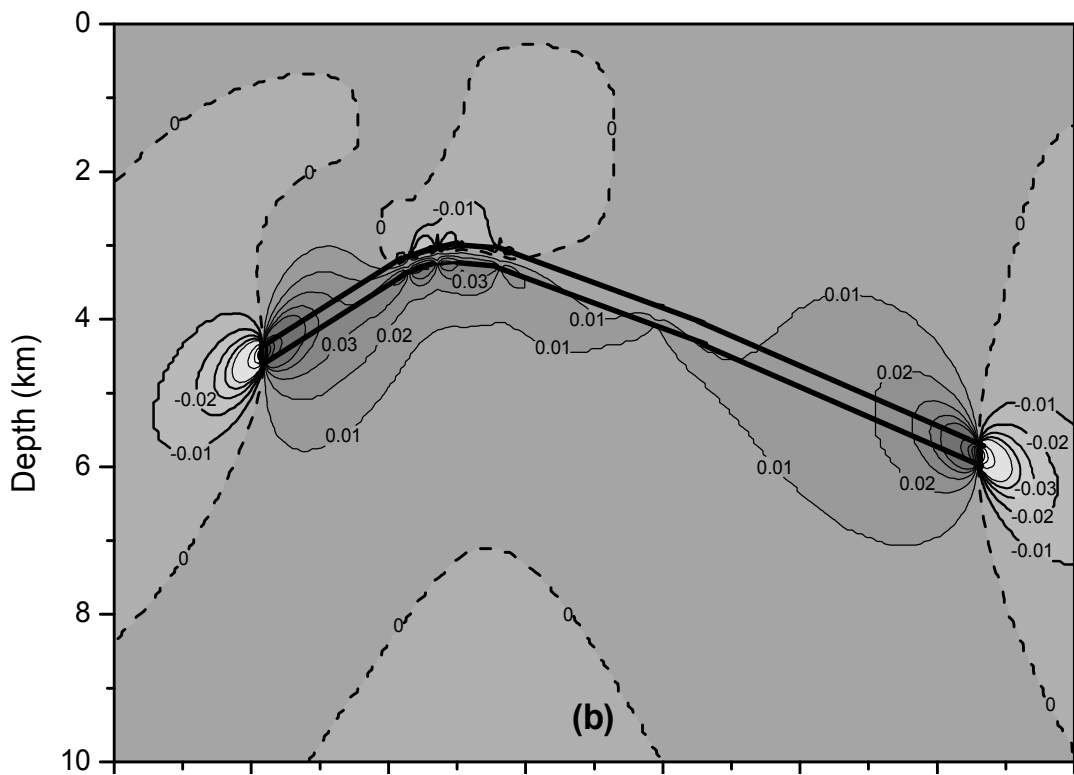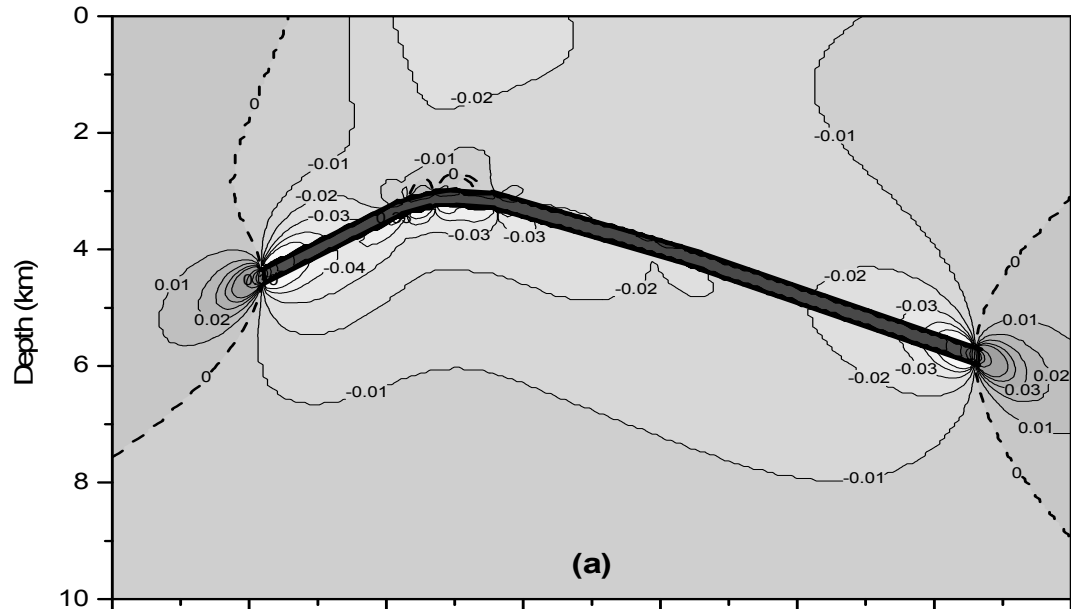
Figure 6.17. Contour plots of normalized stress arching ratios predicted for the Lacq field: (a) normalized horizontal stress arching ratio ($\gamma_{\alpha(H)}$) (b) normalized vertical stress arching ratio ($\gamma_{\alpha(V)}$) (c) normalized shear stress arching ratio ($\gamma_{\alpha(HV)}$).
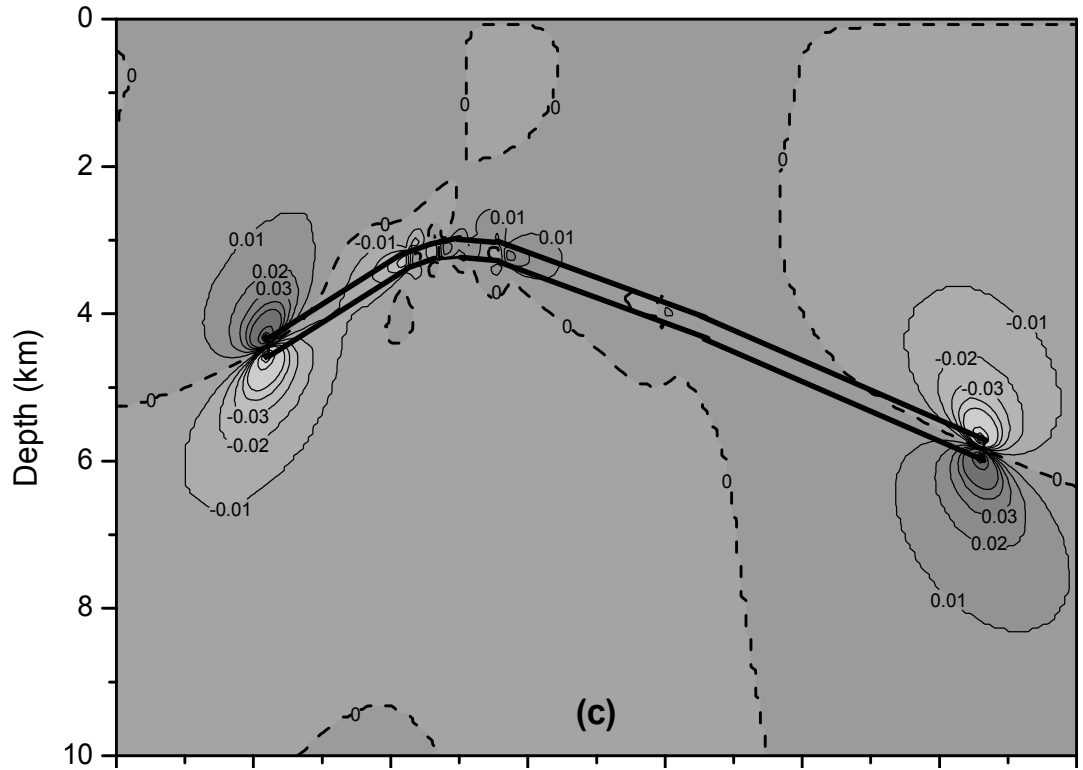
Figure 6.17 (Continued). Contour plots of normalized stress arching ratios predicted for the Lacq field: (a) normalized horizontal stress arching ratio ($\gamma_{\alpha(H)}$) (b) normalized vertical stress arching ratio ($\gamma_{\alpha(V)}$) (c) normalized shear stress arching ratio ($\gamma_{\alpha(HV)}$).

1. The fault planes must have a roughly northwest-southeast strike direction, which is roughly perpendicular to the reservoir cross-section that was analyzed. This criterion is based on the plane strain nature of the analysis, and the limitation of the Coulomb Stress Change methodology developed for this work - which is restricted to thrust and normal fault stress regimes.

2. The event locations must be reasonably close to the cross-section analyzed.

Using these criteria, three fault planes (identified as A, I and G in Feignier and Grasso, 1990) were selected for analysis in this work. These fault planes dip towards northeast (i.e., $\delta_D=-1$ in equation 4.4) with dip angles (θ) equal of 35, 40, and 45 degrees. To simplify the presentation of results in this paper, an average fault plane dip angle of 40° was assumed for all three fault planes (more detailed analyses were conducted to confirm that the effect of 5° variations in dip angle had minimal effect on the results). The locations of seismic events associated with these fault planes are shown

in Figure 6.16. Apparently, the seismic events for these three fault planes occur mainly close to the northern flank of the reservoir.

The results of the induced stress change analysis were used in combination with the fault reactivation factor (λ) to evaluate the reactivation tendencies of the three relevant fault planes. Using equation 4.3, a negative value of λ at a given point during production results in a positive value for the Coulomb Failure Stress Change (ΔCFS), indicating an increased likelihood of fault reactivation. Therefore, the $\lambda = 0$ contour defines the border between regions of increased and reduced fault reactivation potential. Due to the unclear nature of the stress regime for in the Lacq gas reservoir, fault reactivation analyses were carried out for both normal and thrust fault stress regimes (Figure 6.18a and 6.18b), to assess the consistency of each scenario with monitored seismic events in the field.

Comparison of focal points in Figure 6.18a with Figure 6.16b indicates that, for a normal fault stress regime scenario, there is no correlation between the spatial distribution of seismic events and the likely regions for the fault reactivation (i.e., regions with negative values for λ). Conversely, Figure 6.18b shows a very good correlation between the predicted fault reactivation regions and seismic event locations shown in Figure 6.16b. Therefore, in this poroelastic analysis of the Lacq reservoir, the argument for a thrust fault stress regime is much more persuasive than a normal fault stress regime. This is in agreement with the results achieved by Segall et al. (1994) using their poroelastic axisymmetric model for fault reactivation analysis within the Lacq gas reservoir.

An alternative, and potentially more accurate way of presenting the results obtained with this methodology is based on the concept of a critical threshold value for ΔCFS. As mentioned earlier, it is suggested that values of ΔCFS as small as 0.1 MPa can perturb the stress state sufficiently to reactivate faults that are initially close to being critically stressed (e.g., King et al., 1994). Given the fact that the pore pressure change had been roughly 45 MPa at the time that seismic events were used to interpret fault locations (Grasso and Feignier, 1990), the corresponding effective pore pressure change
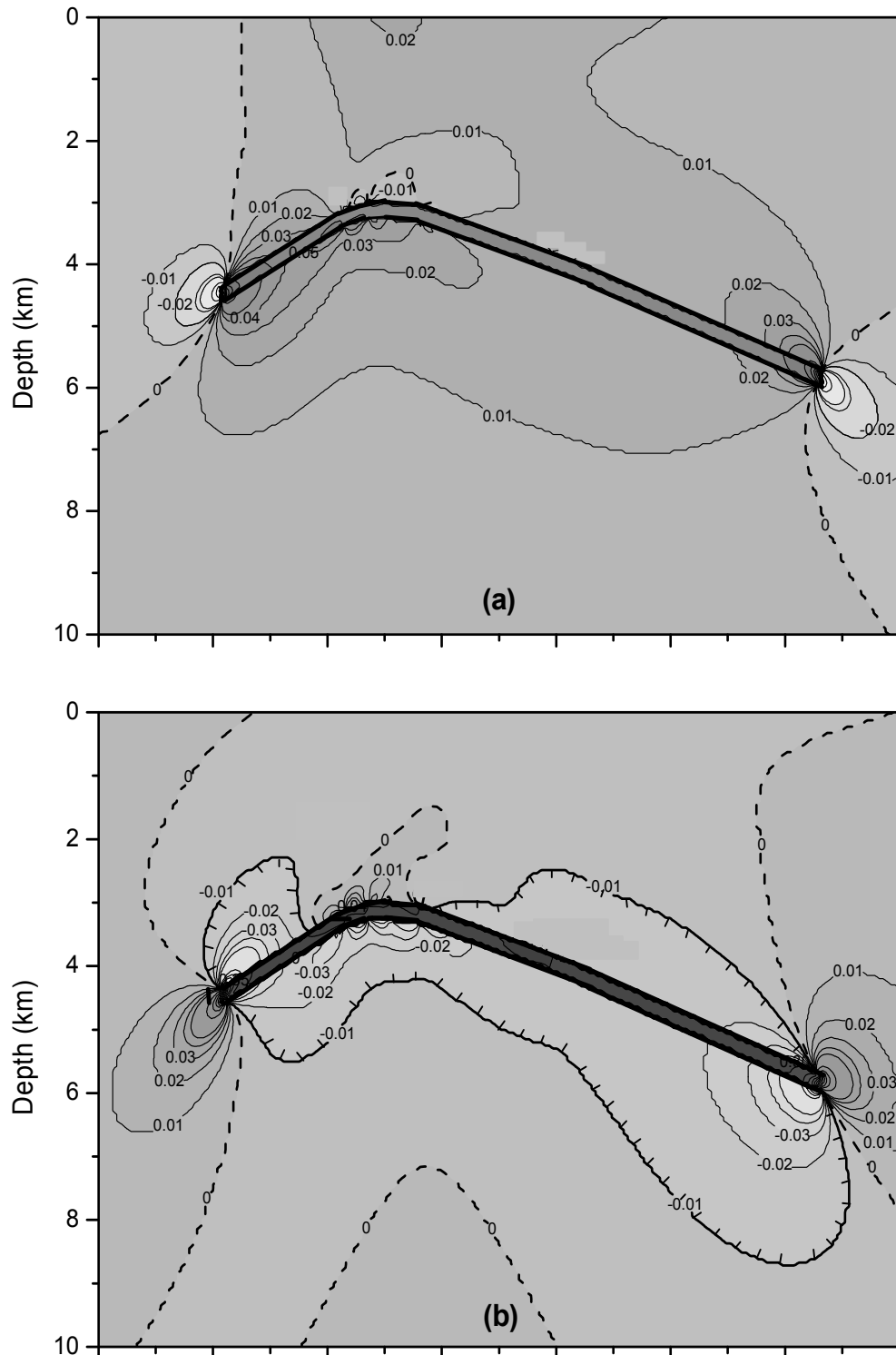
Figure 6.18. Contour plots of predicted fault reactivation factor (λ) for faults in the Lacq field dipping 40° northeast, with strike perpendicular to the cross-sectional plane, in (a) a normal fault stress regime, and (b) a thrust fault stress regime.

($\alpha\Delta P$) was approximately 11 MPa. Substituting this value in equation 4.3 gives a value of λ= -0.01 as a threshold for fault reactivation in the Lacq gas field. The contour for this threshold value is denoted using hash marks in Figure 6.18b. Comparing the potential region of fault reactivation enclosed by this contour with the recorded seismic events in Figure 6.16b demonstrates that almost all focal points lie within this region; i.e., there is a very strong correlation between the developed model and the field data. These results suggest that the proposed poroelastic stress change model, used in conjunction with a Coulomb Failure Stress Change criterion, is capable of predicting locations prone to fault reactivation with acceptable accuracy.

6.5. Fault reactivation and induced fracturing analyses within the Ekofisk Oil and Gas Reservoir, North Sea

The Ekofisk Oil Field is located in the Norwegian sector of the North Sea (Figure 6.19). In 1984, it was observed that the seabed over the Ekofisk Field had subsided by 3 m (Sulak, 1991). Although waterflooding commenced in this field in 1987, subsidence has continued at an almost constant rate (Rutledge et al., 1994) and it has experienced more than 10 m of subsidence (Dusseault et al., 2001). Seismic events
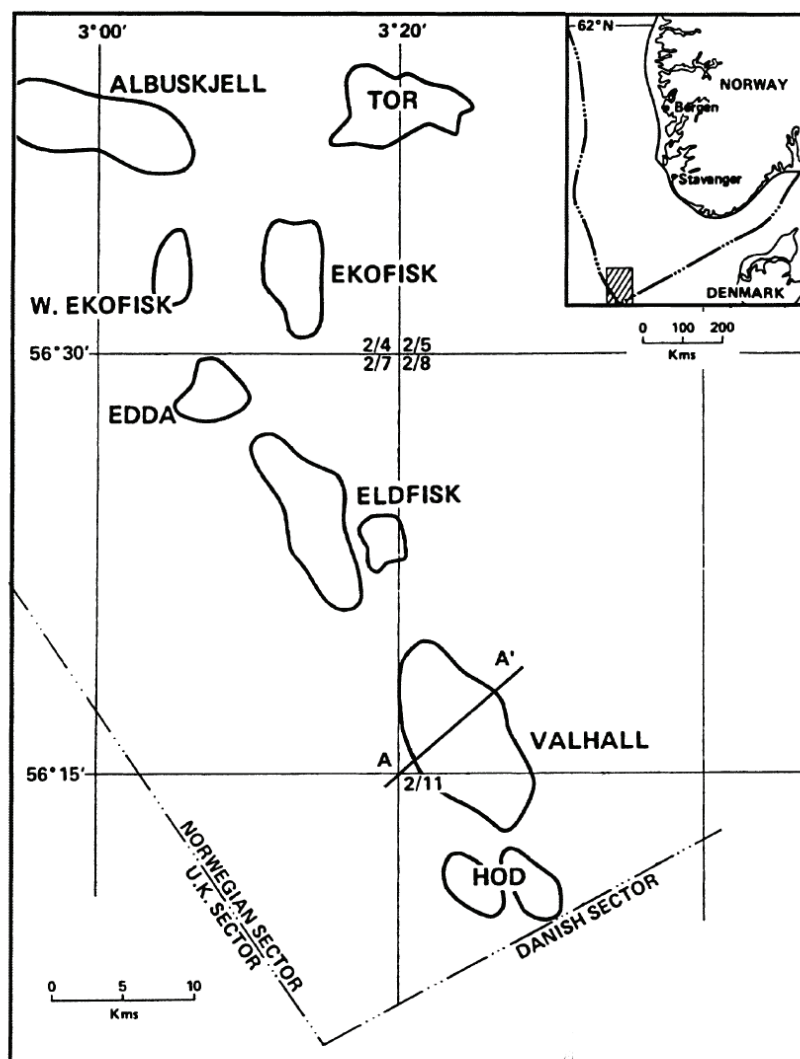
Figure 6.19. Location map of Ekofisk oil and gas field (from Zoback and Zink, 2002)

have been recorded throughout the reservoir's producing life (Rutledge, 1994; Maxwell et al., 1998; Streit and Hillis, 2002). Also, there have been some casing failures in the shale caprock (Schwall et al., 1994) and appreciable gas leakage through the shale caprock, probably by flow through faults (Munns, 2003). All of this evidence suggests that fault reactivation has occurred and/or new fractures have been induced within the reservoir and surrounding rocks. A study on the induced microseismicity in this field shows that the seismic events analyzed in detail near the central part of the reservoir were, in plan view, concentrated in lineations parallel to the dominant orientation of existing faults (NNE-SSW and NW-SE) which suggest that they have been triggered by the reactivation of the existing faults (Maxwell et al., 1998; Maxwell and Urbancic, 2001). However, some researchers have considered the induced fracturing as a responsible reason for the induced seismicity within the reservoir (e.g., Rutledge et al., 1994). Due to considerable evidence of fault reactivation and/or induced fracturing well-documented nature of subsidence and stress-depletion response during production, the Ekofisk field has been selected as a case study to illustrate the use of the methodologies presented previously for induced stress change analysis, fault reactivation, and induced fracturing assessment.

6.5.1. Reservoir characteristics

The Ekofisk structure is an elongated anticlinal structure with a principal fold axis in an approximately north-south direction. The depth to the crest of the anticline is approximately 2840 m. The areal extent of the reservoir is 6.8×9.3 km (Lewis et al., 2003). The average thickness of the oil column is 300 m, including both the Ekofisk and Tor formations (Goulty, 2003). According to in-situ measurements (Teufel, 1987), reservoir pressure has been depleted in the crestal area of the field from approximately 45 MPa in 1975 to 25 MPa in 1990. During this time, minimum horizontal stress decreased from approximately 51 MPa to 35 MPa. A linear relationship has been observed between minimum horizontal stress and reservoir pressure over this time period, with a *K* value of 0.8 as shown in Figure 6.20 (Teufel, 1987). Stated in terms consistent with the material presented in this paper, and using a value of 1.0 for Biot's
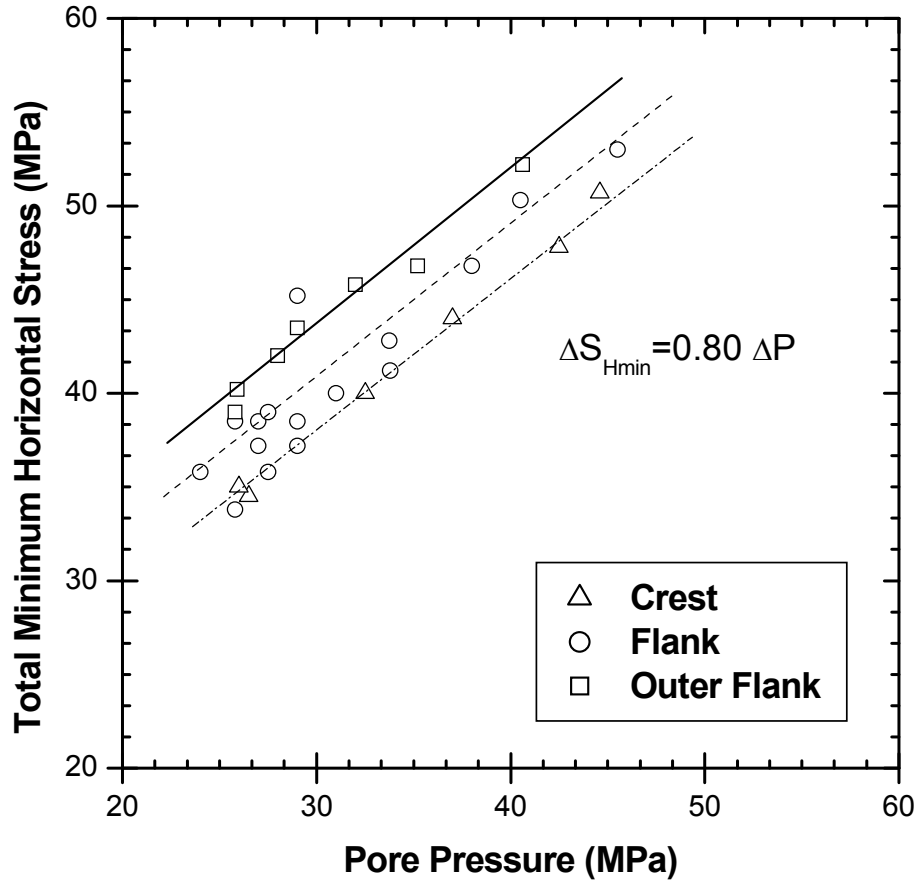
Figure 6.20. Plot of total minimum horizontal stress vs. pore pressure in the Ekofisk field (after Teufel, 1989)

coefficient (see below), this means that the horizontal normalized stress arching ratio for the Ekofisk reservoir is 0.8.

6.5.2. Geomechanical properties

There is a broad scatter of values interpreted for the elastic properties of the Ekofisk reservoir and surrounding rocks reported in the literature. Proposed values for Young's modulus of the reservoir vary between 0.05 GPa to 2.2 GPa, where values for the surrounding rocks vary from 1.1 GPa to 14 GPa (Gutierrez and Hansteen, 1994; Boade et al., 1989; Lewis et al., 2003). Proposed values for Poisson's ratio vary from 0.15 to 0.25 for the reservoir and 0.20 to 0.42 for the surrounding rocks (Gutierrez and Hansteen, 1994; Boade et al., 1989; Lewis et al., 2003; Segall and Fitzgerald, 1998). As

a rough estimation, based on the literature data and the results of back analyses conducted by the authors, it seems reasonable to consider a contrast between reservoir rock and surrounding rocks which correspond to a shear modulus ratio (R_μ) equal to 0.1. This means that the shear modulus of the surrounding rocks is 10 times larger than the reservoir's shear modulus. Also, a value of 0.20 for the Poisson's ratio of the reservoir is deemed to be a reasonable estimate. Given the aforementioned lack of sensitivity of stress arching ratios to Poisson's ratio of the surrounding rock, a value of 0.20 was also assumed for this parameter. Based on laboratory experiments, Teufel and Rhett (1991) proposed a value of 1.0 for Biot's coefficient for the highly fractured Ekofisk reservoir rocks.

Although the Ekofisk oil field is one of the most thoroughly documented reservoirs with respect to geomechanical analysis, differing values occur in the literature for some key parameters such as rock mechanical properties, vertical stress arching ratio, etc.. In this section, the dataset listed in Table 6.1 will be considered as a base case scenario for analyzing induced fracturing and fault reactivation potential within the reservoir, and then other suggested values for key parameters will be used to guide a parameter sensitivity analysis of induced fracturing.

6.5.3. Induced stress change analysis

To obtain a first estimate of induced stress change, the solution developed based on the theory of inclusions may be used (identical material properties for both the reservoir and the surrounding rock). Substituting a reservoir aspect ratio (*e*) of 0.044 (i.e., 300 m / 6800 m) and a depth number (*n*) of 1.20 (i.e., 3400 m / 2840 m) for the Ekofisk field in equation (3.40), the normalized horizontal and vertical stress arching ratios are found to be 0.71 and 0.02, respectively. This estimated value of 0.71 is not very different from the measured value of 0.8. Given the apparent contrast between material properties of the reservoir and surrounding rocks, it would be more reasonable to use the theory of inhomogeneities for the Ekofisk reservoir. Due to the small aspect ratio of this reservoir, the use of this full-space solution is deemed acceptable. Using a reservoir aspect ratio of 0.044 in equation (3.101), the horizontal and vertical normalized

Table 6.1. List of characteristics of Ekofisk oil field, North Sea, applied in this study

Parameter set	Parameter	value
Reservoir geometry	Length [1]	9.3 km
	Width [1]	6.8 km
	Thickness [2]	300 m
	Overburden thickness [1]	2840 m
	Average depth	3000 m
Initial in-situ stresses and reservoir pressure	Vertical [3]	61 MPa
	Horizontal (minimum) [3]	51 MPa
	Horizontal (maximum) [3]	Unknown
	Pore pressure [3]	45 MPa
Reservoir pressure change	Horizontal stress arching ratio [3]	0.8
	Vertical stress arching ratio [3]	0
	Reservoir pressure change (until 1990) [4]	>20 MPa
Reservoir rock mechanical properties	Biot's coefficient (α) [3]	1.0
	cohesion (c) [4]	1 MPa
	coefficient of friction (μ_s) [4]	0.6
Calculated parameters to be used in this paper	λ_p	0.75
	K_0	0.85
	c^*	0.04
	R_σ	0.2
	$R_{\phi\,(Normal)}$	0.32
	$R_{\phi\,(Thrust)}$	3.12

[1] Lewis et al. (2003) [2] Goulty (2003) [3] Teufel and Rhett (1991) [4] Streit and Hillis (2002)

stress arching ratios are found to be 0.80 and 0.18, respectively. This value of the horizontal arching matches the value found by Teufel and Rhett (1991). However, Teufel and Rhett (1991) and other authors (e.g., Zoback and Zink, 2002; Goulty, 2003) implicitly assumed that there has been no change in vertical stress in the Ekofisk reservoir stress because of its large lateral extent relative to its thickness. This assumption differs markedly from the result obtained using the poroelastic model presented in this thesis; i.e., a predicted vertical stress change that is 18% of the pore pressure change. Clearly, field measurements of vertical stress changes would be

beneficial for assessing the accuracy of this model's predictions, which may have significant implications in some reservoirs.

6.5.4. Rock fracturing tendency

Ekofisk is set in a normal fault stress regime, and R_σ is less than R_ϕ (see Table 6.1). Therefore, based on Table 5.1 (or Figure 5.2), the reservoir rock has a tendency towards failure during production. During injection, for smaller values of reservoir pressure change - which are common for reservoirs undergoing waterflooding during hydrocarbon recovery - the stress state moves away from the failure criterion (i.e., stabilization). As a different scenario, for higher values of injection the initially normal fault stress regime changes to a thrust fault stress regime and, consequently, any additional pressure increase leads to a tendency towards shear fracturing. However, during injection, tensile fracturing in the rock occurs before shear fracturing and horizontal tensile fracturing is the dominant mode of fracturing.

6.5.5. Critical pressure change for fracturing

Using equation (5.4) and the input data given in Table 6.1, two different values for critical pressure change to induce shear fractures within the reservoir are calculated: ΔP_f = -16.6 *MPa* (pressure change during production) and ΔP_f =16.3 MPa (pressure change during injection). The Mohr-circles corresponding to these two cases are shown in Figure 6.21. From this figure, the value of the critical pressure change to induce shear fracturing during production is less than the actual pressure change that the reservoir experienced during its producing life (i.e., roughly -20 MPa). Also, during the hypothetical case of injection within the Ekofisk oil field, horizontal tensile fractures would likely be induced before any shear fracturing would occur (i.e., $(\Delta P_f)_{T\ (H)}$ =16 < 16.3 *MPa*). It is worthy to note that during injection, the dilation occurring as a result of shear fracturing would result in some amount of reduction in pore pressure in the fault zone. However, due to the increase in permeability likely associated with dilation, this reduction would likely be short-lived; fluid flow into the fault zone would occur, hence re-equilibrating the local pressure with the larger-scale reservoir pressure.
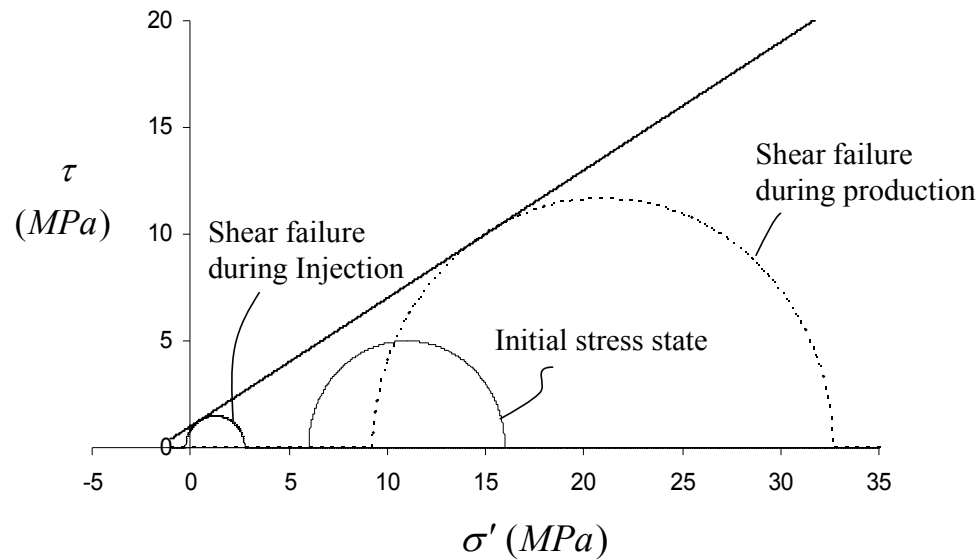
Figure 6.21. Stress state in shear failure state for Ekofisk oil field, North Sea. Note that, in this case, tensile failure would precede shear failure during pressure increase (i.e., injection).

6.5.6. Sensitivity of induced fracturing to in-situ stresses

The in-situ stress state is one of the major uncertainties for many hydrocarbon reservoirs (e.g., Segall et al., 1994; Jimenez, 2006). Therefore, developing a framework for studying the effect of in-situ stress on the tendency towards fracturing is essential for studying many reservoirs where the required data are not available. In this work, the effect of in-situ stress on induced fracturing within the Ekofisk reservoir has been studied by changing the lateral stress coefficient (K_0). In practice, the value of K_0 is constrained by two main conditions: no tensile stress (i.e., $\sigma'_{H0} > 0$ and $\sigma'_{V0} > 0$) and no shear failure in the in-situ stress state. The first condition leads to a minimum value for the K_0 as follows:

$$K_{\min(T)} = \alpha\lambda_p < 1 \tag{6.1}$$

The second condition can be verified by using equation (5.2). Solving this equation to find the boundary values of K_0 in the initial stress state leads to the following equation:

$$K_0 = (1 - \lambda_p) R_\phi + \lambda_p (1 - 2c^* \delta_F \sqrt{R_\phi}) \qquad (6.2)$$

Equation (6.2) gives two values for K_0: a minimum (i.e., $K_{min(S)}$) for a normal stress regime ($\delta_F = 1$) and a maximum (i.e., $K_{max(S)}$) for a thrust stress regime ($\delta_F = -1$). Given these two conditions, any sensible value of K_0 must fit within the range shown by the following inequality:

$$\max\{K_{min(T)}, K_{min(S)}\} \le K_0 \le K_{max(S)} \qquad (6.3)$$

Using equations (6.1) to (6.3) the sensible range of values for K_0 within the Ekofisk reservoir is between $K_{min(S)}=0.80$ and $K_{max(S)}=1.61$ (note that $K_{min(T)} = 0.74 < K_{min(S)}$). Figures 6.22a and 6.22b show the results of a sensitivity analysis of induced fracturing for K_0 values varying across this range. Figure 6.22a shows the results of using equations (5.4) and (5.6) through (5.8) to study the variation of critical pressure change during injection and production as a function of lateral pressure coefficient, and Figure 6.22b demonstrates how the fracturing mode evolves with changing lateral pressure coefficient.

From Figures 6.22a and 6.22b, during production, when $0.80<K_0<0.89$ sub-vertical shear fracturing would occur in a normal mode of fracturing, and critical pressure change increases with increasing K_0. For values of K_0 more than 0.89, the critical pressure change would be more than the in-situ pressure of the reservoir and so fracturing is unlikely to occur. During injection, with gradually increasing K_0, the fracturing mode varies from a horizontal tensile fracturing mode for $0.80 < K_0 < 0.89$, to a thrust mode of fracturing for $0.89 < K_0 < 1.61$ where the critical pressure change decreases gradually. These results emphasize the significant influence of in-situ stress
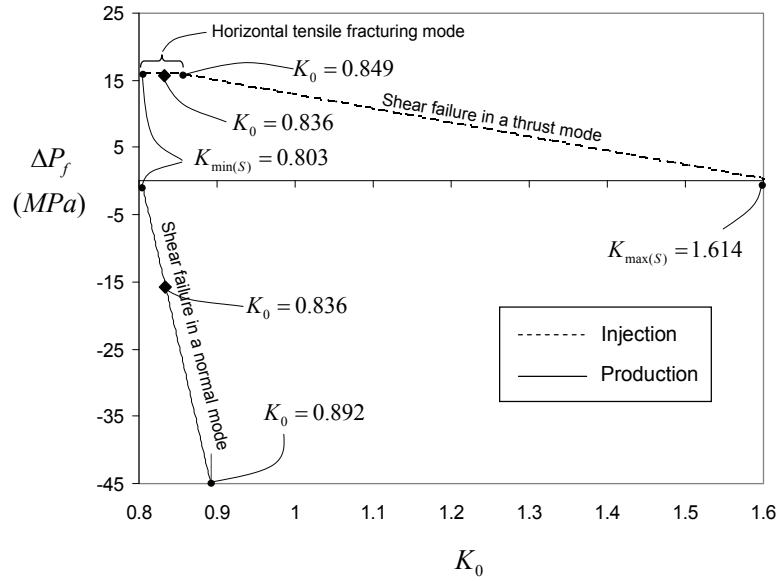
(a)
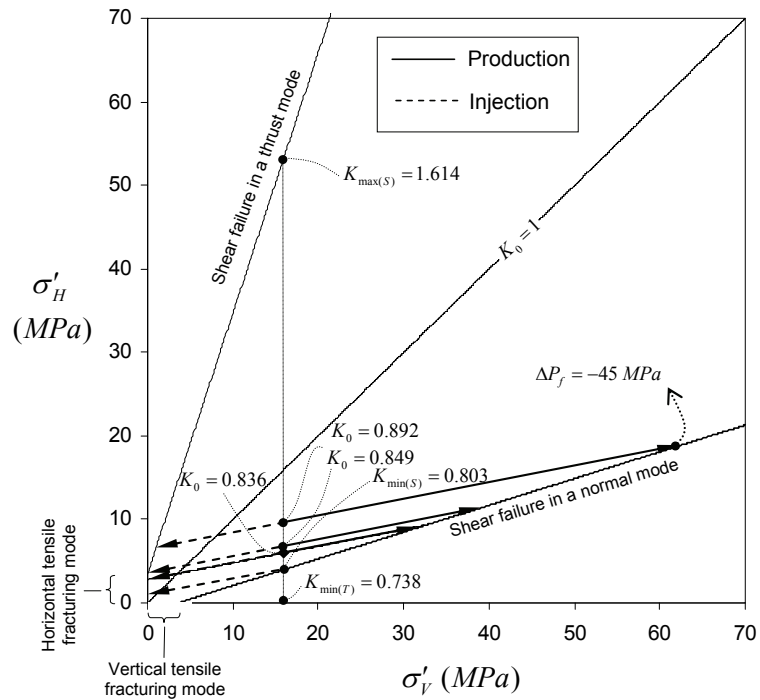
(b)

Figure 6.22. Sensitivity analysis on the lateral pressure coefficient (K_0) for the Ekofisk oil field (a) Critical pressure change to induce fracturing, and (b) evolution of the stress state in a horizontal-vertical effective stress (σ'_H-σ'_V) coordinate system. Solid diamonds in both figures refer to the Ekofisk in-situ stresses referenced in Table 6.1.

state on the critical pressure change, fracturing mode and orientation, hence highlighting the importance of in-situ stress measurements for accurate geomechanical analysis of reservoirs.

6.5.7. Sensitivity of induced fracturing to the stress change path

As mentioned above, in relatively rare cases where field measurements of stress change have been made, these measurements have generally been limited to the change in the minimum horizontal stress. Sometimes, even for this particular component of stress, different stress change parameters have been proposed in the literature (e.g., see Table 2.1). Measurements aside, during the early ages of field development, estimation of induced stress change is only available from modeling analyses. Depending on the underlying assumptions and simplifications of the model used, differing stress change parameters may be predicted. These uncertainties and discrepancies underline the importance of studying the sensitivity of the induced fracturing to stress change parameters (i.e., stress arching ratios and stress path ratio) which, for this reason, has been conducted in this work for the Ekofisk field. The results, shown in Figures 6.23 and 6.24, demonstrate how the critical pressure and fracturing mode change with variations in horizontal and vertical normalized arching ratios ($\gamma_{\alpha(H)}$ and $\gamma_{\alpha(V)}$) and, consequently, with changing stress path ratio (R_σ). As seen in these figures, during injection, by increasing $\gamma_{\alpha(H)}$ from zero to one, which corresponds to a decrease of R_σ from one to zero, the mode of fracturing gradually changes from shear fracturing in a normal mode to a vertical tensile fracturing, and then to a horizontal fracturing mode and finally to a shear fracturing in a thrust mode. Vertical stress change has commonly been considered negligible for reservoirs of large lateral extents by virtue of the assumption that deformation within them is uniaxial (i.e., $\gamma_{\alpha(V)} = 0$). Regrettably, in practice, there is no field measurement to assess the validity of this assumption. Analytical and numerical models do show, however, that arching may have a very significant effect leading to reduction of the contractile strains within the reservoir and redistribution of the in-situ stresses. For instance, Mulders (2003) states that for small reservoirs made up of weak rocks, about 50% of the vertical stress change may be arched away. Using 3D modeling,
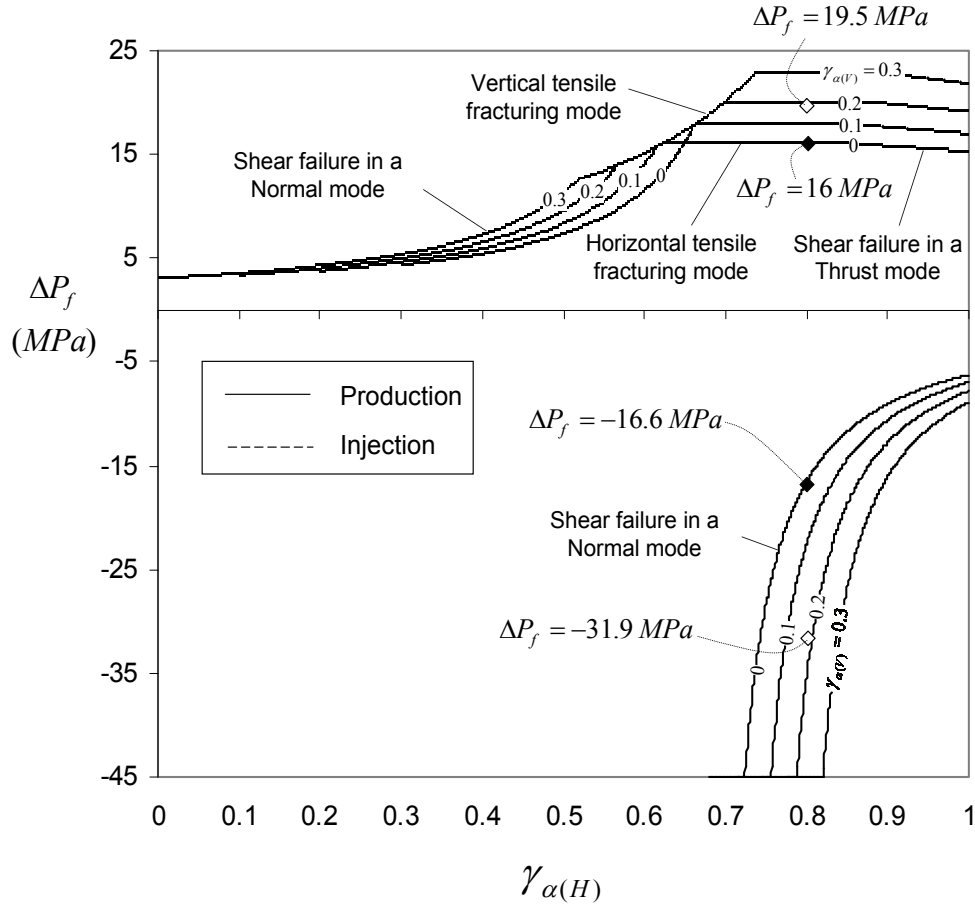
Figure 6.23. Sensitivity analysis on the stress change path: (a) Variation of critical pressure change as a function of stress arching ratios ($\gamma_{\alpha(H)}$, $\gamma_{\alpha(V)}$); Solid diamonds refer to the Ekofisk reference stress change parameters given in Table 6.1, and open diamonds refer to stress change parameters calculated using the theory of inhomogeneities.

Kenter et al. (1998) showed that there was 20% to 30% vertical arching during depletion of the Shearwater gas reservoir, in the northern North Sea. For the case of the Ekofisk oil field, poroelastic modeling conducted using the theory of inhomogeneities in section 6.5.3 suggests a value of 0.18 for the normalized vertical arching ratio within the reservoir (i.e., $R_\sigma = 0.24$). Figures 6.23 shows that, for this value of $\gamma_{\alpha(V)}$, the critical pressure change for fracturing during production ($\Delta P_f = 31.9$ MPa) is about 48% more than the value for the reference case which considers a zero value for $\gamma_{\alpha(V)}$ ($\Delta P_f = 16.6$ MPa). For the case of injection, the change with respect to the reference case ($\gamma_{\alpha(V)} = 0$) is a 22% increase (from 16 to 19.5 MPa), where horizontal fracturing occurs in a tensile mode.
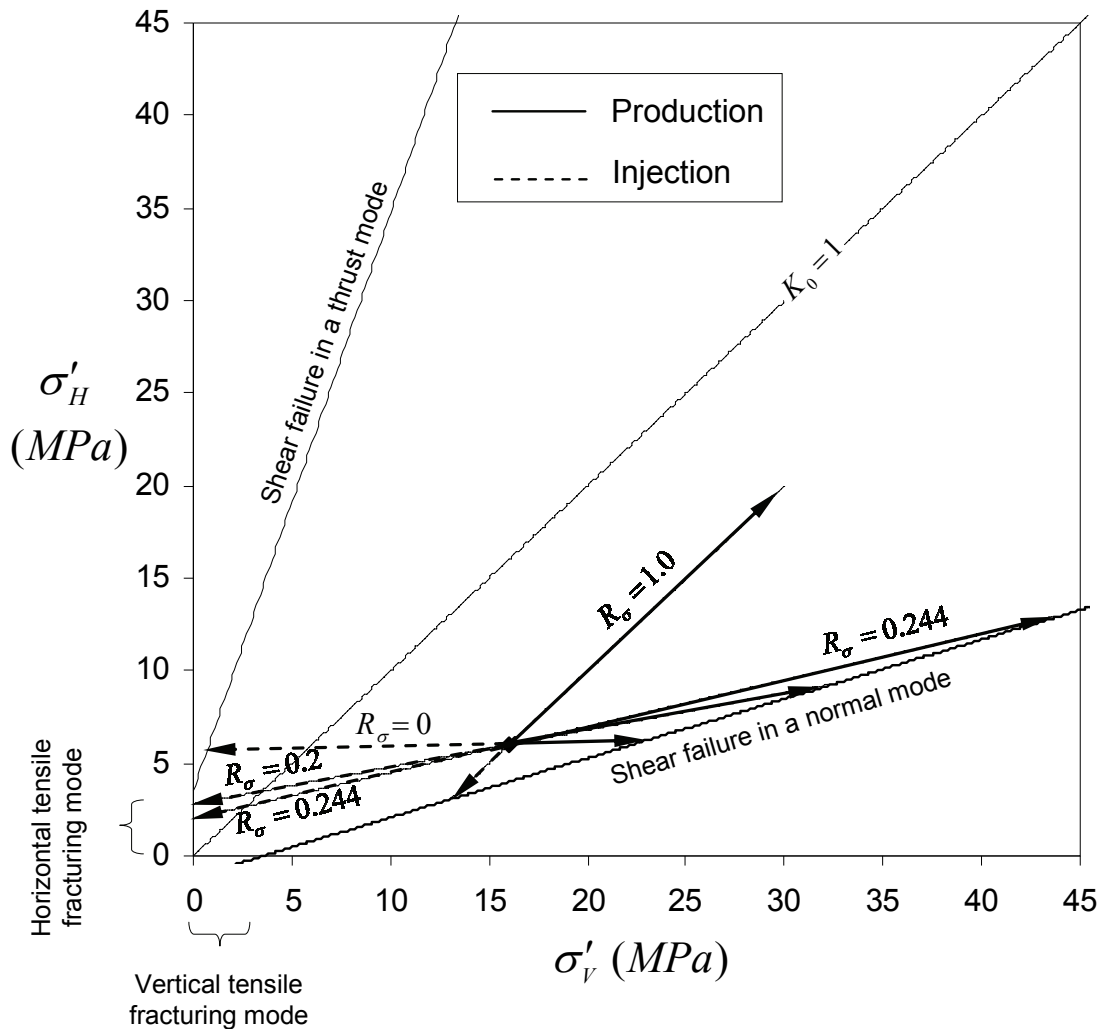
Figure 6.24. Evolution of stress state in a horizontal-vertical effective stress (σ'_H - σ'_V) coordinate system for three different stress path ratios: R_σ=0.2 which refer to the Ekofisk stress change parameters given by Teufel and Rhett (1991), R_σ=0.244 which refers to the stress arching ratios calculated using theory of inhomogeneities, and R_σ=1.0 which refers to the condition of no total stress change within the reservoir (e.g., $\gamma_{a(H)}$ =0 and $\gamma_{a(V)}$=0) .

Due to the hysteretic character of reservoir rocks, a substantial difference between production and injection (i.e., loading and unloading of rock) effects is expected (Holt et al., 2004). This is probably because of the irreversible pore size reduction and/or pore collapses during previously conducted production from a reservoir. A measurement of injection-induced stresses reported by Santarelli et al. (1996) shows that no considerable change in stresses in the reservoir occurs after injection (see Table 2.1). This evidence suggests that the stress arching ratios for a depleted reservoir, when subsequently subjected to injection, might be close to zero (i.e.,

a value of R_σ close to one). As demonstrated in Figures 6.23 and 6.24, the assumption of such a value for R_σ during injection in a normal fault stress regime leads to sub-vertical shear fractures which occur in a normal fracturing mode; for comparison, for the case where R_σ during injection is assumed to be identical to its value during production, fracturing would occur in a horizontal tensile fracturing mode. In addition to a change in fracturing mode, in the case of zero stress change, the critical pressure change would be less. These results show that ignoring the potential effect of hysteresis might lead to a significant over-estimation of the value of critical pressure change for fracturing within the reservoir.

6.5.8. Sensitivity of induced fracturing to rock strength

There is often considerable uncertainty in the values of the rock mechanical properties required for geomechanical analysis of induced fracturing. In many cases, these parameters have not been measured on cores; in other cases, when cores have been obtained and tested, there remains a degree of uncertainty (e.g., unknown extent of sample disturbance during coring; test conditions that fail to match in-situ conditions; sample size effects) and spatial variability that cannot be rigorously accounted for. For example, Streit and Hillis (2002) have argued against the accuracy of rock strength parameters (i.e., $\mu_s = 0.23$ and $c = 4.1$ MPa) measured by Teufel and Rhett (1991) for the Ekofisk oil reservoir, stating that these parameters had been measured in experiments having a a very limited range of effective normal stresses. Their suggested values were $\mu_s = 0.6$ and $c = 1$ to 2 MPa. Therefore it seems essential to consider the effect of changing these parameters on induced fracturing within the reservoir.

The results of such a sensitivity analysis are shown in Figure 6.25, which shows how the critical pressure change varies with changes in the rock strength parameters (i.e., c and $\mu_s = \tan\phi$). As shown in this figure, for these different sets of data the values of critical pressure change during production are considerably different. However, during injection, critical pressure change is not affected by differences in these values because fracturing occurs in a tensile horizontal mode in all cases regardless of the reservoir's shear strength.

From Figure 6.25, for any value of cohesion, there is only a sensible range of μ_s which satisfies the condition of stability of the rock in the initial stress state. For example, for $c = 0$, this sensible range is $\mu_s > 0.51$. Also, this figure shows that, during production, by increasing the value of μ_s, the critical pressure change for fracturing rapidly increases until a point ($\mu_s = 0.90$) where R_ϕ eventually becomes less than R_σ (= 0.2); according to Figure 5.2 (or Table 5.1), for μ_s values exceeding this limit, induced fracturing during production becomes impossible. As mentioned previously, during injection, because fracturing occurs in a horizontal tensile mode, critical pressure change is independent of shear strength for all cases unless the cohesion is negligible. Even in this special case, critical pressure change is not really variable due to the fact that fracturing occurs in a case referred to here as 'pseudo-tensile'. Pseudo-tensile mode is in
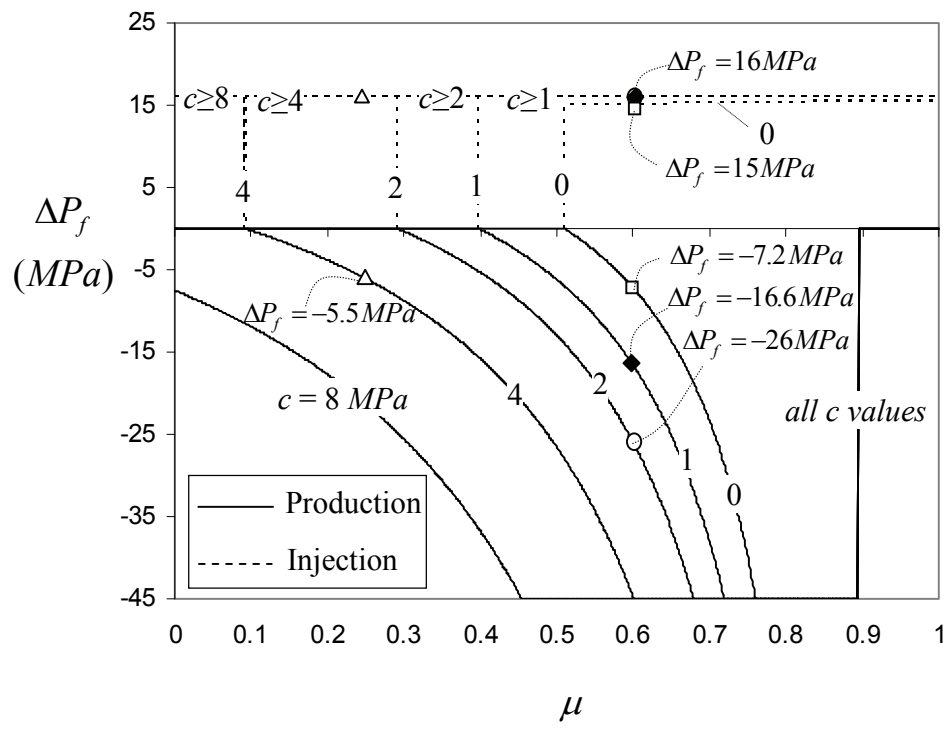
Figure 6.25. Sensitivity analysis on the rock strength parameters (c and μ_s). Solid diamonds refer to the Ekofisk reference rock strength parameters given in Table 6.1. The open circle refers to another value of cohesion (2 MPa) given by Streit and Hillis (2002). Open triangle refers to values of rock strength given by Teufel and Rhett (1991) for the intact rock's strength ($c = 4.1$ MPa and $\mu_s = 0.28$). The open squares refer to strength properties ($c = 0$, $\mu = 0.6$) given by Streit and Hillis (2002) for the fault surfaces in Ekofisk oil field.

fact a shear fracturing in a thrust mode while the value of the vertical effective stress (σ'_V) is negligible.

Although not really an accurate assumption, there has been a tendency towards solving the problem of fault reactivation using the concept of shear failure or so called 'faulting' (e.g., Segall et al., 1994). In this type of solution, an optimum fault dip angle equal to the fracturing plane of intact rock (i.e., 45 - $\phi/2$ in a thrust fault stress regime and 45 + $\phi/2$ in normal fault stress regime) is assumed. Also, in this solution, cohesion (c) is usually considered to be zero and μ_s is the coefficient of friction between two fault surfaces. This solution is only valid if the present initial stress state has remained the same since the occurrence of faulting within the formation, and the fault orientation has not been changed as a result of geological displacements. However, these assumptions are not maintained in many real cases. For the case of Ekofisk, Streit and Hillis (2002) assumed a value of 0.6 for the friction coefficient on the fault surface. From Figure 6.25, for such a value the critical pressure change during production is -7.2 MPa and fracturing occurs in a normal mode. However, during injection, the critical pressure change is 15 MPa and fracturing occurs in a thrust mode or a 'pseudo-tensile' mode. Considering that the critical pressure change for fault reactivation during production (7.2 MPa) is much less than the actual pressure change in the reservoir (~20 MPa), reactivation of existing faults may have been a cause for seismic events, leakage and subsidence observed during production from the Ekofisk reservoir. However, in the following sections, a more detailed study on fault reactivation potential in this reservoir is conducted.

6.5.9. Fault reactivation tendency analysis

The local stress regime is inferred to favor normal faulting, and a friction coefficient of 0.6 is considered to be reasonable for the Ekofisk reservoir chalk (Streit and Hillis, 2002). Using the value of 0.24 for R_σ, equation (4.17) can be used to determine that the range of fault dip angles tending towards reactivation during production is between $44°$ and $77°$. Given that the fault dip angles in the Ekofisk

191

reservoir fall within the upper half of this range, the fact that they were reactivated during production is consistent with the model predictions.

6.5.10. Critical pressure change for fault reactivation

Knowing the original in-situ stress magnitudes, and using the fault reactivation factor, it is possible to use equations (4.28) to (4.36) to find the values of reservoir pressure change that lead to fault reactivation for any given normal fault of known dip angle. The results for different dip angles are shown in Figure 6.26. This figure shows the value of reservoir pressure change required to reactivate faults as a function of dip angle. For convenience, the absolute value of reservoir pressure at fault reactivation is also plotted. This figure shows that, for fault dip angles occurring in Ekofisk reservoir (i.e., $\geq 65°$), reactivation will occur for a reservoir pressure depletion of about 16 MPa. This corresponds to an absolute reservoir pressure of 29 MPa. The reservoir pressure has been approximately 25 MPa from 1990 onwards (Streit and Hillis, 2002). Clearly, the predictions made in this thesis, with a modest amount of input data, are consistent with the observed occurrence of fault reactivation.
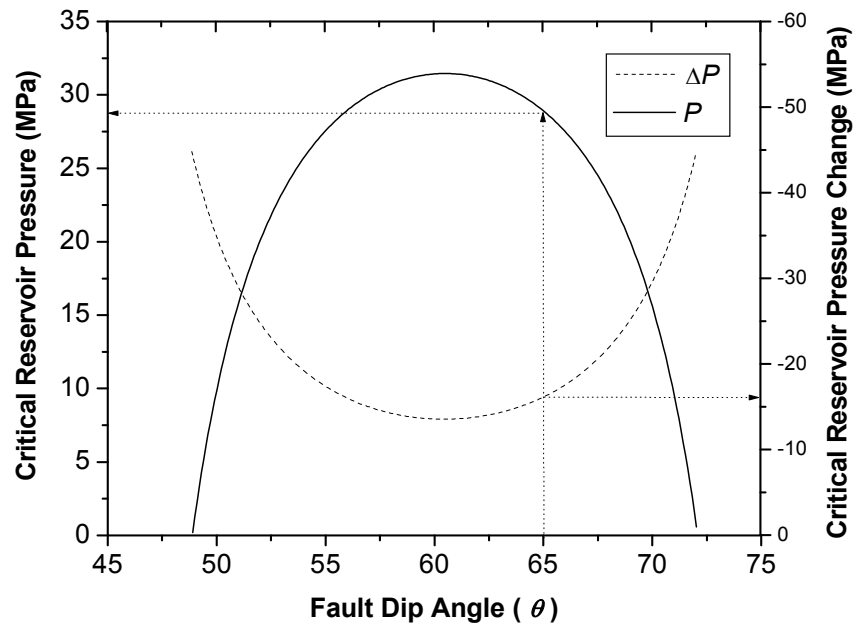
Figure 6.26. Range of fault dip angles that tend towards reactivation during depletion of a laterally infinite reservoir in a normal fault stress regime.

6.6. Fault reactivation and induced fracturing analyses in the Weyburn oil field, Saskatchewan

The Weyburn oil field is located in southeast Saskatchewan (Figure 6.27). It was discovered in 1954 and oil production started in 1955. After a reduction in production rates, water-flooding commenced in 1964. Oil production rose to its historical maximum in 1966. The production steadily decreased after that time and in 1986 additional vertical and horizontal wells were drilled to increase it. However, continuing trend of decreasing oil production lead to decision to implement a new recovery method. Therefore, Enhanced Oil Recovery (EOR) by injection of carbon dioxide started in 2000. Furthermore to enhanced oil recovery, underground storage of CO_2 has become major objective for this project. The source of the CO_2 is anthropogenic, and it is being transported from a coal gasification plant in North Dakota, USA using a 300 mile pipeline system.
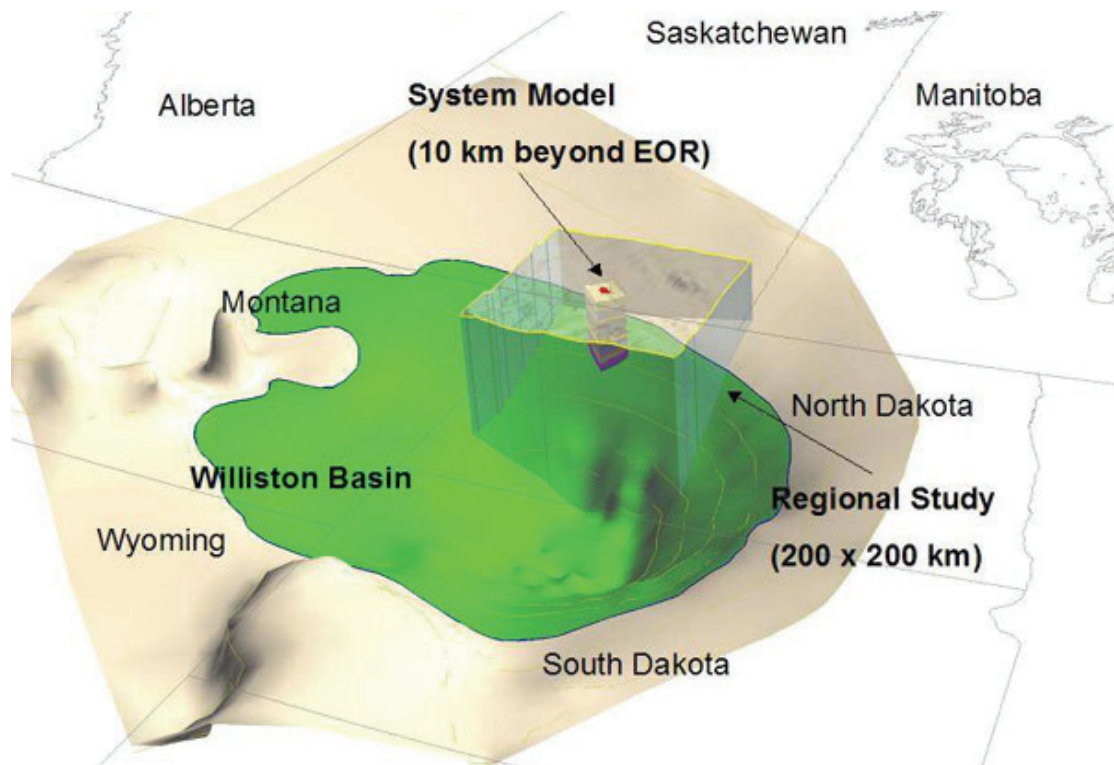
Figure 6.27. Location of Weyburn field and Williston Basin (from Talbot, 2008)

The objective of this case study is to implement the methodologies developed in this research to evaluate the caprock integrity of the Weyburn reservoir for storage of carbon dioxide through studying the likelihood of induced fracturing and fault reactivation.

6.6.1. Reservoir characteristics

The major characteristics of the Weyburn field were reported by Jimenez (2006). The reservoir depth is 1450m with a stratigraphic dip of 8.3m/km southward (Figure 6.28). The initial in-situ pressure and temperature within the reservoir were respectively 14.5 MPa and 65° C. The stratigraphic section of the reservoir and adjacent strata is shown in Figure 6.29. The reservoir consists of two zones: a dolostone Marly zone with a thickness of 1-11m, and a limestone Vuggy zone with a thickness of 10-22m. The Marly zone has an average porosity of 26%, a low to moderate fracture density and a matrix permeability of 0.001 to 0.1 millidarcies. The Vuggy zone consists of two units: first, an Upper Vuggy unit with an average porosity of 10%, a high density of fractures, and a permeability of 0.1-100 (average of 10) millidarcies; second, the Lower Vuggy unit with an average porosity of 15%, a moderate to high fracture density, and a matrix permeability of 1-500 (average 0f 20) millidarcies. The caprock (i.e., Frochisher Evaporite) and the underlying layer (i.e., Midale Evaporite) are both low permeability anhydrites with very low fracture densities.

6.6.2. Geomechanical properties

An extensive study of material properties was conducted by Jimenez (2006). His study was based on both core testing and literature review. His results are shown in Table 6.2. Because of the existing uncertainty, two different sets of elastic properties data were suggested to be applied in geomechanical modeling: stiff elastic properties and soft elastic properties of the rock. Values listed in Table 6.2, which are based on these scenarios, have been used for induced stress change analysis in this research. It is interesting to note that recent, unpublished work conducted by EnCana has suggested that the stiff elastic property scenario is more likely. However, as will be shown later, Young's modulus does not have a significant effect on the results of poroelastic stress

change analysis and Poisson's ratio plays the main role. Due to the similarity of values for this parameter in both the soft and stiff property cases, the results for induced stress change analysis are representative for either case.
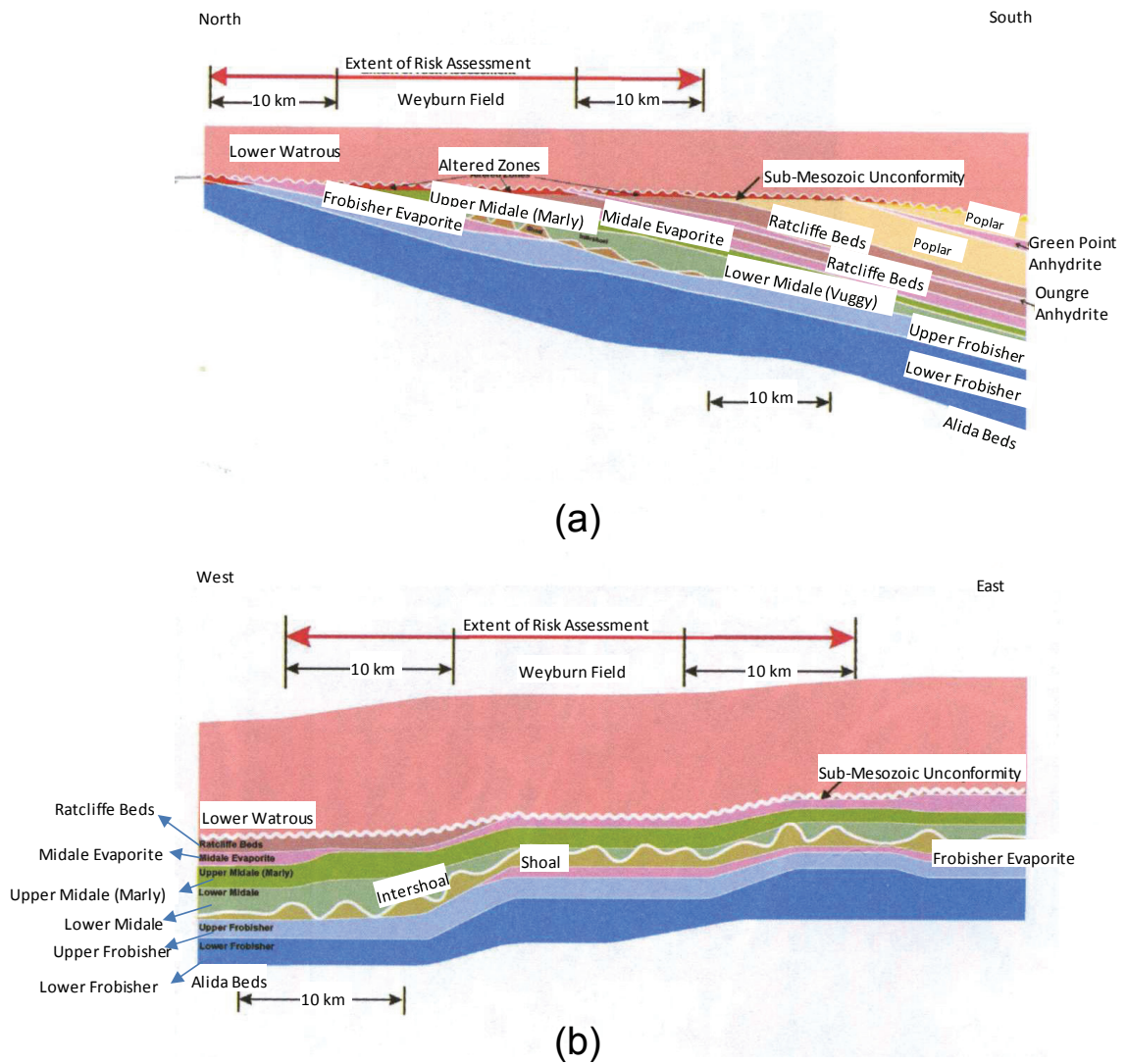
Figure 6.28. Schematic geological profile of Weyburn field in (a) north-south direction and (b) west-east direction (from Whittaker et al., 2004)
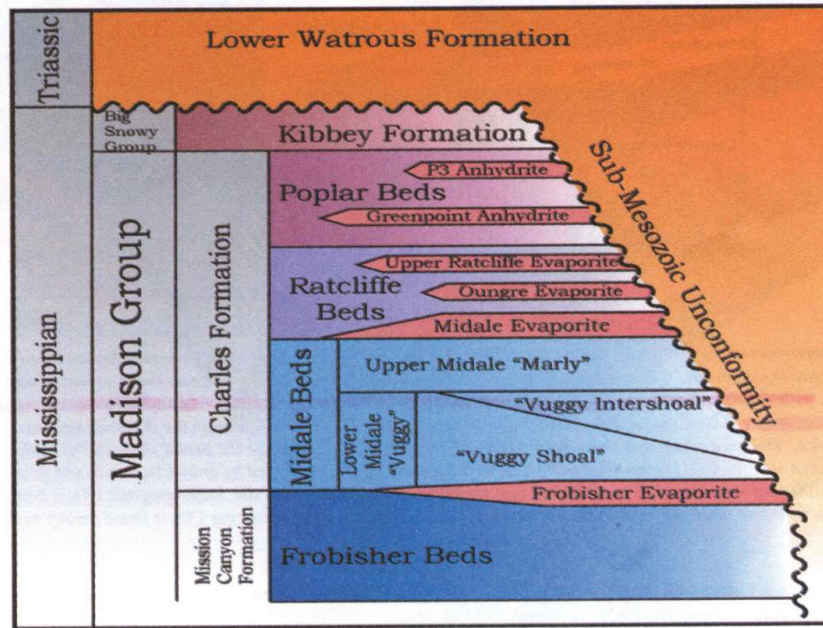
Figure 6.29. Profile of Mississippian group of geological setting in Weyburn field which contain the Weyburn reservoir (From Whittaker et al., 2004)

Table 6.2. Geomechanical properties for Weyburn reservoir and surrounding rock (after Jimenez, 2006)

Formation	Soft properties			Stiff properties			Coulomb properties	
	Young's modulus (GPa)	Poisson's ratio	Shear modulus (GPa)	Young's modulus (GPa)	Poisson's ratio	Shear modulus (GPa)	Friction angle	Cohesion (MPa)
Midale Evaoprite	22.7	0.26	9.0	61.3	0.28	23.9	44.4	18.15
Marly	10.3	0.29	4.0	33.4	0.29	12.9	40	3.5
Upper Vuggy	18.3	0.31	7.0	54.8	0.31	20.9	46.8	3.5
Lower Vuggy	15.4	0.29	6.0	48.7	0.28	19.0		
Frobisher Evaporite	15.8	0.31	6.0	51.6	0.29	20.0	44.4	18.15

6.6.3. In-situ stress state and reservoir pressure history

The orientation of horizontal in-situ stresses can be estimated from the orientations of natural fractures and borehole breakouts. Through studying natural fractures at different depths in the Williston basin, Stauffer and Gendzwill (1987) showed that there are two sets of vertical fractures with average azimuths of 49° and 139°. A study on cores from the Weyburn field by Churcher and Edmunds (1994) showed that the dominant fractures are vertical to sub-vertical, and oriented NE-SW. In a study on borehole breakouts in a nearby oil field (i.e., Midale Field), Bunge (2000) showed an azimuth of 40-50° for the maximum horizontal stress. A study on in-situ stress orientations in the Viking formation in southwest Saskatchewan gave an average azimuth of 47° for the maximum horizontal stress orientation (Hawkes and Hamid, 2008). In the current study an azimuth of 45° has been considered for the maximum horizontal stress orientation. This is consistent with all of the aforementioned study results, and also with the tectonic history of the Western Canada Sedimentary basin (i.e., this orientation is roughly normal to the trend of the Rocky Mountains).

Unfortunately, there are no direct measurements of in-situ stresses for the Weyburn field in public-domain literature or reports, hence the stress regime is not clear. The results of an investigation of in-situ stress measurements and tectonic structure of the Western Canada Sedimentary Basin by Bell and Babock (1986) suggested that the Weyburn field is located near the boundary between strike-slip and normal fault stress regimes (see Figure 6.30).

The only major fault believed to exist in the field, the Souris River fault, is a fault with a vertical surface which is located in Mississippian and Precambrian strata (Whittaker et al., 2004). This indicates that a strike-slip stress regime might have existed at the time that this fault formed. However, normal faulting has been observed in southern Saskatchewan (Gendzwill and Stauffer, 2006). These discrepencies highlight the requirement of considering uncertainty in any geomechanical analysis of this field.
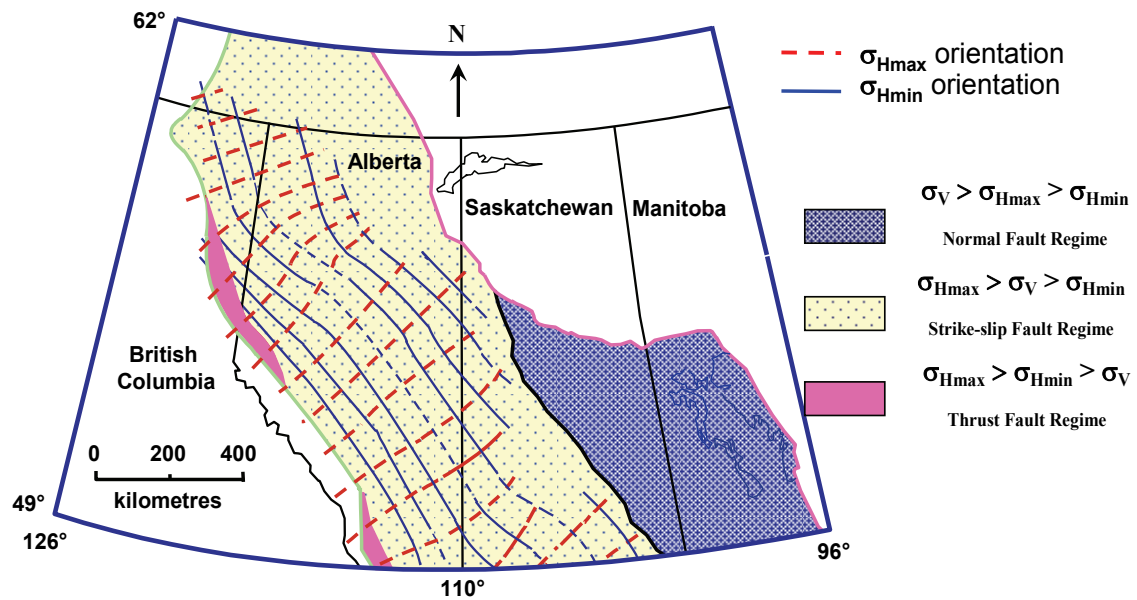
Figure 6.30. Stress regimes and horizontal stress orientations interpreted for the Western Canada Sedimentary Basin (after Bell and Babcock, 1986; Bell et al., 1994).

An average secant gradient of 23 kPa/m was calculated by Chalaturnyk et al. (2003) for vertical in-situ stress close to the Weyburn reservoir level. A study of stress regime in the Viking formation shows values in the 21 to 22 kPa/m range for the secant gradient of vertical stress roughly 100 km west of the Weyburn field (Hawkes and Hamid, 2008). McLellan (1996) suggests a secant gradient of 25 kPa/m for the vertical in-situ stress in the nearby Midale oil field. Jimenez (2006) assumed a value of 24 kPa/m for the vertical in-situ stress secant gradient.

Chalaturnyk et al. (2003) suggest the value of 15.5 kPa/m as a lower bound for the minimum horizontal stress secant gradient, based on mud densities used while drilling. Hawkes and Hamid (2008) found that the minimum horizontal in-situ stress is very depth-sensitive in the Swift Current, Saskatchewan area (roughly 200 km west of the Weyburn field). They found secant gradients of 16 to 19 kPa/m for depths between 1.0 and 1.25 km in the Viking Formation. A value of 16 kPa/m was reported by McLellan (1996) in the nearby Midale oil field. Jimenez (2006) used a value of 18 kPa/m for this parameter in his geomechanical modeling of the Weyburn reservoir.

To calculate the maximum horizontal stress, Chalaturnyk et al. (2003) suggested a lateral pressure coefficient (K_0) between 1.0 and 1.5 (i.e., equivalent to a gradient between 23 and 34.5 kPa/m). Micro-fracturing tests conducted at a depth of about 2.2 km in the Deadwood Formation in Regina show that the value of maximum horizontal stress is equivalent to vertical stress and 1.33 times more than minimum horizontal stress (Bell et al., 1994). This is consistent with the transitional stress regime between normal and strike-slip stress regime interpreted by Gendzwill and Stauffer (2006). Jimenez (2006) used the frictional equilibrium approach with a friction coefficient (μ_s) of 0.6 for a strike-slip faulting stress regime and calculated a upper-bound of 28 kPa/m for the maximum horizontal stress gradient.

In this research, similar to Jimenez (2006), to account for the existing uncertainty in the in-situ stress data, different in-situ stress scenarios will be considered. However, the most probable strike-slip scenario will be treated as the base-case scenario (Table 6.3). Values of the in-situ stresses in these scenarios are based on the assumption of Jimenez (2006).

Figure 6.31 shows the history of reservoir pressure change during the reservoir's exploitation life (up to 2001). The initial pressure in the reservoir was 14.5 MPa. The

Table 6.3. Different scenarios for in-situ stresses in the Weyburn field (after Jimenez, 2006)

In-situ Stress Regime scenario	Vertical stress gradient (kPa/m)	Minimum horizontal stress gradient (kPa/m)	Maximum horizontal stress gradient (kPa/m)
Strike-slip**	24	18	28
Isotropic	24	24	24
Normal	24	18	24
Thrust	24	33	33

** Base case scenario
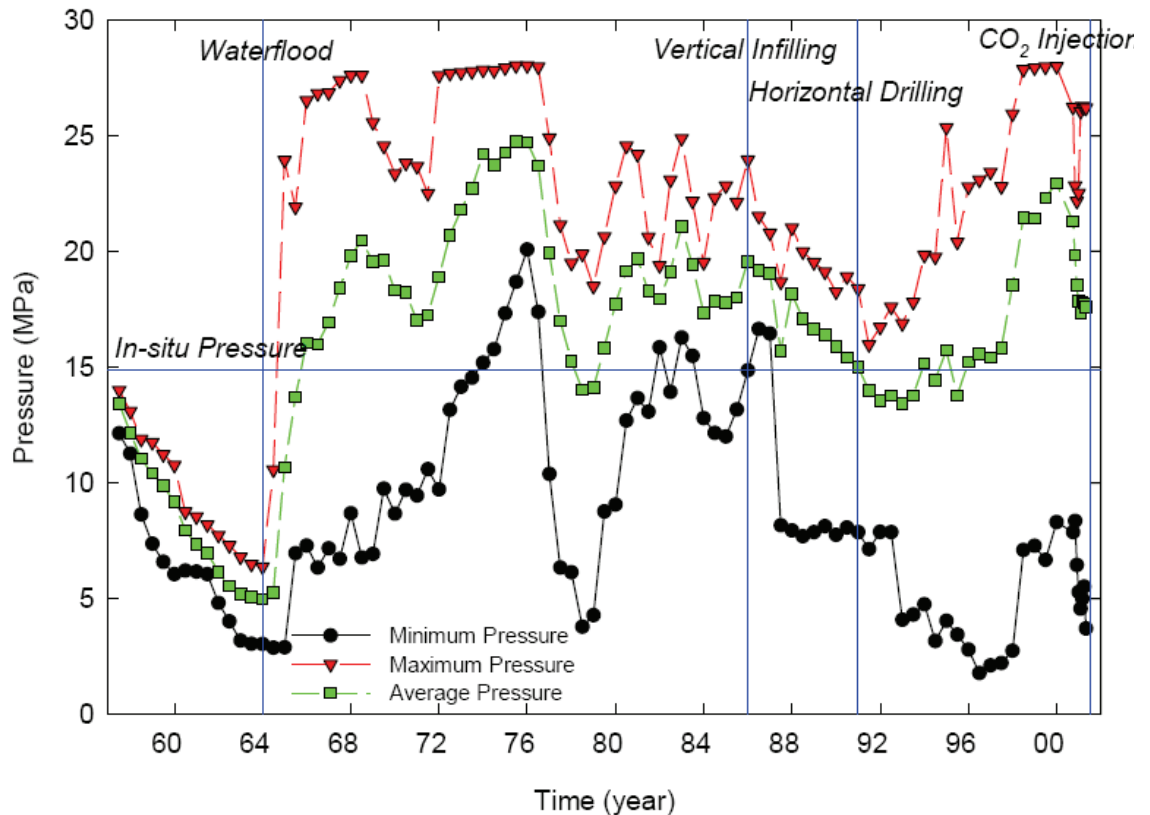
Figure 6.31. Reservoir pressure history for Weyburn oil field (from Jimenez, 2006)

reservoir pressure locally reached a minimum of 2.5 MPa in 1965, after several years of primary production. It has subsequently reached a maximum of about 28 MPa at various points in time due to fluid injection (i.e., waterflooding). Although limited information has been published about reservoir pressures during CO_2 injection, it is believed that pressures during this phase are likely to approach these historical highs. Therefore, representative upper-limits of pressure change (ΔP) in this work are considered to be -12 and 13 MPa, respectively, for production and injection.

6.6.4. Induced stress change analysis

Although the models in Chapter 4 have been developed for homogeneous reservoirs, as it will be shown later, they still can be applied for some specific heterogeneous reservoirs such as Weyburn reservoir. The Weyburn reservoir has a very small thickness compared to its lateral extents, and its aspect ratio (e) has been estimated

as less than 0.005 in this work. Therefore, it can be treated as an infinite layer. Following, the validity of this assumption is evaluated by studying the effects of depth and reservoir heterogeneity on the induced stress change within the reservoir. Later, a numerical model will be used to confirm these results.

Figure 6.32 shows how an assumption of a full-space boundary condition might affect arching ratios within a reservoir with Weyburn's geometry where the theory of inclusions (section 3.5.1) is used to calculate arching ratios. Obviously, noting the tight y-axis scale used on this graph, the effect of depth on arching ratios is negligible. Therefore, the theory of inhomogeneities, which has been developed for a full-space (section 3.6.1), can be used to study the effect of heterogeneity on the geomechanical response of the reservoir.

Figure 6.33 shows the variation in arching ratios as a function of shear modulus
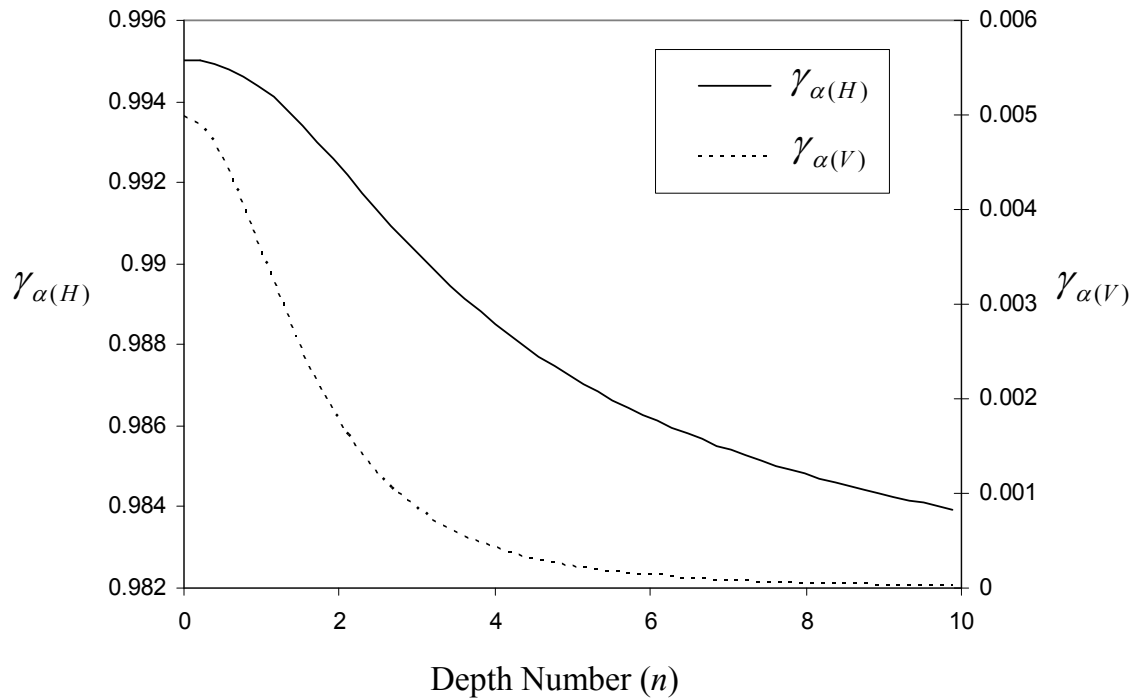
Figure 6.32. Variation of horizontal and vertical stress arching ratios as a function of depth number calculated for the Weyburn field using the theory of inclusions. All the results have been normalized by $(1-2\nu)/(1-\nu)$.

201

ratio calculated using the theory of inhomogeneities. From Table 6.2 the possible range for shear modulus ratio (R_μ) is between 0.4 and 3.5. Figure 6.32 illustrates that, for this range of R_μ, the contrast between the reservoir and its surrounding layer has a very negligible effect on the value of arching ratios. This shows that the heterogeneity of the reservoir does not have a significant effect on its geomechanical response.

Comparing values of horizontal and vertical arching ratios in both Figures 6.32 and 6.33 with values obtained from equation (3-105) shows that the assumption of an infinite layer for the reservoir can be used without any significant error in induced stress change analysis. Using the formulae for an infinite layer (i.e., equation (3-105)) and the mechanical properties presented in Table 6.2, a value of zero is calculated for vertical arching ratio in the entire field and values of 0.60, 0.55, 0.60 and zero, respectively, are calculated for the Marly unit, Upper Vuggy unit, Lower Vuggy unit, and the surrounding rock. It is important to know that zero stress change in the surrounding rock is based on assumption of no pore pressure change in surrounding rock. However, pore pressure change is expected in a limited zone adjacent to the reservoir. This pore pressure change can be determined using a coupled fluid flow-geomechanical model.
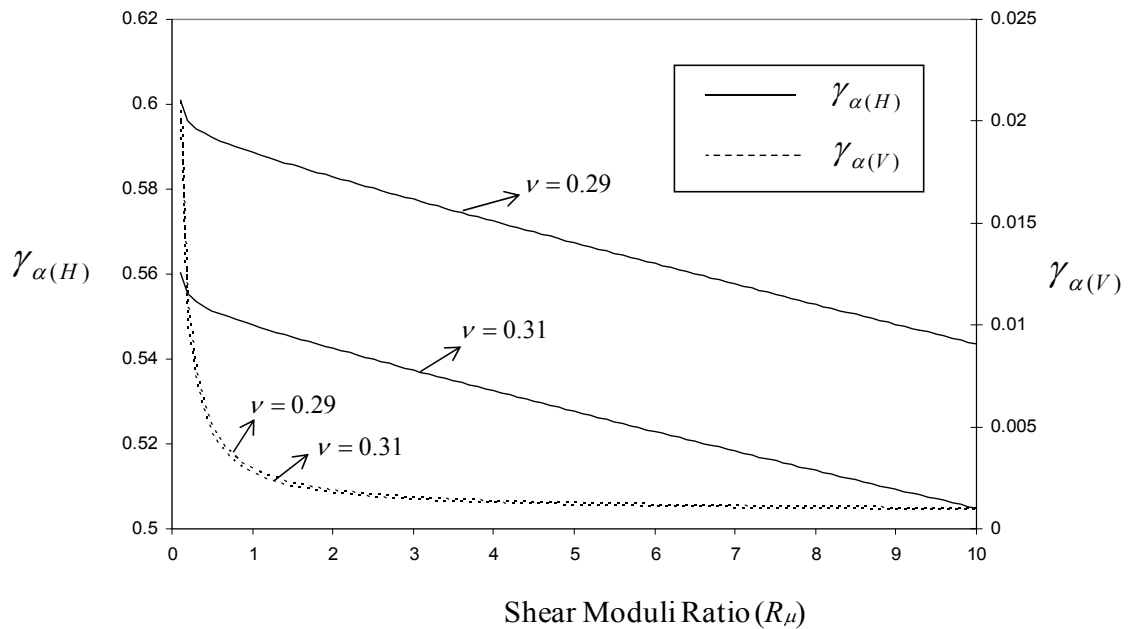
Figure 6.33. Variation of horizontal and vertical stress arching ratios as a function of shear modulus ratio calculated for Weyburn field using theory of inhomogeneities.

The values of arching ratios found above are slightly different from the results found by Jimenez (2006) by implementing FLAC3D as a numerical model. His results show values of 0.53, 0.43, and 0.51 for arching ratios respectively in Marly, Upper Vuggy and Lower Vuggy units. In his model, Jimenez (2006) assumed the reservoir and surrounding rock to be horizontal layers with infinite extension. Due to the uniform assumption of reservoir pressure change, the deformation in this model is expected to behave uniaxially. This behavior means that we can also use a 2D model without losing the accuracy in the results. Therefore, a 2D numerical analysis using FLAC (Figure 6.34) was performed in this research to find the possible reasons for the observed differences in arching ratios. The base-case geometry is the same as Jimenez's (2006) assumption with a thickness of surrounding rock equal to 36m. In other scenarios, this thickness is changed to study the effect of boundary conditions on the model.
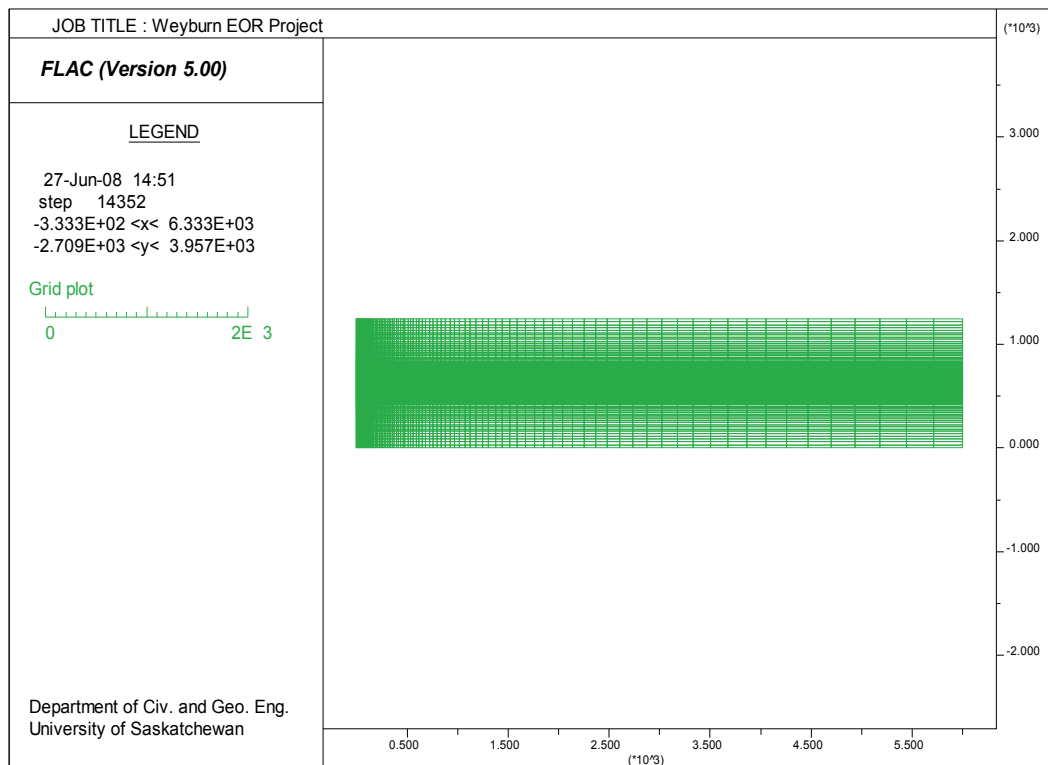
Figure 6.34. FLAC grid for Weyburn oil field

Figures 6.35a to 6.35d demonstrate the profile of horizontal stress change as the result of 1.0 MPa pore pressure change within the reservoir while the surrounding (i.e., overlying and underlying) rock's thickness is respectively 36 m, 100m, 200 m , and 400 m [Note: modeling the stress response using 1.0 MPa pore pressure change means that the resultant stress changes, although dimensional in nature, are numerically equivalent to stress arching ratios.]. Obviously, by increasing in the thickness of surrounding rock (i.e., being closer to the real geometry of the field), the horizontal arching ratios converge to limiting values which are exactly the values predicted by the analytical model. This study shows the importance of choosing the appropriate boundary condition for the numerical model which may be the primary reason for the difference between the results obtained from Jimenez's (2006) numerical model and the analytical model used in this research. Moreover, the coarse grid size (i.e., 12 m vertically and 60 m horizontally) used by Jimenez (2006) could be another reason for the difference.

Aside from validating the magnitude of induced stress change within the reservoir (when using a suitable model geometry), the numerical results presented here also confirm the analytical model's predictions of negligible stress change outside of the reservoir.

6.6.5. Fault reactivation analysis

Stress change analysis conducted for the geometry considered in this work shows that there is no stress change in the surrounding rock. This result, coupled with the assumption of no pressure change in this region, leads to the prediction of no fault reactivation in the surrounding rock. However, within the reservoir there is a potential for fault reactivation which can be analysed for different in-situ stress regime scenarios. The poroelastic stress change analysis in the previous section gives arching ratios of 0.59 for Marly and Lower Vuggy units, and 0.55 for Upper Vuggy unit. However, due to possible hysteresic behaviour of the reservoir during injection, the reservoir might not behave poroelastically. As a lower bound, an arching ratio of zero was considered to replicate the effect of this possible behaviour. Using the methodology described in section 4.7.2 it is possible to calculate the critical pressure change for fault reactivation.
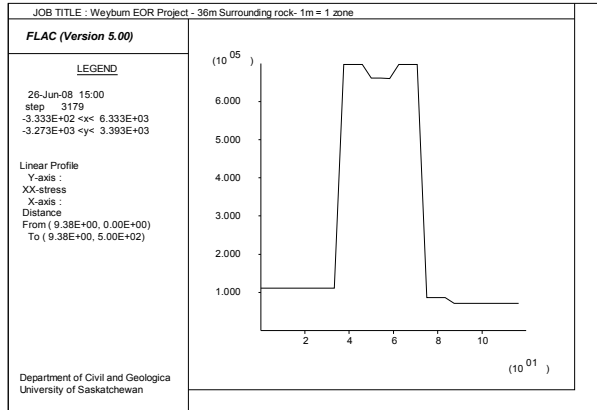
(a)
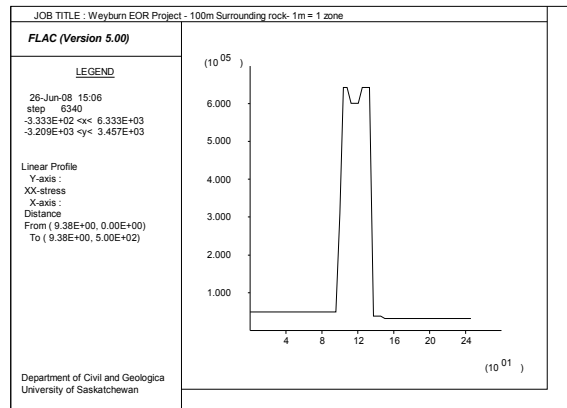
(b)
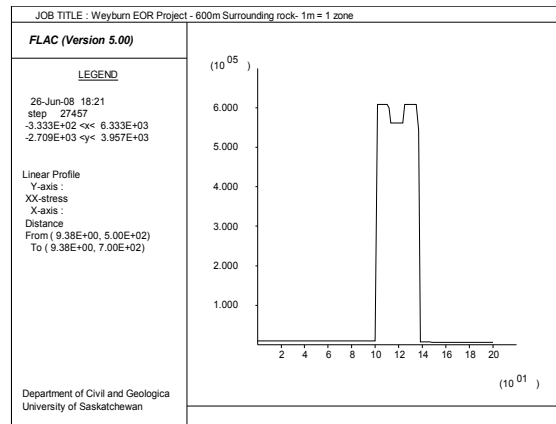
(c)

Figure 6.35. Horizontal stress change (in MPa) induced by a 1 MPa reservoir pressure change, plotted along a vertical cross-section at the reservoir mid-point, for a surrounding rock thickness of (a) 36m (similar to Jimenez's (2006) assumption); (b) 100m; (c) 200m; and (d) 400m. [Note: The "U" shaped stress peak is a result of the mechanical property contrast between the Upper Vuggy unit and the overlying Marly unit and underlying Lower Vuggy Unit (the latter of which have similar properties)].

JOB TITLE : Weyburn EOR Project - 200m Surrounding rock- 1m = 1 zone

FLAC (Version 5.00)

LEGEND

26-Jun-08 15:31
step   17901
-3.333E+02 <x< 6.333E+03
-3.109E+03 <y< 3.557E+03

Linear Profile
  Y-axis :
  XX-stress
  X-axis :
  Distance
  From (9.38E+00, 0.00E+00)
    To (9.38E+00, 5.00E+02)

Department of Civil and Geologica
University of Saskatchewan
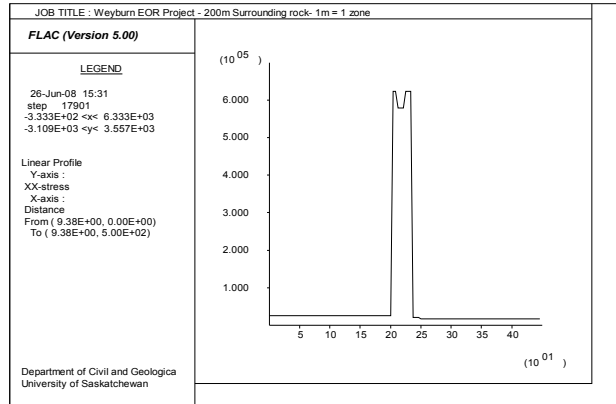
(d)

Figure 6.35. (Continued) Horizontal stress change (in MPa) induced by a 1 MPa reservoir pressure change, plotted along a vertical cross-section at the reservoir mid-point, for a surrounding rock thickness of (a) 36m (similar to Jimenez's (2006) assumption); (b) 100m; (c) 200m; and (d) 400m. [Note: The "U" shaped stress peak is a result of the mechanical property contrast between the Upper Vuggy unit and the overlying Marly unit and underlying Lower Vuggy Unit (the latter of which have similar properties)].

The results of analyses for these different scenarios of stress change are shown in Figures 6.36 to 6.39 for strike-slip, isotropic, normal, and thrust stress regime scenarios, respectively (see Table 6.3 for details). Minimum critical pressures required for fault reactivation in different scenarios are listed in Table 6.4.

This author believes that the most likely scenario for in-situ stress state in Weyburn field is strike-slip. As shown in Figure 6.36a to 6.36c and Table 6.4, the minimum critical pressure for fault reactivation in this scenario (19.3 or 25.5 MPa) is less than the maximum historical value occurring in this reservoir. However, the only identified major fault in the Weyburn field is the Souris River fault is vertical and strikes NNW-SSE (Whittaker et al., 2004). For this specific fault, the critical pressure for reactivation is significantly higher than the maximum reservoir pressure if the field behaves poroelastically (Figures 6.36a and 6.36b) however if no stress change has occured during injection (Figure 6.36c), reservoir pressures exceeding 19.3 MPa would have reactivated this fault. Although it appears possible that fault reactivation may have occurred during historical waterflooding operations, no micro-seismic monitoring was conducted to confirm or refute this. In the near future, once the results of recent micro-

seismic monitoring are published, it may be possible to use these results to refine the models and input data (esp. in-situ stress magnitudes) used in this research. More importantly, if micro-seismic activity is observed and recorded, event locations could confirm the expectation that fault reactivation is confined to the reservoir, hence having no impact on caprock integrity.

Comparing results for different stress regime scenarios reveals some interesting facts about changes which happen as a result of induced stress change within the reservoir. For the case of poroelastic stress change (i.e., $\gamma_{\alpha(H)}$=0.55 or $\gamma_{\alpha(H)}$=0.60), the stress change during injection is anisotropic in such a way that the vertical effective stress decreases more than the horizontal effective stress, hence the initial in-situ stress regime tends towards a thrust fault stress regimes. The consequence of this result on fault reactivation can be seen in Figures 6.36 to 6.39 which shows that in the condition of poroelastic stress change the most critical faults are the ones which are oriented in favour of thrust faulting. In other words, they have low dip angles and strikes that parallel the initial minimum horizontal stress orientation. When there is no stress change (i.e., $\gamma_{\alpha(H)}$=0), as expected, the initial in-situ stress state remains unchanged during injection.
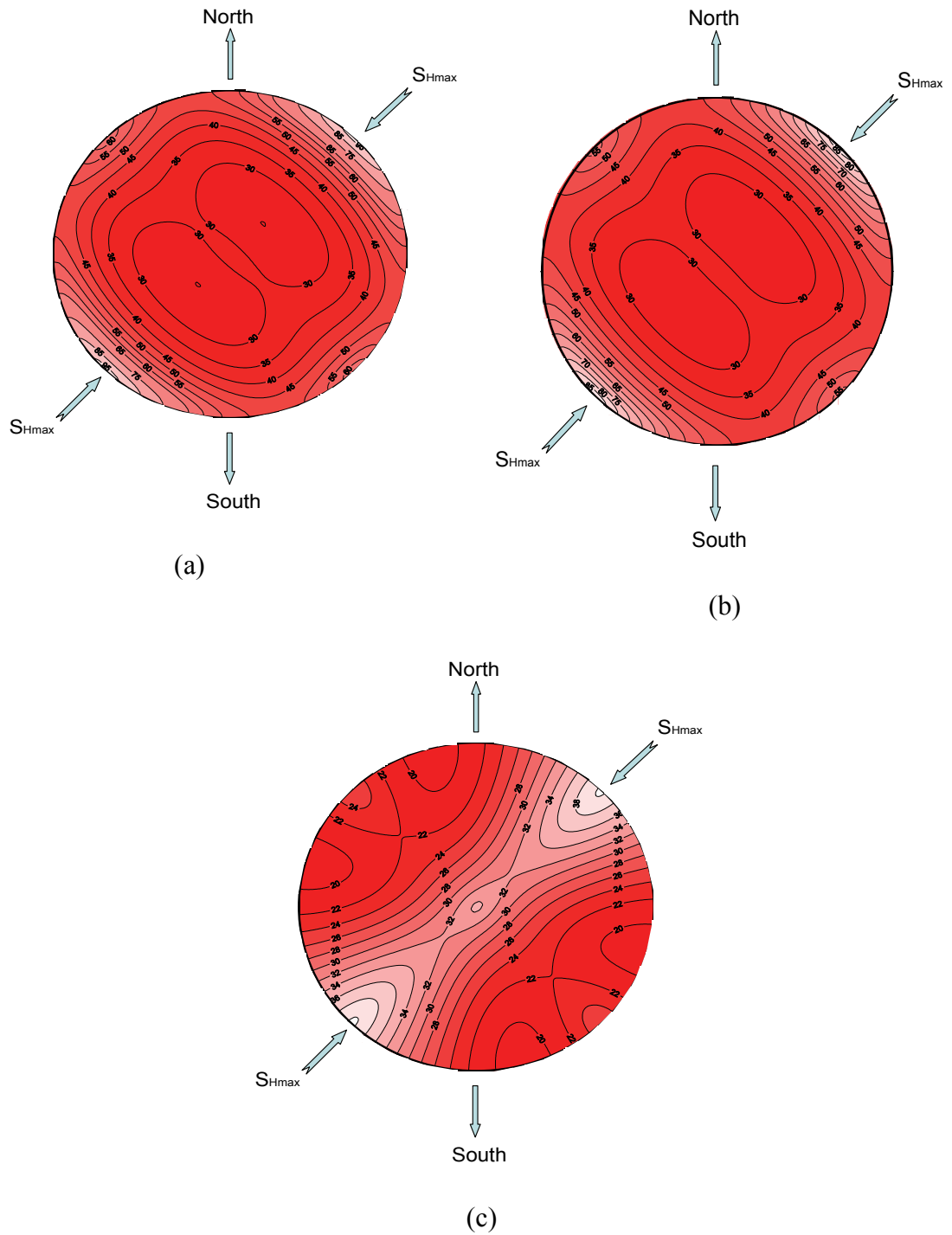
Figure 6.36. Contours of critical pressure for fault reactivation in the strike-slip stress regime scenario for (a) arching ratio=0.6 (b) arching ratio=0.55 (c) arching ratio=0. (Equal angle, lower hemisphere stereographic projection for poles to fault or fracture planes .)
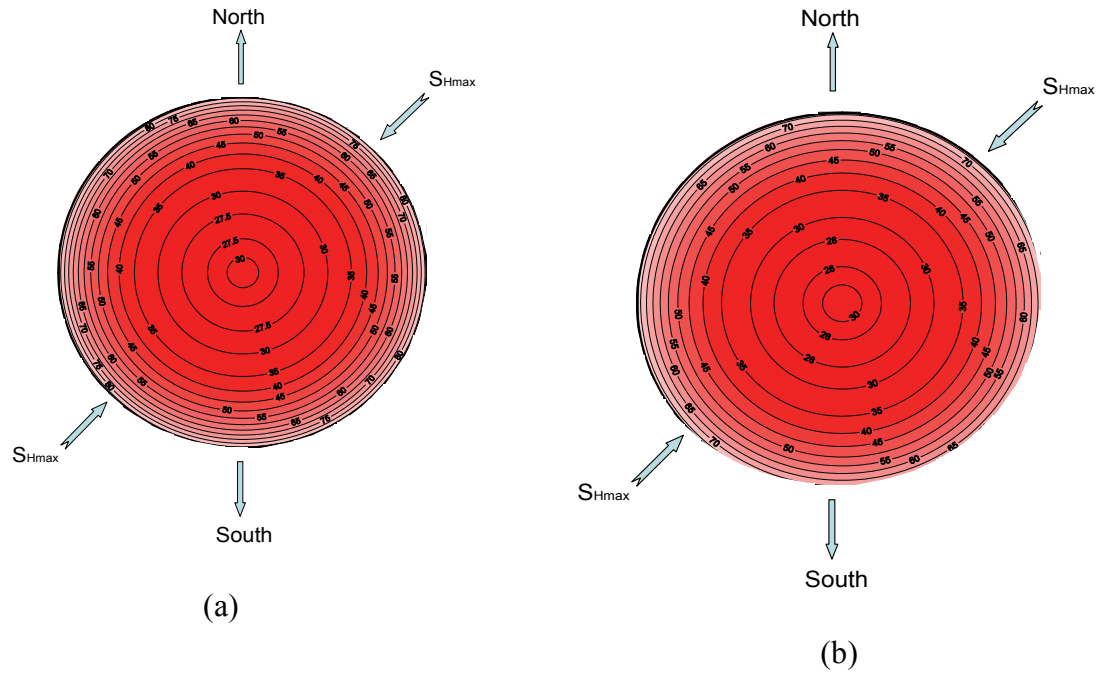
Figure 6.37. Contours of critical pressure for fault reactivation in the isotropic stress regime scenario for (a) arching ratio=0.6 (b) arching ratio=0.55. (Equal angle, lower hemisphere stereographic projection for poles to fault or fracture planes.)
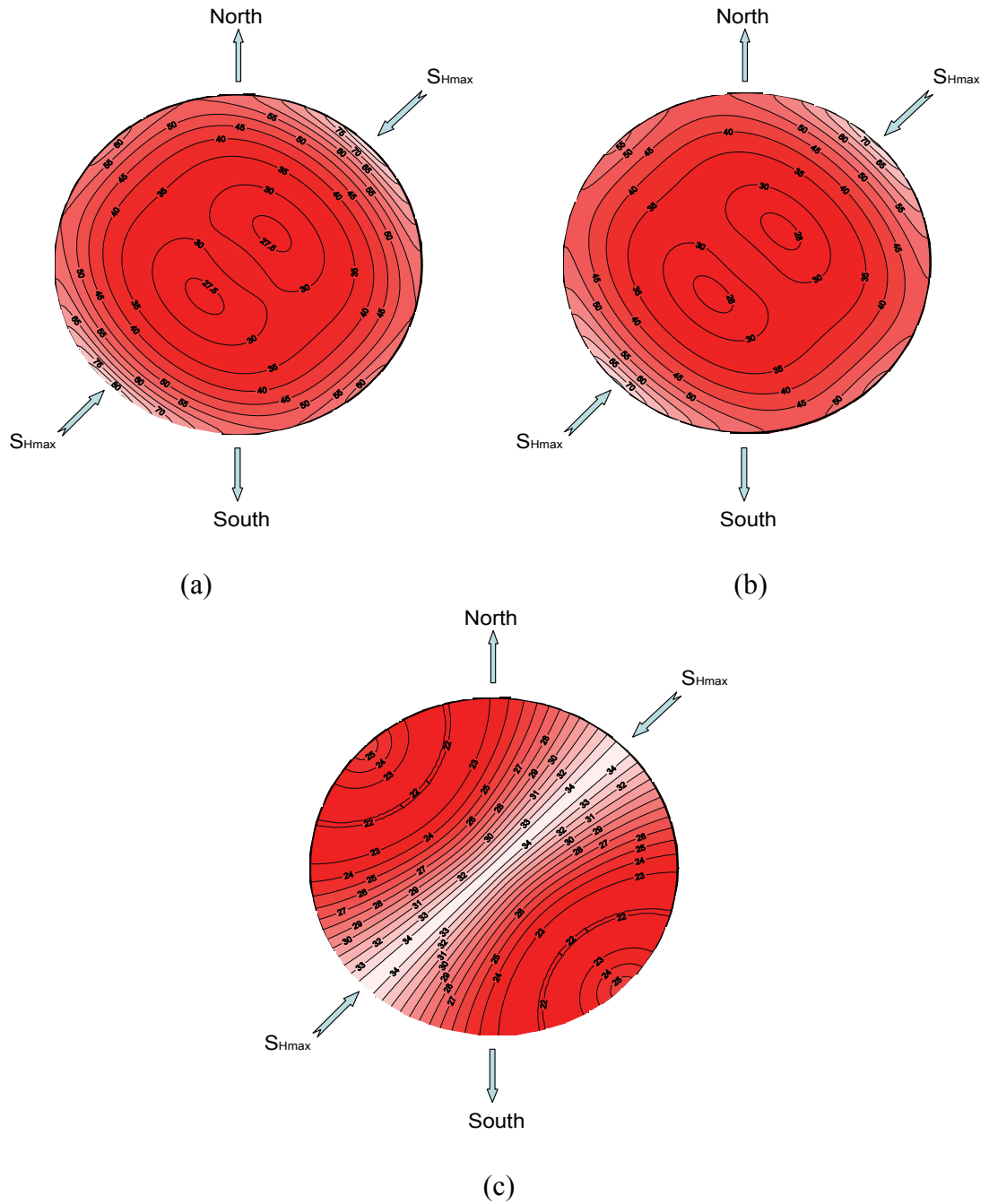
Figure 6.38. Contours of critical pressure for fault reactivation in the normal stress regime scenario for (a) arching ratio=0.6 (b) arching ratio=0.55 (c) arching ratio=0. (Equal angle, lower hemisphere stereographic projection for poles to fault or fracture planes.)
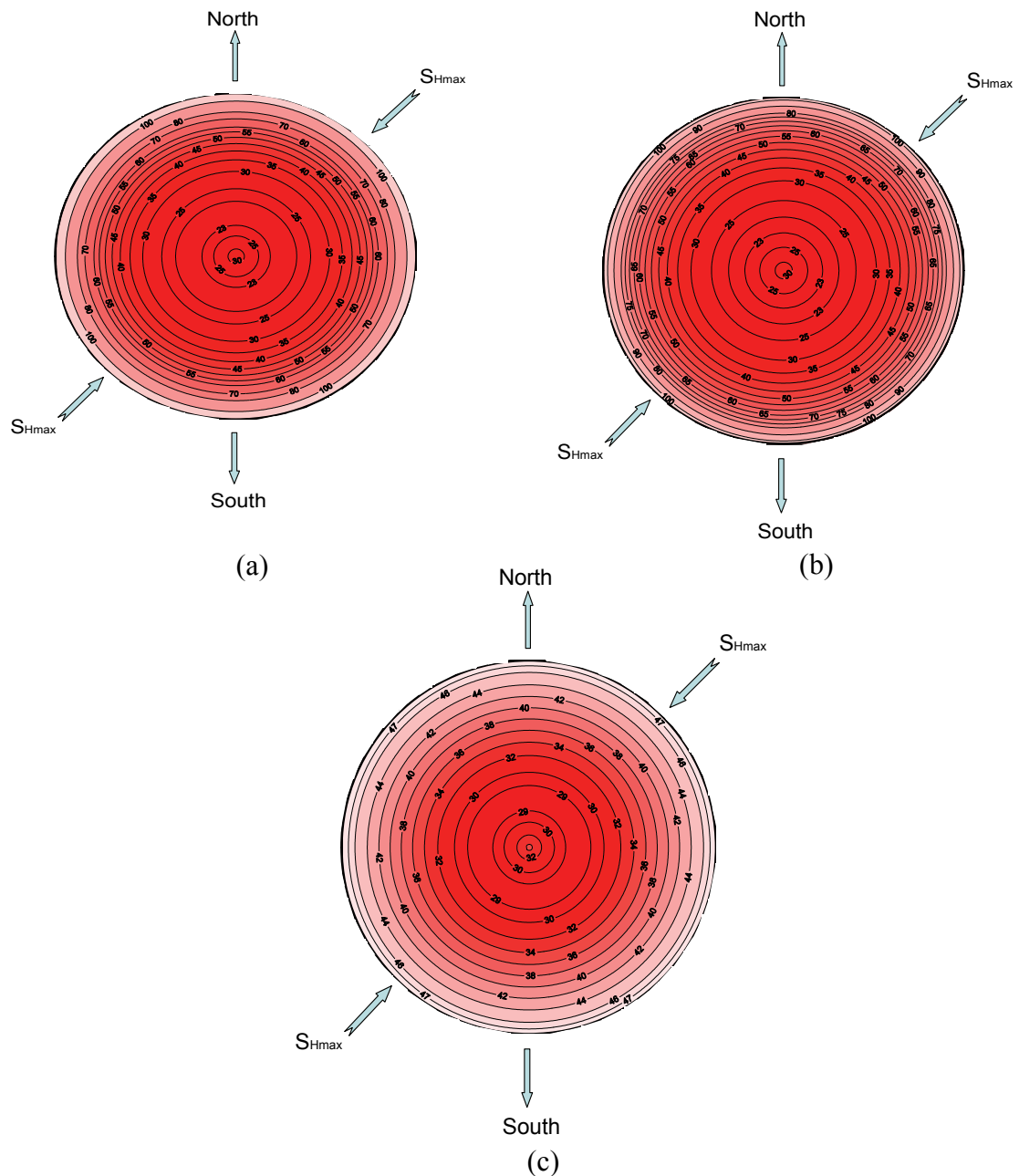
Figure 6.39. Contours of critical pressure for fault reactivation in thrust stress regime scenario for (a) Arching ratio=0.6 (b) arching ratio=0.55 (c) arching ratio=0. (Equal angle, lower hemisphere stereographic projection for poles to fault or fracture planes.)

6.6.6. Induced fracturing analysis

The poroelastic models implemented for stress analysis show no stress change in the surrounding rock, which means that no induced fracturing is predicted in this region. However, there is a possibility of induced fracturing within the reservoir. The critical

Table 6.4. Minimum critical pressure for fault reactivation for different stress regime scenarios

Stress Regime scenario	Minimum critical pressure for fault reactivation (MPa)		
	$\gamma_{\alpha(H)}$=0.6	$\gamma_{\alpha(H)}$=0.55	$\gamma_{\alpha(H)}$=0
Strike-slip	25	25.5	19.3
Isotropic	27.1	27.6	Not Possible
Normal	27.1	27.6	22
Thrust	22.3	22.7	28.6

pressure change for shear fracturing in this region can be calculated by implementing either Coulomb or Drucker-Prager failure criteria as described in section 5.4. The main difference between these two criteria is the fact that the Coulomb criterion does not consider the effect of intermediate principal stress on failure.

The critical pressure changes for different in-situ stress scenarios are shown in Table 6.5 for both Coulomb and circumscribed Drucker-Prager failure criteria. This table includes calculated critical pressure change for tensile fracturing and shear fracturing. Critical pressure change for shear fracturing in this table has been calculated by considering both the subscribed Drucker-Prager and Coulomb failure criteria. [Note: Results based on the inscribed Drucker-Prager failure criterion are not included in this table because its predictions for critical pressure change seem unrealistically far from the Coulomb failure criterion.] For some cases the difference between predicted values for two different failure criteria is significant, which demonstrates the significant role of intermediate principal stress. For the most likely scenario (i.e., strike-slip stress regime). the Coulomb failure criterion predicts a value of ΔP_f=19.6 MPa when the stress is changing poroelastically during injection, while for the case of no stress change the dominant mode of fracturing is tensile and occurs at ΔP_f=11.6 MPa. The significant difference between the two conditions of stress change (i.e., poroelastic stress change and no stress change) highlights the requirement of suitable tests and measurements to assess the potential hysteretic behaviour of the rock during injection and production.

Table 6.5. Critical pressure change for shear and tensile fracturing within the Weyburn reservoir

In-situ Stress scenario	Layer	Critical pressure change for shear fracturing (MPa) Drucker-Prager failure criterion				Critical pressure change for shear fracturing (MPa) Coulomb failure criterion						Critical pressure change for tensile fracturing (MPa)						Critical Pressure change for fracturing (MPa)			
		Circumscribed		Inscribed		$\sigma_{Hmax} - \sigma_{Hmin}$ Plane		$\sigma_{Hmax} - \sigma_v$ Plane		$\sigma_v - \sigma_{Hmin}$ Plane		For fracturing plane normal to σ_{Hmax}		For fracturing plane normal to σ_{Hmin}		For fracturing plane normal to σ_v		Minimum (Circumscribed Drucker-Prager vs. tensile)		Minimum (Coulomb vs. tensile)	
		No stress change	Elastic	No stress change	Elastic	No stress change	Elastic	No stress change	Elastic	No stress change	Elastic	No stress change	Elastic	No stress change	Elastic	No stress change	Elastic	No stress change	Elastic	No stress change	Elastic
Strike - slip	Marly	8.7	11.4	-	-	11.8	28.6	22.9	19.6	13.4	23	26.1	63.7	11.6	28.3	20.3	20.3	8.7	11.4	11.6	19.6
	Upper Vuggy	9.3	12.3	-	-	12.1	26.8	22.7	20.3	13.3	23	26.1	58	11.6	25.8	20.3	20.3	9.3	12.3	11.6	20.3
	Lower Vuggy	9.3	12.2	-	-	12.1	29.5	22.7	20.1	13.3	22.8	26.1	63.7	11.6	28.3	20.3	20.3	9.3	12.2	11.6	20.1
Isotropic	Marly	32.8	19.4	32.8	14.4	24.5	59.7	24.5	21	24.5	21	20.3	49.5	20.3	49.5	20.3	20.3	20.3	19.4	20.3	20.3
	Upper Vuggy	30.9	20.2	30.9	14.3	23.8	53	23.8	21.4	23.8	21.4	20.3	45.1	20.3	45.1	20.3	20.3	20.3	20.2	20.3	20.3
	Lower Vuggy	30.9	19.7	30.9	14.9	23.8	58.1	23.8	21.3	23.8	21.3	20.3	49.5	20.3	49.5	20.3	20.3	20.3	19.7	20.3	20.3
Normal	Marly	14	18.8	5.3	12	13.4	59.7	24.5	21	13.4	23.1	20.3	49.5	11.6	28.3	20.3	20.3	11.6	18.8	11.6	20.3
	Upper Vuggy	13.8	19.1	5.1	11.7	13.3	53	23.8	21.4	13.3	23	20.3	45.1	11.6	25.8	20.3	20.3	11.6	19.1	11.6	20.3
	Lower Vuggy	13.8	18.8	5.1	11.7	13.3	58.1	23.8	21.2	13.3	22.8	20.3	49.5	11.6	28.3	20.3	20.3	11.6	18.8	11.6	20.3
Thrust	Marly	17.6	10.4	4.5	2	37.5	91.5	20.8	18.1	20.8	18.1	33.4	81.3	33.4	81.3	20.3	20.3	17.6	10.4	20.3	17.9
	Upper Vuggy	18.3	12	5.3	2.5	36.4	82	21.1	19.5	21.1	19.5	33.4	74.1	33.4	74.1	20.3	20.3	18.3	12	20.3	18.9
	Lower Vuggy	18.3	11.7	5.3	2.5	36.4	90	21.1	19.4	21.1	19.4	33.4	81.3	33.4	81.3	20.3	20.3	18.3	11.7	20.3	18.8

6.6.7. Temperature-induced stress change and fault reactivation

Temperature changes induced by injection might have a significant geomechanical effect on the reservoir. Segall and Fitzgerald (1998) show that in geothermal reservoirs thermal stresses during steam production might be eight times (or more) larger than poroelastic stresses. Noorishad and Tsang (1987) suggest that injection might decrease the hydrofracturing pressure by 10 MPa. The significant impact of temperature change on in-situ stresses was also shown by Jimenez (2006).

To study the geomechanical effect of temperature change on the reservoir and surrounding rock in the Weyburn field the concept of thermoelastic arching ratios in section 3.3 was applied and thermoelastic arching ratios were calculated using equation (3.37). The linear expansion coefficient (η) in this work was assumed to be 1.3e-5 $°C^{-1}$, a representative value for limestone, as suggested by Jimenez (2006). Due to the specific geometry of the reservoir (i.e., laterally infinite layer) thermoelastic arching ratios (and consequently thermally induced stresses) in the caprock are zero. In addition, the vertical thermoelastic arching ratio within the reservoir is zero. Horizontal thermoelastic arching ratios within the reservoir were calculated as 0.41, 0.63, and 0.61 MPa/°C respectively for the Marly, Upper Vuggy, and Lower Vuggy units when the soft elastic properties scenario (see Table 6.2) is selected. For the stiff elastic properties scenario these values are 1.33, 1.88, and 2.05 MPa/°C.

In a similar manner to pore pressure change (see sections 4.7.2 and 6.6.5) the calculated arching ratios can be used to calculate the critical temperature change for fault reactivation within the reservoir. Figures 6.40 and 6.41, respectively, demonstrate the results for soft and stiff elastic properties scenarios. The stress regime scenario in these figures is assumed to be a strike-slip regime (i.e., the base case in Table 6.4). As shown in these figures, in the soft elastic properties scenario a temperature change as small as -8 °C is enough to reactivate some of the potentially existing faults in the field. This value is about -2 °C for a stiff elastic properties scenario. For the Souris River fault the

most critical temperature changes are -19 °C and -6 °C for soft and stiff elastic properties scenarios, respectively.

The small values of critical temperature change for fault reactivation show the significant importance of thermo-mechanical analysis in studying caprock integrity for CO_2 sequestration projects. However, the gradual nature of temperature change induced by injection (Segall and Fitzgerald, 1998), convection of temperature change outward of the storage area, the limited area for the zone of influence of temperature change effects (e.g., Jimenez, 2006), nonlinearity, plasticity and discontinuity of the rock, and thermal dependence of geomechanical and fluid properties are among some factors that amplify the complexity of the problem and highlight the importance of more sophisticated studies for thermo-poro-mechnaical analysis.
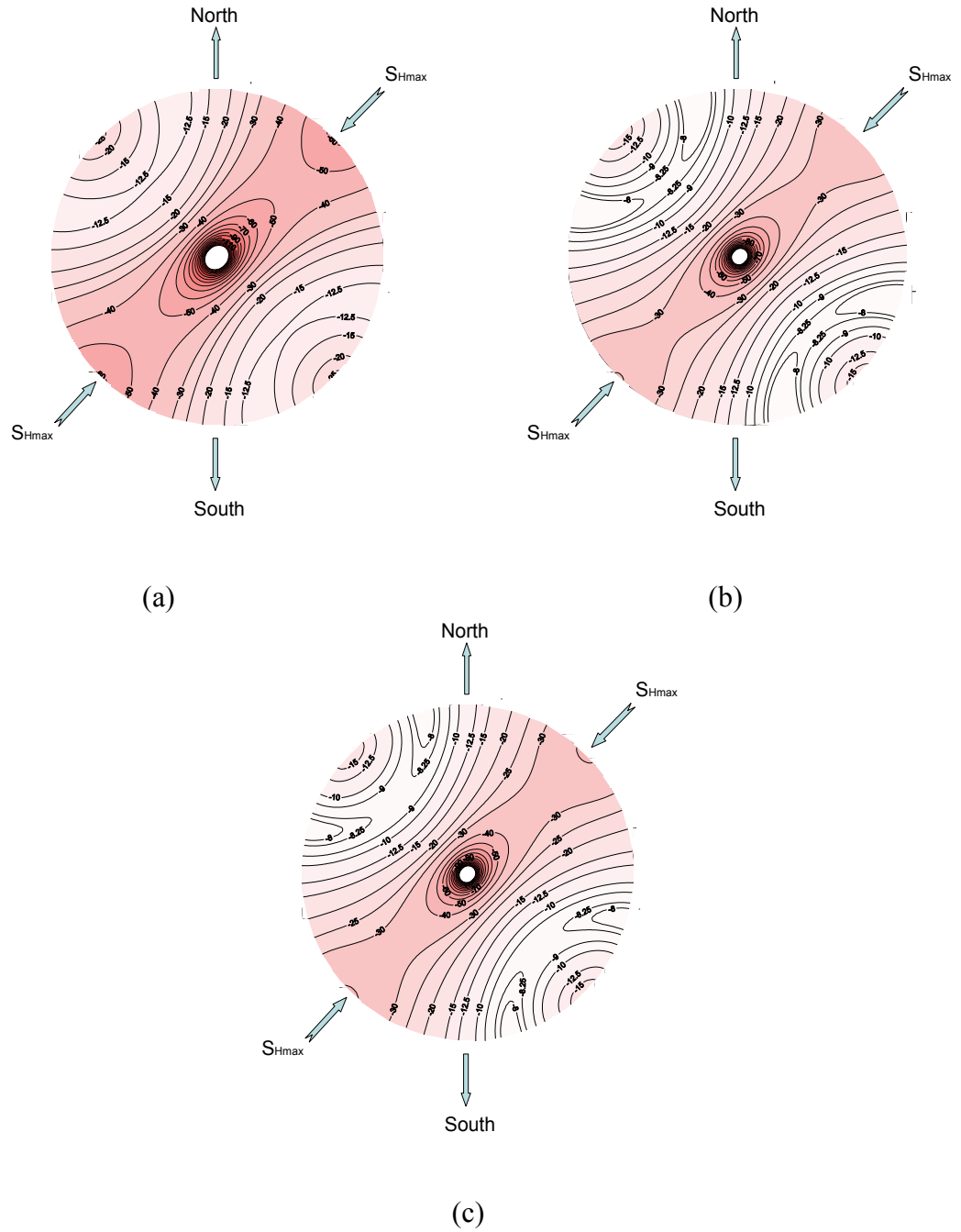
Figure 6.40. Contours of critical temperature change for fault reactivation in the strike-slip stress regime and assuming a soft rock scenario for (a) arching ratio=0.41 (b) arching ratio=0.63 (c) arching ratio=0.61. (Equal angle, lower hemisphere stereographic projection for poles to fault or fracture planes.)
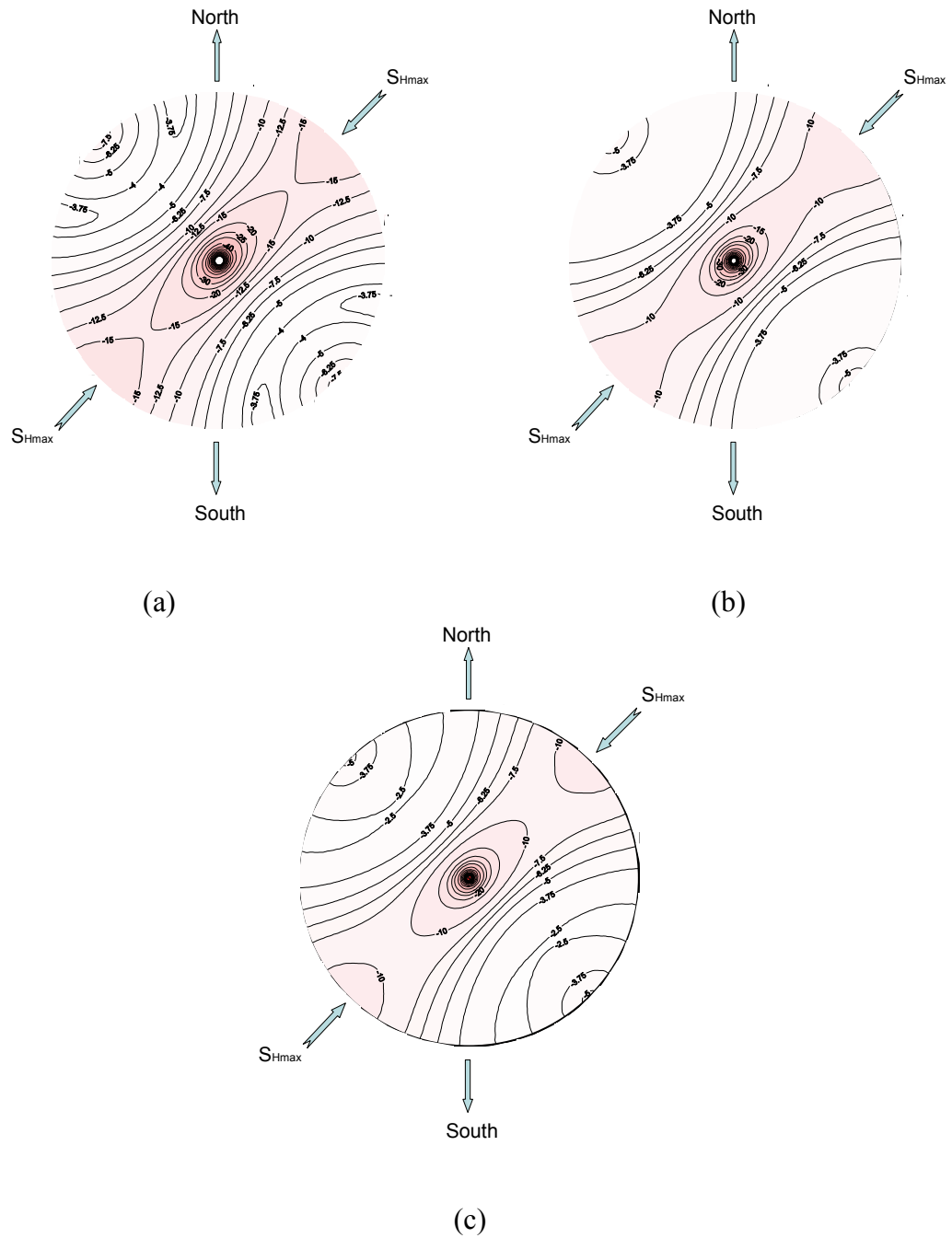
Figure 6.41. Contours of critical temperature change for fault reactivation in the strike-slip stress regime and assuming a soft rock scenario for (a) arching ratio=1.31 (b) arching ratio=1.88 (c) arching ratio=2.05. (Equal angle, lower hemisphere stereographic projection for poles to fault or fracture planes.)

6.7. Fault reactivation and induced fracturing analyses for Zama Acid Gas Injection Project, Alberta

The Zama oil field is located in northwestern Alberta, Canada, and covers an area of $1200 \, \text{km}^2$. The field contains more than 400 pinnacle reefs of the Middle Devonian Keg River Formation. Injection of a stream of acid gas (approximately 70% CO_2 and 30% H_2S) started in December 2006. To date, injection has occurred in four pinnacles; the goal is to inject into several more pinnacles in the coming years. In this section, the effects of geomechanical processes on the hydraulic integrity of a single, representative pinnacle reef is investigated. For the case considered, the reservoir consists of dolomite of varying porosity and permeability. In reality, it is overlain and laterally bounded by anhydrites of the Muskeg Formation, and underlain by lower-porosity carbonates of the Keg River Formation. For the purposes of this work, the reservoir will be analyzed as if it were completely surrounded by the Muskeg Formation. The effects of historical pressure depletion due to oil production will be considered in this work, as well as future pressure increases due to fluid injection (waterflooding conducted mid-life in the reservoir's history, and more recently acid gas injection).

6.7.1. Reservoir geometry

The actual reservoir shape to be analyzed is a pinnacle (see Figure 6.42) of 90 m height and $0.16 \, \text{km}^2$ base area, at a mid-point depth of 1500 m. To enable the use of the closed-form solutions presented earlier in this thesis, the reservoir shape was simplified to an axisymmetric spheroid with the same height and volume of the reservoir; this gives a reservoir width of 320 m. [Note: This same reservoir width has been used in all of the analyses that follow, even though the concept of reservoir volume is ill-defined in the case of plane-strain (i.e., infinitely long) reservoir geometries.] As such, the idealized reservoir has the following geometrical characteristics:

- aspect ratio, $e = 90/320 = 0.28$
- depth number, $n = (320/2) / 1500 = 0.11$
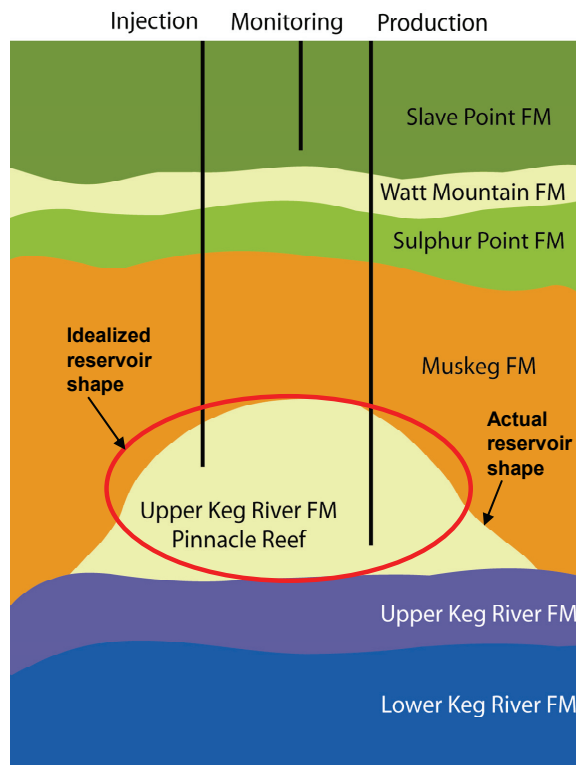
Figure 6.42. Schematic of actual and idealized cross-sectional reservoir geometry (after Smith et al., 2008)

Based on a comparison of these geometrical parameters with the criteria presented in Section 3.5.2, full-space solutions can be used for this reservoir without incurring significant error.

6.7.2. In-situ stresses and pressure history

Bachu at al. (2008) estimated values of 17 and 24 kPa/m, respectively, for typical minimum horizontal and vertical stress gradients in the Keg River formation in the Zama field. Bell and Babcock (1986) believe that the ratio of maximum to minimum horizontal stress in Western Canadian Sedimentary Basin varies between 1.3 to 1.6. A value of 1.4 was used in this specific case, which leads to a value o 24 kPa/m for the gradient of maximum horizontal stress. As such, the stress regime interpreted for this site is transitional between strike-slip and normal.

An initial reservoir pressure of 14.5 MPa was used for this site. During primary production, pressure decreased to slightly less than 4 MPa. During injection, pore pressure will remain lower than the minimum in-situ stress in the caprock,

which – based on the information presented above - is the minimum horizontal stress. Its magnitude is estimated as 17 kPa/m × 1500 m = 25.5 MPa. For the sake of working in round numbers, pore pressure change scenarios of ± 10 MPa were considered in this work.

6.7.3. Rock mechanical properties

Based on geophysical log analysis and laboratory testing on core samples, mechanical properties of the Keg River Formation reservoir rocks and the "surrounding" Muskeg Formation anhydrite were reported by Smith et al. (2008). Table 6.6 lists the mechanical properties selected for use in this paper. Based on these values, the shear modulus ratio ($R_\mu = \mu^*/\mu$) was calculated as 0.46. It is worthy to note that Poisson's ratio of the surrounding rock does not have a significant effect on the stress change induced by pressure change (Section 3.6.1). Peak strength properties in Table 6.6 (e.g., friction angle and cohesion) were used in this work to evaluate the onset of shear fracturing. Residual friction angle was used as a friction angle on potentially existing faults in the field. A Biot's coefficient of 1.0 was used for both the Keg River and Muskeg formations.

6.7.4. Induced stress change analysis

Equations (3.34), (3.51), (3.101), and (3.98) were used to calculate the normalized stress arching ratios for production (pressure depletion) and injection (pressure increase) for three different reservoir scenarios: (i) a plane strain elliptical inclusion, analyzed in a cross-sectional plane aligned parallel to the minimum horizontal stress; (ii) a plane strain elliptical inhomogeneity, also analyzed in a cross-sectional plane aligned parallel to the minimum horizontal stress; and (iii) an axisymmetric inclusion. These arching ratios were then used to calculate induced stress changes in the field at the following locations: (i) within the reservoir; (ii) at a point in the caprock immediately overlying the centre of the reservoir (referred to as "caprock" in the following discussion and figures); (iii) at a point in the caprock immediately adjacent to the side of the reservoir in the cross-sectional plane (referred to as the "sideburden, in the σ_{Hmin} direction" in the following discussion and figures); and (iv) at a point "in front of" the reservoir; i.e., in the surrounding rock

Table 6.6. Rock mechancial properties for a representative pinnacle reef in the Zama oil field.

Geomechancial properties	Reservoir (Keg River Formation)	Surrounding rock (Muskeg Formation)
Static shear modulus (μ)	11 GPa	24 GPa
Static Poisson's ratio (ν)	0.23	0.26
Peak friction angle (ϕ_p)	37°	53°
Peak cohesion (c_p)	4 MPa	12 MPa
Residual friction angle (ϕ_r)	34°	44°
Residual cohesion (c_r)	2.2 MPa	6.5 MPa
Permeability (k)	95–175 mD	
Porosity (ϕ)	12%	2%

immediately adjacent to the side of the reservoir in the out-of-plane direction (referred to as the "sideburden, in the σ_{Hmax} direction"). [Note: The latter point is only applicable for the axisymmetric case.]

The total stress changes calculated for the aforementioned locations for a pore pressure increase of 10 MPa ($\Delta P = 10$ MPa) are shown in Table 6.7. Due to the linear elastic nature of the solutions used, the stress changes for a depletion scenario ($\Delta P = -10$ MPa) would be identical to those listed in Table 6.7, multiplied by -1. Figures 6.43 and 6.44 show both total and effective in-situ stress states before and after a 10 MPa pore pressure change for a production scenario and an injection scenario, respectively. Using these figures or Table 6.7, it can be seen that, during injection, the following stress changes occur:

- Within the reservoir, all stress changes are tensile.
- In the caprock, in-plane horizontal stress change is tensile; vertical stress change is compressive; out-of-plane horizontal stress change varies for the different scenarios.
- In the sideburden (σ_{Hmin} direction), in-plane horizontal stress change is compressive; vertical stress change is tensile; out-of-plane horizontal stress change is either zero (plane-strain inclusion) or tensile.
- In the sideburden (σ_{Hmax} direction – axisymmetric case only), in-plane horizontal stress change is tensile; vertical stress change is tensile; out-of-plane horizontal stress change compressive.

Table 6.7. Calculated stress changes for a 10 MPa pore pressure increase.

Location	Stress change component	Stress change (MPa)		
		Plane strain inclusion	Plane strain inhomogeneity	Axisymmetric inclusion (oblate spheroid)
Within reservoir	$\Delta\sigma_H$	7	7.6	5.9
	$\Delta\sigma_h$	5.5	6.9	5.9
	$\Delta\sigma_V$	1.5	2.7	2.3
Caprock	$\Delta\sigma_H$	0	0.4	-1.1
	$\Delta\sigma_h$	-1.5	-1.2	-1.1
	$\Delta\sigma_V$	1.5	2.7	2.3
Sideburden (in the σ_{Hmin} Direction)	$\Delta\sigma_H$	0	-1.4	-1.1
	$\Delta\sigma_h$	5.5	6.9	5.9
	$\Delta\sigma_V$	-5.5	-12.5	-4.7
Sideburden (in the σ_{Hmax} direction)	$\Delta\sigma_H$	N/A	N/A	5.9
	$\Delta\sigma_h$	N/A	N/A	-1.1
	$\Delta\sigma_V$	N/A	N/A	-4.7

Conceptually, all of these stress changes can be understood on the grounds that, during injection, the reservoir is expanding; hence, pushing outwards on the surrounding rock. For the pressure depletion case, in which the reservoir is contracting, the stress changes are exactly opposite to those summarized above.

One final point worth noting is the fact that the vertical stress increase predicted in the sideburden is markedly larger for the plane-strain inhomogeneity case compared to both of the inclusion cases, which are similar in magnitude. This is a consequence of the fact that, for the former case, the surrounding rock is stiffer than the reservoir. As the latter presses outwards (during injection), this induces a large stress in the sideburden in the direction that is tangential to the reservoir – host rock interface (i.e., the vertical direction).

6.7.5. Failure analysis

Analyses of induced shear fracturing and fault reactivation are described in this section of the work. Although these analyses could be conducted with any of the induced stress change models described in the previous section, the axisymmetric solution based on the theory of inclusions has been selected for use in this work; Although it neglects the effects of material property contrasts, it better captures the actual reservoir geometry.

Scenario	Effective stresses	Total Stresses
Initial in-situ stresses	21.8 MPa; 11 MPa; 21.8 MPa; 22.4 MPa; 11.3 MPa; 22.4 MPa; 22.4 MPa; 22.4 MPa; 22.4 MPa; 22.4 MPa; 11.3; 11.3 MPa; 22.4 MPa	35.8 MPa; 25 MPa; 35.8 MPa; 36.9 MPa; 25.8 MPa; 36.9 MPa; 36.9 MPa; 36.9 MPa; 36.9 MPa; 25.8 MPa; 25.8 MP; 25.8 MPa; 36.9 MPa
After production (Plane strain inclusion)	20.3MPa; 12.5MPa; 21.8 MPa; 30.9MPa; 15.8MPa; 25.4MPa; 27.9MPa; 5.8 MPa; 22.4MPa	34.3 MPa; 26.5 MPa; 35.8 MPa; 35.4 MPa; 20.3 MPa; 29.9 MPa; 42.4 MPa; 20.3 MPa; 36.9 MPa
After production (Plane strain inhomogeneity)	19.1 MPa; 19.3 MPa; 23.3 MPa; 29.7 MPa; 14.4 MPa; 24.8 MPa; 27.8 MPa; 4.4 MPa; 22 MPa	33.1 MPa; 33.3 MPa; 37.3 MPa; 34.2 MPa; 18.9 MPa; 29.3 MPa; 42.3 MPa; 18.9 MPa; 36.5 MPa
After production (Axisymmetric oblate inclusion)	19.6 MPa; 12.1 MPa; 22.9 MPa; 30.1 MPa; 15.4 MPa; 26.5 MPa; 27.1 MPa; 5.4 N; 23.5 MPa; 27.1 MPa; 12.4 MPa; 16.5 MPa	33.6 MPa; 26.1 MPa; 36.9 MPa; 34.6 MPa; 19.9 MPa; 31 MPa; 41.6 MPa; 19.9 MP; 38 MPa; 41.6; 26.9 MPa; 31 MPa

Figure 6.43. Total and effective stresses before and after pressure depletion of 10 MPa, calculated for different reservoir scenarios.

Peak strength properties in Table 6.6 were used for induced shear fracturing analysis, and residual friction angles were used to calculate the friction coefficients of faults or natural fractures, which were assumed to have no cohesive strength. Given that no data are available on the presence of, nor the orientation of, faults or natural fractures, the conservative assumption of "critically oriented" faults or fractures was used; i.e., reactivation was assessed for hypothetical faults or fractures that are oriented such that they are most likely to fail.

Scenario	Effective stresses	Total Stresses
Initial in-situ stresses		
After injection (Plane strain inclusion)		
After injection (Plane strain inhomogeneity)		
After injection (Axisymmetric oblate inclusion)		
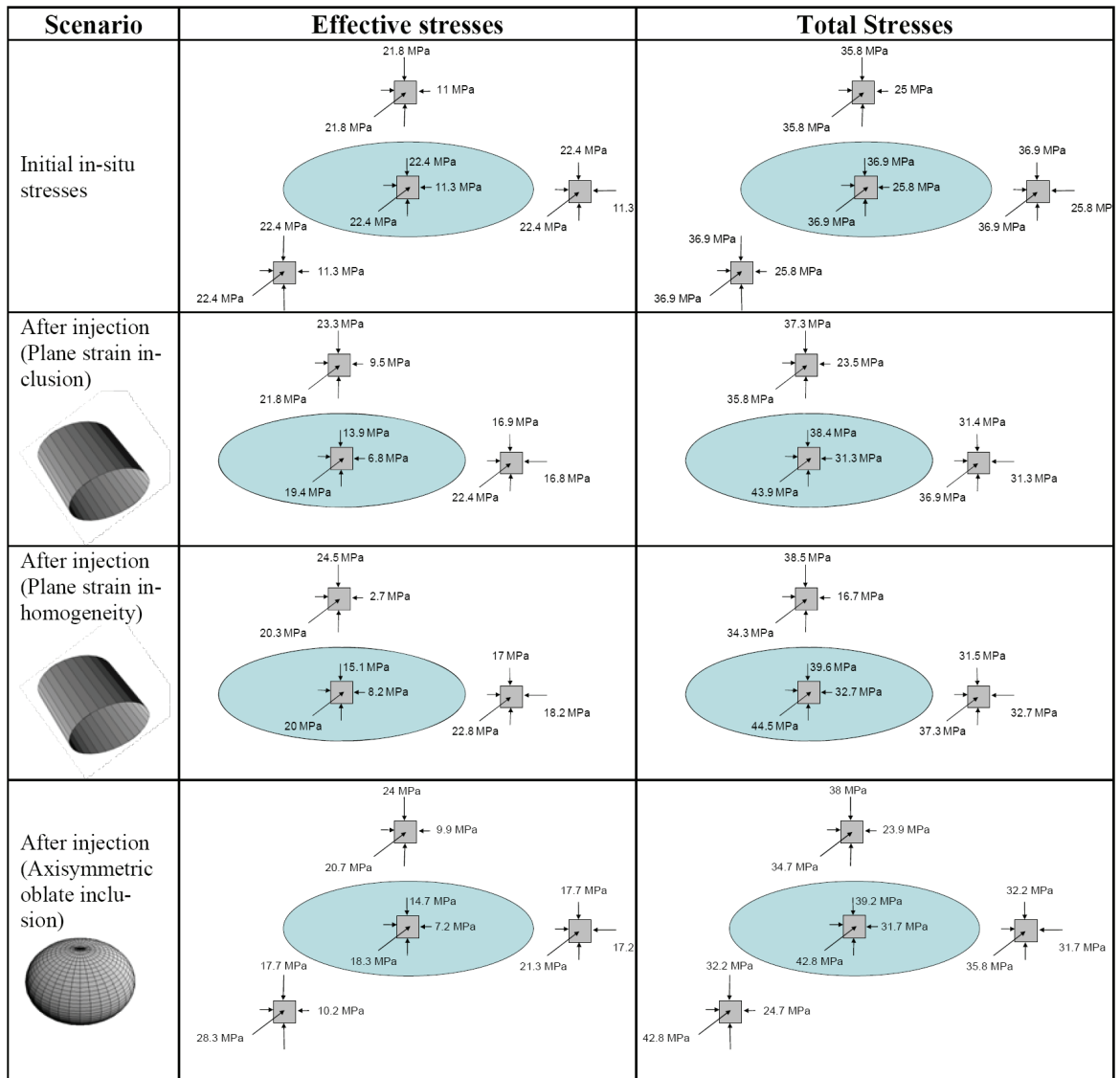
Figure 6.44. Total and effective stresses before and after 10 MPa pressure increase due to injection, calculated for different reservoir scenarios.

The stress states calculated before and after reservoir pressure change are presented using Mohr circles in Figures 6.45 and 6.46 for production (i.e., pressure depletion) and injection, respectively. These figures show that:

1) Within the reservoir:

   a. During production, though the increase of effective stresses moves the stress state away from both the intact rock and fault failure criteria, the increase in deviatoric stress partially opposes this beneficial effect. Ultimately, the net effect is such that the stress state would have shifted toward a more stable condition during historical production operations (Figure 6.45a).

b. During injection, the stress state is predicted to become more critical; i.e., the stress state shifts towards the fault and intact rock failure criteria (Figure 6.46a). Although this suggests an increased potential for failure in a relative sense, it is significant to note that neither of these failure criteria is met in an absolute sense.

2) In the sideburden aligned with the minimum horizontal stress (i.e., σ_{Hmin} direction):

a. During production, due to the increase in vertical stress and maximum horizontal stress and the decrease in minimum horizontal stress, the stress state becomes more deviatoric. As such, during production the stress state may have come close to meeting the failure criterion for optimally oriented faults (or natural fractures), *if* any were present (Figure 6.45b). In this case, the "most" optimally oriented faults would have steep dips (~60°) and strike directions sub-parallel to the maximum horizontal stress azimuth; however, sub-vertical faults striking at acute angles (~30°) to the maximum horizontal stress would be only "slightly less" optimally oriented. As for induced fracturing, given the high strength of the Muskeg Formation (i.e., the failure criterion is barely visible in the top left corner of the graph), the stress state during production is not likely to have induced new shear fractures.

b. During injection, due to the decrease in vertical stress and maximum horizontal stress and the increase in minimum horizontal stress, the stress state is predicted to become more isotropic, leading to a more stable rock condition (Figure 6.46b).

3) In the sideburden aligned with maximum horizontal stress (i.e., σ_{Hmax} direction):

a. During production, minimal change in the potential for fault reactivation or induced fracturing is likely to have occurred (Figure 6.45c).

b. During injection, although vertical stress decreases, the increase in maximum horizontal stress and the decrease in minimum horizontal stress results in an increase in the deviatoric stress in the horizontal plane. As shown in Figure 6.46c, this results in a modest increase in the potential for failure.

4) In the caprock:

a. During production, minimal change (a slight reduction, in fact) in the potential for fault reactivation or induced fracturing is likely to have occurred (Figure 6.45d).

b. During injection, due to the increase in vertical stress and the decrease in horizontal stresses, the deviatoric stress increases. As such, the stress state would become slightly more critical, but still quite far from failure in an absolute sense (Figure 6.46d).

The effective stress state did not approach a tensile condition for any of the scenarios analyzed; i.e., the potential for induced tensile fracturing within and surrounding the reservoir is predicted to be low for these scenarios.

(a)

(b)

(c)
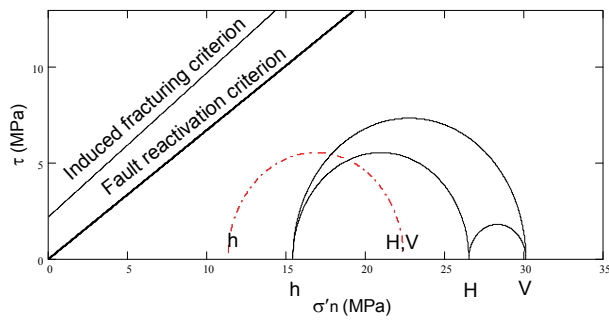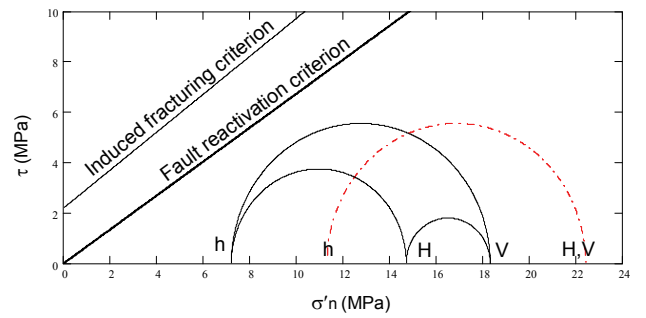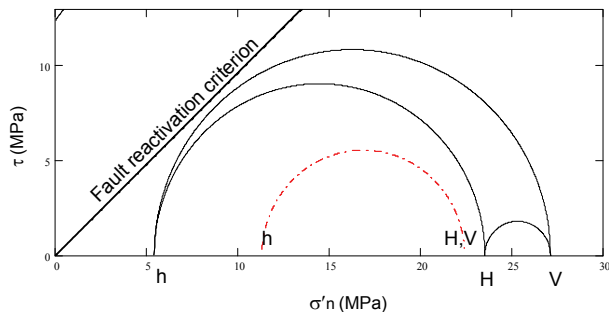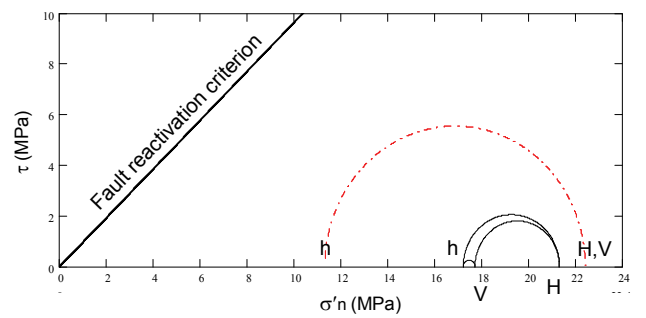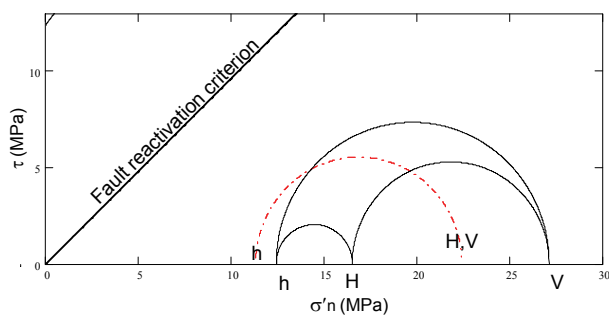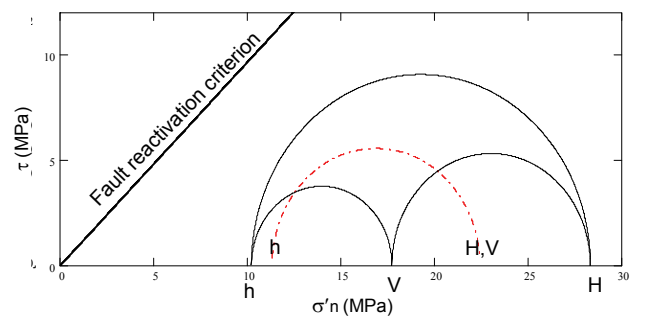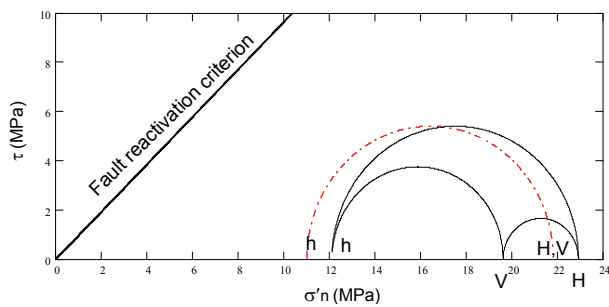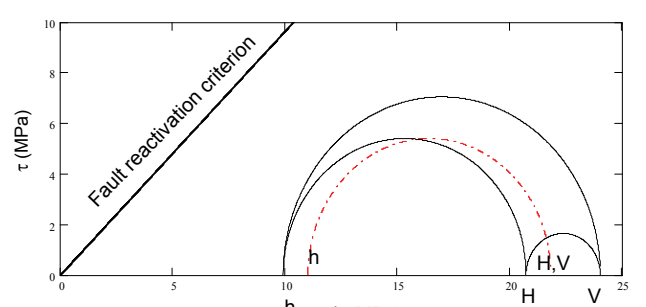
(d)

Figure 6.45. Effective stress state after pressure depletion of 10 MPa: (a) within the reservoir; (b) in the sideburden aligned with minimum horizontal stress; (c) in the sideburden aligned with maximum horizontal stress; and (d) in the caprock. The dashed circle represents the original stress state, in which the maximum horizontal stress and the vertical stress magnitudes are equal. H denotes the maximum horizontal stress, h denotes the minimum horizontal stress, and V denotes the vertical stress.

(a)

(b)

(c)

(d)

Figure 6.46. Effective stress state after a pressure increase of 10 MPa: (a) within the reservoir; (b) in the sideburden aligned with minimum horizontal stress; (c) in the sideburden aligned with maximum horizontal stress; and (d) in the caprock. The dashed circle represents the original stress state, in which the maximum horizontal stress and the vertical stress magnitudes are equal. H denotes the maximum horizontal stress, h denotes the minimum horizontal stress, and V denotes the vertical stress.

227

6.8. Summary and conclusion

For the first case study, a poroelastic stress analysis approach was used for stress analysis of a synthetic case with a rectangular reservoir embedded in a field set in a normal fault stress regime with a number of faults with various locations and orientations. The results showed that fault reactivation was only likely to occur for certain faults located within the reservoir. During production, fault reactivation was only likely to occur for a fault of certain geometry (i.e., dip angle). However, during injection, all the faults within the reservoir were likely to reactivate during injection with a nearly similar magnitude of reservoir pressure change. This phenomenon can be explained using a pseudo-tensile mode of failure during injection.

A sensitivity analysis was carried out to study the effect of variations in fault surface friction coefficient on the critical reservoir pressure change. Results showed that, during production, there was only a limited range of friction coefficient which might lead to fault reactivation. During injection, fault reactivation was almost independent of friction coefficient, which can be explained by the occurrence of a pseudo-tensile mode of failure during injection.

For the second case study, using a poroelastic analysis model based on the theory of inclusions, in-situ stress evolution of strains and stresses in both cases of production and injection for reservoirs in normal and thrust fault stress regimes were studied. The results showed that stress evolution could be interpreted by using a so-called 'cavity pattern' for the change in stress orientation and magnitude. Similar to a cavity, under injection, the maximum principal stress tended to become "radial" (i.e., perpendicular to the reservoir boundaries) while, during production, this stress tended to be tangential (i.e., parallel to the reservoir boundaries).

A mathematical methodology was proposed to determine the critical pressure change both for induced tensile and shear fracturing during production or injection for initially normal and thrust fault stress regimes. Patterns of fracturing for both cases of normal and thrust stress regime were found to be the same, but the magnitudes of critical pressure changes were different.

During production, major fractures formed in an area which extended above the reservoir shoulders and the boundary between the central and peripheral deformation

regions. In this area, fractures formed at the reservoir's sides in a high-angle orientation and migrated upward and towards the center while their dip angle simultaneously decreased, to form a cone-shaped sliding volume (with convex upwards curvature) above the reservoir. In addition, high-angle fracturing (creating normal faults) was possible in the regions adjacent to the reservoir flanks and near the ground surface in peripheral deformation regions, while low-angle induced fracturing (creating thrust faults) occurred on the central deformation region. All of these observations are in qualitative agreement with field and experimental observations.

During injection, although low-angle thrust fractures were likely to form in a small region adjacent to the reservoir, the greatest tendency towards sub-vertical fracturing occurred in the central deformation region, and a cylindrical sliding volume around the limits of the reservoir was expected to move upward.

The Lacq gas field in France was used in this chapter as a demonstration case study for fault reactivation, because depletion-induced pore pressure changes in this field have resulted in numerous well-documented seismic events over time. The induced stress changes predicted for this domed-shaped reservoir showed some differences with the results predicted by simpler models that assume a planar reservoir geometry. The in-situ stress regime in the Lacq field is unknown, in spite of several decades of investigation. Fault reactivation tendencies predicted for an assumed thrust fault stress regime showed a strong correlation to recorded seismic event locations. Conversely, there was no correlation between model predictions and seismic event data when a normal fault stress regime was assumed. As such, further to providing reliable predictions of fault reactivation tendency, the model results enabled the inference of a thrust fault stress regime for the field.

The developed framework in this research was applied to study the potential for fracturing and fault reactivation within the Ekofisk oil field in the North Sea; a field which has shown evidence of significant stress change during its production life. The results are consistent with previous interpretations of induced fracturing in this field.

A parameter sensitivity analysis was conducted for the Ekofisk field. The results showed that variations in the lateral pressure coefficient (K_0) strongly affect both the critical pressure change for fracturing and the fracturing mode. A similar effect was

observed in analyzing the effect of the stress change path. Specifically, the common assumption of no change in vertical stress might lead to an under-estimation of the critical pressure change for fracturing. In addition, it was shown that the difference between rock deformability during production and injection must be considered during induced fracturing analysis, due to the hysteresis effect on the stress change path which can affect both the critical pressure change and the mode of fracturing. The sensitivity analysis on rock strength parameters showed their significant effect on shear fracturing during production, while they had a modest effect on during injection in which fracturing mainly occurred in a horizontal tensile or a pseudo-tensile mode.

The geomechanical response to reservoir pressure change was studied for the Weyburn oil field in Saskatchewan by comparing numerical and analytical model results. This comparison showed that, for this specific field, a simple analytical model is able to give a very good estimation of induced stress changes. Both numerical and semi-analytical models showed a negligible stress change in the surrounding rock, which suggests minimal risk of fault reactivation and induced fracturing in these rocks. Within the reservoir, the calculated critical pressure changes for fault reactivation and induced fracturing showed a significant difference for different in-situ stress scenarios, which highlights the importance of in-situ stress measurement for fault reactivation analysis. Implementing both Coulomb and Drucker-Prager failure criteria for calculating critical pressure change for induced shear fracturing showed a significant difference between these two models and emphasized the considerable effect of intermediate in-situ principal stress. In addition, this study showed the importance to distinguish between the rock responses to injection and production, which might significantly affect the results of fault reactivation and induced-fracturing analysis. Thermoelastic analysis of temperature change on fault reactivation within the reservoir showed the significant effect of temperature and highlights the requirement for further studies.

The final case study was an analysis of induced stress changes due to historical oil production, with resultant pore pressure depletion, and pore pressure increases resulting from waterflooding and/or acid gas injection in a pinnacle reef in the Zama oil field, Alberta. The results generated are consistent with the expectation that, during injection,

230

the reservoir is expanding; hence, pushing outwards on the surrounding rock. This results in a compressive stress change in directions oriented normal to the reservoir-host rock interface, and a tensile stress change in direction tangential to the interface. The results generated for a plane-strain reservoir geometry, in which the high stiffness of the host rock relative to the reservoir was accounted for, demonstrate that this contrast can significantly increase some of the stress change magnitudes. During pressure depletion, the stress changes are exactly opposite to those described for injection.

Failure analyses for both the fault reactivation and induced fracturing were performed, using the stress changes predicted for an axisymmetric ellipsoidal reservoir geometry. These analyses showed that the potential to induce shear fracturing was not significant at any point within the reservoir or the surrounding rock during both production and injection. Similarly, fault reactivation was not predicted for the reservoir or any of the points that were analyzed in the surrounding rock. However, fault orientations at points in the sideburden having the greatest potential for reactivating during historical production operations were identified. This illustrates a means of using geomechanical models to focus geological characterization efforts on the features that are most critical to acid gas containment.

Chapter 7

Summary and Conclusion

7.1. Summary

Existing analytical, semi-analytical, and numerical approaches for induced stress change analysis and their application in the technical literature have been assessed in this thesis. A comprehensive description of the theories of strain nuclei, inclusions, and inhomogeneities, along with their implementation to solve elasticity field equations for induced stress change analysis during fluid production and injection in porous geological reservoirs, were presented. The theory of inclusions was used for plane strain semi-analytical analysis of the entire half-space field for reservoirs with different geometries. A plane strain semi-analytical analysis was conducted using the theory of inhomogeneities for the entire full-space and a reservoir of elliptical cross-section with different properties from the surrounding rock. New analytical formulations were derived to calculate the induced stress change parameters within reservoirs for different variations of an ellipsoidal geometry for the case of a homogeneous field and material property contrast between the reservoir and surrounding rock. A set of sensitivity analyses was performed to assess the significance of different parameters such as: reservoir geometry (including shape, depth and "tilt" or dip angle); and material properties of the reservoir and surrounding rock.

The Coulomb Failure Stress concept was used to study the patterns of fault reactivation in the entire field during production or injection. A methodology was

developed to find the range of fault dip angles which are likely to reactivate during injection or production. A comprehensive study was performed on the likelihood of fault reactivation within reservoirs. A set of sensitivity analyses was conducted to study the effect of different parameters such as coefficient of friction, reservoir geometry, and depth on the results. Closed-form formulae were derived to find the critical pressure change for fault reactivation for a plane strain induced stress change analysis in the entire field, and also for a three dimensional induced stress change analysis within the reservoir.

Using the Coulomb failure criterion, different modes of fracturing within a reservoir were studied. In addition, simple approaches were developed to identify the tendency of the intact rock towards (or away from) fracturing during injection or production. For a Coulomb failure criterion, a set of closed-form formulae was derived to calculate the critical pressure change for induced fracturing within the reservoir and in the entire field for a plane strain induced stress change analysis. Similarly, using the Drucker-Prager failure criterion a formulation was derived to calculate the critical pressure change for fracturing within the reservoir for a three-dimensional induced stress change analysis.

Different aspects of the developed models and approaches were applied to study induced stress change, fault reactivation and induced fracturing in six different cases: Two synthetic case studies; the Lacq gas reservoir in France; the Ekofisk oil field in North Sea; the Weyburn oil field in Saskatchewan, and the Zama oil field in Alberta. Scenario analyses and sensitivity analyses were performed to attain an improved understanding of the geomechanical behavior of porous geological formations (and in some cases their surroundings) during injection and production.

In the first synthetic case study, the theory of inclusions was used for induced stress change analysis throughout the entire field. The tendency toward fault reactivation and critical pressure change for fault reactivation was determined for the existing faults in the field. In addition, patterns of fault reactivation and sensitivity of critical pressure

change to coefficient of friction were studied.

In the second synthetic case study, the theory of inclusions was implemented for induced stress change and deformation analysis throughout the field. The results of this analysis were used to study general patterns of change in the magnitude and orientation of in-situ stresses in the entire field during injection and production. In addition, by determination of critical pressure change for the entire field, general patterns of faulting/fracturing during production were recognized. A good correlation was observed in comparison of the identified patterns of faulting/fracturing with field observation and results of physical models.

The Lacq gas field, in France, has shown induced seismic activity during its prodcing life. The objective of this case study was the implementation of the models and methodologies developed in this research to the study of fault reactivation in this field. The theory of inclusions was implemented to study induced stress change in the field and fault reactivation tendency was studied by using the Coulomb Failure Stress change methodology. The model-predicted regions of fault reactivation likelihood were in a good correlation with the distribution of seismic events. In this case study, patterns of induced stress change for inclined reservoir geometry were also compared to a rectangular geometry.

During its producing life, the Ekofisk reservoir has shown evidence of seismic activity that is believed to be the result of fault reactivation and/or induced fracturing. In this case study, both of these issues have been studied using the methodologies developed in this research. The theory of inhomogeneities was used for induced stress change analysis within the reservoir. Analysis of critical pressure change for fault reactivation shows the likelihood of fault reactivation during the reservoir's producing life. Also, the calculated critical pressure change for induced fracturing within the reservoir shows that fracturing has likely occurred within the reservoir. Sensitivity analyses were performed to study the effect of different parameters such as in-situ stresses, stress change path, and rock strength on the magnitude and type of induced

fracturing within the reservoir.

In the year 2000, carbon dioxide injection started in Weyburn oil field both for the purpose of enhanced oil recovery and for CO_2 storage. To increase the security of CO_2 containment, it is important to assess caprock integrity. By comparing the results of a relatively simple analytical model with a numerical model, it was shown that the analytical formulation can predict the induced stress change for this specific field with a high degree of confidence. Prediction of negligible stress change in the surrounding rock suggests negligible risk of fracturing and fault reactivation in the rocks that bound the reservoir. The high variation of critical pressure change for fault reactivation and induced fracturing within the reservoir calculated for different scenarios of in-situ stress regime in the field highlights the need of in-situ stress measurements in the field. The significant effect of temperature change on induced stress change and failure analysis suggests the importance of further thermo-poro-mechanical analysis.

The use of the approach presented in this thesis was illustrated with an analysis of a pinnacle reef with dimensions and properties representative of reefs in the Zama oil field, northwestern Alberta, Canada. Scenarios of pore pressure decrease (during historical production operations) and pore pressure increase (during several years of water-flooding and acid gas injection operations) were analyzed, for three different idealizations of reservoir properties and geometry (two plane strain and one axisymmetric). These results suggest that that the potential for induced fracturing is not significant at any point within the reservoir or the surrounding rock for both the production and injection scenarios that were simulated. Similarly, fault reactivation was not predicted for the reservoir or any of the points that were analyzed in the surrounding rock. However, fault orientations having the greatest potential for reactivating during historical production operations were identified; thus, illustrating a means of using geomechanical models to focus geological characterization efforts on the features that are most critical to acid gas containment.

7.2. Conclusion

The proposed models and methodologies, while being relatively simple, are quite general and flexible in terms of their applicability. These attributes, coupled with the modest computational effort required to implement these models and methodologies, make them ideally suited for parameter sensitivity analyses to: (i) identify key input parameters and understand their potential effects on reservoir performance; (ii) aid in the screening process during site selection for hydrocarbon production, waste disposal or geological sequestration; and (iii) account for parameter uncertainty in preliminary design analyses. In general, however, more detailed and sophisticated models may be required for the final performance prediction analyses for such projects. Following, some of the major results of this research projects in four different areas are stated: (1) induced stress change analysis (2) general patterns of in-situ stress change (3) general patterns of fault reactivation (4) general patterns of induced fracturing.

7.2.1. Induced stress change analysis

Parameter sensitivity analyses on the geometry of the reservoir indicate that induced vertical stresses increase as the reservoir becomes more equi-dimensional in cross-section. Induced horizontal stresses decrease as the reservoir becomes more equi-dimensional in cross-section, except for cases where the shear modulus of the reservoir is less than the surrounding rock. Although neglected in many cases, depending on the geometry and material property contrast, vertical stress change might be significant even for laterally extended reservoirs.

Using the theory of inhomogeneities, it has been shown that within the reservoir, vertical and horizontal induced stresses both decrease as the reservoir:matrix shear modulus ratio increases. Also vertical and horizontal induced stresses increase as the Poisson's ratio of the reservoir decreases. The Poisson's ratio of the matrix has limited effect on induced stresses. As such, it will usually be acceptable to make use of the simplifying assumption that the matrix and the inhomogeneity have identical Poisson's ratios. With decreasing rigidity of the inhomogeneity, the magnitude of induced stress

changes in the matrix increases.

A simple relationship between thermoelastic and poroelastic stress changes has been presented, which enables the calculation of thermally induced stress changes using the formulations presented in this thesis for normalized poroelastic stress arching ratios.

7.2.2. General patterns of induced stress change and in-situ stress evolution

Three different regions can be recognized during geomechanical analysis of the "field" (i.e., the reservoir and the rocks within which it is embedded): (1) the reservoir; (2) the central deformation region, which includes overburden and underburden; and (3) the peripheral deformation region, which contains the sideburdens. Within the reservoir, induced stress change is extensional during injection within the reservoir. In the central deformation region, during injection vertical stress change is compressive and horizontal stress change is tensile while in the peripheral region, the vertical stress change is extensional and the horizontal stress change is compressive. During production, all of the results are exactly opposite. Shear stresses during reservoir pressure change are concentrated at the corners of the reservoir. Studies on the tilted reservoirs and dome-shaped reservoirs show that reservoir geometry might affect these general patterns of induced stress change.

During reservoir pressure change, the orientations and magnitudes of in-situ stresses follow a specific pattern. The stress evolution can be interpreted by using a so-called 'cavity pattern' for the change in stress orientation and magnitude. Similar to a cavity, under injection, the maximum principal stress tends to become "radial" (i.e., perpendicular to the reservoir boundaries), while, during production, this stress tends to be tangential (i.e., parallel to the reservoir boundaries). Change in in-situ stresses starts from the boundary between the central and peripheral deformation regions and, with increasing reservoir pressure change, it expands toward the middle part of the central deformation region. In the central part of reservoir, where the induced shear stress is negligible, the in-situ stress regime might change as a result of pressure change but the

principal stresses remain horizontal or vertical.

7.2.3. General patterns of fault reactivation

The application of Coulomb Failure Stress Change (ΔCFS) in case studies shows a very good correlation with field observation. The same methodology was used to identify general patterns of fault reactivation in a field which shows that, in a normal fault stress regime during production, the regions within and near the lateral flanks of the reservoir tend towards reactivation; during injection, the underlying and overlying regions of the reservoir tend towards reactivation. For a thrust fault stress regime, the overlying and underlying rocks tend towards reactivation during production while, during injection, the reservoir and rocks near the lateral flanks of the reservoir tend towards reactivation.

It has been demonstrated that, within a reservoir located in a setting with a thrust fault stress regime, all fault dip angles tend toward reactivation during injection and stabilization during production (unless a stress regime change occurs). For normal fault stress regimes, faults with moderate angles around the optimum dip angle tend toward reactivation during production and stabilization during injection, while the opposite response is predicted for other dip angles.

Stress path ratio, which is defined in this work as the ratio of horizontal effective stress change to vertical effective stress change, has a significant role in the determination of fault dip angles tending most strongly toward reactivation for faults located within the reservoir. The results show that there is a significant effect of elastic property contrast between a reservoir and its surrounding rocks on the stress path, and consequently on fault reactivation tendency. Specifically, for a normal fault stress regime, fault reactivation is less likely within relatively rigid reservoirs during production. In addition, results show that, for a normal fault stress regime, faults in reservoirs with larger lateral extents relative to their thicknesses are more likely to reactivate during production.

Sensitivity analyses of patterns of fault reactivation to coefficient of friction show that critical pressure change for fault reactivation within the reservoir is very sensitive to the fault strength during production while it is less dependent during injection. In the entire field, the boundary between regions tending towards reactivation and stabilization is relatively insensitive to the value of the friction coefficient. It has been shown that fault reactivation potential is dependent on reservoir geometry and dip angle; hence it is important to consider the real reservoir geometry in the analysis of induced seismicity and caprock integrity.

7.2.4. General patterns of induced fracturing and faulting

Patterns of fracturing in the entire field for both cases of normal and thrust stress regime are the same, but the magnitudes of critical pressure changes are different. During production, major fractures form in an area which extends above the reservoir shoulders and the boundary between the central and peripheral deformation regions. In this area, fractures form at the reservoir's sides in a high-angle orientation and migrate upward and toward the center while their dip angle simultaneously decreases, to form a cone-shaped sliding volume (with convex upwards curvature) above the reservoir. In addition, high-angle normal induced-fracturing is possible in the regions adjacent to the reservoir flanks and near the ground surface in peripheral deformation regions, while low-angle induced fracturing occurs on the central deformation region. All of these observations are in qualitative agreement with field and experimental observations. During injection, although low-angle thrust fractures are likely to form in a small region adjacent to the reservoir, the greatest tendency towards sub-vertical fracturing occurs in the central deformation region, and a cylindrical sliding volume around the limits of the reservoir is expected to move upward.

Within the reservoir, depending on the initial stress state, the reservoir rock's strength parameters, and the path of induced stress change during reservoir production or injection, four different modes of fracturing have been recognized: horizontal tensile fracturing, vertical tensile fracturing, shear fracturing in a thrust mode (i.e., sub-

239

horizontal fractures), and shear fracturing in a normal mode (i.e., sub-vertical fractures).

Parameter sensitivity analyses showed that variations in the in-situ stresses strongly affect both the critical pressure change for fracturing and the fracturing mode, which highlights the importance of in-situ stress measurement in the field. A similar effect was observed in analyzing the effect of the stress change path. Specifically, the common assumption of no change in vertical stress might lead to an under-estimation of the critical pressure change for fracturing. In addition, it was shown that the difference between rock deformability during production and injection must be considered during induced fracturing analysis, due to the hysteresis effect on the stress change path which can affect both the critical pressure change and the mode of fracturing. The sensitivity analysis on rock strength parameters shows their significant effect on shear fracturing during production, while they have a modest effect during injection, in which fracturing mainly occurs in a horizontal tensile or a pseudo-tensile mode. Comparing Mohr-Coulomb and Drucker-Prager failure criteria shows a significant difference between these two criteria.

7.3. Recommendations for future research

Following is a list of recommendations which can help to improve the achievement of this thesis:

- Numerical models can be implemented to study some features which cannot be considered using models presented in this research, such as:
  - o Nonlinearity and irreversibility (i.e., plasticity) in mechanical properties of the reservoir and surrounding rock.
  - o Geomechanical heterogeneity of the reservoir and surrounding rock
  - o Dislocation of faults and other discontinuities.
  - o Coupling between fluid flow, thermal and geomechanical response of the field.
- Evaluation of the presented methodologies using more case studies.
- Laboratory and field tests to study the hysteresis response of the field materials to injection and production.

Even though sufficient data may be lacking to address the effects of these more complex material behaviours in most practical field problems, it would be useful to study their effects through sensitivity analyses in order to understand their consequences at a conceptual level.

LIST OF REFERENCES

Addis, M.A. 1997. The stress depletion response of reservoirs. SPE Annual Technical Conference and Exhibition, San Antonio, Texas. SPE 38720, 5-8 October.

Adushkin V., Rodionov V.N., and Turuntaev S. 2000. Seismicity in the Oil Field. Oilfield Review, **1:** 2–17.

Bell, J.S., Price, P.R., McLellan, P.J. 1994. In-situ Stress in the Western Canada Sedimentary Basin; In Geological Atlas of the Western Canada Sedimentary Basin, G.D. Mossop and I. Shetsen (comps.), Calgary, Canadian Society of Petroleum Geologists and Alberta Research Council. pp. 439-446.

Al-Shaieb, Z., Puckette, J., Patchett, J., Deyhim, P., Li, H., Close, A., and Birkenfeld, R. 2000. Identification and characterization of reservoirs and seals in the Vicksburg formation, TCB Field, Klebberg County, Texas. As a report for the Gas Research Institute, July.

Bachu S., Haug K., and Michael K. 2008. Stress Regime at Acid-Gas Injection Operations in Western Canada. ERCB/AGS Special Report 094 (March).

Baranova, V., Mustaqeem, A., and Bell S. 1999. A model for induced seismicity caused by hydrocarbon production in the Western Canada Sedimentary Basin. Canadian Journal of Earth Science, **36:** 47–64.

Bardainne, T., Sénéchal, G., and Grasso, G.R. 2003. Study of a gas field fracturing based on induced seismicity in 3D seismic data. EGS-AGU-EUG Joint Assembly, Nice, France, 06-11 April. And also in Geophysical research abstracts 5, 06453.

Barlet-Goueʹdard , V., Rimmeleʹ, G. , Porcherie, O., Quisel, N., Desroches, J. 2008. A solution against well cement degradation under CO_2 geological storage environment, doi:10.1016/j.ijggc.2008.07.005.

Bell, J.S., and E.A. Babcock, 1986. The stress regime of the Western Canadian basin and implications for hydrocarbon production: Bulletin of Canadian Petroleum Geology, **34:**, 364–378.

Boade, R.R., Chin, L.Y., and Siemers, W.T. 1989. Forecasting of Ekofisk reservoir compaction and subsidence by numerical simulation. Journal of Petroleum Technology **41(7):** 723-728. SPE 17855.

Brown, G.A., Kennedy, B., and Meling, T. 2000. Using fibre-optic distributed temperature measurements to provide real-time reservoir surveillance data on Wytch Farm Field horizontal extended-reach wells, SPE Annual Technical Conference and Exhibition, Dallas, Texas, 1-4 October. SPE 62952.

Bruno M.S., 1992. Subsidence-induced well failure. SPE drilling engineering, **7(22)**:148-152.

Bunge, R.J. 2000. Midale Reservoir Fracture Characterization Using Integrated Well and Seismic Data, Weyburn Field, Saskatchewan. Colorado School of Mines.

Byerlee J.D. 1978. Friction of Rocks. Pure and Applied Geophysics, **116:**615-626.

Carey, J.W., Wigand, M., Chipera S.J., WoldeGabriel, G., Pawer, R., Lichtner, P.C., Wehner S.C., Raines, M.A., Guthrie, G.D. 2007.Analysis and performance of oil well cement with 30 years of CO_2 exposure from the SACROC Unit, West Texas, USA, International Journal of Greenhouse Gas Control, **1:** 75–85.

Celia, M.A., Bachu, S., Nordbotten, J.M., Gasda, S., and Dahle, H.K. 2004. Quantitative estimation of CO_2 leakage from geological storage: Analytical models, numerical models, and data needs, In: 7th International conference on Greenhouse Gas Control Technologies. Vancouver, British Columbia, Canada. September.

Chalaturnyk, R.J., Jimenez, J., Moreno, F., Deisman, N., Talman, S. 2003. Geomechanical performance and integrity assessment of the Weyburn field for geological storage of CO_2, Report.

Chan, A.W., and Zoback, M.D. 2002. Deformation Analysis in Reservoir Space (DARS): A simple formalism for prediction of reservoir deformation with depletion. SPE/ISRM Rock Mechanics Conference, Irving, Texas, 20-23 October. SPE 78174.

Chen, H., and Teufel, L.W. 2001, Reservoir Stress Changes Induced by Production/Injection, SPE Rocky Mountain Petroleum Technology Conference, Keystone, Colorado, 21-23 May, SPE 71087.

Chin, L.Y., and Nagel, N. B. 2004. Modeling of Subsidence and Reservoir Compaction under Waterflood Operations, International Journal of Geomechanics, **4(1):** 28-34.

Churcher, P.L., and Edmunds, A.C. 1994. Reservoir Characterization and Geological Study of the Weyburn Unit, Shoutheastern Saskatchewan: Report Number 1. Proposed Miscible Flood, Horizontal Well, and Waterflood Optimization Areas. PanCanadian Petroleum Ltd.

Coffer, H.F., Frank, G.W., and Bray, B.G. 1970. Project Rulison and the economic potential of nuclear gas stimulation. Gas Industry Symposium, Omaha, Nebraska, 21-22 May. SPE 2876.

Cook, C.C., and Berkke, K. 2004. Productivity preservation through hydraulic propped fractures in the Eldfisk North Sea chalk field. SPE Reservoir Evaluation & Engineering **7(2):** 105-114. SPE 88031.

Dake, L.P. 2001, Foundamentals of reservoir engineering, Elsevier, Amsterdam.

Damen, K., Faaij, A., Turkenburg, W. 2003. Health, safety, and environment risks of underground CO_2 sequestration, As s report to Copernicus Institute for Sustainable Development and Innovation.

de Lanlay, J. 1990. Lacq profound-calage de l'historiqe sur la modele, Elf Aquitance. Technical Report EP/S/PRO/GIN/No E.90.020, Pau, France.

Desbrandes, R., and Yildiz, T. 1991. Field applications of wireline formation testers in low-permeability gas reservoirs. SPE Gas Technology Symposium, Houston, Texas, 22-24 January. SPE 21502.

Du, J., and Olson, J.E. 2001. A poroelastic reservoir model for predicting subsidence and mapping subsurface pressure fronts. Journal of Petroleum Science and Engineering, **30:**181–197.

Du, J., and Olson, J.E. 2001. A poroelastic reservoir model for predicting subsidence and mapping subsurface pressure fronts. Journal of Petroleum Science and Engineering, 30: 181–197

Dusseault M.B., Bruno, M.S., Barrera, J. 2001. Casing shear: causes, cases, cures. SPE Drilling & Completion, **6:**98–107.

Engelder, T., and Fischer, M.P. 1994. Influence of poroelastic behavior on the magnitude of minimum horizontal stress, S_h, in overpressured parts of sedimentary basins, Geology, **22:** 949-952.

Eshelby, J.D. 1957. The determination of the elastic field of an ellipsoidal inclusion and related problems, Proceeding of the Royal Society of London, **A241(1226):** 326-396.

Eshelby, J.D. 1959. The elastic field outside an ellipsoidal inclusion. Proceeding of the

Royal Society of London, **A252(1271):** 561-569.

Eshelby, J.D. 1961. Elastic inclusions and inhomogeneities. Published in: Progress in solid mechanics by I.N. Sneddon and R. Hill (Editors), North Holland, Amsterdam, pp. 89-140.

Feignier, B., and Grasso, J.R. 1990. Seismicity induced by gas production, I: Correlation of focal Mechanisms and dome structure. Pure and Applied Geophysics. **134(3):** 405-426.

Fjær, E., Holt, R.M., Horsrud, P., Raaen, A.M., and Risnes, R. 2008. Petroleum related rock mechanics – 2nd edition, Elsevier, Amsterdam, The Netherland. pp 395-398.

Gambolati, G., Teatini, P., and Tomasi, L. 1999. Stress-strain analysis in productive gas/oil reservoirs. International Journal of Numerical and Analytical Methods in Geomechanicas **23 (13):** 1495– 1519.

Geertsma J. 1966. Problems of rock mechanics in petroleum production engineering. In: Proc. 1st Congress of the International Society of Rock Mechanics, Lisbon **vol. I,** pp. 585–594

Geertsma, J. 1973. Land Subsidence above Compacting Oil and Gas Reservoirs. Journal of Petroleum Technology, **25:** 734–744.

Gendzwill, D.J., and Stauffer, M.R. 2006. Shallow faults, upper Cretaceous clinoforms, and the Colonsay Collapse, Saskatchewan, Canadian Journal of Earth Science, **43:** 1859-1875.

Goodier, J.N., 1937. On the integration of the thermoelastic equations. Philosophical Magazine, 7(23): 1017-1032.

Goulty, N.R. 2003. Reservoir stress path during depletion of Norwegian chalk oilfields. Petroleum Geoscience, **9(3):** 233-241.

Grasso, J.R. 1992. Mechanics of seismic instabilities induced by the recovery of hydrocarbons, in induced seismicity: Pure and Applied Geophysics, **139(3-4):** 507-534.

Grasso, J.R., and Feignier, B. 1990. Seismicity induced by gas production, II: Lithology correlated events, induced stresses and deformation. Pure and Applied Geophysics. **134(3):** 427-450.

Grasso, J.R., and Wittlinger, G. 1990. Ten years of seismic monitoring over a gas field. Bulletin of the Seismological Society of America **80(2):** 450-473.

Guha, S.K. 2000. Induced earthquakes. Kluwer Academic Publishers, Dordrecht, The

Netherlands, and Boston, Mass.

Gutierrez, M., Hansteen, H. 1994. Fully coupled analysis of reservoir compaction and subsidence. European Petroleum Conference, London, U.K., 25-27 October. SPE 28900.

Guyoton, F., Grasso, J.R., and Volant P. 1992. Interrelation between induced seismic instabilities and complex geological structure. Journal of Geophysical Research. **19(7):** 705-708.

Hawkes, C.D., Hamid, O. 2008. In-situ stress regime in the Viking Formation, Southwest Saskatchewan. 61st Canadian Geotechnical Conference, Edmonton, 21-24 September.

Hawkes, C.D., McLellan, P.J., and Bachu, S. 2005. Geomechanical factors affecting geological storage of CO2 in depleted oil and gas reservoirs. Journal of Canadian Petroleum Technology, **44(10):** 52-61.

Hettema, M., Papamichos, E., and Schutjens, P. 2002. Subsidence delay: Field observations and analysis. Journal of Oil & Gas Science and Technology, **57:** 5,443-458.

Hickman, S.H., Barton, C.A., Zoback, M.D., Morin, R., Sass, J., and Benoit, R. 1997. In situ stress and fracture permeability along the Stillwater fault zone, Dixie Valley, Nevada: *International Journal of Rock Mechanics and Mining Sciences*, **34:** 126-136.

Hilbert, L.B., Fredrick, J.T., Bruno, M.S., Deitrich G.L., and Roufflignae, E. 1996. Two dimensional nonlinear finite element analysis of well damage due to reservoir compaction, well to well interactions and localization. Proceedings of 2nd North American Rock Mechanics Symposium, Montrea, Belkema, Vol. 2, pp. 1863-1870.

Holt, R.M., Flornes, O., Li, L., and Fjær, E. 2004. Consequences of depletion-induced stress change on reservoir compaction and recovery. The 6th North America Rock mechanics Symposium (NARMS): Rock Mechanics across Borders and Disciplines, Houston, Texas, 5-9 June.

Jimenez, J.A., 2006. Geomechanical performance assessment of CO_2-EOR geological storage projects, Ph.D. Thesis, University of Alberta, Canada.

Jimenez, J.A., and Chalaturnyk, R.J. 2002. Integrity of bounding seals for geological storage of greenhouse gases. SPE/ISRM Rock Mechanics Conference. Irving, Texas, 20-23 October. SPE 78196.

Johnson,. J.P., Rhett, D.W., and Wemers, W.T. 1989. Rock Mechanics of the Ekofisk

Reservoir in the Evaluation of Subsidence, Journal of Petroleum Technology, July. SPE 17854.

Kenter, C.J.., Blanton, T.L., Schreppers, G.M.A., Baaijens, M.N., and Ramos, G.G. 1998. Compaction Study for Shearwater Field. SPE/ISRM Rock Mechanics in Petroleum Engineering, Trondheim, Norway, 8-10 July. SPE 47280.

Khan, M., and Teufel, L.W. 1996. Prediction of production-induced changes in reservoir stress state using numerical model. SPE Annual Technical Conference and Exhibition, Denver, Colorado, 6-9 October. SPE 36697.

Khan, M., Teufel, L.W., Zheng, Z., and Baker, A. 2000. Determining the Effect of Geological and Geomechanical Parameters on Reservoir Stress path through Numerical Simulation. SPE Annual Technical Conference and Exhibition, Dallas, Texas, 1-4 October. SPE 63261.

Khilyuk L.F., Chilingar G.V., Robertson J.O., Endres B. 2000. Gas Migration: Events Preceding Earthquakes. Butterworth-Heinemann, USA.

King, G.C.P., Stein, R.S., and Lin, J. 1994. Static stress changes and the triggering of earthquakes. The Bulletin of the Seismological Society of America **84:** 935-953.

Koide, H., Tazaki, Y., Noguchi, Y., Nakayama, S., Iijima, M., Ito, K., and Shindo, Y. 1992. Subterranean containment and long-term storage of carbon dioxide in unused aquifers and in depleted natural gas reservoirs. Energy Conversion & Management, **36:** 619-626.

LaFleur, K.K., and Johnson, A.K. 1973. Well stimulation in the North Sea: a survey. SPE European Meeting, London, United Kingdom, 2-3 April. SPE 4315.

Lahaie, F., and Grasso, J.R. 1999. Loading rate impact on fracturing pattern: Lessons from hydrocarbon recovery, Lacq gas field, France. Journal of Geophysical Research. **104(B8)**: 17941-17954.

Lewis R.W., Makurat, A., and Pao, W.K.S. 2003. Fully coupled modeling of seabed subsidence and reservoir compaction of North Sear oil fields. Hydrogeology Journal 11(1): 142-161.

Love, A.E.H. 1944. A treatise on the mathematical theory of elasticity, Dover Publications, New York, pp. 186-189.

Lubomir, F.J., and Urrea, V.H.N. 1990. Geology and diagenetic history of overpressured sandstone reservoirs, Venture gas field, offshore Nova Scotia, Canada. AAPG Bulletin 74(10): 1640-1658

Mase G.E. 1970. Continuum Mechanics, Schaum's Outline Series, McGraw-Hill, New

York, 8-23.

Mathsoft, 2002. Mathcad 11 User's Guide. Mathsoft Engineering and Education Inc., Cambridge MA.

Maury, V.M.R., Grasso, J.R., and Wittlinger, G. 1992. Monitoring of subsidence and induced seismicity in the Lacq Gas Field (France): the consequences on gas production and field operation. *Engineering Geology* **32:**123.

Maxwell, S.C., Urbancic, T.I. 2001. The role of passive microseismic monitoring in the instrumented oil field, The Leading Edge **20(6):** 636-639.

Maxwell, S.C., Young, R.P., Bossu, R., Jupe, A., and Dangerfield, J. 1998. Microseismic Logging of the Ekofisk Reservoir, in Eurock98, Proceedings SPE/ISRM Rock Mechanics in Petroleum Engineering, Trondheim, Norway, 8-10 July 1998, Vol. 1, pp. 387-394. SPE 47276.

McLellan, P.J., Lawrence, K.H., and Cormier, K.W. 1992. A multiple-zone acid stimulation treatment of a horizontal well, Midale, Saskatchewan, Journal of Canadian Petroluem Technology, **31(4):** 71-82.

Mindlin, R.D. 1936. Force at a point in the interior of a semi-infinity solid, *Physics,* **13:** 195-202.

Mindiin, R.D., and Cheng, D.H. 1950. Nuclei of strain in the semi-infinite solid, Journal of Applied Physics, **21:** 926-930.

Morita, N., Whitfill, D.L., Nygaard, O., and Bale, A. 1989. A Quick Method To Determine Subsidence, Reservoir Compaction, and In-Situ Stress Induced by Reservoir Depletion. Journal of Petroleum Technology **41(1):** 71-79. SPE 17150.

Morrow, C., Radney, B., and Byerlee, J. 1992. Frictional strength and the effective pressure law of montmorillonite and illite clays. In: Earthquake Mechanics and Transport Properties of Rocks, Editors: B. Evans and T.F. Wong, London: Academic Press, pp. 69-88.

Mulders, F.M.M. 2003. Modelling of stress development and fault slip in and around a producing gas reservoir. Ph.D. Thesis. Delft University of Technology, Netherlands.

Munns, J.W. 1985. The Valhall Field: A geological overview. *Marine and Petroleum Geology* **2(1):** 23-43.

Mura, T. 1982. Micromechanics of defects in solids. Martinus Nijhoff Publishers, The Hague, Netherlands.

NASCENT. 2005. Natural analogues for the geological storage of CO2. NASCENT Report 2005/6 March.

Noorishad, J., and Tsang, C.F. 1987. Simulation of coupled thermal-hydraulic-mechanical interactions in fluid injection into fractured rocks. In: Coupled Processes Associated with Nuclear Waste Repositories. Ed. Tsang, C.-F.: Academic Press. p. 673-678.

Ochs D.E., Chen, H., Teufel, L.W. 1997. Reslating in-situ stresses and transient pressure testing for a fractured well, SPE Annual Technical Conference and Exhibition, San Antonio, Texas, 5-8 October. SPE 38674.

Odonne F., Ménard, I., Gérard, J.M., and Rolando, J.P. 1999. Abnormal reverse faulting above a depleting reservoir. Geology; **27(2):** 111–114.

Orlic, B., and Schroot, B. 2005. The mechanical impact of CO_2 injection, EAGE 67th Conference & Exhibition, Madrid, Spain, 13 - 16 June.

Ottemöller L., Nielsen, H.H., Atakan, K., Braunmiller, J., and Havskov, J. 2005. The 7 May 2001 induced seismic event in the Ekofisk oil field, North Sea, Journal of Geophysical Research, **110:B10301.**

Papamichos, E., Vardoulaskis, I., and Hell, K. 2001. Overburden modeling above a compacting reservoir using a trap apparatus. Physics and Chemistry of the Earth. 26(1-2): 69-74.

Rodin, G.J. 1996. Eshelby's inclusion problem for polygons and polyhedra. Journal of Mechanics and Physics of Solids, **44:** 1977-1995.

Roest, J.P.A., and Kuilman, W. 1994. Geomechanical analysis of small earthquakes at the Eleved gas reservoir, SPE/ISRM Rock Mechanics in Petroleum Engineering Conference, Delft, The Netherlands, 29-13 August. SPE 28097.

Rudnicki, J.W. 1999. Alteration of regional stress by reservoirs and other inhomogeneities: stabilizing or destabilizing? Proceeding of 9th International. Congress on Rock Mechanics, Paris, France. Swets & Zeitlinger, Lisse, Netherlands, Vol. 3, pp. 1629-1637.

Rutledge J.T., Fairbanks, T.D., Albright, J.N., Boade, R.R., Dangerfield, J., Landa, G.H. 1994. Reservoir microseismicity at the Ekofisk oil field. Eurock 94: International Conference on Rock Mechanics in Petroleum Engineering, Balkema, Rotterdam, 29 August-1 September. SPE 28099.

Rutqvist, J., Wu, Y.S., Tsang, C.F., Bodvarsson, G. 2002. A modeling approach for analysis of coupled multiphase fluid flow, heat transfer, and deformation in fractured porous rock, International Journal of Rock Mechanics & Mining

Sciences 39: 429–442.

Samier, P., Onaisi, A., Fontaine, G. 2006. Comparisons of uncoupled and various coupling techniques for practical field examples, SPE Journal, 11(1): 89-102. SPE 79698.

Santarelli, F.J., Tronvoll, J.T., Svennekjaier, M., Skeie, H., Henriksen, R., and Bratli, R.K. 1996. Reservoir Stress Path: The Depletion and the Rebound. SPE/ISRM Rock Mechanics in Petroleum Engineering, Trondheim, Norway, 8-10 July. SPE 47350.

Schutjens, P.M.T.M., Hanssen, T.H., Hettema, M.H.H., Merour, J., de Bree, J.Ph., Coremans, J.W.A., and Helliesen, G. 2001. Compaction-induced porosity/permeability reduction in sandstone reservoirs: Data and model for elasticity-dominated deformation. SPE Annual Technical Conference and Exhibition, SPE, New Orleans, Louisiana, 30 September-3 October.

Schwall, G.H., and Denney, C.A. 1994. Subsidence induced casing deformation mechanisms in the Ekofisk Field. Rock Mechanics in Petroleum Engineering, Balkema, Rotterdam, Netherland, 29 August-1 September. SPE 28091.

Segall, P. 1985. Stress and subsidence resulting from subsurface fluid withdrawal in the epicentral region of 1983 Coalinga earthquake. *Journal of Geophysical Research* **90:** 6801-6816.

Segall, P. 1989. Earthquakes Triggered by Fluid Extraction, Geology **17:** 942-946.

Segall, P. 1992. Induced stresses due to fluid extraction from axisymmetric reservoirs. Pure & Applied Geophysics, **139:** 535–560.

Segall, P., and Fitzgerald, S.D. 1998. A note on induced stress change in hydrocarbon and geothermal reservoirs. Tectonophysics, **289(1-3):** 117-128.

Segall, P., Grasso, J.R., and Mossop, A. 1994. Poroelastic stressing and induced seismicity near the Lacq gas field, southwestern France. Journal of Geophysical Research **99(B8):** 15423-15438.

Seremet, V.D. 2003. Handbook of Green's Functions and Matrices. WIT Press: Boston.

Sminchak, J., and Gupta, N. 2003. Aspects of induced seismic activity and deep-well sequestration of carbon dioxide. Environmental Geosciences, **10(2):** 81-89.

Smith S.A., McLellan P., Hawkes C.D., Steadman E.N., and Harju J.A. 2008, Geomechanical Testing and Modeling of Reservoir and Cap Rock Integrity in an Acid Gas EOR/Sequestration Project, Zama, Alberta, Canada. Poster presented at the 9th International Conference on Greenhouse Gas Control Technologies,

November 16 – 20, 2008, Washington DC.

Smith S.A., Sorensen J.A., Steadman E.N., Harju J.A., Jackson W.A., Nimchuk D., and Lavoie, R. 2007. Zama Acid Gas EOR, CO2 Sequestration and Monitoring Project. Sixth Annual Conference on Carbon Capture & Sequestration, Pittsburgh, PA, USA, May 7, 2007.

Stauffer, M.R., and Gendzwill, D.J. 1987. Fracture in the Northern plains, stream patterns, and the mid-continent stress field. Canadian Journal of Earth Science, **24(6):** 1086-1097.

Strachan, C.J., Heath, S.M., White, K., and Williams, G. 2004. Experience with Pre-Emptive Squeeze Treatments on BP Magnus with Aqueous Based Scale Inhibitors. SPE International Symposium on Oilfield Scale, Aberdeen, United Kingdom, 26-27 May. SPE 87462.

Streit, J.E., and Hillis, R.R. 2002. Estimating fluid pressures that can induce reservoir failure during hydrocarbon depletion. Rock Mechanics Conference, SPE/ISRM, Irving, Texas, 20-23 October.

Sulak, R.M. 1991. Ekofisk Field: the first 20 years. Journal of Petroleum Technology, October, 1265-1271. SPE 20773.

Talbot, D. 2008. Observing Buried Carbon Dioxide: A project proves that millions of tons of the sequestered gas can be safely monitored. Techonlogy Review Published by MIT. November 20. Web address: http://www.technologyreview.com/printer_friendly_article.aspx?id=21694&channel=energy&section=

Teufel, L.W., and Rhett, D.W. 1991. Geomechanical evidence for shear failure of chalk during production of the Ekofisk field. 66th Annual Technical Conference and Exhibition of the Society of Petroleum Engineering, Dallas, Texas, 6-9 October. SPE 22755.

Teufel, L.W., Rhett, D.W., and Farrell, H.E. 1991. Effect of reservoir depletion and pore pressure drawdown on in situ stress and deformation in the Ekofisk Field, North Sea. In: Roegiers J.C. Rock Mechanics as a Multidisciplinary Science . Balkema, Rotterdam, pp. 63–72.

Townend, J., and Zoback, M.D. 2000. How faulting keeps the crust strong. Geology, **28:** 399-402.

Tucker, R.L. 1979. Practical pressure analysis in evaluation of proppant selection for the low-permeability highly geopressured reservoirs of the McAllen Ranch (Vicksburg) Field. Symposium on Low Permeability Gas Reservoirs, Denver,

Colorado, 20-22 May. SPE 7925.

Warner, D.L. 1968. Subsurface disposal of liquid industrial wastes by deep-well injection. In: Subsurface Disposal in Geological Basins - A Study of Reservoir Strata. Editor: J.E. Galley, American Association of Petroleum Geologists, pp. 11-20.

Wesson, R.L., and Nicholson, C. 1987. .Earthquake Hazard Associated with Deep Well Injection. Prepared by the U.S. Geological Survey. Open-File Report, pp. 87-331.

Wiprut, D., Zoback, M.D. 2000. Fault reactivation and fluid flow along a previously dormant normal fault in the northern North Sea. Geology, **28:** 595-598.

Wetmiller, R.J. 1986. Earthquakes near Rocky Mountains House, Alberta and their relationship to gas production facilities: Canadian Journal of Earth Sciences, **23:** 172–181.

Whittaker, S., Rostron, B., Khan, D., Hajnal, Z., Qing, H., Penner, L., Maathuis, H., and Goussev, S. 2004. Theme 1: Geological Charactrization In: IEA GHG Weyburn CO_2 Monitoring & Storage Project Summary Report 2000-2004 Edited by: M. Wilson, and M. Monea, PTRC, Regina.

Wong R.C.K, and Lau, J. 2008. Surface heave induced by steam stimulation in oil sand reservoirs, Journal of Canadian Petroleum Engineering, **47(1):** 13-17.

Wu, B., and Addis, M.A. 1998. Stress Estimation in Faulted Regions: The Effect of Residual Friction. SPE/ISRM Rock Mechanics in Petroleum Engineering, Trondheim, Norway, 8-10 July. SPE 47210.

Yerkes, R.F., Castle, R.O. 1970. Surface deformation associated with oil and gas field operations in the United States, Proceeding of International Association of Hydrological Science and UNESCO Land Subsidence Symposium, Vol. VI, pp. 55-66.

Zoback, M.D. 2007. Reservoir Geomechanics, Cambridge University Press, Cambridge.

Zoback, M.D., and Zinke, J.C. 2002. Production-induced normal faulting in the Valhall and Ekofisk oil fields. Pure & Applied Geophysics **159:** 403-420.

Zweigel, P., and Heil, L.K. 2003. Studies on the likelihood for caprock fracturing in the Sleipner CO_2 injection case, Report from Sinteff Petroleum Research.